FABRICATION OF HYBRID INORGANIC AND ORGANIC PHOTOVOLTAIC CELLS

David Ian Black

Emerging Technologies Research Centre

Thesis submitted to De Montfort University for the degree of Doctor of Philosophy

(May 2011)

Author's Declaration

This thesis contains the results of research undertaken by the author, under the supervision of Dr Shashi Paul and Dr Iulia Salaoru between April 2008 and May 2011, at the Emerging Technologies Research Centre, De Montfort University. All results are entirely the outcome of my own research and nothing is done in collaboration except where explicitly stated or indicated by citations.

The contents of this thesis have not been submitted, in whole or in part, for any other degree or diploma at any other academic institutions.

Permission is hereby granted to consult or copy the information contained herein for the purpose of private study only.

This thesis has been prepared in accordance with the regulations underlined by De Montfort University for the degree of Doctor of Philosophy.

The information contained within this thesis is confidential.

David Ian Black

Abstract

The world's energy demands are increasing annually, as a result of both an increasing population and increasing industrialisation. Photovoltaics offer one potential low carbon (in use if not in fabrication) method of generating electrical power. Traditional semiconductor devices have been used for over a century now and can be used for applications as varied as home use, grid power generation or in satellites in space.

Organic photovoltaic devices are a relatively recent development which offers potentially low cost easy to fabricate devices that can be deposited on a variety of substrates. Organic photovoltaic devices are let down by their generally low efficiencies when compared to inorganic or conventional semiconductor devices. A method to increase the efficiency of these devices is to blend the best qualities of organic and inorganic materials into a hybrid solar cell. Two main groups of hybrid photovoltaic devices currently exist, the Grätzel Cell and some varieties of bulk heterojunction solar cells. It was decided to focus on bulk heterojunction cells for a variety of reasons of which the most important is ease of fabrication.

Organic heterojunction photovoltaic devices with active layers comprising poly(3-hexylthiophene) (P3HT) and [6, 6]-phenyl-C_{61}-butyric acid methyl ester (PCBM) have been investigated by many research groups since the 1990s and offer the potential of flexible devices with a small number of steps in the fabrication process. These devices have not yet reached their full potential, but their efficiency is increasing year on year. This thesis demonstrates for the first time that, by fabricating hybrid heterojunction devices using ferroelectric nanostructures in the active layer, the characteristics of these hybrid devices show improvements when compared to control samples without ferroelectric nanoparticles. Electrical and spectroscopic measurements show that there are increases in the permittivity of the active layer, the absorption of photons in the visible spectrum, photoconductivity and in the overall relative efficiency of the devices. These effects have been demonstrated for both poly(3-hexylthiophene) and dihexyl-sexithiophene devices. In the P3HT devices with ferroelectric nanoparticles an almost fourfold increase in efficiency was demonstrated compared to the P3HT/PCBM control with power conversion efficiencies of 2.52% and 0.53% respectively.

Acknowledgements

I would like to express my gratitude to the following people and organisations:
Dr Shashi Paul for his expert advice and guidance and for his support and training.

Dr Iulia Salaoru for assistance and training in spin coating, FTIR measurements and optimising and fabricating solar cells.

Dr Richard Cross for assistance and training in the use of many pieces of equipment within EMTERC and for allowing me to assist in repairs to broken down machinery where possible.

Mr Paul Taylor, for ordering equipment, supplies and components and for training on the use of and repairing the equipment.

Dr Michael Needham and Miss Rachel Keeling for taking the SEM images from my samples.

My fellow students for support and encouragement.

The Graduate School Office for their advice and training courses.

My wife Lorraine and our children Louise and Rebekah for their support of me giving up full time permanent employment to undertake my PhD.

Mr Mick Kissoon for helping keep me grounded in reality.

The Engineering and Physical Sciences Research Council (EPSRC) for paying my university fees and providing me with a bursary to cover living expenses.

Table of Contents

Table of Figures

Table of Tables

Chapter 1

1 Thesis Synopsis

1.1 Introduction

The work described in this thesis began at De Montfort University in April 2008 as part of an EPSRC funded studentship. Initially there were two possible avenues of investigation; thin film inorganic photovoltaic devices or organic photovoltaic devices. While both options were promising avenues of investigation, after a brief initial literature review, organic photovoltaics were felt to offer the greatest opportunities for original work.

Organic photovoltaic devices are a relatively recent development and were first investigated in the 1990s [1]. They offer potentially low cost, easy-to-fabricate devices that can be deposited on a variety of substrates. They have a number of significant drawbacks such as: photovoltaic efficiencies demonstrated to date are lower than inorganic devices, lifetimes of devices are significantly lower than traditional materials and the devices degrade quickly after fabrication if not encapsulated as they absorb moisture from the air [2, 3]. A possible solution to this inefficiency was to blend the best qualities of organic and inorganic materials into a hybrid solar cell. Two main groups of hybrid photovoltaic devices currently exist, dye sensitised solar cells of which the most widely known is the Grätzel Cell and some varieties of bulk heterojunction solar cells [4-6]. It was decided to focus on bulk heterojunction cells for a variety of reasons; Firstly the efficiency of dye sensitised cells has remained virtually static for over a decade now, while bulk heterojunction devices improve continually and will most likely achieve efficiencies greater than those shown by dye sensitised cells in a few years or less [1, 7]. Secondly, many iterations of dye sensitised cells use liquid electrolytes which can potentially leak resulting in either a reduction in function or complete failure of the device and those using solid state electrolytes have a much reduced efficiency [8-10]. Thirdly, they can be quickly and simply fabricated onto glass or flexible plastic

substrates which could potentially result in cost savings compared to traditional silicon devices.

An extensive, and ongoing, literature review took place in parallel with learning the fabrication and characterisation techniques necessary to investigate the properties of these devices. One fact revealed by this review was that organic semiconductor devices operate in a subtly different way to conventional inorganic semiconductors; in organic devices rather than producing an electron-hole pair on absorption of a photon of the appropriate wavelength an exciton is produced. An exciton is a quasi particle that comprises an electron and a hole bound by Coulomb forces. It became apparent that the properties of excitonic materials were strongly dependent upon permittivity and that by increasing the permittivity the active layer of the cell the efficiency might be increased [11, 12].

A number of materials including metallic and ferroelectric nanoparticles have been used to increase the permittivity of polymers and epoxy blends for use in capacitors, gate dielectrics, memory devices and power storage devices [13, 14]. A number of these materials including silver nanoparticles (§Appendix C) and ferroelectric nanoparticles were considered before concluding that ferroelectric nanoparticles were the most suitable materials for this work [13-17]. Ferroelectric nanoparticles were selected because of their high permittivities, relatively low toxicity and demonstrated increase in permittivity when used as filler in a polymer matrix [13, 17, 18].

This thesis describes the theoretical framework for both inorganic and organic semiconductor photovoltaic devices and the experimental methodology and results that were carried out in an attempt to demonstate the improvements obtained by incorporating ferroelectric nanoparticles into polymer matrices.

1.2 Organisation of thesis

This thesis is divided into nine subsequent describing the history, science, fabrication methodology, characterisation and results of this work.

Chapter 2 gives a brief introduction to the background of this thesis, including a brief history of photovoltaic devices and an overview of current global energy use and the reasons for attempting this work. This chapter also includes an overview of itself and the subsequent chapters in the thesis.

Chapter 3 comprises an introduction to the science of both inorganic and organic photovoltaic devices culminating in an introduction to the exciton and a description of how the dissociation of this pseudo particle is responsible for the generation of charge carriers in organic photovoltaic devices. An overview of the basic types of solar cells is also included in this chapter.

Chapter 4 describes the various materials used in this work including polymers, carbon allotropes, silver nanomaterials and ferroelectric nanoparticles.

Chapter 5 describes the various methods used in the fabrication of the devices used in this work from cleaning of substrate materials through to the fabrication of a fully functioning multi-layer photovoltaic device.

Chapter 6 introduces the characterisation techniques used to determine the optical and electrical characteristics of the devices fabricated in this work along with various microscopy techniques used to visualise the component particles and surfaces of the finished devices.

Chapter 7 describes the optimisation and characterisation of the transparent electrode layer from the deposition of the indium tin oxide layer to a comparison with commercially procured films with and without a layer of PEDOT:PSS.

Chapter 8 introduces the concept of permittivity in both insulating and conductive mediums and describes how this material property affects the production and dissociation of excitons in photoconductive materials.

Chapter 9 describes the optimisation and characterisation of the active layer of the solar cell, including results for completed photovoltaic devices. The results are discussed in detail and it is shown that the addition of ferroelectric nanoparticles to the active layer of these devices clearly produces a measurable effect in the electrical characteristics of the devices.

Finally Chapter 10 reviews the previous chapters and presents the conclusions of this thesis in one place together with some suggestions on how the work could have been improved and some possible future lines of enquiry should funding be available to continue with this work.

There are also three appendices:

Appendix A contains detailed methodologies used in this work

Appendix B contains descriptions of the shadow masks used in this work.

Appendix C Silver Nanomaterials

Appendix D contains a glossary of the main abbreviations used in this thesis.

1.3 Peer Reviewed Publications and Conference Presentations

1.3.1 Conference Papers

Black, D., I Salaoru and S. Paul, Fabrication of Photovoltaic Devices using Novel Organic Polymer/Nanostructure Blends, MRS Fall 2010 Mater.Res.Soc.Symp.Proc, 1303, (2011), Boston, (Published).

Black, D. and S. Paul, Photoconductivity Measurements of Sublimated Organic Polymer/Nanostructure Blends compared with similar blends prepared by spin coating, in MRS Spring 2010. 2010, MRS: San Francisco. (Published)

Black, D. and S. Paul. Getting Power from Plastic - Solar Power Generation Using Blends of Organic Polymers and Nanostructures. in Energy and Sustainable Development: 1st Annual IESD PhD Conference. 2010. De Montfort University, Leicester: De Montfort University. (Published)

1.3.2 Publications

Black, D., S. Paul, and I. Salaoru, Ferroelectric Nanoparticles in Polyvinyl Acetate (PVAc) Matrix - A Method to Enhance the Dielectric Constant of Polymers, Nanoscience and Nanotechnology Letters, 2010. 2: p. 41-45. (published)

S. Paul and D. Black, UK Patent No. GB0916833.7 (2009) (published)

1.3.3 Work in Progress

Black, D., I. Salaoru and S. Paul, Fabrication of Efficient Photovoltaic Devices using P3HT/PCBM blends with additional Ferroelectric Nanoparticles, Organic Electronics, submitted for review.

1.4 Important Outcomes of the Research

The following section details the important outcomes obtained while carrying out this research.

Transparent electrode layers of indium tin oxide have been optimised by radio frequency magnetron sputtering as part of this work; although commercially available films are available this is the first time this has been achieved at De Montfort University (§ Chapter 7).

By carrying out capacitance measurements to metal insulator metal (MIM) and metal semiconductor metal (MSM) structures an increase in permittivity has been observed for ferroelectric nanoparticle and polymer blends (§ 8.8 and 8.9).

Spectroscopic studies have revealed that the absorption of photons in the visible part of the spectrum is increased in polymer blends containing ferroelectric nanoparticles (FENP) compared to a control sample without FENP (§ Chapter 9).

Current-Voltage (I-V) measurements (§ 6.3.1) of polymer blends with aluminium gap cells (§ Appendix A), under illuminated and non illuminated conditions, have measured an increase in the photonconductivity of polymer blends containing FENP compared to those without (§ Chapter 9).

A novel blend of ferroelectric nanostructures, poly(3-hexylthiophene) (P3HT) and [6, 6]-phenyl-C_{61}-butyric acid methyl ester (PCBM) has been used to fabricate hybrid organic/inorganic photovoltaic devices. These devices comprise a glass substrate coated with indium tin oxide (ITO) and a layer of PEDOT:PSS to form the first electrode. The active layer was deposited by spin coating and finally, metallic top contacts have been added by thermal evaporation. The devices were characterized using standard I-V measurements under illuminated and dark conditions using a solar simulator and a source-voltage device and the results indicate a difference in efficiency compared to similar devices fabricated at the same time without the novel nanostructures. Additional UV-Vis measurements were used to determine the absorption characteristics of the active layers. The results demonstrate an improvement in the absorption of light in the visible region and higher open circuit voltages and short circuit currents compared to P3HT/PCBM alone leading to higher relative power conversion efficiencies of 2.52% with FENP and 0.53% for the P3HT/PCBM control samples (§ 9.3).

Chapter 2

2 Background Information

2.1 World Energy Use

The worlds demand for energy is increasing year on year and it is essential that cost effective and non carbon emitting ways to produce energy are adopted. Global warming is now accepted as fact by the majority of the scientific and political communities; this combined with the fact that our fossil fuel reserves have a limited life means that a move towards alternative forms of energy production is essential. In the terms of this thesis alternative energy is defined as any form of energy not derived from fossil fuel products.

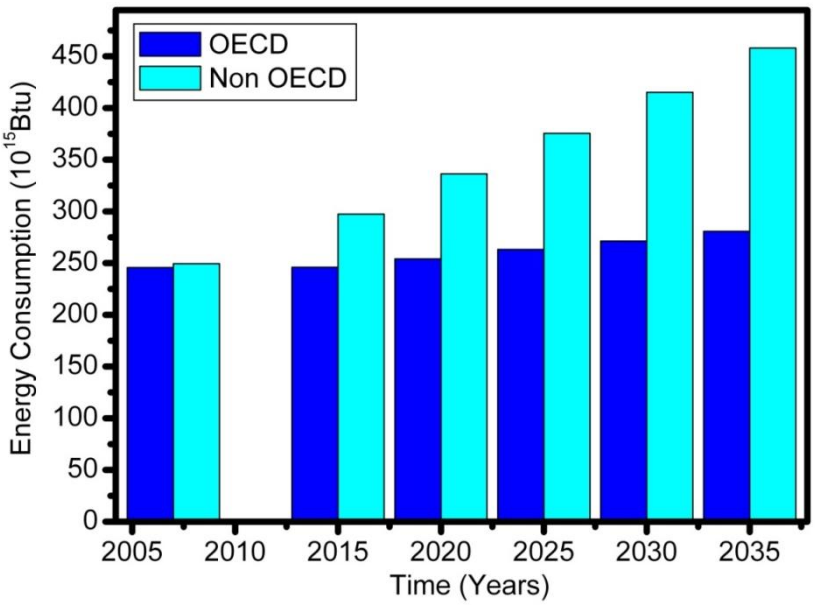

Figure 2-1. Increasing energy use by type (source US Energy Information Administration (2008) [19]).

As can be seen from Figure 2-1, based on data from the US EIA for countries both within and without the Organization for Economic Cooperation and Development (OECD), the world consumption of energy is increasing steadily. The units on the y axis of this graph are in quadrillion (10^{15}) British thermal units (Btu), where one Btu

is equivalent to 1,055.05585 joules. With the growth of technology in countries with large populations such as India and China is set to carry on increasing into the foreseeable future.

In a world with limited natural resources it therefore makes good sense for the long term survival and prosperity of mankind to move away from polluting sources of energy to "green" energy sources, however, at present the economics of renewable energy do not always make it a viable alternative to fossil fuels.

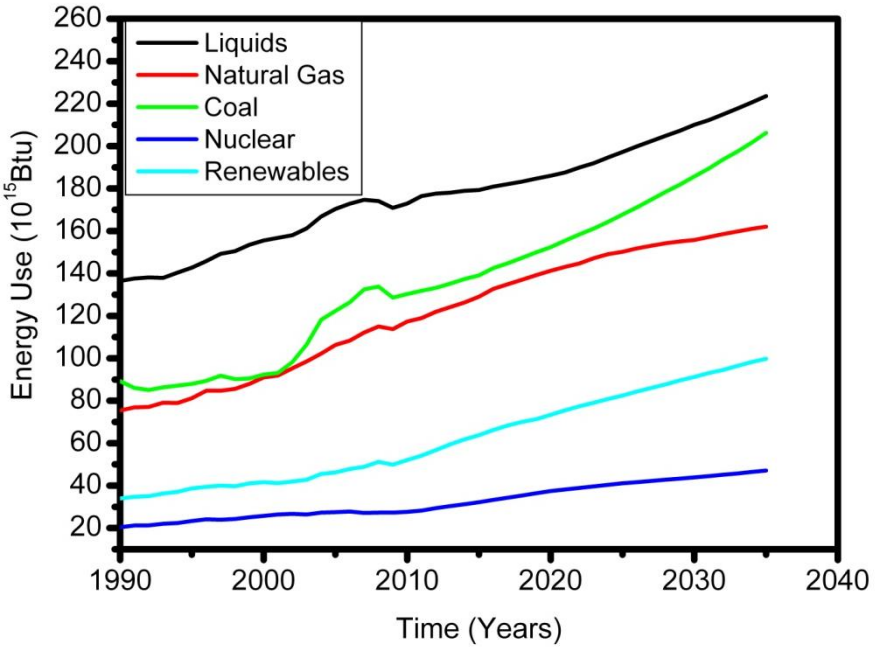

Figure 2-2. Projected world energy use by type, 1990-2035, (source US Energy Information Administration (2008) [19]).

Figure 2-2 above shows the same data as Figure 2-1, but broken down by type as it is projected to 2035. In this Figure "liquids" can be said to include oil and related fossil fuels. As can be seen at present there is still a tremendous reliance on fossil fuels with approximately 87% of the worlds energy needs being met from this source, nuclear and hydro-electric power are the major non fossil fuels but even these combined produce only 12% of the worlds energy needs [19]. The remaining 1% includes solar and all other non fossil fuel.

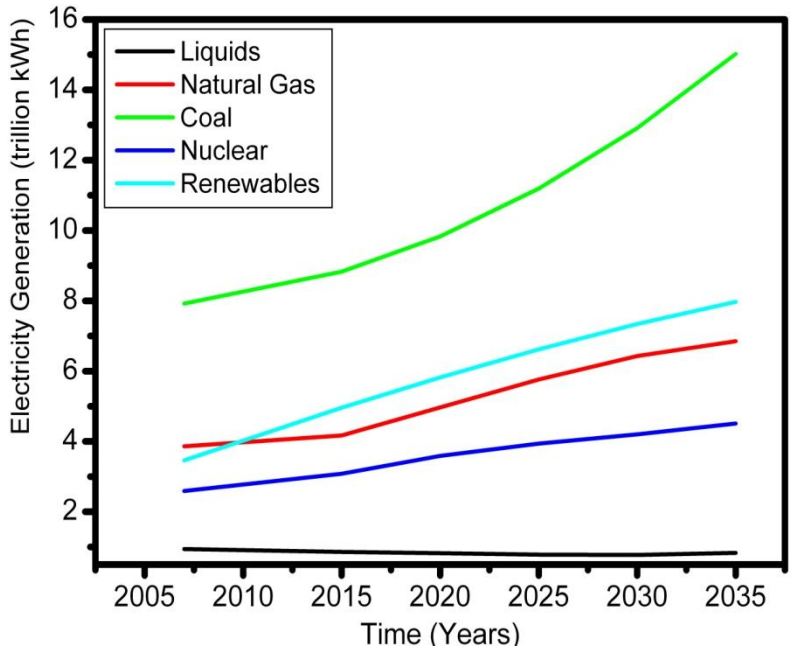

Figure 2-3. Electricity generation by type (source US Energy Information Administration (2008) [19]).

Figure 2-3 shows the current breakdown of the generation of electrical power in trillion kWh by various types of energy. Coal can be seen to be the most commonly used fuel for power generation, but renewable sources are set to increase into second place. Reliance on nuclear power is likely to increase in the near future as reserves of oil, coal, and natural gas diminish. Although uranium and other radioactive materials are also limited it is not envisaged modern fast breeder reactors will overcome this hurdle as they generate fuel for other reactors.

2.2 A Brief History of Solar Cells

The first reports of the photovoltaic effect date back to 1839, when Edmund Becquerel observed that a platinum electrode immersed in an electrolyte and exposed to a light source produced an electric current [20]. This work was improved upon 40 years later by William Adams and Richard Day, who discovered that selenium, when brought together with heated platinum contacts, produced an electric current. In 1894, the first large area solar cell was produced by Charles Fritts, which comprised a layer of selenium sandwiched between a layer of gold and another metal [20] and

this type of cell now bears his name. Over subsequent years the photovoltaic effect was discovered in other combinations of metals including copper-copper oxide, lead sulphide and thallium sulphide. It was discovered by Goldman and Brodsky [20] in 1914 that the photoelectric effects so far were the result of the barrier to current flow in one of the semiconductor interfaces, this idea was further developed in the 1930s by Walter Schottky and others and this barrier now bears his name.

It was not until the 1950s that silicon p-n junctions were manufactured, which led to the development of silicon electronics. Following this, in 1954, Chapin, Fuller and Pearson of Bell Laboratories produced the first silicon solar cell, which had an efficiency of 6%, which was a significant improvement over other attempts of the same era [21], other cells soon followed including a cadmium sulphide p-n junction which also had an efficiency of 6%, although this failed to supplant silicon as the foremost photovoltaic (PV) material. The efficiency of PV devices continued to improve over the next few years and in the decades to follow.

The early solar cells were constructed using Czochralski grown monocrystalline silicon [21, 22] and this material continues to be used as a component of solar cells to date. Over the rest of the 1950s and 60s the use of solar cells increased as they were predominately used to power satellites, although they were too costly for domestic energy production, costing in the region of $200 per Watt at the time [20]. The first oil crisis in the 1970s prompted a surge of interest in PV and other alternative energy sources and led to increased funding and research in these areas this led to the development of the first non single crystal PV devices such as; polycrystalline silicon, amorphous silicon and thin film and organic semi-conductors [20, 21]. The commercialisation of solar power was pioneered by Dr Elliot Berman, who concentrated on using lower grade silicon to produce devices and reduced the cost from $200/W to $20/W [23]. He then utilised the technology to power cathodic protection systems in oil pipelines and signals on railway lines [23]

Since the 1970s interest in photovoltaics has increased and in the year 2008 PV production increased by 80% on the previous year with thin film devices accounting

for 12-14% of the market share [24]. During this time many advancements have taken place including; the first thin film devices in the late 1970s, multi-junction devices in the 1980s and organic devices in the 1990s [1, 23].

Use of photovoltaics in power generation is now taken very seriously and it is possible to obtain much of the power necessary to run a household from solar energy, indeed Germany is leading the way in Europe as the largest consumer of PV devices [25]. The increased efficiencies of the various types of PV cells are shown in Figure 2-4 below.

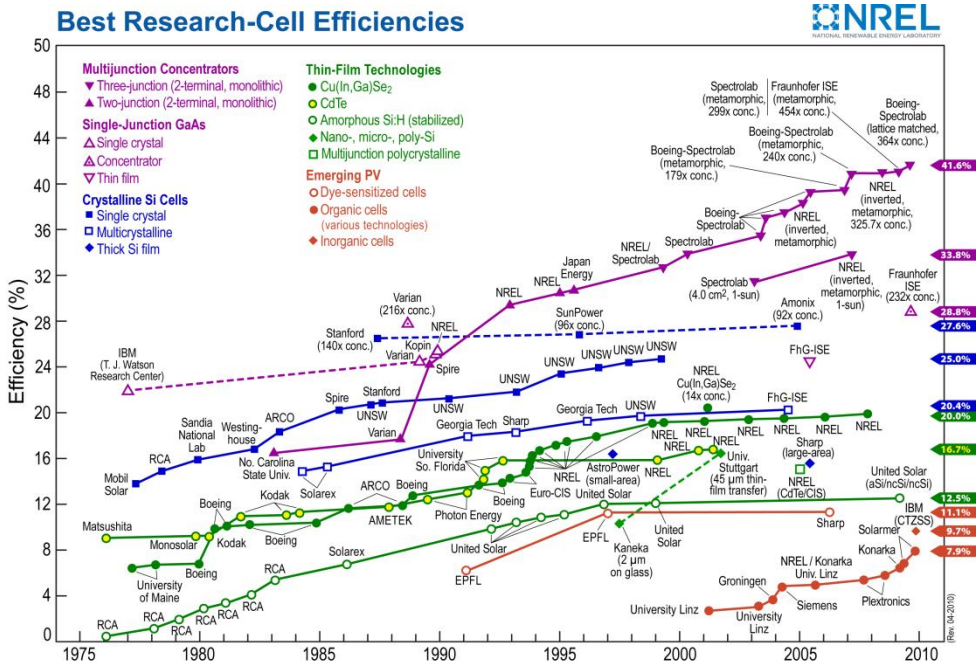

Figure 2-4. Improvements in solar cell efficiencies by type over time (Kazmerski (2010) [1], reproduced under licence).

As can be seen Si crystals still dominate as the primary material for PV devices, while they show very high efficiencies, these are usually obtained under laboratory conditions, the best commercially available PV devices generally have efficiencies in the region of around 22% [1].

The main driver for PV development is cost, in particular the cost per Watt of power generated. Although the efficiency of thin film, organic and other novel PV devices is still a long way below that of traditional PV cells it is anticipated that the relative

ease of processing these devices will result in cheaper solar cells in the future. At present there are two barriers to overcome; the first is the technical barrier of increasing the efficiency of organic PV devices to a level where they are commercially viable and the second is the cost of photoconductive polymers used in organic and hybrid photovoltaic devices, at present these materials are expensive, but this is probably due to the fact that only small quantities are produced. It may be that as production increases the cost will decrease, as with silicon which decrease in cost by 20% for each doubling of production [23].

2.3 Motivation for undertaking this work

Although photovoltaic power production currently represents only a fraction of the renewable energy production it is the fastest growing area of renewable energy [25]. Although there are a number of significant problems with solar energy, such as being unable to produce electricity at night, it has the potential to offer affordable energy production for much of the world's population. In addition the availability of materials such as Si is affected by the microelectronic market and there have been periods of shortages of these materials.

Organic solar cells have the potential to offer a cheaper, flexible alternative to silicon-based cells, although it should be clearly stated that the maximum efficiency of organic devices is unlikely to ever approach that of silicon or even the best thin film devices. The benefits will arise due to flexibility and reduced processing costs provided that the cost of electronic grade polymeric materials can be reduced by economies of scale. Currently the price of organic materials is not affected by fluctuations in the microelectronics market but the cost of research grade materials is high. The high material costs can in part be compensated for by the relatively quick and simple fabrication methods such as spin coating and inkjet printing.

The goal of this research was to investigate the potential for improving the efficiency of organic solar cells by modifying them with inorganic materials in particular ferroelectric nanoparticles such as barium titanate, strontium titanate and barium strontium titanate. It was decided to use the current "gold standard" of

heterojunction organic photovoltaic devices comprising a blend of Poly (3-Hexylthiophene) (P3HT) and Phenyl-C61-butyric acid methyl ester (PCBM) on ITO coated glass as the benchmark for this work. The main part of this work was to demonstrate that by adding ferroelectric nanoparticles to the active layer blend it was possible to cause a relative improvement in the efficiency of the hybrid blend. Ferroelectric and metallic nanoparticles have a proven effect in bi-stable organic memory devices, having been combined with insulating polymers such as poly-vinyl acetate (PVAc) and polystyrene (PS) [8-10]. Given the ease of processability of PVAc, this material was selected as a likely candidate material to test the permittivity enhancing properties of titanates. Once the permittivity enhancing effects could be demonstrated in an insulating polymer the effect could then be measured in conducting polymers [26, 27].

The maximum efficiency obtained in this work is not higher than that of the best current devices, largely due to the fact that it was not possible to fabricate them in a neutral atmosphere. The improvement demonstrated in this work is therefore an improvement on the best quality P3HT/PCBM control sample possible with the equipment available compared with the hybrid devices prepared in an identical way except that ferroelectric nanoparticles were added to the mix.

Chapter 3

3 Literature Review and Theory of Solar Cells

This chapter introduces the scientific concepts behind inorganic and organic solar cells and highlights the differences between the two. It begins with a general overview of the principles of inorganic photovoltaic devices, many of which are also applicable to organic devices. This section also includes an introduction to band theory and electron orbital's. The chapter concludes with sections on the characteristics of solar cells and comparisons of charge generation in inorganic and organic devices, in particular focussing on the excitonic nature of the latter.

3.1 The Science of Solar Cells

Although this work is primarily about organic photovoltaic devices it would be incomplete without an overview of the physics of Conventional Semiconductor (CSC) devices. Furthermore by understanding the underlying physics behind CSC devices will be useful in subsequent sections and will aid in understanding the operation of Excitonic Semiconductor (XSC) devices, which operate by similar, if more complicated, mechanisms.

3.1.1 Electrons in Solids

In order to define what a semiconductor device is it is necessary to understand the behaviour of electrons in solid materials, which in turn requires an understanding of the structure of atoms and how they fit together to form solid materials.

Solid materials can occur in either of two states; crystalline or amorphous, in crystalline materials the atoms form into regular arrays and in amorphous materials the atoms have short range order, i.e. over a few inter-atomic distances, but have no long range order. Examples of this include glasses such as silica (SiO_2).

Atoms comprise a positive core of protons and neutrons surrounded by a cloud of orbiting electrons which are negatively charged subatomic particles. The outermost

shell of electrons, called the valence electrons, is responsible for the chemical bonds between atoms. Three types of chemical bond exist – co-valent bonds, where atoms share electrons to complete their outer shells the theory of which was proposed by Lewis [28] and expanded upon by Langmuir [29], ionic bonds, where an atom gains or loses an electron to form an ion and metallic bonds, where the valence electrons are free to roam in the crystal lattice and hold the structure together due to attraction between the electrons and the positive nuclei.

Depending upon the constituent atoms and the type of structure, materials can be broken down into three groups; conductors, insulators and semiconductors. Conductors are generally, but not always, metallic and crystalline and have additional "free" electrons which allow electrical current to flow through the material. Insulators have no free electrons and do not generally allow electrical current to flow except under breakdown conditions when the material essentially fails in some way. Semiconductors, as the name implies, allow electrical current to flow in certain circumstances. And are essentially a halfway house between an insulator and a conductor. Semiconductors are very important materials in electronics and are the basis of devices such as diodes, transistors and photovoltaic cells.

3.1.2 Electrons, bands and orbitals

Electrons are part of a family of subatomic particles known as Fermions and obey the Pauli Exclusion Principle which states that no electrons in the same atom can occupy the same quantum state. In 1925 Louis De Broglie showed that electrons possess both particle and wave like qualities, which won him a Nobel prize [30] in 1929, a year after De Broglie's discovery Erwin Schrödinger proposed a generalised application of the wave equation to the hydrogen atom [31], which gave rise to the equation that now bears his name. The quantum state of an electron arises out of the time independent Schrödinger equation [31-33]:

$$\frac{-\hbar^2}{2m}\nabla^2\,\psi(r) + V\psi(r) = E\psi(r) \qquad 3.1$$

$\hbar$ is the reduced version of Plank's constant and equals h/2π, m is the effective mass of the electron, ψ is the wavefunction of the particle, r is the position of the particle in a given co-ordinate system, E is the energy of the particle, including both rest mass and kinetic energy, V is the potential energy of the particle and ∇^2 is a mathematical operator called Grad Squared and in Cartesian co-ordinates is equal to [34]:

$$\frac{\partial^2}{\partial x^2} + \frac{\partial^2}{\partial y^2} + \frac{\partial^2}{\partial z^2} \qquad 3.2$$

Thus for an infinitely deep potential well of width L, where $0 < x < L$, no solutions are allowed outside the potential well and ψ must be 0 at when $x = 0$ and L. Thus the Schrödinger equation becomes [32]:

$$\frac{-\hbar^2}{2m}\nabla^2\,\psi(r) = E\psi(r) \qquad 3.3$$

One possible solution to this equation is:

$$\psi = A\,sin\,kx + B\cos kx \qquad 3.4$$

Where A and B are proportionality constants and k is the wave vector. Since $\psi = 0$ at $x = 0$ then $B = 0$ and since $\psi = 0$ at $x = L$ then $A = 0$ or sin $kL = 0$. Thus:

$$k = n_x\pi/L \qquad 3.5$$

By substituting equation 3.5 into equations 3.3 and 2.4 we get:

$$E = h^2 n_x^2/8m^* L^2 \qquad 3.6$$

From this we can see that in this simple one dimensional case the energy levels allowed to the electron are defined by the quantum number n. This case has been used to

demonstrate the principle of energy levels in atoms, but in reality the picture is more complicated. Firstly this example has used Cartesian co-ordinates, but in order to properly model an atom in three dimensions it is necessary to use spherical co-ordinates. So for an isolated atom the potential energy (V) depends upon the radial distance *r* which is equal to $r = \sqrt{x^2 + y^2 + z^2}$, these co-ordinates have the following geometric relations [34, 35]:

$z = r \cos \theta$

$x = r \sin \theta \cos \varphi$

$y = r \sin \theta \sin \varphi$

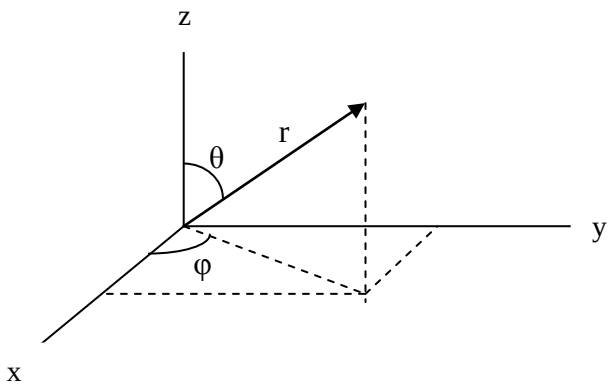

Figure 3-1. Geometric relations between spherical and rectangular co-ordinates.

The Schrödinger equation can also be expressed in spherical co-ordinates as shown below [35]:

$$-\frac{\hbar^2}{2mr^2}\frac{\partial}{\partial r}\left(r^2\frac{\partial\psi}{\partial r}\right)-\frac{\hbar^2}{2mr^2}\left[\frac{1}{\sin\theta}\frac{\partial}{\partial\theta}\left(\sin\theta\frac{\partial\psi}{\partial\theta}\right)+\frac{1}{sin^2\theta}\frac{\partial^2\psi}{\partial\varphi^2}\right]+V(r)\psi=E\psi \qquad 3.7$$

By making a number of substitutions and separating the variables of the above equation it becomes apparent that three quantum numbers are required to describe the behaviour of electrons orbiting a nucleus. For a full mathematical treatment of this, see appendix n of Eisberg and Resnick [36]. Rather than determining an energy level the spherical treatment of the Schrodinger equation predicts energy shells which have sub-structures known as orbitals. The three quantum numbers are; *n* which is known as the principle quantum number and determines which shell the electron inhabits, *l* is the azimuthal quantum number and determines the orbital angular momentum and *m* is known as the magnetic quantum number and is a projection of orbital angular momentum along a particular axis.

The later discovery by Pauli of the property of spin resulted in a fourth quantum number, it also became apparent that the Dirac equation which is a relativistic treatment of the Schrödinger equation also predicts the existence of spin [37]. This quantum number is called the spin projection quantum number and is the intrinsic angular momentum of the electron. The four quantum numbers are interdependent and are detailed in Table 1 [38] below:

Table 1. Quantum numbers and their meanings and relationships

Name of Quantum Number (QN)	Symbol	Meaning	Range of Values	Example Values
Principle QN	n	Determines the shell.	$1 \leq n$	n = 1, 2, 3,...
Azimuthal QN	l	Determines the sub-shell or orbital	$0 \leq l \leq n$-1	For n = 3 l = 0, 1, 2 (s, p, d)
Magnetic QN	m_l	Determines the orientation of the orbital	$-l \leq m_l \leq l$	For l = 2 m_l = -2, -1, 0, 1, 2
Spin projection QN	m_s	Spin of the electron	-½, ½	-½ (anti-clockwise) ½ (clockwise)

As can be seen the azimuthal quantum number determines which orbital the electron resides in, s, p and d denote the types of orbital, each of which has a specific shape. Additionally each orbital can only accept a maximum of two electrons, which will have opposite spins and ensures that the Pauli Exclusion Principle is not violated.

The name orbitals is a misnomer that dates back to Bohr theory where electrons were thought to orbit the nucleus of the atom in a way analogous to the orbits of the planets around the sun rather than the currently accepted quantum mechanical view that the electrons exist in a probabilistic cloud around the nucleus but in a quantised way that limits them to certain regions [33]. The shape of these regions is determined by the radial distribution function P(r) and the probability of finding an electron in the spherical shell of radius r and thickness dr is P(r)dr [39].

$$P(r)dr = \int_0^{2\pi} d\phi \int_0^{\pi} d\theta \psi^* \psi r^2 sin\,\theta\, dr \qquad 3.8$$

From this it is possible to deduce the shape of the orbital's as shown in Figure 3-2 [40] below.

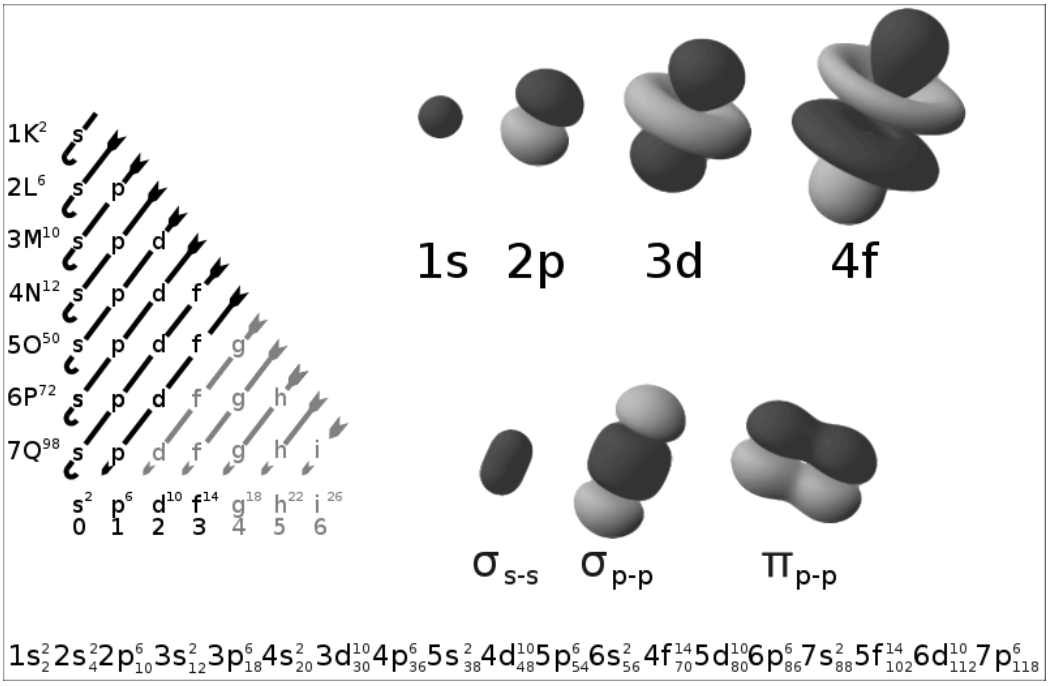

Figure 3-2. Shapes and order of electron orbital's in atomic shells (Fidi and Paul (2006) [40], reproduced with permission (public domain)).

As can be seen there are a variety of shapes of orbital and the order of the s and p orbitals is shown along the bottom of the figure. The majority of organic solar cells contain conjugated polymers, these are long chain polymers consisting of alternating single and double covalent bonds, in these materials conduction band electron(s) reside in the outermost p orbital [6, 41], these orbital's overlap to form a π bond (see bottom right of Figure 3-2) in a similar way to s orbital's which can overlap to form a σ bond. π Bonds are weaker than σ bonds and are partially responsible for conductivity in conjugated polymers by forming a delocalised π system i.e. one that can encompass the entire length of the polymer [42].

3.1.3 Crystal structure

The previous section describes the energy levels of a single atomic nucleus and its associated electron(s) but solar cells are not made of single atoms, but of bulk quantities of materials. When atoms join together in a solid they can form into either amorphous material or into an ordered crystalline state. Amorphous materials are similar to crystalline materials on a small scale e.g. have short range order, but on larger scales become randomly organised [20].

Crystalline materials are defined in terms of three translation vectors **a, b, c** so that the arrangement of atoms is identical when viewed from point **r** as from point **r'** such that:

$$r' = r + ua + vb + wc \qquad 3.9$$

where u, v and w are arbitrary integers. But this is merely a mathematical construction where the set of points in equation 3.9 defines a lattice, a crystal structure can only be formed when a basis of atoms is attached to each point of the lattice. The relationship can therefore be seen to be **Lattice + basis = crystal structure.** Therefore any two identical points in the lattice will be connected by a translation vector **T**, where:

$$T = ua + vb + wc \qquad 3.10$$

There are seven crystal lattice systems in three dimensions, which in combination with the six lattice centrings below and rotational symmetry (R) make a total of 14 Bravais lattices. These are detailed in Table 2 below. The lattice centrings are as follows [43] and relate to the crystal axes in Figure 3-3:

1. Primitive (P) – Latice points are located only at the corner of the cell.
2. Body Centred (I) – An additional lattice point at the centre of the cell
3. Face centred (F) – One additional lattice point at the centre of each face on the cell.

4. Centred on a single face (A, B or C) - One additional lattice point at the centre of face A, B or C.

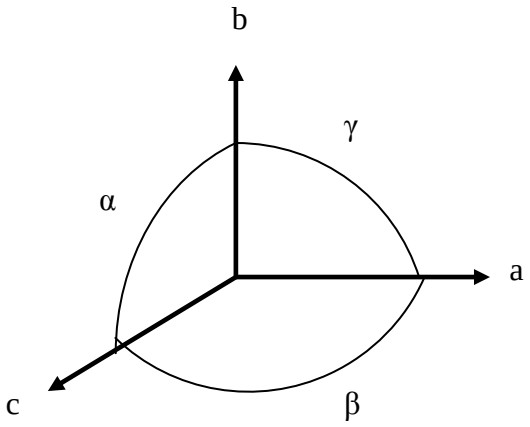

Figure 3-3. Crystal axes a, b and c, also showing angles α, β and γ.

Table 2. The fourteen Bravais lattices in three dimensions

Crystal System	Axes Restrictions	Angle Restrictions	Centre
Triclinic	$a \neq b \neq c$	$\alpha \neq \beta \neq \gamma$	P
Monoclinic	$a \neq b \neq c$	$\alpha = \gamma = 90^o \neq \beta$	P
			C
Orthorhombic	$a \neq b \neq c$	$\alpha = \beta = \gamma = 90^o$	P
			C
			I
			F
Tetragonal	$a = b \neq c$	$\alpha = \beta = \gamma = 90^o$	P
			I
Cubic	$a = b = c$	$\alpha = \beta = \gamma = 90^o$	P
			I
			F
Trigonal	$a = b = c$	$\alpha = \beta = \gamma = 120^o$, $\neq 90^o$	R (rotational symmetry)
Hexagonal	$a = b \neq c$	$\alpha = \beta = 90^o$ $\gamma = 120^o$	P

The position and orientation of crystal planes within the lattice can be described by a system called Miller Indices, which are made up of three integers, *h*, *k*, and *l*. The rules for Miller indices are [43]:

1. Find the intercepts for a plane on the axes a, b and c in terms of the lattice constants.
2. Take reciprocals of these numbers and reduce to three integers having the same ratio and present the result in the form (*hkl*).
3. Reciprocals with a negative value are presented with a bar over the negative term.

Examples of a few of the most important Miller Indices are presented in Figure 3-4 below.

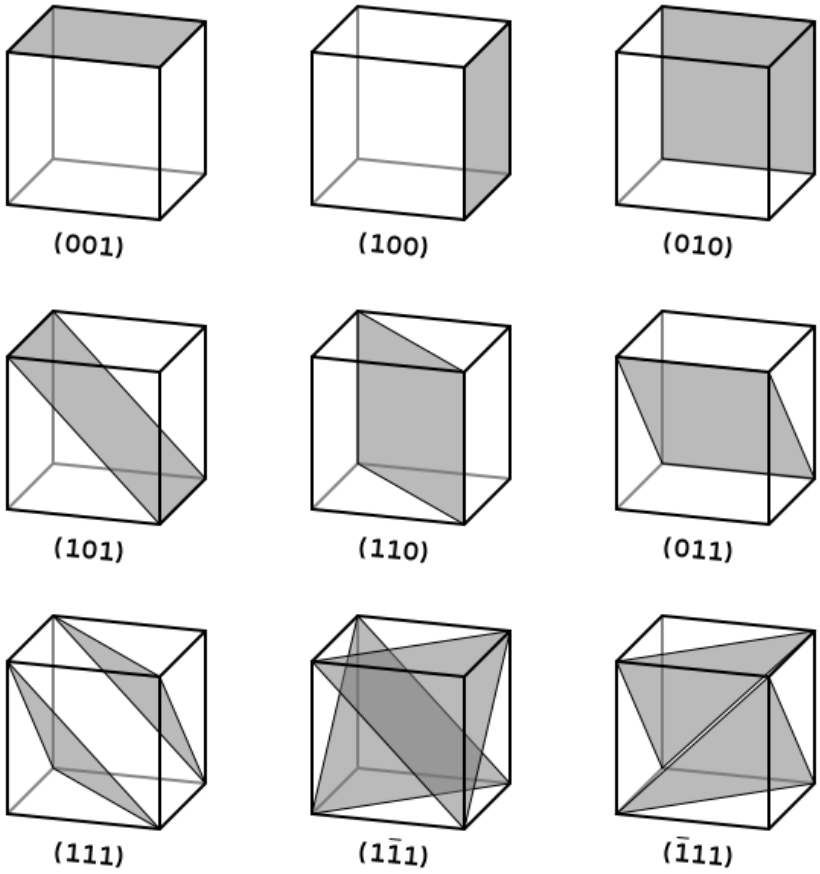

Figure 3-4. Examples of nine of the most common and important Miller Indices presented in a cubic crystal form for ease of understanding (Dang (2009) [44], reproduced under licence).

3.1.4 The Band Gap and Density of States

As two atoms are brought together their atomic orbitals combine and split into pairs of energy levels one of which is slightly higher and one of which is lower than the original states. As more atoms are added the splitting continues and the energy levels form a continuum of almost evenly spaced levels known as a band. In the simplest case of a monatomic material with atoms spaced a distance *a* apart the nuclei form a periodically varying potential [32]. Solving Schrödinger's equation (3.1) for the periodic potential shows that the wavefunction ψ must also have periodic solutions, these solutions are known as Bloch Waves [32, 43, 45] and are of the form:

$$\psi_k(r) = e^{jk.r} U_n(k, r) \tag{3.11}$$

Where $U_n(\boldsymbol{k}, \boldsymbol{r})$ is a periodic function in r and n is the band number. Bloch waves obey the Bragg equation which states that when the path difference between an integer number *n* of wavelengths then the scattered waves will interfere constructively. Numerically this is given as:

$$n\lambda = 2d \sin\theta \tag{3.12}$$

Where λ is the wavelength, *d* is the distance between reflective planes and θ is the angle of incidence of the waves. For a special case where the angle of incidence is normal to the reflective plane the Bragg equation reduces to:

$$n\lambda = 2d \tag{3.13}$$

This can be written in terms of the wave vector k as:

$$k = n\pi/d \tag{3.14}$$

For waves the energy in terms of the wavevector is given by:

$$E = \hbar^2 k^2 / 2m \qquad 3.15$$

In free space the *E-k* curve forms a parabola, but in a periodic potential the Bloch waves form standing waves which have two solutions depending upon the electron density in the material. These two solutions result in discontinuities of the E-k diagram which are known as Brillouin zones.

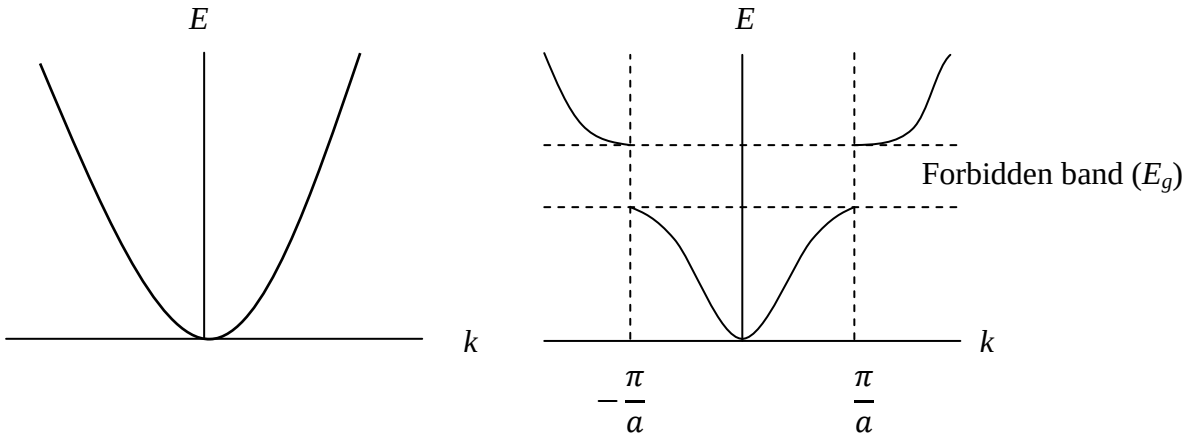

Figure 3-5. (a) Plot of Energy versus Wavevector for free electron. (b) Plot of energy versus wavevector for electron in monatomic lattice of lattice spacing a. The first Bragg reflection is at k = π/a and the energy gap Eg is shown (after Tanner and Kittel [32, 43].

The highest occupied band is called the Valence Band by physicists or Highest Occupied Molecular Orbital (HOMO) by chemists and the lowest unoccupied band is called the Conduction Band by physicists and the Lowest Unoccupied Molecular Orbital (LUMO) by chemists, these terms are interchangeable and will be used in both forms throughout this thesis. Where there is no band gap between the valence and conduction bands a continuum exists and the crystal lattice is conductive, where a band gap exists electrons will be less likely to cross the band gap. Typically at a temperature of absolute zero these materials will act as insulators, as they are warmed the atoms and electrons in the lattice gain energy and eventually electrons can become free. A material that does not have the capacity to have free electrons at room temperature is called an insulator [20]. An intermittent state with a band gap that is not as large as that

of an insulator is called a semiconductor; these materials are the subject of much of the rest of this section.

The Density of States (DoS) is dependent upon the dimensions of the material and the value of the wavevector **k** in that material. Since electrons can have either spin up or spin down there can be two states for each value of **k**. For example, in a cubic crystal of volume L^3, $(L/2\pi)^3$ values for **k** can exist. Thus per unit volume there can be $(1/2\pi)^3$ **k** states. It is more convenient however, to discuss DoS in terms of energy, so for the conduction band E (**k**) is a minimum and the DoS can be given by [20]:

$$E(\mathrm{k}) = E_{c0} + \frac{\hbar^2 |\mathrm{k} - \mathrm{k}_{c0}|^2}{2m_c^*} \qquad 3.16$$

Where $E_{c0} = E_c(\mathbf{k}_0)$ and m_c^* is the effective mass of the electrons in the conduction band and can be described by:

$$\frac{1}{m_0^*} = \frac{1}{\hbar^2}\frac{\partial^2 E_c(k)}{\partial k^2} \qquad 3.17$$

The effective mass is a tensor related to the force felt by the electron as it accelerates through a periodic potential, due to the electric and magnetic fields the electron behaves as a particle in a vacuum, but with a different mass. However, where the energy regions are a minimum the tensor can be approximated to a scalar value. Similarly for the valence band:

$$E(\mathrm{k}) = E_{v0} - \frac{\hbar^2 |\mathrm{k} - \mathrm{k}_{v0}|^2}{2m_c^*} \qquad 3.18$$

where the energy is a maximum near the top of the band. However, in this state the charge carriers are called “holes” and can be thought of as absences of electrons in a sea of electrons. The hole therefore appears to have a positive charge and moves in the opposite direction to an electron in an applied electric field, thus its effective mass is:

$$\frac{\mathbf{1}}{\boldsymbol{m_0^*}} = -\frac{\mathbf{1}}{\hbar^2}\frac{\boldsymbol{\partial^2 E_v(k)}}{\boldsymbol{\partial k^2}} \quad 3.19$$

In general in semiconductor materials the effective mass of the hole is higher than that of an electron, which results in lower mobility; hence electrons are generally the preferred charge carrier in most semi-conductor devices [20, 32].

The above paragraphs describe the energy levels available for occupation by electrons or holes, in order to determine the likelihood of a particular quantum state being occupied it is necessary to use probability function. In the case being considered in this thesis i.e. that of electrons and related charge carriers, Fermi-Dirac statistics is the appropriate method of determining the probability distribution of these particles as electrons are fermions and are subject to the Pauli Exclusion Principle. At a temperature of absolute zero (0K or -273.15^{o}C) electrons fill the lowest available energy levels from the bottom up, the level up to which the vacancies are filled is called the Fermi energy (E_F). At higher temperatures levels above this can be full leaving vacancies below. At thermal equilibrium there will be no net transfer of energy from the semiconductor to its surroundings and all carriers will have the same kinetic energy of 3/2 k_BT, where k_B is Boltzmann's constant [20, 45]. In this case:

$$f(k,r) = f_0(E(k), E_F, T) \quad 3.20$$

Where f_0 is the Fermi-Dirac distribution, which can be written as:

$$f_0(E) = \frac{1}{\exp\left(\frac{E-E_f}{k_B T}\right)+1} \quad 3.21$$

By solving equations 3.17 and 3.18 for the lowest level of the conduction band and the highest level of the valence band for various values of **k** it is possible to represent the bands graphically by plotting *E* versus **k**. There are two types of result possible; when the valence band maximum and conduction band minimum occur for the same value of k, the band gap is said to be direct, when the maxima and minima occur at different values of k the band gap is said to be indirect. In a direct band gap material an electron

can be excited from the valence band to the conduction band directly by absorption of a photon of appropriate wavelength, whereas in an indirect band gap material an additional process is required as a phonon or lattice vibration is necessary to conserve momentum in the crystal lattice [20].

In contrast to the Fermi energy level, the vacuum energy is the level at which an electron can be thought of as being free and stationary i.e. not subject to any external forces. In general where two metals come into contact the Fermi levels will align whereas when a metal and a semiconductor are brought into contact the vacuum levels may align, this alignment occurs at the Schottky-Mott limit and results in the formation of the Schottky barrier [32, 46].

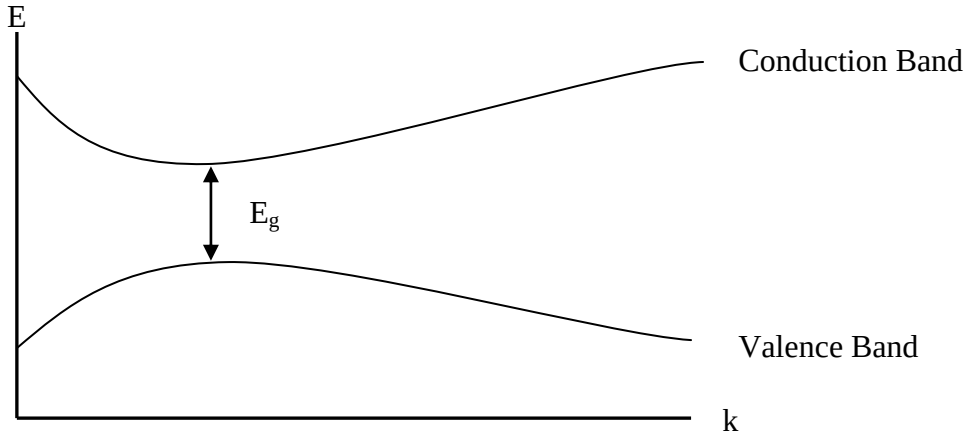

Figure 3-6. E-k diagram of a direct band gap in a semiconductor

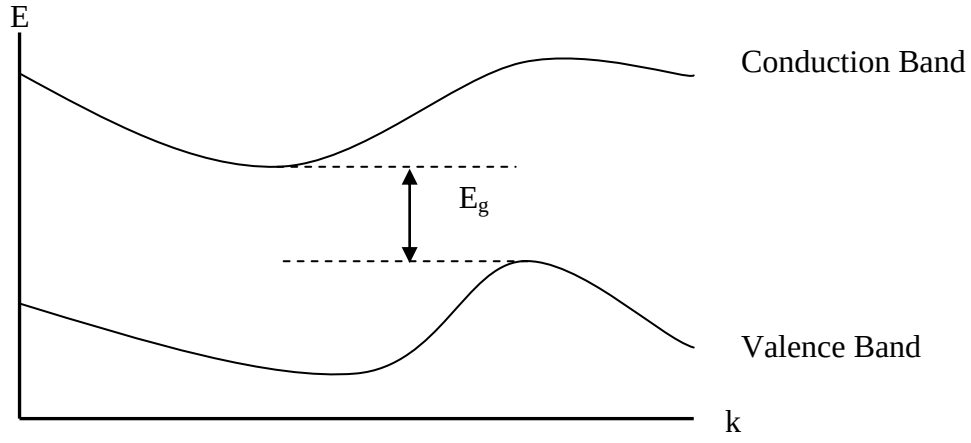

Figure 3-7. E-k diagram of an indirect band gap in a semiconductor

3.2 Conventional Semiconductor Photovoltaic Devices

3.2.1 Introduction

Both CSC and XSC solar cells work by absorbing photons from the sun and converting them into electrical energy. Photons are quantised light particles or more accurately wave packets, each with a specific energy determined by its wavelength. This can be given by the De Broglie relation [33]:

$$E = \hbar\omega \tag{3.22}$$

where ω is the frequency of the light and is equal to c|k|, where c is the speed of light and |k| is the wavevector and ħ is the reduced version of Plank's constant. Since ħ=h/2π and k=2π/L where L in this case is equal to the wavelength of light (λ):

$$E = \frac{hc}{\lambda} \tag{3.23}$$

When the energy of an incoming photon is equal to or greater than the band gap E_g then it is possible for the photon to be absorbed and an electron can be "promoted" from the valence band to the conduction band leaving a hole in the valence band. If there is a driving force, such as a potential difference between electrodes with different work functions, then the charge carriers can be taken to the electrodes for use as electrical energy, if no driving force is present there is the possibility that the electron will re-emit the photon and relax back to its original state, recombining with the hole in a process known as radiative recombination [20].

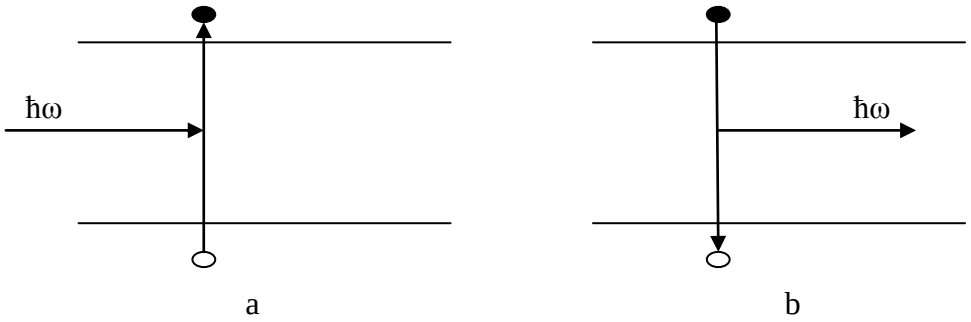

Figure 3-8. (a.) Photon absorption and electron excitation, (b.) radiative recombination.

It is common practice to present the band gap and work functions of materials in terms of electron volts (eV), in this case equation 3.23 can be written as [20, 35]:

$$E(eV) = \frac{1240}{\lambda(nm)} \qquad 3.24$$

Firstly, the band gap of semiconductors should be of the right order to permit the absorption of light from the visible part of the spectrum; insulators have too wide a band gap for this process. Most semiconductors have band gaps in the range 0.5-3eV, the ideal band gap is ~1.4eV and the closest materials to this are cadmium telluride and gallium arsenide with band gaps of 1.44eV and 1.43eV respectively [20]. The band gap of silicon is ~1.1eV which limits the maximum efficiency of the material, but compensates for this by being cheaper and more abundant. Secondly the band gap is necessary to allow the excited electrons to remain in the higher energy levels long enough to be converted into useful output, conductors have a continuous band structure which means that excited charge carriers could relax back to their original state too quickly to be useful in the photovoltaic process [20]. An ideal photo converter:

- Has energy gap between conduction and valence bands, ideally between 0.5 and 3 eV, ideally ~1.4eV
- All incident light with $E > E_g$ is absorbed.
- Each absorbed photon creates 1 electron-hole pair.

- Light absorption – increasing the thickness of a semi-conductor increases its optical depth. Light absorption requires a high optical depth and perfect charge collection; this is a difficult and expensive combination to achieve.
- Charge separation – Need an asymmetry in the material to drive electrons away from the point of promotion. This can be an E field or gradient in the charge density. Charge separation can be achieved by use of contacts or junctions between two electronically dissimilar materials either at the surface or beneath the surface. For maximum efficiency this should not affect the electrical potential energy of the electrons as they are pulled though the material. In practice this limits the materials available.

3.2.2 Photogeneration and Thermalisation

In dark conditions and in thermal equilibrium with its surroundings a solar cell will radiate as a blackbody of temperature T_a, additionally it will absorb thermal photons generated at its surface. This results in a cycle of absorption and spontaneous emission similar to that shown in Figure 3-8. Under illumination the light absorbed by the material is attenuated in accordance with the Beer-Lambert Law, which for a material with a uniform absorption coefficient (α) can be written as [20]:

$$I(x) = I_0 e^{-\alpha x} \tag{3.25}$$

Where *I(x)* is the intensity of the incoming light at a depth *x* and I_0 is the intensity of light immediately inside the surface after reflection has been accounted for. For an inhomogeneous absorbing material the general case can be given as:

$$I(x) = I_0 e^{-\int_0^x \alpha(E,x')dx'} \tag{3.26}$$

If it is assumed that each incoming absorbed photon creates one electron hole pair, then the rate of generation of charge carriers (g) per unit volume at a certain depth can be calculated using:

$$g(E,x) = b(E,x)\alpha(E,x) \quad 3.27$$

Where b is the photon flux at x. The rate of generation (g) can be related to the incoming photon flux (I_s) by accounting for reflection from the front face of the material. The light is attenuated as shown in Figure 3-9 below:

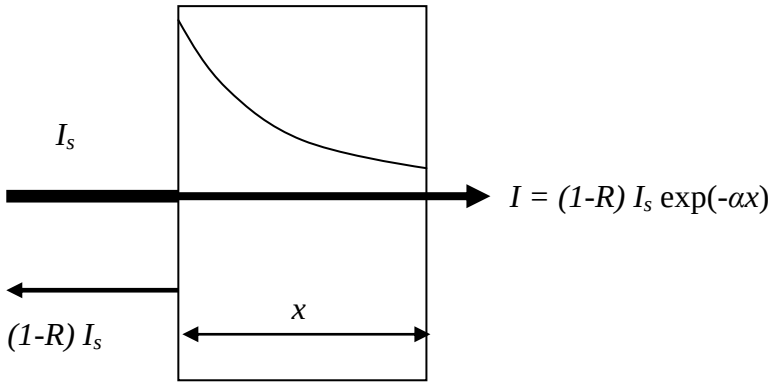

Figure 3-9. Light attenuation in a slab of material of absorption coefficient *α*, reflectivity R and thickness *x* (after Nelson [20])

Therefore in a general case the carrier generation as a proportion of incoming photons of a given energy can be written as:

$$g(E,x) = \big(1 - R(E)\big)\alpha(E)b_s(E)e^{-\int_0^x \alpha(E,x')dx'} \quad 3.28$$

Where b_s is the incident photon flux and *R(E)* is the reflectivity to normally incident light of energy *E*. In order to obtain the total rate of generation of charge carriers it is necessary to integrate over the range of photon energies that could result in a charge carrier being generated.

$$G(x) = \int g(E,x)dE \quad 3.29$$

Where the incoming energy of a photon is greater than the band gap charge carriers with an increased amount of kinetic energy are created, however this energy is soon lost due to collisions in the crystal lattice until the energy is reduced to E_g, this process is known as thermalisation. Therefore the most important factor in charge generation is not the

total energy of the incoming photons, but the number of photons capable of producing charge carriers. In a typical organic solar cell the distance x is of the order 60nm-2μm for efficient devices [47] .

3.3 Solar Cell Characteristics

3.3.1 Equivalent Circuit

Solar cells can generally be described in terms of a simple electrical circuit, as shown in Figure 3-10 below.

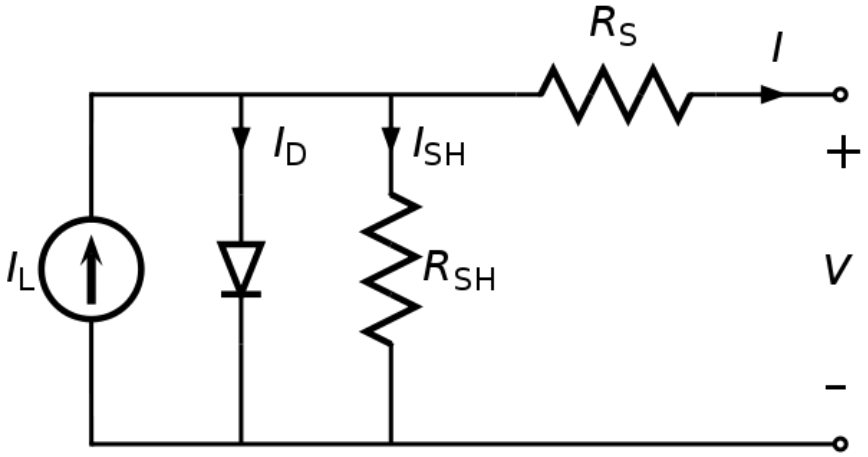

Figure 3-10. Equivalent circuit diagram (McPhee (2008) [48], reproduced under licence)

This circuit is equivalent to a current generator in parallel with a diode and produces a photocurrent proportional to the light intensity under illumination [20]; however in reality power is dissipated in the circuit by leakage currents and contact resistance which are represented by two parasitic resistances one in series (R_S) and one parallel to the cell (R_{SH}). In an ideal solar cell R_S would be zero and R_{SH} would be infinite, which would reduce resistive losses to zero, in reality all solar cells have some resistive losses.

3.3.2 Thermodynamic Efficiency

Solar cells operate as quantum energy conversion devices; this limits their efficiency as they cannot absorb photons with energy below the band gap of the absorber. Photons with energy below the band gap level are converted into heat energy, which is wasted.

Only a relatively small percentage of photons with energy levels above the band gap are converted into useful output, the remainder are converted into kinetic energy, which is then converted into heat by phonon interactions as the particles lose kinetic energy and achieve equilibrium velocity. This loss is known as the "Thermodynamic Efficiency Limit". For conventional solar cells using unconcentrated sunlight the limit is ~43%, if the sunlight is concentrated then this can be increased to around 85% [49, 50].

By having multiple band gaps in the absorber material the efficiency is increased as it is possible to capture photons from a wider section of the spectrum. In essence the solar spectrum may be broken down into smaller bins where the thermodynamic efficiency limit is higher for each bin [50, 51].

3.3.3 Quantum Efficiency

When a photon is captured by a solar cell it is converted into electron–hole pair, which is mobile and can travel to the surface of the cell and contribute to the electric current produced by the cell.

The QE of a solar cell is defined as the percentage of photons converted into useable electrical current as not all electron hole pairs arrive at the surface, some can recombine and become part of the crystal lattice of the device again. The theoretical maximum QE is 100% and there have been organic heterojunction devices comprising poly[N-9″-hepta-decanyl-2,7-carbazole-alt-5,5-(4′,7′-di-2-thienyl-2′,1′,3′-benzothiadiazole) (PCDTBT): [6,6]-phenyl C_{71}-butyric acid methyl ester ($PC_{70}BM$) that have come close to achieving this efficiency [52].

There are two types of QE; external quantum efficiency is the measurement of the fraction of incident photons that are converted into electrical current, while internal QE is the percentage of incident photons converted into electrical current after reflection is taken into consideration. If a perfect non-reflective coating is used the two will be the same.

Therefore the QE(E) is the probability that an incident photon of energy E will produce an electron in the external circuit [20]. The photo current density produced in the external circuit can then be defined as:

$$J_{sc} = q \int b_s(E) QE(E) dE \qquad 3.30$$

Where $b_s(E)$ is the incident spectral photon flux density i.e. the number of photons in the range E to E + dE that fall upon the unit area of the photovoltaic surface per unit time, QE is dependent upon the absorption coefficient of the solar cell material, charge separation efficiency and the efficiency of charge collection in the device.

QE and b_s can be written either as functions of photon energy (E) or wavelength (λ) using equation 3.30.

3.3.4 Open Circuit Voltage and Dark Current

The majority of solar cells act like diodes in the dark, allowing a larger current to pass under forward bias (V>0) than under reverse bias (V<0). The reverse current is known as dark current $I_{dark}(V)$ which is analogous to the current generated when a load is present between the terminals of the cell. This current acts in the opposite direction to the photocurrent and reduces the net current produced from its short circuit value [20]. For an ideal diode the dark current density varies as:

$$J_{dark}(V) = J_0(e^{(qV/k_BT)} - 1) \qquad 3.31$$

Where: J_0 is a constant, k_B is Boltzmann's constant and T is the temperature in Kelvin.
The short circuit value is the current produced when the terminals of the solar cell are connected (I_{sc}), this has an associated current density J_{sc}. The overall current voltage response of the cell, known as the *current voltage characteristic* is generally approximated as the sum of the short circuit photocurrent and the dark current. The sign convention is that photovoltaic current is positive and that negative bias has a negative sign. This means that the summation equates to:

$$J(V) = J_{sc} - J_{dark}\,(V) \tag{3.32}$$

For an idealised diode this becomes:

$$J = J_{sc} - J_0\left(e^{qV/k_BT} - 1\right) \tag{3.33}$$

The open circuit voltage is defined as being the potential difference when the contacts are isolated and is equivalent to a condition where the dark current and short circuit photocurrent exactly cancel out [20]. The value of V_{oc} arises from the difference between the valence and conduction bands and is a property of the materials used in the device [53, 54]. For an ideal diode this is given by:

$$V_{OC} = \frac{kT}{q}\ln\left(\frac{J_{SC}}{J_0} + 1\right) \tag{3.34}$$

Equation 3.34 shows that V_{oc} increases logarithmically with light intensity.

3.3.5 Standard Test Conditions (STC)

In order to have a way to measure the efficiency of solar cells that is comparable for all experimenters a standard set of test conditions has been determined. These are based on the amount of solar irradiance that reaches the cell's surface after absorption and scattering effects have been taken into consideration. This degree to which this occurs is determined by the "air mass (AM)", which is defined as the secant of the angle between the sun and the zenith (sec θ) and measures the atmospheric path length against the minimum path length where the sun is directly overhead [45]. There are three AM curves which are used in different circumstances:

- AM0, for use in space is similar to a black body spectrum at 5760K with an irradiance of 1353 W/m^2 [20, 45];
- AM1, is equivalent to the spectrum when the sun is at its zenith with an incident power of 925 W/m^2 [45];
- AM1.5 conditions represent a typical weighted average for terrestrial conditions, the sun is assumed to be 45^o above the horizon with an irradiance of 844 W/m^2 [45];

Standard Test Conditions use the AM1.5 spectrum, but it is normalised so that the integrated incident power intensity is 1000 W/m^2 and has a temperature of 25^{o}C with the sun 42^o above the horizon [20]. For a solar cell of test area 1 cm^2 the incident power is 0.1W.

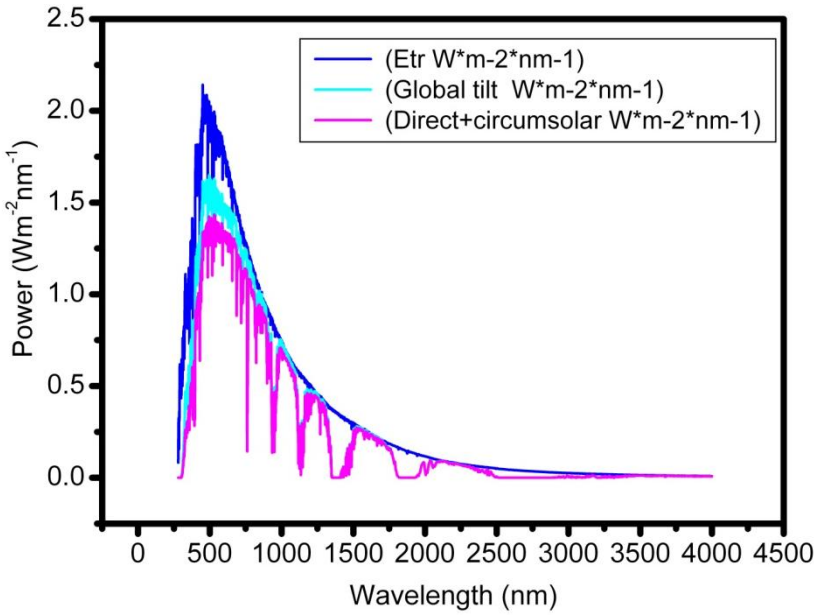

Figure 3-11. Reference Solar Spectrum Irradiance Air Mass 1. (data from Emery and Myers (2003) [55] with permission).

3.3.6 Fill Factor and Diode Ideality

The fill factor is defined as being the ratio:

$$FF = \frac{J_m V_m}{J_{sc} V_{OC}} \qquad 3.35$$

and describes the squareness of the J-V curve (Figure 3-12) [20], it should be noted that as all of the devices used in this work are a standard 1cm^2 that the values J-V and I-V are interchangeable.

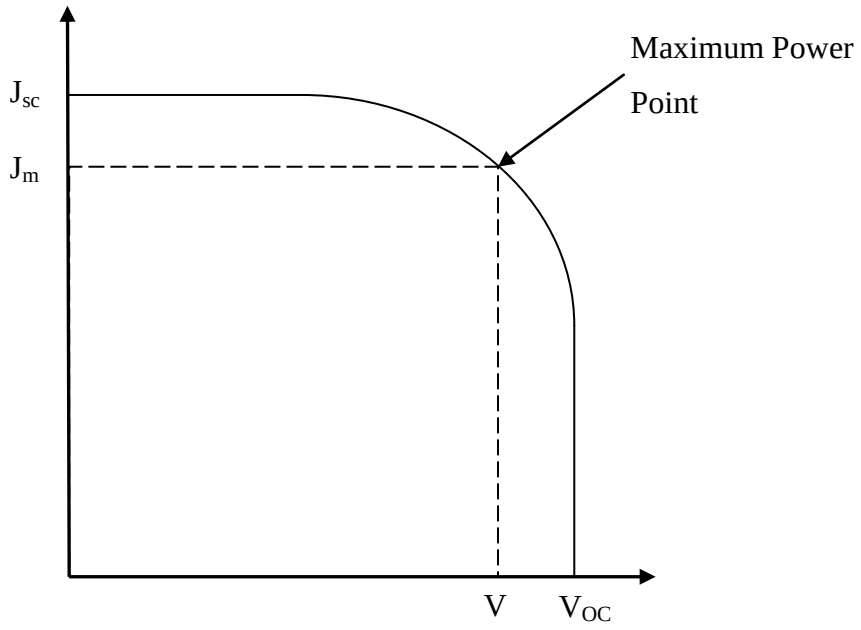

Figure 3-12. Typical J-V curve for an inorganic photovoltaic device, for an organic device the J_{sc} is negative and hence the curve is inverted.

For an ideal diode with a fill factor of 1 the maximum power would equal the product of the open circuit voltage and the short circuit current. However, in reality a solar cell will be subject to the two resistances shown in the circuit diagram in Figure 3-10. The series resistance occurs because the materials in the cell, particularly the contacts resist the flow of current [20]. This has the effect of increasing the slope of the voltage component of the J-V curve which has the added effect of reducing the maximum power point. The series resistance (r_s) can be calculated from the slope of the line so that:

$$r_s = \frac{\Delta V}{\Delta I} \tag{3.36}$$

The shunt or parallel resistance (r_{sh}) is generally caused by leakage current in the cell and has the effect of increasing the slope of the current component of the J-V curve. The shunt resistance can be written in terms of the open circuit voltage, provided that $r_s \ll r_{sh}$ [56].

$$\frac{V_{OC}}{r_{sh}} = J_{sc} - J_{dark}\left(\exp\left(\frac{qV_{OC}}{mkT}\right) - 1\right) \tag{3.37}$$

Since when r_{sh} is infinite the first term becomes zero as would be expected.

By including terms to describe the parasitic resistances equation 3.33 can be re-written as:

$$J = J_{sc} - J_0\left(e^{q(V+JAr_s/k_BT} - 1\right) - \frac{V+JAr_s}{r_{sh}} \quad 3.38$$

Where A is the area of the solar cell, which for test purposes is typically 1cm^2. Equation 3.38 can be reduced to the following form for non-ideal diodes, which includes the resistances and other characteristics affecting behaviour of the diode in the term *m*, which is usually a factor between 1 and 2.

$$J = J_{sc} - J_0\left(e^{qV/mk_BT} - 1\right) \quad 3.39$$

Rearranging and solving for m when $J = 0$ we get:

$$m = \frac{qV_{oc}}{(\ln J_{sc} - \ln J_{dark})k_BT} \quad 3.40$$

So by measuring the current under illuminated and dark conditions we can obtain values for V_{oc}, J_{sc} and J_{dark}, the temperature (T) can be measured or assumed to be ~300K and therefore a value for m can be estimated. Having obtained a value for m and by re-arranging equation 3.37 we can obtain an estimate for r_{sh}:

$$r_{sh} = \frac{V_{oc}}{J_{sc} - J_{dark}\left(\exp\left(\frac{qV_{oc}}{mk_BT}\right) - 1\right)} \quad 3.41$$

The effects of the series and shunt resistances on the J-V curve are shown in Figure 3-13 below:

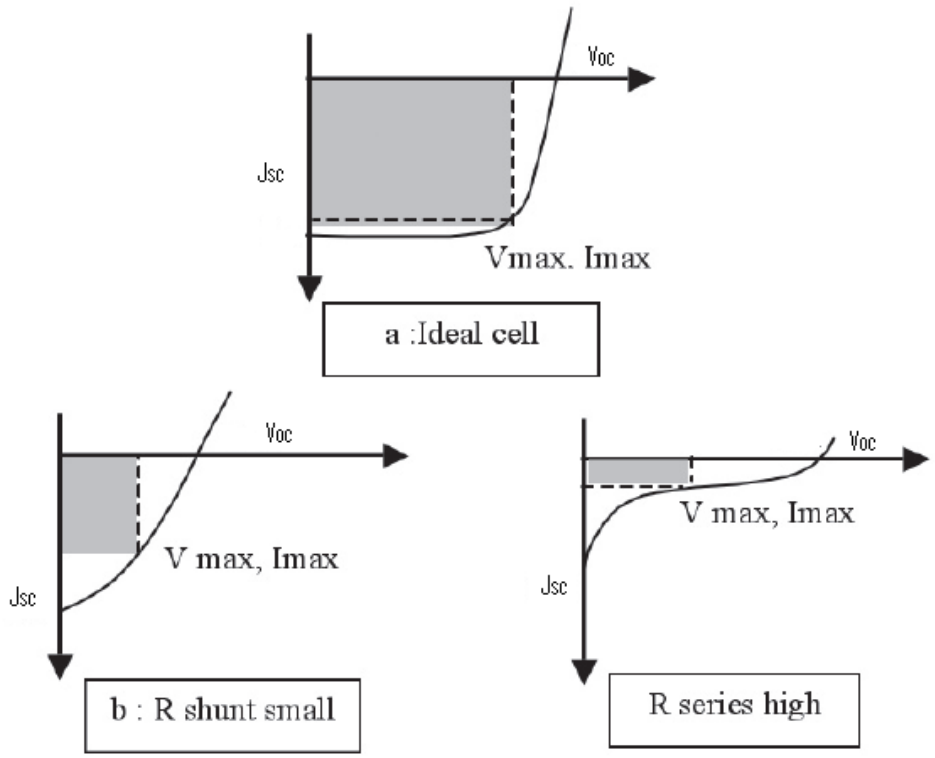

Figure 3-13. The shape of the J-V curve for organic photovoltaic devices for a. an ideal diode, b. a diode with low shunt resistance and c. a diode with a high series resistance (from Bernede (2008) [57]).

As can be seen from Figure 3-13 b. the reduction of the shunt resistance arising from leakage currents in the diode causes the shape of the curve to flatten along the x axis leading to a potential reduction in the V_{oc} of the device compared to an ideal diode, the leakage currents can arise from pinholes and recombination traps in the active layer [57, 58]. Figure 3-13 c. show that a high series resistance causes a flattening of the curve on the y- axis, resulting in a reduction of the maximum current produced by the cell and is a result of interfacial resistances between the active layer and the electrodes [20, 57, 59]. Work by Xue et al has shown that this effect is not limited to the top electrode and also arises at the ITO electrode, particularly when that electrode has been modified with a layer of PEDOT:PSS (§4.2.3) [59].

Furthermore by plotting the I-V data as shown in Figure 3-14 below it is possible to estimate whether the interface between the polymeric material and the metallic electrode produces an ohmic or a rectifying contact.

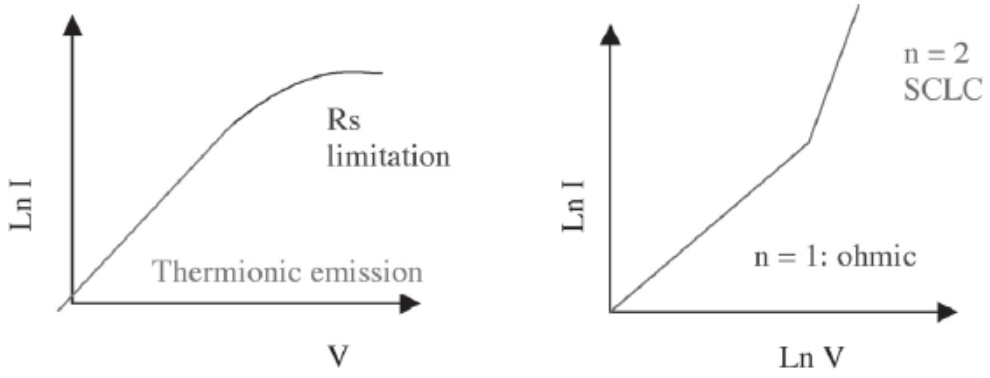

Figure 3-14. Determining thermionic emission and space charge limited current from natural logarithmic graphs (from Bernede (2008) [57]).

Thermionic emission occurs at the rectifying contact when the thermal energy of a charge carrier is sufficient to overcome the potential barrier that can arise at the interface between the polymer and metallic electrode. For non zero values of r_s thermionic emission obeys the following form of the diode equation [57]:

$$J = J_s\left(exp\left(\frac{e(V-JR_s)}{k_BT}-1\right)\right) \qquad 3.42$$

Where Js is the reverse saturation current density (dark current) and all other terms are as defined previously (§3.3).

Where no potential barrier exists between the electrode and the polymer the behaviour of the charge carriers is ohmic and obeys Ohms law which can be written as [57]:

$$J_{ohm} = qn\mu\left({}^{V}/_{d}\right) \qquad 3.43$$

Where *n* is the charge carrier density, *q* is the electronic charge, μ is the carrier mobility, *V* is the applied voltage and *d* is the film thickness. In OPV devices ohmic breaks down at the space charge limit which occurs when the electric field generated by the charge carriers is greater than the applied bias [57]. The simplest case of space charge limited

current (SCLC) is given by Child's Law and applies when there are no charge traps or all the traps are filled:

$$J_{SCLC} = \left({}^{9}/_{8}\right)\varepsilon_r \varepsilon_0 \mu \left({}^{V^2}/_{d^3}\right) \quad 3.44$$

As can be seen from above, the slope of the lnI vs lnV graphs shows it can be possible to determine which case applies, where the slope is 1 the contact is ohmic and where it is 2 becomes space charge limited.

3.3.7 Power Conversion Efficiency

The Power Conversion Efficiency (PCE) of a solar cell is the percentage of power converted from light (collected) to electricity and is denoted by the symbol η. The efficiency is calculated using the following equation [20]:

$$\eta = \frac{P_m}{E \times A_c} = \frac{V_{OC}\, I_{sc}\, FF}{E \times A_C} \quad 3.45$$

Where: Pm is the maximum power point, that is the device produces the maximum power (VxI), as photovoltaic devices operate over a range of currents and voltages this will be found somewhere between the short circuit and open circuit conditions, Ac is the surface area of the solar cell and E is the energy (irradiance) received from the sun in W/m^2 under standard test conditions (STC). For a solar cell of test area 1 cm^2 under normalised 1.5AM illumination the incident power is 0.1W.

The remainder of the energy not converted into electricity is lost in a variety of ways, including; Reflectance losses, thermodynamic efficiency, recombination losses and resistive electrical loss.

A related value is the Internal Photon to Current Conversion Efficiency (IPCE) [57], which describes the efficiency of a solar cell in converting photons of a given

wavelength into current. IPCE for a given wavelength is determined by the following formula:

$$IPCE = \left({}^{hc}/_{q}\right)\left({}^{J_{sc}}/_{\lambda Pi}\right) \quad 3.46$$

Where Pi is the incident photon flux and the other values are as stated previously. This can also be expressed as a percentage:

$$IPCE\% = 1240.\left({}^{J_{sc}}/_{\lambda Pi}\right) \quad 3.47$$

Where J_{sc} is in Acm^{-2}, Pi is in Wm^{-2} and λ is in μm [57].

The maximum efficiency of a single p-n junction solar cell was first calculated by Schockley and Queisser in 1961 [20, 60] and was determined to be ~ 44% at a band gap of 2.2eV for a sun that was assumed to radiate as a black body with a temeprature of 6000K. It was further determined by Henry in 1980 that by concentrating the light the efficiency could be optimised at a lower band gap, this then produced a Schockley-Queisser limit of 37% with a band gap of 1.1eV with the suns light concentrate by a factor of 1000 [20, 61]. The current maximum PCE claimed for a single junction OPV device is 8.3% by Konarka Ltd, this has been confirmed by the National Renewable Energy Laboratory (NREL) [7, 62].

3.4 Excitons

3.4.1 Differences between CSC and XSC Solar Cells

There are two main differences between CSC and XSC materials, the first is that the magnitude of the relative permittivity (ε) of XSCs is low compared with that of CSCs; the second is that the Bohr radius of the charge carriers in XSCs is also small. These differences have a number of effects; firstly in a CSC cell the incident photon creates free carriers immediately once absorbed whereas the XSC creates electrostatically

bound charge carriers called excitons. In CSC materials the charge carriers are not bound by coulomb attraction but in XSC material they are as the permittivity is responsible for determining the magnitude of the electrostatic attraction between charge carriers i.e. electrons and holes. In both cases the amount of charge carriers produced are proportional to the square of the permittivity [12]. See section 8.4 below for a more complete treatment of the effect of permittivity on excitonic behaviour.

3.4.2 Excitonic Behaviour

Excitons are quasi-particles that are composed of a bound state of an electron and a hole (a virtual positive particle). Electrons (e^-) and holes (h^+) are both Fermions, which are particles that have half integer spin and obey Fermi-Dirac statistics [33], but as the exciton is made up of two Fermions, which can have either the same or opposite spins the sum of the spins add up to either zero or an integer value and therefore they behave as Bosons and obey Bose-Einstein statistics [63].

Excitons exist as two main types; Frenkel excitons which are tightly bound and generally have a radius equivalent to roughly one lattice spacing and Mott-Wannier excitons which are loosely bound and can extend over many lattice spacings [23, 27, 45, 46]. Which of the two types is present in a given material depends upon the permittivity of the material, in general low permittivity materials (those with a permittivity less than silicon dioxide ~3.7-3.9) form Frenkel excitons and high permittivity materials form Mott-Wannier excitons. The majority of polymeric materials used in solar cells have relatively low permittivity and therefore form Frenkel excitons.

Due to the half integer spin each type of exciton can be subdivided into two types of exciton – Singlet and triplet [11, 12, 43, 64], the singlet is generally the ground state and the triplet state is an excited state [64].

- Singlet – pairs of electrons and holes with opposite spin creating a spin 0 quasi-particle with only one possible energy level and a shorter lifespan.

- Triplet – pairs of electrons-holes with same spin leading to a spin 1 quasi-particle, this gives three potential energy levels (hence the name). These have generally a longer lifespan than singlet excitons.

The energy states of Frenkel excitons in a crystalline matrix can propagate as waves, so for a crystal of *N* atoms either in a line or a ring and the ground state of atom *j* is u_j then the wavefunction can be written as [43]:

$$\psi_g = u_1 u_2 \ldots . u_{N-1} u_N \tag{3.48}$$

And in an excited state v_j the structure can be described by:

$$\varphi_j = u_1 u_2 \ldots . u_{j-1} u_{j+1} \ldots . u_N \tag{3.49}$$

The Hamiltonian (quantum mechanical energy operator) can be used to obtain the eigenfunctions, which can then be solved to obtain specific eigenvalues, so:

$$\mathcal{H}\varphi_j = \epsilon\varphi_j + T(\varphi_{j-1} + \varphi_{j+1}) \tag{3.50}$$

The eigenfunctions of this Hamiltonian are Bloch waves of the form:

$$\psi_k = \sum_j \exp(ijka)\, \varphi_j \tag{3.51}$$

Where a is the lattice spacing. Equation 3.51 can be solved to give the energy eigenvalues:

$$E_k = \epsilon + 2T\cos ka \tag{3.52}$$

Where k has the allowed values of:

$$k = \frac{2\pi s}{N}; s = -\frac{1}{2}N, -\frac{1}{2}N + 1 \ldots ., \frac{1}{2}N - 1 \tag{3.53}$$

In a crystal matrix with parallel polymer chains, interactions between the chains can result in splits in the observable energy levels of excitons, this is known as Davydov splitting [65, 66].

3.4.2.1 Diffusion Length and Photocurrent

Excitons in photoconductive polymers have a short lifetime ~a few hundred picoseconds to a few nanoseconds [67, 68] and as such travel only short distances before recombining, it is therefore essential for an exciton to be able to travel far enough to encounter an interfacial boundary and be able to separate into useful charge carriers.
It is thought that the travel mechanism is by Förster energy transfer, where the excitation "hops" from molecule to molecule [69]. In general exciton diffusion is thought to follow a Fickean diffusion mechanism such that the diffusion length (L_{ED}) is given by [70-72]:

$$L_{ED} = \sqrt{D\tau_o} \qquad 3.54$$

Where D is the diffusion constant for the material in cm^2/s and τ_0 is the lifetime of the exciton. There are a number of models for diffusion of excitons in polymers, in fact far too many to describe fully here, many of the most widely used are based upon the work of Ghosh and Feng in 1978 [73] whose model is presented below:

$$0 = D\frac{d^2n}{dx^2} - \frac{n}{\tau} + \alpha\theta N \exp(-\alpha x) \qquad 3.55$$

Where n is the number of excitons, α is the absorption coefficient, θ is the quantum efficiency of exciton generation, x is the depth of the material and N is the number of incident photons per centimetre squared. It is then possible to obtain a term for the exciton density at a given depth as shown by Yang et al [74]:

$$n(z) = \frac{\alpha\theta I_0}{\beta^2 - \alpha^2}\left[\left(\frac{e^{\beta L} - e^{-\alpha L}}{e^{-\beta L} - e^{\beta L}}\right)e^{-\beta z} - \left(\left(\frac{e^{-\beta L} - e^{-\alpha L}}{e^{-\beta L} - e^{\beta L}}\right)e^{\beta z} + e^{-\alpha z}\right)\right] \quad 3.56$$

Where $\beta = 1/\sqrt{D\tau}$, L is the overall thickness of the material and the other meanings are the same as above. At $z = 0$, the current density $j = -De(dn/dz)$ is given by:

$$j_S = \frac{\alpha\theta I_0 De}{(\beta^2 - \alpha^2)} \times \frac{2\beta - e^{-\alpha L}\left(\beta e^{-\alpha L} + \beta e^{\beta L} - \alpha e^{-\beta L} + \alpha e^{\beta L}\right)}{e^{-\beta L} - e^{\beta L}} \quad 3.57$$

This current response follows the shape of the absorption spectrum and is sometimes known as the symbatic response. By setting $z = L$ and allowing for the assumption of Ghosh and Feng that excitons only separate at one interface, then we get a response that is opposed to the absorption spectrum, sometimes known as the antibatic response. The current density here is given by:

$$j_A = \frac{\alpha\theta I_0 De}{(\beta^2 - \alpha^2)} \times \frac{\beta\left(e^{-\beta L} - e^{-\alpha L}\right) + \beta\left(e^{-\beta L} - e^{-\alpha L}\right) + \alpha\left(e^{-\beta L} - e^{\beta L}\right)}{e^{-\beta L} - e^{\beta L}} \quad 3.58$$

For an organic film at a given bias (x_s) the total photocurrent (J) can be considered to be a combination of j_S and j_A:

$$J = (1 - x_s) \cdot j_A + x_s \cdot j_s \quad 3.59$$

Working from similar principles to Yang et al, Stübinger and Brüting [75] have demonstrated that the position of maximum exciton density occurs at position x_{max} which is given by:

$$x_{max} = \frac{L \ln(\alpha L)}{\alpha L - 1} \quad 3.60$$

Measurements taken by Terao et al [76] suggest that the short circuit current in organic solar cells is directly linked to hole mobility and exciton diffusion length and work done by Lunt et al and Kurrle and Pflaum shows that increasing the order of the polymer

matrix can potentially increase the diffusion length in certain polymers by up to 4 times [72, 77].

3.4.3 Exciton Dissociation into Charge Carriers

Persson and Inganäs [78] have suggested a seven step model for the generation of power by organic solar cells; the seven processes are as follows:

1. Incoupling of the photon – The material should be as transparent as possible to light and reflection and other losses should be minimised either by antireflective coatings or by the composition of the material itself.
2. Photon absorption – Optical absorption is related to the distribution of the modulus of the optical electrical field$|E|^2$, which is dependent upon the local dielectric function and the geometry of the device.
3. Exciton formation – The excitation of an organic solid produces an exciton, usually the type of excitons produced in organic polymers are Singlet Frenkel excitons [79].
4. Exciton Migration – Exciton migration is described in terms of the Diffusion Length (L_D) and is generally of the order of 5-10nm in organic materials [6], although some experiments by Kurrle and Pflaum using the polymer diindenoperylene (DIP) have demonstrated diffusion lengths of up to ~100nm and exciton lifetimes of ~10ns [72]. Excitons have a finite lifetime, and can decay by a variety of mechanisms, some of which are beneficial such as dissociation into electrons and holes and some of which are not such as radiative decay which results in the creation of a photon which is re-emitted and lost, thermal and vibronic decays also result in a loss.
5. Exciton Dissociation – Dissociation generally requires an external influence such as an interface between materials in order to occur. In general an inhomogeneity is required for dissociation to occur; this is often due to a difference in the electron affinities of two materials. Once excitons have dissociated they can either become useful charge carriers or they can occasionally recombine to form new excitons. There are two types of recombination, geminate, where the electron and hole from the original exciton

recombine and non-geminate biomolecular recombination where electrons and holes from different dissociated excitons recombine.

6. Charge Transport – Once the excitons have dissociated into electrons and holes, the charge carriers must be free to migrate to the electrodes. Electrons and holes have different mobilities within materials and can become trapped or recombine if the distance to the electrode is too great.
7. Charge collection at the electrodes – Whether charges can be collected at the electrode are a function of the surface of the electrode and the interface between the electrode and the polymer. Collected charges are then free to pass into the electrical circuit.

This process is expressed in the flow diagram in Figure 3-15 below, except that in this case photon incoupling and absorption have been combined into one process.

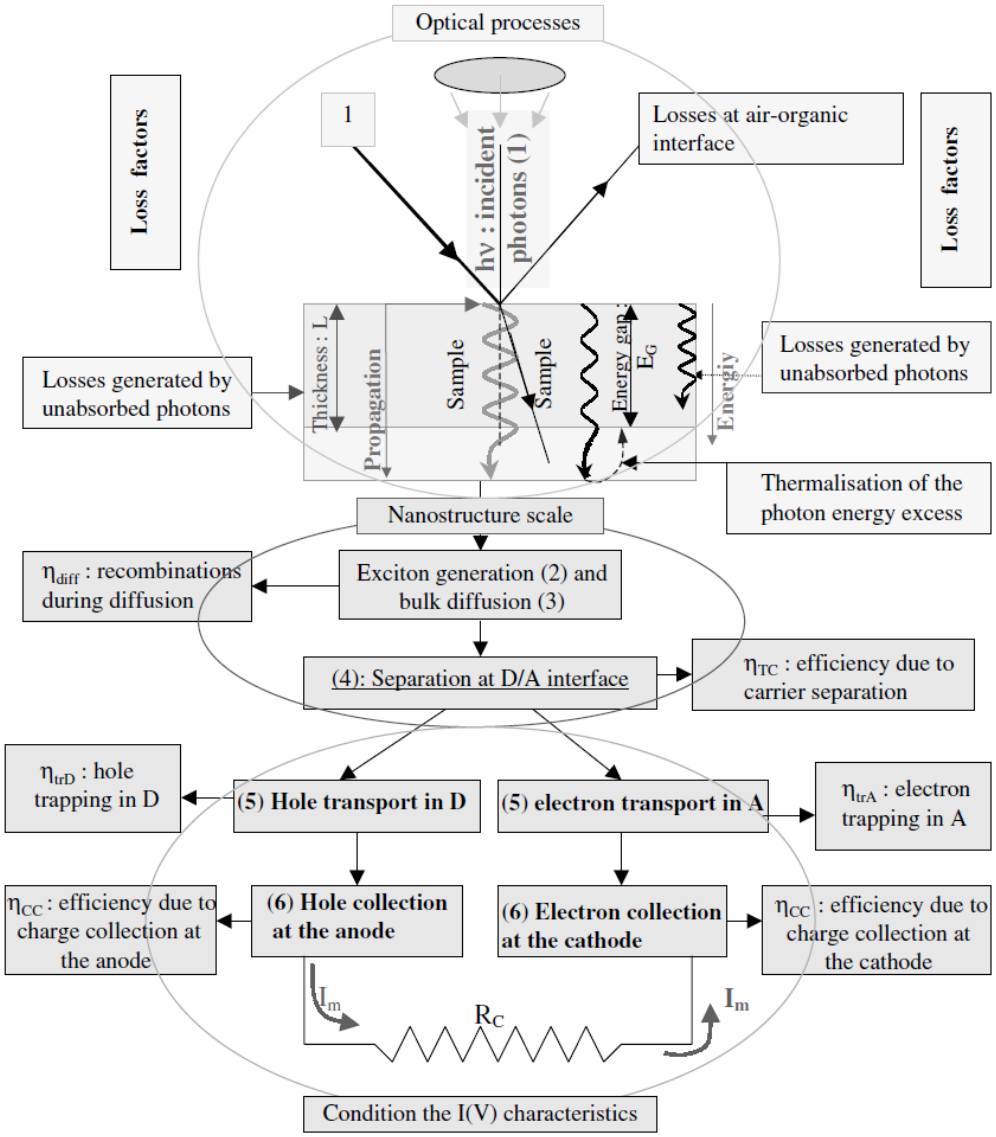

Figure 3-15. Charge generation process in organic solar cells (reproduced from Moliton and Nunzi (2006) [80] with permission).

The charge separation process can also be thought of in terms of the energy levels of the exciton before and after separation occurs. This energy diagram is presented in Figure 3-16 below. The initial (ground state) of the electron donor material is denoted S_0 and this state represents the energy level of the donor material before the photon is absorbed. Upon absorption the energy level of the donor material is elevated to the S_1 state which is the summation of the S_0 state with the energy of the absorbed photon.

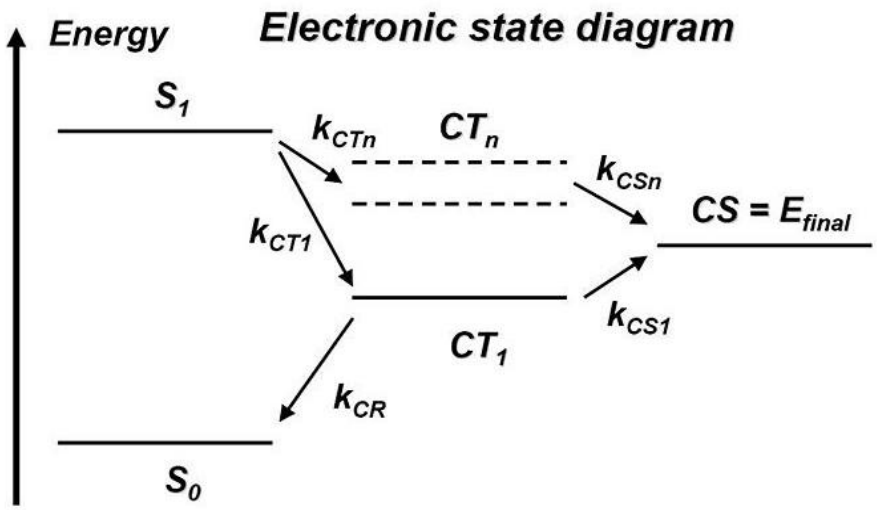

Figure 3-16. Electronic State Diagram showing exciton energy states before and after separation (Reproduced from Taylor (2009) [81] under license)

The generated exciton then migrates through the material in the k_c state. There are two possible groups of states possible at this point, k_{CTn} and k_{CR}, which represent the charge transfer (CT) state and the charge recombination (CR) states respectively, n is the energy level number. In this case CT_1 is the lowest energy level at which charge transfer can occur; below this level recombination in some manner will always occur as the coulomb forces in the exciton outweigh the ability of the forces at the interface to separate the charges. In order to reach the CT state it is necessary for the exciton to reach an interface between the donor and acceptor materials before recombination takes place. The CT_n state occurs when the electron is within the acceptor material leaving the hole in the donor material. Even at this point recombination is possible and separation is not guaranteed, at k_{CR} the recombination of the electron and hole occurs and the donor material returns to the ground state along with an emission of energy either a photon or phonon or other loss of energy to the surrounding material. If recombination does not take place then it is possible for the CT_n state to become the CS state resulting in separated charges which are then free to migrate to the electrodes. It can be seen that many of the CT_n states involve a loss of energy at charge separation, but the CT_1 state requires additional energy to be imparted to the exciton to separate the charges, whether from the acceptor material's electric field or lattice vibrations. As the

coulomb forces are overcome at the potential barrier the charges separate and the CS or E_{final} state is reached.

Even after the charges separate it is still possible for them to be lost before reaching the electrodes either by charge trapping at imperfections in the material or by non-geminate recombination, which is where charge carriers dissociated from different excitons can recombine to form a new exciton.

It has recently been demonstrated that by incorporating a ferroelectric layer into organic solar cells that the charge transfer process can be enhanced, this is thought to be due to the internal field created by the ferroelectric particles and serves to both aid charge separation and prevent recombination [82].

3.5 Types and structure of Solar Cells

Photovoltaic devices can be broadly divided into two categories, conventional semiconductor devices (CSC) and excitonic semiconductor devices (XSC) [12], where CSC type devices are fabricated from silicon and related materials and XSC devices describes photovoltaic devices fabricated using polymers and other organic materials in their active later [78]. CSC devices, as the name implies, function in the same way as other semiconductor devices, in this case an incoming photon of the appropriate wavelength will excite the material causing an electron to be promoted to the conduction band and a hole left behind in the valence band [20]. In an XSC device the process is more involved and is further complicated by the use of different terminology as the descriptive terms were developed by organics chemists in this case. In XSC devices the valence band is known as the Lowest Occupied Molecular Orbital (LUMO) and the conduction band is known as the Highest Unoccupied Molecular Orbital (HOMO) as organic chemistry tends to describe effects in terms of molecular orbitals rather than energy levels, but the meanings are interchangeable. In this case an incoming photon will cause an excitation of the active layer, but rather than promoting an electron to the HOMO from the LUMO will create an electron-hole pair bound by coulomb forces, this state is known as an exciton (§ 3.4). A brief overview of the major types of solar cells is given in the sections below.

3.5.1 First Generation

The earliest (first generation [83]) solar cells were bulk silicon cells comprising a single layer of mono-crystalline silicon grown using the Czochralski method, whereby a melt of pure silicon is held in a crucible and a seed crystal is lowered into the melt and then slowly removed vertically [22, 84], although silicon is used in this case the Czochralski method can be used for many different materials [85] . This results in the formation of a vertical cylindrical column of single crystalline silicon that can be cut into thin wafers using a diamond saw.

Figure 3-17. Example of a single crystal, Czochralski grown silicion crystal (from Stahlkocher (2005) [86], with permission)

This was an expensive process for a number of reasons including; the high temperatures involved, the fact that silicon reacts with the vessel of every type of crucible to some extent [22] and the fact that it is necessary to have an oxygen free atmosphere [22, 84]. In the early days of this form of processing up to 50% of the high grade silicon required for solar cell use was wasted in the cutting process, later developments enabled these losses to be reduced by roughly 30% with the use of the multi-wire saw [20]. As the

Czochralski method involves the creation of a single crystal rod, the subsequent slices are approximately circular and therefore area is wasted when constructing a bank of cells due to the difference in area between the circular crystal and the square cell.

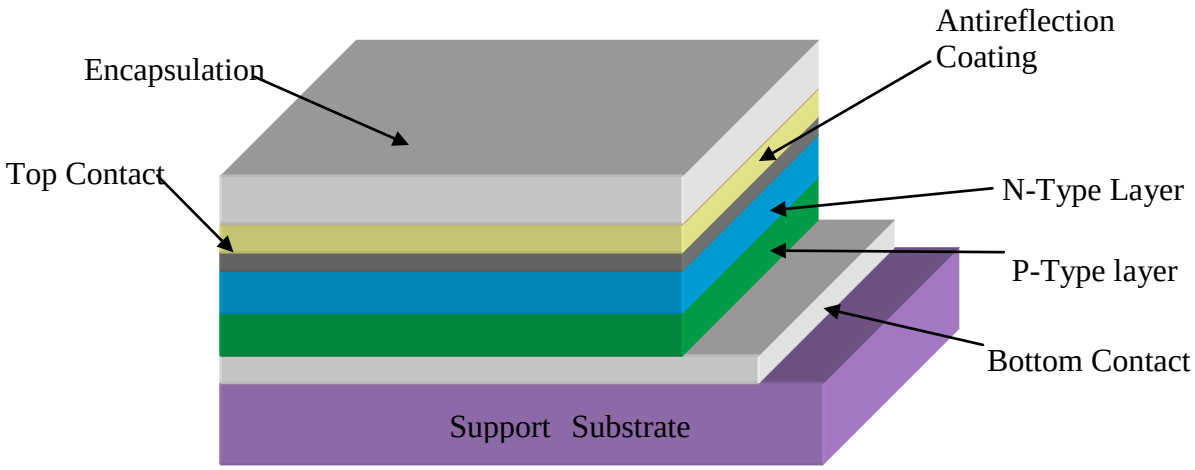

Figure 3-18. Typical silicon solar cell structure.

First Generation CSC solar cells are essentially p-n junctions formed from p and n doped material (usually Monocrystalline silicon, but polycrystalline silicon is also used), although in practice it is rare for two separate pieces of silicon to be used, standard practice being to dope either a p or n type wafer to form a p-n junction or a p-i-n junction, where the i stands for intrinsic, i.e. undoped material. These types of solar cell are still the most widely used and relatively efficient as the majority of solar cells are still of this type [20] and they regularly achieve mass produced efficiencies in excess of 20% [1, 20, 83]

An alternative to the Chochralski method is a process called block casting which results in a multi-crystalline structure (mc-Si) and is cheaper and can be formed into regular shaped sections prior to cutting [20, 21], the device structure is still similar to that described above for bulk silicon

3.5.2 Second Generation

Second generation solar cells, as defined by Bagnall and Boreland [83], comprise thin film alternatives to bulk crystalline silicon cells, the aim being to produce similar

efficiencies while dramatically reducing the amount of material used, and hence reduce the overall the cost of this type of cell.

Materials used in thin films include, amorphous silicon, $CuIn(Ga)Se_2$ (CIGS) and CdTe/CdS (CdTe) which has overtaken silicon as the most widely used [83, 88]. Included in this group are the Schottky barrier cells which use the rectifying characteristics of the junction between a metal contact and a photoactive semiconductor to act as a thin solar cell [89]. In general these materials are sublimated onto substrates by themal evaporation or sputtering [90]. Until recently thin film solar cells have required high temperature processes during fabrication (>300^{o}C), however a number of groups around the world including Zhu et al [90], Beaucarne et al [91] and Myong et al [87] have investigated and found low temperature (<150^{o}C) methods of fabricating these materials.

Hydrogenated amorphous silicon (a-Si) has a glass like material structure, insofar as it has no regular crystalline structure, the hydrogen in the material passivates dangling bonds that would otherwise prevent it being used in electronic devices due to the very high density of states in the bandgap. The use of a-Si is growing in popularity as a material for making solar cells; these are widely fabricated using rf plasma enhanced chemical vapour deposition (PECVD) [87]. Amorphous silicon does not currently have the potential for efficiency of single or multi crystalline silicon due to the presence of numerous traps and impurities produced in the fabrication process.

3.5.3 Third Generation

Third generation solar cells comprise multi-junction cells which are built up of layers of materials with different band gaps to enable the widest part of the spectrum of incoming photons to be captured and converted into energy. The material that has been used most often in these types of devices is gallium arsenide (GaAs); this has been developed by the US military for use in satellites since the mid 1950s, but has increased in use since the invention of the metal organic chemical vapour deposition method (MOCVD) [88]. Gallium arsenide and related devices are known as III-V Semiconductor Devices and have reported efficiencies of up to 26.8% [88]. Silicon is still used in these devices

and p-Si and a-Si multi-junction devices have reported efficiencies of 19.8% and 13% at AM1.5 respectively [88].

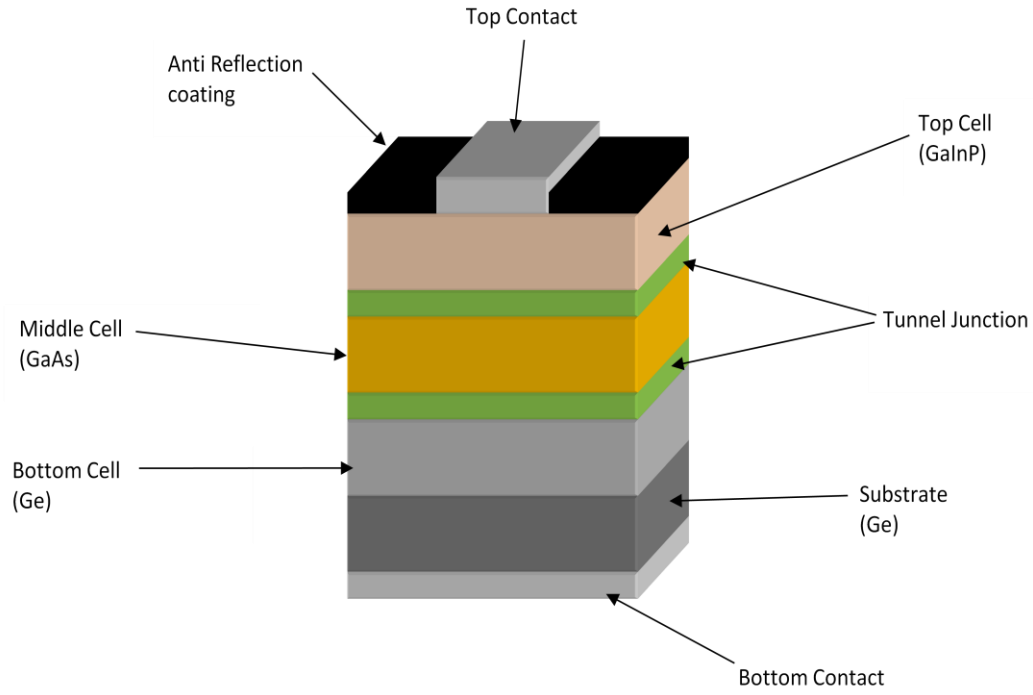

Figure 3-19. Typical Third Generation Conventional Semiconductor Cell Structure

As it is essential for each layer to absorb the maximum amount of photons of each energy range it is thought that the number of layers should be limited to create the most efficient devices. It is generally held that the optimum number of junctions is three, this is because the overall device thickness can be kept to a level where sufficient photons can still penetrate to the bottom junction and the charge carriers can migrate to the electrodes without recombination occuring [50, 61].

3.5.4 Organic Photovoltaics

Although organic solar cells are a relatively recent development there has been a profusion of different types ranging from those based on plant chlorophylls [92], single and multilayer polymeric devices, bulk heterojunction cells and dye sensitised cells [93]. This section gives a brief overview of the history of this type of cell and the main types currently being researched. Subsequent sections and chapters will be devoted to the development of hybrid organic/inorganic bulk heterojunction cells as this is the main goal of this work.

The earliest organic solar cells were single layer devices based upon organic photosynthetic molecules sandwiched between two metal electrodes forming a Schottky barrier at one contact and an ohmic contact at the other [93, 94]. Ghosh and Feng used this kind of cell to develop their theory of exciton diffusion in 1978 [73]. These devices are inherently inefficient as the active region is limited to within a few nm of the Schottky contact, efficiency is further reduced by exciton quenching which occurs at the metallic-organic interface [93].

The first heterojunction devices which comprise two layers of organic materials, a hole transporting (p-type) material and a layer of electron transporting (n-type) organic material were fabricated by Harima et al in 1984 [93]. A year later the first proper working organic solar cell was developed by Tang [95], although and comprised a two layer structure between gold and ITO contacts on a glass substrate. In this case the two layers used were copper phthalocyanine (p-type) and a derivative of perlyene tetracarboxylic (n-type), the device developed an efficiency of around 1% under AM2 illumination. The efficiency of this type of device is limited as the excitons will only dissociate near to the junction between the two layers, but if the layers are too thin photons will pass through without producing an exciton. Heterojunctions were the first devices to truly work in the way described in section 3.4.2 above. Many different p-type π-conjugated polymers, such as polyphenyl vinylene (PPV) or a polythiophene such as poly(3-hexylthiophene) (P3HT) are used in this type of device. These are made up of monomers linked by a chain of alternating single and double sp^2 bonds [41], the

energy states of these bonds can overlap and form a continuum similar to that which forms the band gap that is known as a π bond. By doping the material (often by oxidation) electrons become more mobile and the π bands overlap to form a conductive state along the chain of the molecule [42].

As with the Schottky cell, heterojunctions are limited as the photogenerating region is confined to a narrow band at the interface between the two layers. In time tri-layer devices were developed by scientists at Princeton [93] which broke the 1% efficiency barrier. However, in the early 1990s two developments took place that drastically improved the outlook for organic photovoltaics; Michael Gratzel invented the type of dye sensitised cell that bears his name, a hybrid device that is discussed in more detail in section 3.5.5 below and the first bulk heterojunction devices were fabricated.

In a bulk heterojunction the p and n type materials are blended together so that instead of a single layer junction there are many junctions created at very small intervals, this increases the possibility of excitons being dissociated before recombining as they have less distance to travel before encountering a junction or dissociation region. Sariciftci and others created bulk heterojunction devices using blends of organic polymers such as poly[2-methoxy,5-(2'-ethyl-hexoloxy)-p-phenylene vinylene] (MEH_PPV) [96] and oligothiophenes [97] and the recently discovered, at the time, allotrope of carbon C_{60} or buckminsterfullerene, which was discovered to have excellent properties as an electron acceptor [93, 96, 97].

These early heterojunction cells were relatively inefficient (less than 1% [93]), due to a number of factors including poor quality of films due in part to the fact that C60 does not dissolve well in many organic solvents. Over the subsequent years a number of improvements have been made in the photoconductive polymers used with many of the best cells being based upon various polythiophene blends [47, 98] and by attaching a butyric acid ligand to fullerene to form Phenyl-C61-butyric acid methyl ester (PCBM) which prevents interdiffusion of the C60 molecule which leads to loss of the interface [67]. Recent reports by Park et al [52] and others suggest that the best efficiencies to

date are of the order of 6% and generally use a structure similar to that shown in Figure 3-20 below.

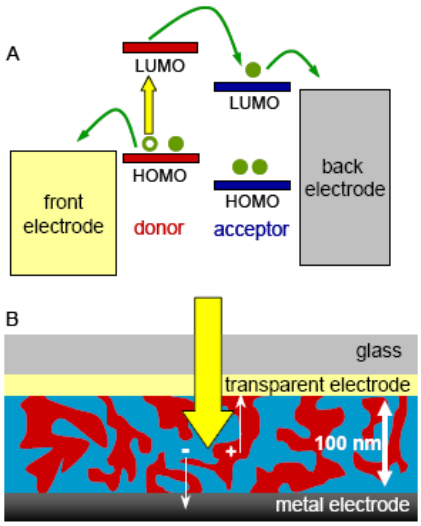

Figure 3-20. The bulk heterojunction concept. After absorption of light by the photoactive material, charge transfer can easily occur due to the nanoscopic mixing of the donor and acceptor (solid and dashed lines). Subsequently, the photogenerated charges are transported and collected at the electrodes (reproduced from Janssen (2002) [41], with permission).

3.5.5 Hybrid Solar

Hybrid solar cells represent a new stage in the evolution of photovoltaic devices, and as suggested by the name, involve the blending of inorganic and organic material to form a solar cell. A wide range of materials have been used as the inorganic components such as; dyes, nanoparticles, quantum dots, carbon nanotubes and metallic and non metallic nanorods.

Figure 3-21 below details the structure of a dye sensitised solar cell, made famous by Michael Gratzel after whom this particular version is named [4].

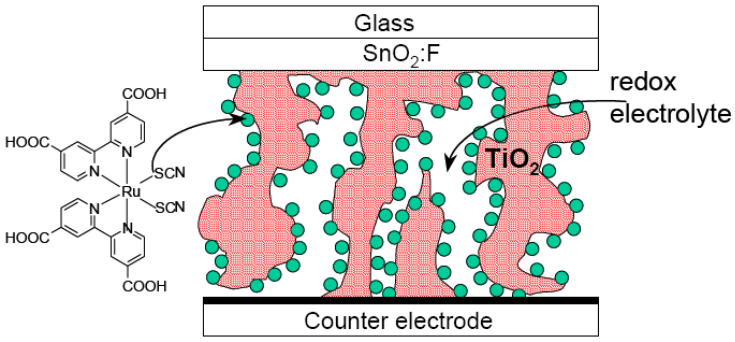

Figure 3-21. The dye-sensitised solar cell structure with an active layer comprising TiO_2, ruthenium dye and I^-/I_3^- redox electrolyte (reproduced from Janssen (2002) [41], with permission).

In this type of cell photons are absorbed by the dye which results in the transfer of an electron to the TiO_2, the dye is then reduced by the electrolyte which is in turn reduced at the metallic electrode leading to the transfer of a positive charge being transferred to the SnO_2:F electrode, while the electron is transferred to the metallic electrode [9, 99]. Grätzel cells have achieved efficiencies of up to 12% by 1991, but have remained static for some time [99]. The liquid electrolyte was not ideal and work has been done to replace this with a solid hole transporting material which it is reported combines light absorption and charge (hole) transport in a single material [8, 10].

Given the many advantages of bulk heterojunction devices this seemed to be the logical type of solar cell to modify by the addition of inorganic materials. The structure of the devices investigated as part of this work is as shown in Figure 3-22, with the exception that no exciton blocking layer was used.

This work has investigated the potential of modifying the properties of a Poly (3-Hexylthiophene) (P3HT) / Phenyl-C61-butyric acid methyl ester (PCBM) blend active layer by including ferroelectric, paraelectric and metallic nanoparticles.

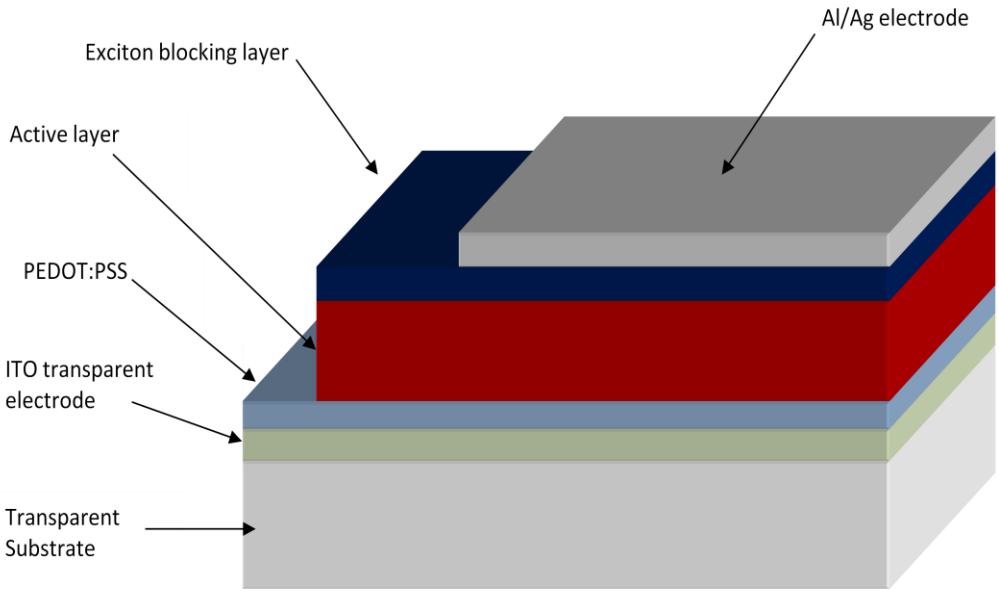

Figure 3-22. Typical Heterojunction Structure for Either Organic Cell or Hybrid Cell.

One important component of any solar cell is the transparent electrode, which is required to transmit light, most commonly, in the visible and near infrared part of the spectrum while still retaining its electrical conductivity. The vast majority of solar cells, both organic and silicon, at present operate in the visible spectrum. However, recently attempts have been made to develop cells that operate in the IR spectrum so that they can function at night as well as in the day, although with reduced efficiency due to the reduced ambient flux [10].

The transparent electrode materials currently in use are Transparent Conducting Oxides (TCO), of which the most widely used in this field of research is still indium tin oxide (ITO), while in the commercial sector fluorine doped tin oxide (SnO_2:F) is used. ITO is a combination of indium oxide (In_2O_3) and tin oxide (SnO) and has good transparency to visible light and the near infrared while retaining a high level of conductivity and high work function.

Due to concerns about the long term availability of indium other oxides, that have characteristics comparable to ITO, are used in the commercial sector such as SnO_2:F [100]. These oxides offer low resistivity (of the order of 10^{-5} Ωcm) and in general their component materials are inexpensive and non-toxic [101]. Other materials currently being investigated by various groups around the world to act as alternatives to ITO include; layers of nanomaterials such as multiwalled carbon nanotubes [102, 103]; Silver nanowire meshes which are flexible and have comparable levels of transparency and conductivity to ITO [104] and can be deposited from solution by a variety of methods including the Langmuir-Blodgett method [105] and aligned using electrical fields[106]; Graphene layers, potentially have good electrical properties and flexibility, provided that a way is found to produce continuous graphene layers of sufficient size [107, 108]; Thin gold layers (<30nm) combined with polymeric materials to aid adhesion to glass and ensure continuity have also fabricated by thermal deposition, these are electrically quite promising, but not as transparent as ITO or other metallic oxides [109].

Although it was planned to carry out some investigations into alternative TCLs alongside this work, the most important aspect of this body of research was to realise functional and efficient organic solar cells.

As can be seen the solar cell in Figure 3-22 has two additional layers than the cell shown in Figure 3-20, the layer of Poly(3,4-ethylenedioxythiophene) poly(styrenesulfonate) (PEDOT:PSS) is used to modify the work function of the ITO layer and to improve the adhesion between the transparent electrode and the active layer. Other methods of increasing the work function of ITO include modification by

treatment with acid mixtures (Piranha treatment) or plasma treatment [110], to date neither have proven more successful that PEDOT:PSS.

The second additional layer is the exciton blocking layer which, as the name suggest, prevents excitons from leaving the active layer before they have dissociated into charge carriers [111]. This has the additional effect of preventing quenching, a form of recombination, of excitons at the cathode which in turn has the potential to increase efficiency as more excitons are available to dissociate into charge carriers [68, 112]. The blocking layer is generally very thin, usually only a few nanometres. A layer thicker than this is also likely to prevent the charge carrier's from reaching the electrode [111, 113]. No EBL has been used here as the purpose of this work was to investigate the relative properties of the active layers of devices with and without ferroelectric nanoparticles and the use of this layer was not deemed necessary to this investigation.

3.6 Summary

This chapter has introduced the science and concepts involved in both conventional and organic photovoltaics devices. It has shown how the devices work from photon absorption through to carrier transport to the electrodes. A comparison between CSC and XSC devices has introduced the concept of the exciton, a quasi particle comprising an electron-hole pair bound by coulomb forces that is formed when a photon of appropriate energy is absorbed by a photoconductive polymer. The exciton has a short lifetime and needs to move to a region, usually an interface between polymer and nanoparticles, where it can dissociate into its constituent charge carriers which can then move to the electrodes and be used as electrical power. This process requires multiple steps and recombination can occur at many points in the process, which is one of the likely reasons for the inefficiency of organic solar cells when compared to conventional silicon or gallium arsenide cells.

A brief description has been given of the evolution of solar cells from the first generation of mono-crystalline and multi-crystalline silicon devices through second generation thin film amorphous, polycrystalline silicon and cadmium tellaride devices to third generation multi-junction GaAs based devices. This then led into descriptions

of the various organic solar cells, which include single layer devices, multi-junction devices and have progressed to hybrid devices that use a combination or organic polymers and inorganic materials and comprise such devices as the Grätzel Cell and the bulk heterojunction devices used in this work.

Chapter 4

4 Organic Solar Cells: Materials used in this Work.

This chapter introduces the materials used in this work and also touches on those materials commonly used in bulk heterojunction solar cells that have not been used in this work. Section 4.1 describes the material properties of Indium Tin Oxide (ITO), Section 4.2 details the polymeric materials used in this work and Section 4.3 details the nanomaterials used in this work.

4.1 Indium Tin Oxide

Indium tin oxide (ITO) is combination of indium oxide and tin oxide that has good electrical conductivity and high transparency at optical wavelengths; this makes it an ideal material for use as a transparent electrode layer. It is yellowish green to brown in colour and is made by doping indium oxide with 5-10% of tin, usually in the form of tin oxide. The tin replaces a proportion of the indium and acts as an n-type dopant releasing electrons into the conduction band [114, 115]. The amount of oxygen contained in the compound is critical to the transparency of ITO, more oxygen in the matrix increases the transparency of the material, but it is a balance as the oxygen also fills up vacancies and reduces the overall conductivity of the material [114].

Thin films of ITO generally have a low electrical resistivity (~2-4 x 10^{-4} Ωcm) which is a result of high carrier concentrations (10^{20} - 10^{21} cm^{-3}) which in turn are due to the fact that the Fermi level is higher than the conduction band [116]. In addition to low resistivity ITO is highly transparent in the visible part of the spectrum (>85% in good quality films) which is due to the wide band gap of the material (3.5 – 4.3eV) [116, 117]. The band gap of ITO can be further modified by the addition of a layer of PEDOT:PSS (see below). Because ITO is a good hole injector [116], it is used as the anode in a wide range of electronic devices including photovoltaics [114], light emitting diodes (LED), particularly organic LEDs (OLED) [116, 118], and others such as displays and anti-reflection coatings [119, 120].

Depending upon the method of deposition the structure of ITO layers can vary from amorphous to highly crystalline [120-122]. This structure can be further modified by annealing at relatively low ($200^{o}C$ – $400^{o}C$) temperatures [114, 120, 123]. The work of Kurdesau et al [122] shows that different methods of producing ITO produce different types of film, for example; ITO deposited by RF sputtering as in this work grows in a columnar fashion and has a cubic bixbyite structure, as also suggested by Bashar [114], but DC sputtered ITO has an amorphous structure [122], in both cases the crystallinity is improved by annealing.

The surface of ITO is not always hospitable to the addition of polymers and other materials such as nanomaterials, this can result in shorting and unstable I-V characteristics and other electrical faults [124]. One possible explanation for this incompatibility is that ITO is a polar oxide with hydrophilic properties and this can prevent adhesion by non-polar organic layers [110]. Therefore to prevent faults occuring some form of surface modification is required in order for other layers to properly adhere to the ITO and for suitable electrical continuity between layers. This surface modification can be obtained either by surface plasma treatment or chemical treatment methods [118, 124-126]. In this work the layer has been modified by the addition of a layer of PEDOT:PSS (see below) which both enhances the band gap and improves the adhesion of subsequent spin coated layers [127, 128].

There are numerous methods for preparing layers of ITO including; radio frequency (RF) sputtering [114, 123], DC sputtering [120-122], closed field reactive magnetron sputtering [129, 130], thermal evaporation [114, 131], sol gel processing [132], pulsed laser deposition [133] and others. The methods investigated in this work were thermal evaporation and RF sputtering and the optimisation process is described in Chapter 6.

4.2 Polymeric Materials

Organic polymers are long chain macromolecules made up of smaller monomers, which are connected to each other by co-valent bonds, usually alternating double and single bonds. With the exception of poly-vinyl acetate (PVAc), the polymers used in this work are based upon the monomer thiophene, which has the chemical formula C_4H_4S and forms a distinctive ring shape similar to that of benzene [42].

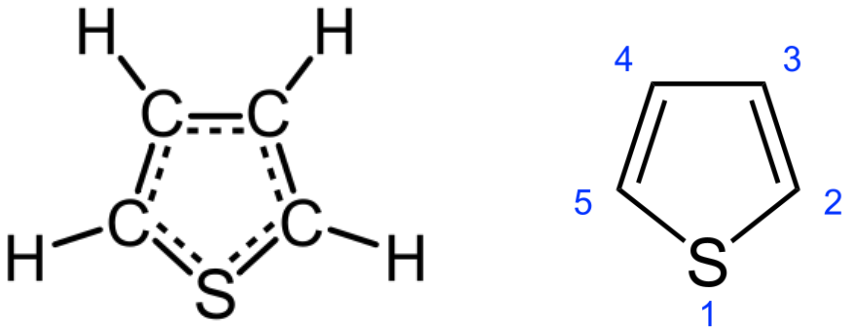

Figure 4-1. Two dimensional representation of the ring structure of thiophene, the image on the left represents the actual structure of the molecule, while the skeletal image on the right indicates the types of bonds and the numbering convention for the atoms in the ring. (Ephemeronium (2010) [134], reproduced with permission).

Thiophene is a clear liquid that can be polymerised by electrosynthesis [42] or by various catalytic processes [135]. The polymers or oligomers (short chains of monomers e.g. sexithiophene) produced are solids and can be dried and removed from the suspension for use in whichever devices they are required. The polymers used in this work were not synthesised in our laboratory, but were purchased from chemical suppliers including Sigma Aldrich and Alfa Aeasar.

Thiophenes have been used in organic electronics for a number of reasons; firstly they are environmentally stable and are relatively robust molecules, secondly they can contribute to conductive or semi-conductive behaviour and have a band gap of ~2.1eV [136], which make them suitable components for photovoltaic and other similar devices such as organic light emitting diodes (OLEDs) [137, 138]. In this work four main thiophene based polymers were used; Sexithiophene (6T), dihexyl-sexithiophene

(DH6T), poly (3-hexylthiophene) (P3HT) and Poly(3,4-ethylenedioxythiophene) poly(styrenesulfonate) (PEDOT:PSS), these are described in detail below.

4.2.1 Sexithiophenes

Sexithiophenes are a group of polymerised oligomers with good light absorbing properties and electrical characteristics. They exhibit photoconductive properties both alone and when blended with various nanostructures and can be deposited by both sublimation and wet processing methods [27]. Although not as photoconductive as P3HT these materials were useful in the optimisation process as they were less expensive than P3HT. However their generally low levels of solubility [139] makes them poor candidate materials for use in industrial scale processes, for this reason the majority of 6T films that have been researched have been prepared by thermal evaporation [46, 140, 141].

Sexithiophene (6T) is an oligomer comprising six thiophene molecules that exists in two basic configurations, the first and most common is α6T and the second is β6T [139]. The α6T molecule is conjugated at the alpha (α) configuration which, using the numbering system defined in Figure 4-1 above, is bonded at the 2-5 position [42]. In the β6T configuration molecule the inner four thiophene monomers are bonded at the 2-5 position, the same as in the α configuration, but the end molecules are bonded at the 4-5 position. B6T is even less soluble than α6T and the maximum absorption peak in the UV-Vis part of the spectrum is different to that of α6T (413 and 435nm respectively). The orientation of the 6T molecule relative to the surface of the substrate onto which it has been deposited is strongly dependent on the material and the method of deposition; for example in films deposited on silicon dioxide or glass by evaporation the polymers are oriented parallel to the surface, which is useful in that it increases contact between the oligomer and any electrode deposited onto it [140, 142]. This has also been shown on other substrates such as titanium dioxide [143] and verified by both infrared and x-ray spectroscopy [143, 144]. Horowitz et al carried out much of the ground breaking work on this molecule in 1997 and showed that photoconductivity was at a maximum around 450nm and was of the order of 10^{-8}A, coincidentally photoluminescence was a

minimum at this wavelength [141]. These values correspond well with the maximum absorption wavelength in the visible part of the spectrum.

Because of the generally low levels of solubility of 6T in many of the commonly used solvents it was decided to use a variant that had an additional hexyl or thiohexyl end chains to improve the solubility of the molecules while retaining their useful electrical characteristics [144, 145]. As a suitable molecule was available commercially from Sigma Aldrich, α,ω-dihexylsexithiophene (DH6T) was selected, this was an α6T molecule with terminal hexyl end chains $CH_3(CH_2)_4CH_2$ joined at position 5 of each terminal thiophene to the CH_2 component with the CH_3 being the free end that increases wetability with common solvents such as dichlorobenzene and chloroform [146].

DH6T orients itself in films deposited by thermal evaporation in the same way as 6T with the added benefit that the hexyl chains increase the order of the film [147, 148]. Comparisons' were carried out between samples that were spin coated (see 5.6.1) and thermally evaporated (see 5.4) and it is apparent that films of blends of DH6T and nanoparticles prepared by both methods have photoconductive properties, but those that are spin coated are consistently higher [27] (§9.1). Kwon et al have suggested that the band gap of DH6T is ~2.4eV, which is greater than that of α-sexithiophene [146], Duhm et al suggest that this small difference is due to the presence of the hexyl chain which influences the π band structure of the molecule [148].

4.2.2 Polythiophenes

Polythiophenes are long chain molecules made up of multiple (many thousands in some cases) thiophene molecules. Poly (3-hexylthiophene) (P3HT), comprises a string of thiophene molecules each with a $CH_3(CH_2)_4CH_2$ hexyl chain attached at position 3 on the molecule, as with sexithiophene each monomer, with hexyl chain, can be joined at the 2-5 (head to tail), 2-2 (head –head) or 5-5 (tail-tail) positions. Where the ratio of head to tail bonds is greater than other bonds (>2:1) the molecule has what is known as a regioregular structure and has better electrical properties than P3HT without this structure (known as regiorandom) [98, 149, 150]. The higher the ratio of head to tail bonds to other bond types the more photoconductive the material will be.

P3HT has a band gap of around 1.9eV [151, 152] and is generally classed as a low band gap polymer i.e. has a band gap less than 2eV and absorbs light with wavelengths longer than 620nm [153, 154]. P3HT is a p-type material i.e. an electron donor and is used in the majority of the most efficient heterojunction type organic heterojunction solar cells currently under investigation around the world [152]. The most successful OPV devices of this type to date comprise a blend of P3HT and PCBM (§ 4.3.1) [98, 155, 156]. However, blends with other electron acceptors such as zinc sulphide and cadmium selenide are being investigated and show promise as they produce high open circuit voltages [151, 157].

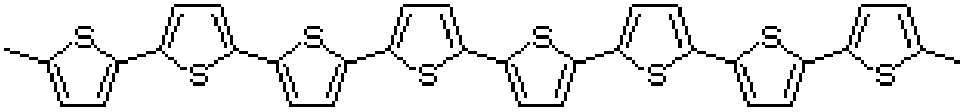

Figure 4-2. Backbone structure of unsubstituted polythiophene showing alternative double and single co-valent bonds (reproduced from Flanagan (2007) [158] under license).

P3HT is made up of a backbone of alternating single and double co-valent bonds as shown in Figure 4-2 above. The double bonds are present in the thiophene molecule and the single bonds connect the thiophenes at points 2 and 5 as described above. The optoelectrical properties of P3HT and other polythiophenes arise from the fact that electrons are delocalised among overlapping π bonds along the length of the polymer. Where the thiophene molecules are co-planar i.e. in the same plane, it is easier for the π bands to overlap or *conjugate*. The conjugation length of a polymer is the distance between adjacent energy levels capable of overlapping, where the backbone is co-planar over a large number of thiophene monomers the conjugation length is long and the absorption wavelength is higher [159-161]. This overlapping of orbitals leads to energy level splitting and the formation of band structures similar to those in inorganic crystalline materials. The ideal P3HT for use in organic photovoltaic devices is therefore one with a high ratio of head to tail bonds and where the majority of monomers are co-planar.

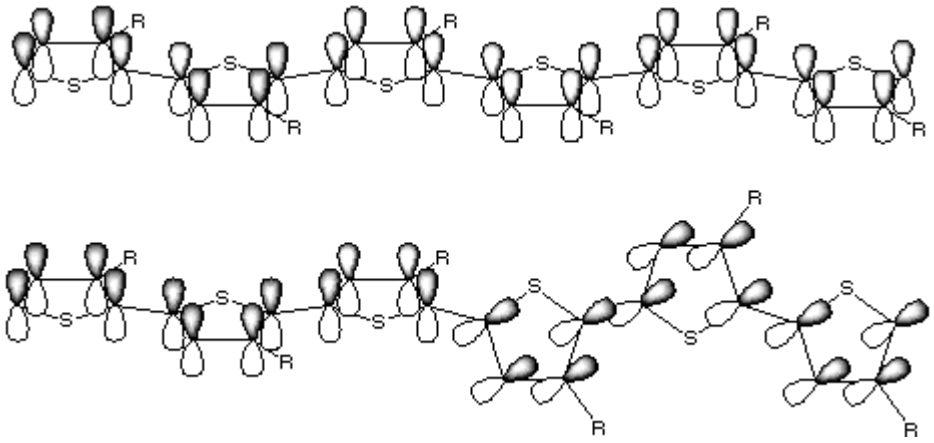

Figure 4-3. Polythiophene molecules with co-planar thiophenes (top) resulting in long conjugation length and disordered thiophenes (bottom) with short conjugation length (reproduced from Flanagan (2007) [162] under license).

P3HT is highly soluble in many of the commonly used solvents such as chloroform and dichlorobenzene; experience accrued during this work suggests that chloroform is a superior solvent for the purposes of forming good quality films by spin coating (§ 5.6.1).

Two types of P3HT were used in this work; standard regioregular Poly(3-hexylthiophene-2,5-diyl and electronic grade of the same, both supplied by Sigma Aldrich. The standard grade was used for optimisation purposes as it was significantly cheaper than the electronic grade which was used once the devices had been optimised and the approach taken in fabrication was determined to be successful.

4.2.3 Poly(3,4-ethylenedioxythiophene) poly(styrenesulfonate)

Poly(3,4-ethylenedioxythiophene) (PEDOT) is a highly transparent electrically conductive ionomer based on the 3,4-ethylenedioxythiophene (EDOT) monomer that carries positive charges [163, 164]. An ionomer is a polymer with repeating electrically neutral units of which a fraction, generally no more than ~15%, are ionised [163, 164]. PEDOT is generally used to modify the electrical characteristics of ITO layers in

transparent electrodes and other optoelectrical devices [127]. The structure of PEDOT is as shown in Figure 4-4 below.

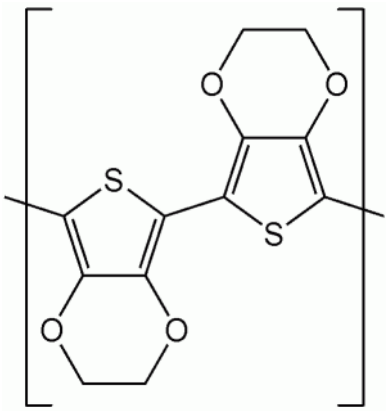

Figure 4-4. Structure of Poly(3,4-ethylenedioxythiophene) (PEDOT) repeating units (Reproduced from Shaddack (2007) [165] with permission).

The useful electrical characteristics of PEDOT arise due to the fact that it, like P3HT, is a conjugated polymer. Its useful features are, however, balanced by the fact that it is poorly soluble in many of the commonly used solvents and therefore difficult to make into useful thin films. This fault is overcome by the addition of a sulfonated polystyrene (poly(styrenesulfonate) (PSS)) chain which carries negative charges and enhances solubility [166, 167]. The combined polymer (PEDOT:PSS) therefore comprises electron and proton charge carriers and has good conductive properties ~150 Scm^{-1} for an 18μm thick film [168].

PEDOT:PSS is usually sold as a dispersion in water, but this does not form high quality films when drop cast or spin coated (§ 5.6.1) because water is quite slow to evaporate in comparison with alcohol based or similar solvents. By adding ethanol or methanol in a 1:1 ratio with the PEDOT:PSS suspension the evaporation rate and ability to bond to surfaces is enhanced and good quality films can be fabricated [127, 169]. This layer is water soluble and can be surface modified by RF plasma treatment [127, 128], it has been shown that it is possible to replace the ITO layer with PEDOT:PSS completely in certain circumstances [170]. PEDOT:PSS is a very transparent material that has a virtually flat absoption spectrum in the visible region and typically reduces the amount

of photons passing through to the active layer by less than 5% (§7.1.1) [171]. The advantages in performance gained by increasing the work function of ITO from ~4.7eV to ~5.2eV offsets these minimal losses [172].

It is anticipated that PEDOT:PSS can be used to modify the work function of ITO transparent electrodes [128, 169], improve the electrical continuity of transparent silver nanowires electrodes [104] and can be used with other materials such as gold nanoparticles [109] and silicate as a transparent electrode [170]. The PEDOT:PSS used in this work was purchased from Sigma Aldrich as an aqueous suspension.

4.2.4 Poly-vinyl Acetate

Poly-vinyl acetate (PVAc) is an insulating polymer derived from the vinyl acetate monomer which in turn is prepared from the combustion of ethylene in the presence of oxygen and acetic acid and a palladium catalyst [173]. In its solid form it is a clear pellet that is colourless or slightly translucent, it has a density of ~ 1.18g/ml [174]. It is readily soluble in methanol and other alcohols and can be easily spin coated or drop cast from solution to form a milky white coloured thin film.

According to the literature PVAc has a relative permittivity of ~3.2 [175] and has a known history of being blended with barium titanate making it the ideal material to test the proposed increase in permittivity arising from the addition of ferroelectric nanoparticles to insulating polymer layers [17, 176, 177].

4.3 Nanomaterials; Properties, Fabrication and Modification

Nanomaterials can have structures that are extremely small; generally defined as being ~100nm or less. Given that a human hair has a diameter in the order of 100μm, the nanomaterials used in this work are at least a thousand times smaller than this and a single nanometre is one hundred thousand times small than this. Thus if the entire length of the UK was to represent the distance of one metre a nanometre would be of the order of a single millimetre. In addition to their small size nanomaterials can have widely differing properties than the bulk material from which they are derived. Many

of the most interesting nanostructures are allotropes of carbon such as graphene, carbon nanotubes and fullerenes or metals and metal oxides. The nanomaterials that have been used in this work include; fullerenes, silver nanostructures, barium titanate nanoparticles (BT) and strontium titanate (ST) nanoparticles.

4.3.1 Carbon Allotropes

The carbon allotropes known as fullerenes are all part of a family with similar molecular structures but widely differing shapes. One of the most commonly occurring natural types of carbon is graphite, which is a silvery grey substance often used in pencils. Graphite is built up of flat of layers of carbon atoms, each layer containing carbon atoms arranged in a plane of interconnected hexagonal structures. Each plane in graphite is essentially a layer of graphene, which is a fullerene comprising carbon atoms in a hybridised sp^2 configuration, i.e. a combination of s and p^2 orbitals that results in a each carbon atom in the lattice having one s orbital and two p orbitals forming the main mechanical bonds in the lattice with an angle of 120^o between each p orbital. The remaining p orbital is oriented perpendicular to the plane of the material and hybridises to form the π^* (conduction) and π (valence) states of the material [178]. Graphene has many properties that make it an ideal candidate material for use in solar cells should a method be invented to fabricate it in large areas; these include, high electrical conductivity and electron mobility (200,000 cm^2Vs at room temperature), transparency and high mechanical strength [178]. It can be fabricated by a number of methods including; mechanical exfoliation, the so called "scotch tape method" where a sticky tape is used to pull layers of graphene from a graphite block, supported growth on various substrates using chemical vapour disposition (CVD) and a number of wet chemical processes [178]. Graphene has a two dimensional (2D) structure i.e. planar, carbon nanotubes (CNT) have a quasi-1D structure, that can be thought of in terms of a "rolled up" section of graphene [178, 179] and buckminsterfullerene, named after the inventor of the geodesic dome, has a 0D structure [178] and can be thought of as a graphene sheet that has been turned into a spherical structure. This structural changes in both CNTs and fullerenes involve the sp^2 state being stretched which results in a distorted state in which the internal angle are greater than 120^o and the π states do not fully overlap [180].

Carbon nanotubes come in a variety of types, single wall carbon nanotubes (SWCNT) and multiwall carbon nanotubes (MWCNT), which as the names suggest are made up of either a single layer of atoms or multiple layers. CNTs have a diameter of the order ~1-30 nm but can be up to several centimetres long. Each type can be further sub-divided into those with conductive (metallic) or semi-conductive properties. These properties arise from the way the nanotubes are "rolled up" from a graphene sheet (see Figure 4-5 below). This "chirality vector"($\mathbf{C_h}$) determines the orientation of the crystal structure along with the translation vector **T** (see 3.1.3) and can be calculated using:

$$\mathbf{C_h} = na_1 + ma_2 \qquad 4.1$$

Where *n* and *m* are integers and a_1 and a_2 are the unit vectors of graphene in real space. When m=0 the configuration is known as zigzag, when n=m the configuration is called an armchair and all other configurations are chiral. Nanotubes where |n - m| = 3q are metallic and those where |n – m| = 3q ± 1 are semiconducting, q is an integer [181]. The ends of carbon nanotubes can be open or capped with semi-spherical structures made up of hexagonal and pentagonal arrangements of atoms and are equivalent to half a C_{60} molecule.

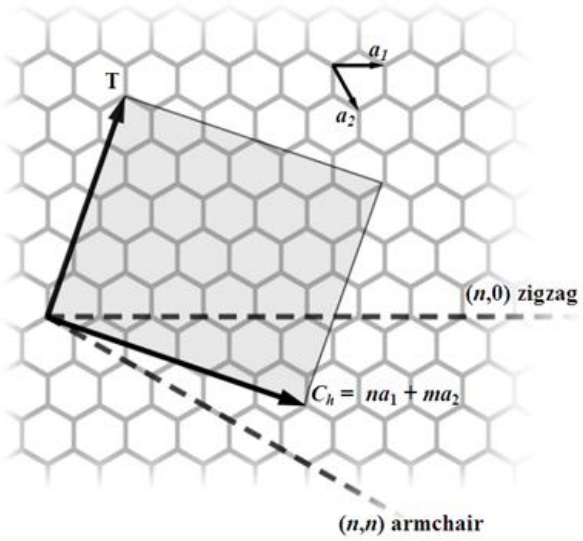

Figure 4-5. Flat graphene sheet showing the chirality and translation vectors and indicating the types of nanotubes available for each possible value of *n* and *m*. (reproduced from Kebes (2005) [182] with permission).

Carbon nanotubes can be grown by a variety of methods including [183]:

- vapour phase growth of nanowires;
- vapour-liquid-solid growth (VLS);
- oxide-assisted growth;
- vapour-solid growth;
- carbothermal reactions;
- solution based growth;
- highly anisotropic crystal structures;
- template based synthesis.

Fullerenes are isotopes of carbon that form regular ball shaped structures from a combination of hexagonal and pentagonal structures known as a truncated icosahedron [184], with alternating double and single bonds they typically have diameters greater than 1nm. They come in a variety of different allotropes including; C_{20}, C_{26}, C_{60}, C_{70}, C_{84} and C_{100}, of which C_{60} and C_{70} are the most common. They form either discrete layers or can be distributed into a photoconductive polymer matrix to form a bulk heterojunction. C_{60} has been found to form spontaneously in condensing carbon vapour [185].

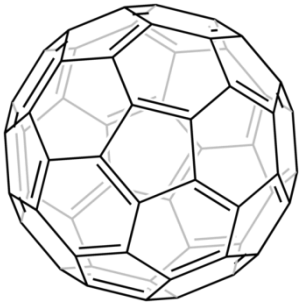

Figure 4-6– Typical buckminsterfullerene (C_{60}) structure (Mills 2007 [185], reproduced with permission).

Buckminsterfullerene (C_{60}) is a strong electron acceptor as it has a three layer LUMO capable of taking up to 6 extra electrons [93] they are often combined with materials such as pentacene which are strong π-conjugated electron donors [113]. Fullerenes are often prepared with ligands to enable them to more evenly distribute through the bulk polymer and to prevent clumping, one of the most common ligand attached fullerenes is

[6, 6]-phenyl-C_{61}-butyric acid methyl ester (PCBM) and is used in a variety of different solar cells [95, 186, 187]. The fullerenes, C60 and PCBM were used as supplied by Sigma Aldrich.

4.3.2 Barium and Strontium Titanate Nanostructures

Barium titanate ($BaTiO_3$) is a ceramic oxide of barium and titanium while strontium titanate is an oxide of strontium and titanium. Both of these materials have similar crystal structures and appearance and similar but not identical chemical and electrical properties. All titanates have a Perovskite structure of the form A B X_3 where A and B are cations (positive ions) of different and X is an anion (negative ion) that is bonded to both cations [188]. The structure of the primitive cell is a single A cation located at a corner of the lattice structure with a B cation at the body centre of the lattice and the three X anions are all face centred.

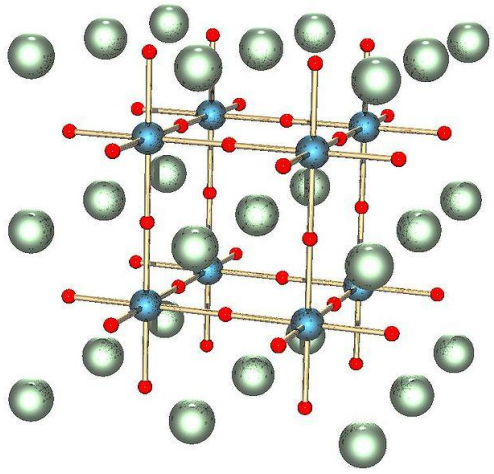

Figure 4-7. This image shows the 3D Perovskite structure shown in the cubic phase, although other phases such as orthorhombic, tetragonal and rhombohedral are possible. The green spheres represent the A cations, the blue spheres represent the B cations and the red spheres represent the X anions (Reproduced from Cadmium (2007) [189](in public domain))

The shape of nanomaterials can have a significant effect on their electrical and chemical properties and by altering the shape of nanoparticles we can exploit these changes in making new polymer nanoparticle blends.

The property of titanates most important to this work is ferroelectricity. Ferroelectric crystals spontaneously polarise at certain temperatures and this polarisation can be reversed when an external electric field is applied [190]. Numerous ferroelectric materials have been used to affect the permittivity of polymers and epoxy resins [16, 191-194].

4.3.2.1 Barium titanate

Barium titanate, which has been used extensively in this work to modify the permittivity of polymer layers has five phases as a solid; hexagonal, cubic, tetragonal, orthorhombic and rhombohedral [190]. It is a high permittivity ceramic material that can be ferroelectric in its tetragonal phase and paraelectric in its cubic phase [195-197], it is the tetragonal phase that is of most interest in this work as this is the phase that can increase the permittivity of polymers [13, 17, 193]. The permittivity of $BaTiO_3$ is strongly dependent on a number of factors including; tetragonality of the crystals at room temperature [190, 198], size and internal structure of the particles [199].

The barium titanate used in this work was obtained from Sigma Aldrich and had a mean particle size of ~100nm with a relative permittivity of 150. From a safety point of view barium titanate is harmful by inhalation, swallowing and can cause skin damage, and should be disposed of with care as it can also cause damage to certain aquatic organisms [200].

4.3.2.2 Strontium titanate

Strontium titanate, like barium titanate is paraelectric in its cubic phase, it can undergo a phase transition to tetragonality at very low temperatures <100K and according to the literaturealso develops ferroelectric properties at ~1400^{o}C [201, 202]. When this was attempted at EMTERC the ST annealed into a light purple coloured solid, but friable, mass. Lower annealing temperatures were attempted and ST was found to anneal into a suitable form for this work under the same conditions as BT.

The strontium titanate used in this work was obtained from Sigma Aldrich and had a mean particle size of ~70nm with a relative permittivity of 300. Unlike barium titanate, strontium titanate is, surprisingly, not harmful under normal circumstances and can be disposed of without damage to aquatic ecosystems [203].

4.3.2.3 Annealing Titanates to Affect Their Properties

The barium titanate nanoparticles used in these experiments were obtained from Sigma Aldrich and in the as bought state are in a cubic phase and are ~100nm in size [168]. It has been demonstrated by Kwon and Yoon [18], and Salaoru and Paul [176], that annealing cubic barium tianate nanoparticles at high temperature will induce a phase change to tetragonality, however it also causes an increase in particle size (~300nm) which could potentially affect the device functionality by causing short circuits. The phase change has been confirmed by SEM and XRD.

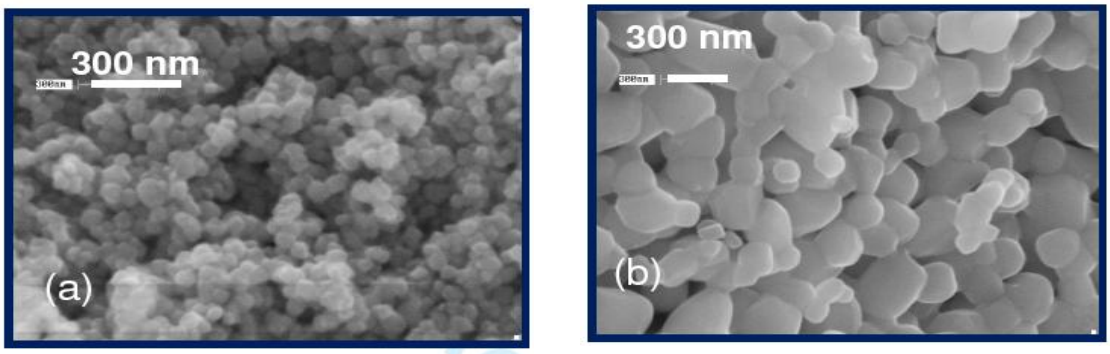

Figure 4-8. SEM images of a. cubic barium titanate and b. tetragonal barium titanate (from Salaoru and Paul (2009) [176], with permission).

The process is not without its drawbacks however; as the heating process can cause the particle size to increase which then has implications such as requiring a thicker polymer layer to eliminate the possibility of short circuits which then reduces the device efficiency [18, 176]. This can clearly be seen in Figure 4-8 above.

The X-Ray diffraction (XRD) results shown in Figure 4-9 below show a distinct difference between the cubic and tetragonal phases at the $2\theta = 45^{o}$ position. The shape of the peak at this point has a distinct shoulder in the tetragonal phase not found in the cubic phase. This clearly indicates that the phase change has occurred.

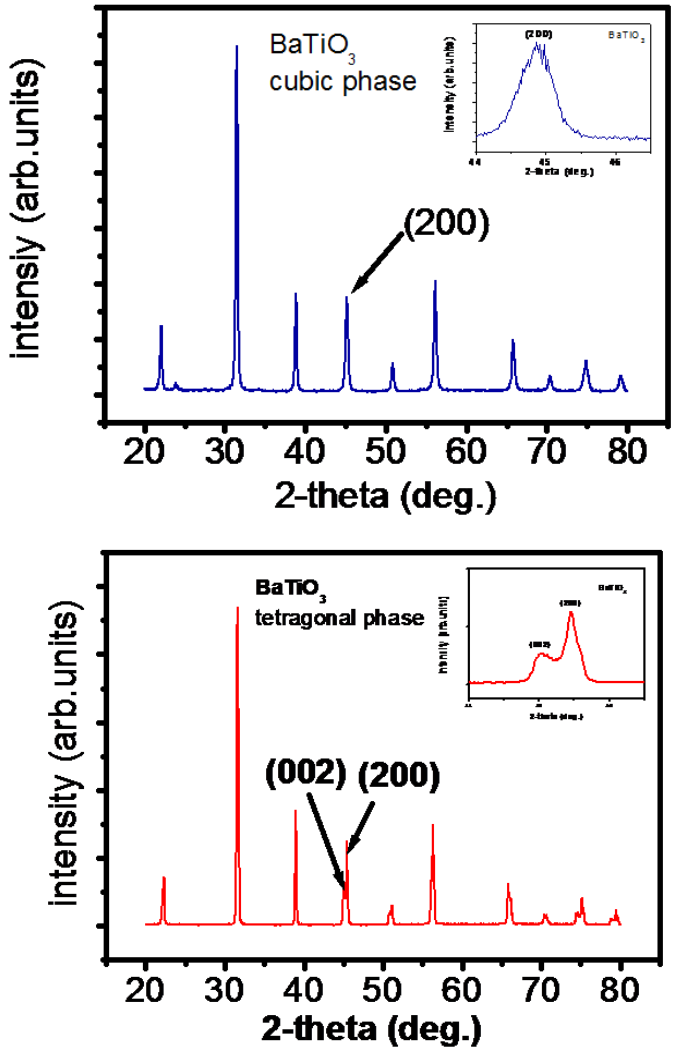

Figure 4-9. XRD images of cubic barium titanate (top) and tetragonal barium titanate (bottom) (from Salaoru and Paul (2009) [176], with permission).

The process of annealing is a relatively simple one; a measured quantity of BT is placed in a ceramic boat and heated in a Carbolite furnace, for one hour at 1000^{o}C in air [18, 26, 176]. The literature suggests that for strontium titanate the annealing temperature is 1400^{o}C for four hours [198, 204-206], but when this was attempted as part of this work it became apparent that while a phase change was induced in the $SrTiO_3$ particles they increased in size quite dramatically (~2μm) and would have been of little use in films ~100nm thick. For this reason it was decided to anneal $SrTiO_3$ at 1000^{o}C like BaTiO3

and this successfully produced particles of the correct size. Furthermore the high temperature produced a colour change from white to a lilac colour that implied a chemical change in the material, but it was not possible to confirm this. The colour change and increase in particle size took place at 1400^{o}C with durations of 1hour and 4 hours, no differences were discernible between the samples annealed at this temperature. It is important not to use inert gases in this process as the oxygen in air is required to fill vacancies created as oxygen is liberated by the heating process. Using nitrogen for example produces a material that is not ferroelectric and has a mean particle size ~300nm.

4.3.2.4 Attaching Ligands to Titanates

Neither barium titanate nor strontium titanate are particularly soluble in the organic solvents typically used in the fabrication of organic photovoltaic devices. In order to produce the types of high quality film necessary for photovoltaic devices it is necessary to modify the particles without losing their inherent properties. One method of doing this is by attaching a ligand, a particle or molecule that bonds to metallic ions while having a free end molecule that renders the combined molecule more soluble in a group of solvents compatible with the end molecule.

The procedure for attaching ligands to titanates is as follows (based on the methodology of Kim et al [13]) (§ Appendix A).

4.4 Summary

This chapter has introduced and given a detailed description of the properties of each of the polymers and nanomaterials the materials used in this work. This includes those that have been used either in the fabrication of the final solar cells or as test materials to prove principles such as the effect of ferroelectric nanostructures on the permittivity of polymers.

A general overview has been provided for each class of materials with brief description of the material and how they can be produced, although it should be stated that the vast

majority of materials were used as purchased with little modification. The exception to this being barium and strontium titanate nanoparticles which require annealing in air at 1000^{o}C to change their structure from the initial cubic paraelectric state to the tetragonal ferroelectric state necessary for the modification of the electrical properties of solar cells such as permittivity, which it is anticipated will lead to an increase in efficiency due to an increase in charge carrier separation.

Chapter 5

5 Organic Solar Cells; Fabrication Techniques

5.1 Overview

This chapter will describe the techniques and materials used in the fabrication of organic and hybrid heterojunction solar cells. All aspects of solar cell fabrication will be covered from methods for cleaning slides to the techniques used to deposit the various layers and the use of solvents and the preparation and modification of polymers and nanomaterials used in this work.

5.2 Cleaning of Substrates

There are two main methods used in cleaning glass substrates; plasma cleaning and chemical cleaning processes. There were three main types of substrate used throughout this work; corning glass slides, ITO covered slide (Sigma Aldrich) and P type silicon wafers. Typically both types of glass slide were cut into 25mm squares prior to cleaning and the silicon wafer was cut in ~1cm squares after cleaning. Plasma cleaning was used for both ITO covered glass and the silicon wafers, while chemical cleaning was used for both types of glass, Corning and ITO covered.

5.2.1 Chemical Cleaning

The process for cleaning glass is a follows, the whole process took place in a Class 100 clean room and with the exception of the drying process took place in a laminar flow bench to ensure both a dust free environment and to prevent the escape of fumes from the chemicals:

The glass was placed in a beaker with a 5% solution of Decon 90 detergent and de-ionised water, this was placed in an ultrasonic bath and sonicated for 40 minutes. Upon completion of this process the samples were rinsed in fresh de-ionised water for 2 minutes in the ultrasonic bath, this was repeated five times. The samples were then placed in a fresh beaker and covered with acetone, the beaker was then placed in the

ultrasonic bath for fifteen minutes. The samples were removed to another fresh beaker and covered in isopropyl alcohol and ultrasonicated for a further fifteen minutes. The slides were then rinsed a further five times as described above. The slides were then placed onto a clean drying rack and blown dry using the nitrogen gun. The slide holder was then placed in an oven at 100^{o}C for one hour to completely dry the slides. The slides were left in the oven to cool, once cool they were removed to a clean slide box and stored until needed.

5.2.2 Plasma Cleaning

The samples to be cleaned were placed in a suitable quartz glass holder and inserted into the chamber of the Bio-Rad PT7100 barrel etcher. The chamber was pumped down to a vacuum ~10^{-2} torr and gas was introduced to the chamber until a pressure of ~10^{-1} torr was reached. A radio frequency generator (RF) in the barrel etcher was then used by tuning the input and reflected power and maintaining the gas pressure plasma was produced. The samples were left in the plasma until clean (typically ~10 minutes). Argon gas was used in most cases, but where more aggressive cleaning or etching of the surface was required oxygen was introduced to the plasma.

Figure 5-1. The PT7100 Barrel Etcher, used for plasma cleaning and surface modification of glass and silicon wafers.

5.3 Vacuum Systems in General

A number of processes used in the fabrication of solar cells use vacuum systems of one form or another, in order to avoid repetition the basic principles of the types of vacuum systems used here will be described now and the subsequent sections will deal with the deposition processes. There are a number of important reasons for depositing materials in a vacuum such as:

1. Reduction or elimination of contamination, by removing air and other gas and dust particles from the chamber the possibility of contamination or oxidation is reduced;
2. Improved film quality, in air the mean free path of a molecule is ~10 x 10^{-6} cm i.e. a molecule can on average travel that distance before colliding with another molecule. The mean free path (MFP) is inversely proportional to the amount of gas (pressure) in the chamber, so by reducing the pressure we increase the MFP and hence reduce scattering which results in a better quality film deposition. For a vacuum of the order 10^{-6} mbar, the MFP is increased to around 5cm. Typically a molecule can have up to 10 collisions before any noticeable deviation is made from its original path, so as long as the distance between the material and the substrate is less than 10MFP then the quality of the film will be maintained [207].

The typical arrangement of a vacuum system is shown in Figure 5-3 below. Two pumps are used in each device, a mechanical (usually rotary) pump is used to bring the system down to a pressure where the high vacuum pumps can operate (~10^{-2} mbar). The vacuum systems at EMTERC have two types of high vacuum pumps, the thermal evaporators use diffusion pumps see Figure 5-2 and the RF Magnetron sputterer uses a cryopump.

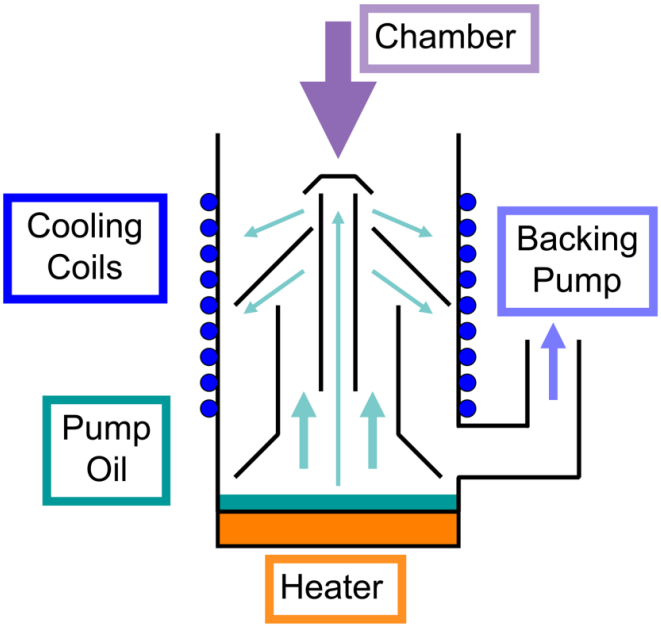

Figure 5-2 – Schematic of Diffusion Pump (Murray 2008 [208], reproduced under licence).

The diffusion pump works by heating an oil which evaporates through a series of concentric tubes [209], water is pumped around the outside of the pump to cool the oil, as the oil condenses it falls back. The convection effect caused by this action draws down the gas from the chamber which is taken away by the backing pump. The oil remains in the pump unless exposed to pressures greater than 10^{-2} mbar while hot in which case the oil can then vent into the chamber causing contamination. Diffusion pump efficiency can be improved by having a "cold trap" at the top of the pump into which liquid nitrogen can be placed. This cools the pump further and helps prevent "backstreaming", where oil vapour escapes into the chamber. The oil will require periodic replacement as it becomes contaminated after repeated use [209].

Cryopumps work by freezing gas or vapour form the chamber onto very cold surfaces; they are typically cooled to ~15K by means of liquid helium from a compressor unit, which is continuously circulated through the system. The pumped out gases remain frozen in the pump, except for very light elements which cannot be frozen out completely and are often removed with additional carbon traps. Because the gases are frozen in the pumps it is necessary to periodically "regenerate" the pump, i.e. allow it to

warm so that trapped gasses can escape. If a cryopump is not regenerated it becomes less efficient [209].

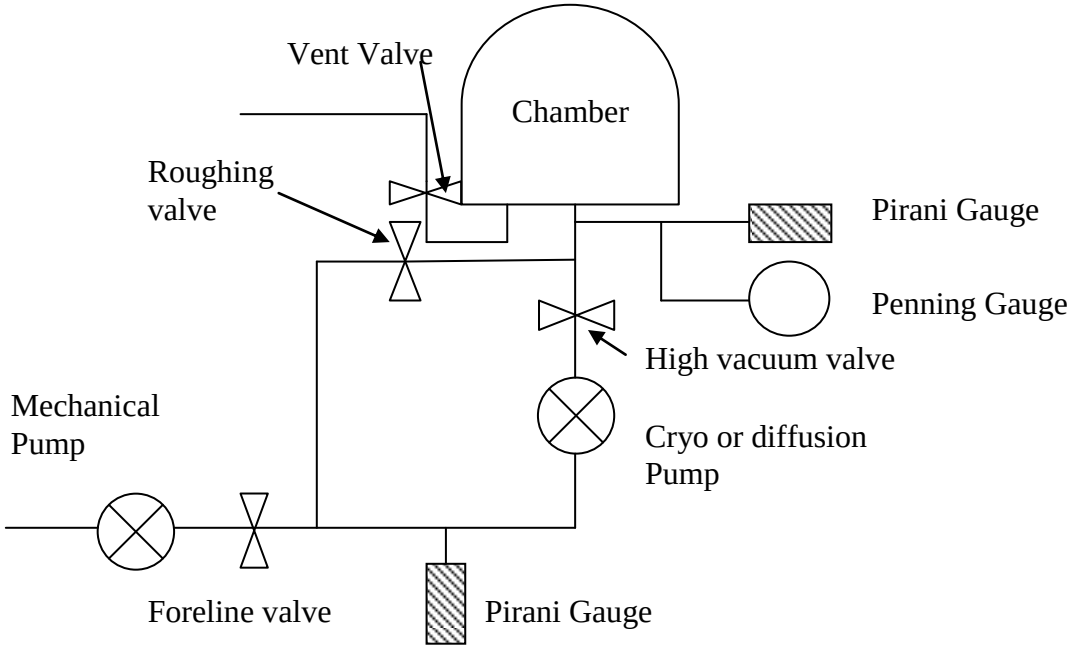

Figure 5-3. Typical arrangement of high vacuum system

5.4 Thermal Evaporation

Thermal evaporation, as the name suggests, is a process for preparing thin films of materials by evaporating the target substance onto a suitable substrate. It is a technique that is suitable for a wide range of materials including; metals, metallic oxides and some organic materials. The general appearance of a thermal evaporator is shown in Figure 5-4 below. The general principles of thermal evaporation are as follows; use a shaped filament or a powder holder known as a boat made from materials with a very high melting point to hold the material to be evaporated and pass a high current through the filament to heat it, the material held by the filament is then evaporated and can be deposited onto a suitable substrate A crystal thickness monitor is used to determine the thickness of the films. In general materials with a high melting point or a low vapour pressure are difficult to deposit by thermal evaporation, although measures can be taken to alleviate this by using a heated boat or filament.

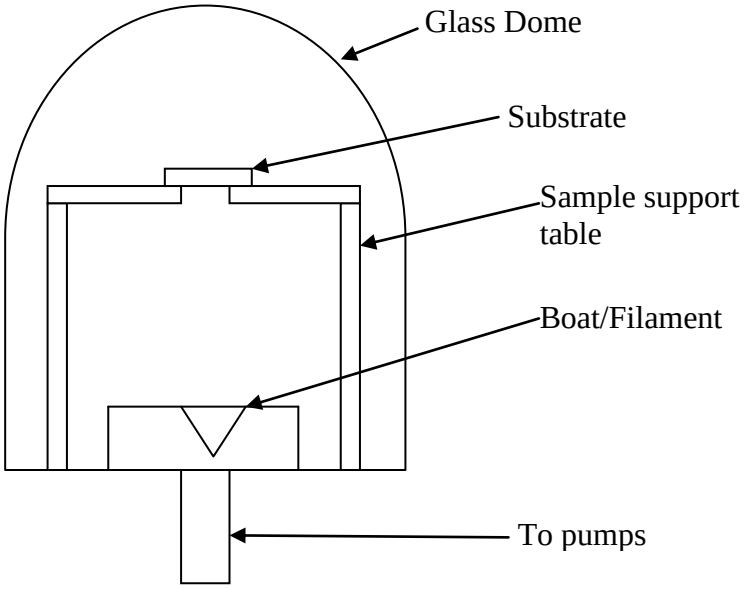

Figure 5-4. Cross Section through a Typical Thermal Evaporator Chamber.

Figure 5-5. The Edwards general use evaporator at EMTERC.

5.5 RF Sputtering

RF sputtering is an alternative process to evaporation and can be used to produce thin films of a wide range of metallic oxides. If direct current (DC) is applied the process can also be used for metals or other conducting materials, in particular those with high melting points or low vapour pressures. DC sputtering can result in very high quality smooth films [210]. DC sputtering is not suitable for non conductive layers, although it is suitable for conducting oxide layers such as ITO. RF sputtering has been used in this work. This section will describe the general RF sputtering process for metallic oxides with a more detailed description of how this can be applied for indium tin oxide. A full description of the investigation of ITO can be found in Chapter 7.

5.5.1 General Principles

The principle, if not the practice, of RF sputtering is relatively simple, plasma is generated and the high energy particles in the plasma bombard the surface of the target material and release atoms or molecules out of the target to be deposited on the substrate. The sputterer used in the Emerging Technology Research Centre at De Montfort University is a Nordiko Ltd model 1500 RF sputterer which incorporates three 8 inch (203mm) removable targets that can be selected individually. The system is

water-cooled and has a vacuum chamber that can be accessed either via the front panel or can be lifted entirely for maintenance purposes. The general appearance of the system is as shown in Figure 5-6 and a schematic of the system is shown in Figure 5-8, both below.

Figure 5-6. Photograph of the EMTERC Nordico 1500 RF Magnetron Sputterer.

The plasma is generated by an RF power supply connected to the target electrode, while the samples to be sputtered are held face down over the target by a bespoke sample holder (Figure 5-7).

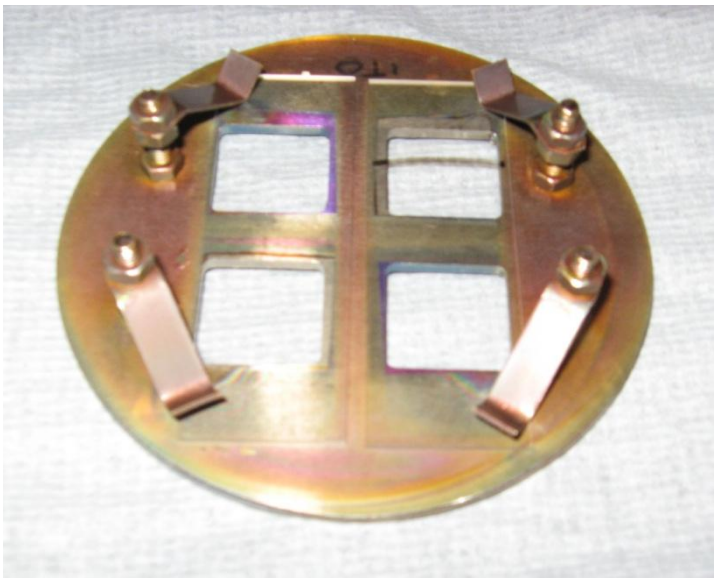

Figure 5-7. Bespoke sample holder for glass slides to be coated in ITO.

A high negative bias develops on the target due to the low mass electrons which accumulate here, this results in heavy high energy cations being accelerated towards the surface of the target, atoms or molecules of the target material are knocked out and if the vacuum is low enough can be deposited onto the substrate without interacting with any other particles. There are two methods of RF sputtering; reactive and non reactive. Reactive sputtering is generally used with oxides such as ITO or ZnO where a stoichiometric amount of oxygen is added to the plasma to complete any vacancies and improve the characteristics of the film. For example in ITO, which is sputtered from a target of indium oxide and tin oxide in a 90:10 ratio, the conductivity reduces as oxygen vacancies are filled but the transparency increases. Thus a sputtered layer of ITO is optimised to find the ideal mix for the characteristics required, § 6.3.2 and 7.1.1 below.

The RF power supply operates at 13.56MHz and the system is tuned to so that the resonant frequency of the circuit matches the frequency of the generator. This results in a purely resistive circuit where the resistance is a minimum, 50Ω, and the power output is at its maximum [35]. The resonant frequency (*f*) of an *RLC* (resistor (*R*), inductor (*L*) and capacitor (*C*)) circuit varies according to.

$$f = \frac{1}{2\pi\sqrt{LC}} \qquad 5.1$$

Where *L* is the inductance of the circuit and *C* is the capacitance of the circuit. For this unit the maximum power occurs when $LC \sim 140$ when *L* is measured in μH (micro Henry) and *C* is measured in pF (pico Farad).

The system is tuned by use of three methods [211]:

- Blocking Capacitors: A series of 200pF capacitors hardwired in parallel which reduce the value of C in the resonant circuit. This system is wired in and cannot be varied.
- The Main Matching Coil: This is a copper coil of 5 ½ turns which contributes to the inductance L of the system, the inductance can be varied by shorting out adjacent turns of the coil with copper straps controlled by the coupling dial.

- The Tuning Coil: A few turns of rotatable copper coil controlled using the tuning dial which adds or subtracts from the inductance in a continuously variable way.

In the Nordiko 1500 sputterer the reflected power should ideally be kept below 5% of the forward power, the system can cope with higher reflected powers, but this can result in damage to the RF generator over long term use. There is a safety feature that will cut off power to the target if the reflected power is higher than 75W.

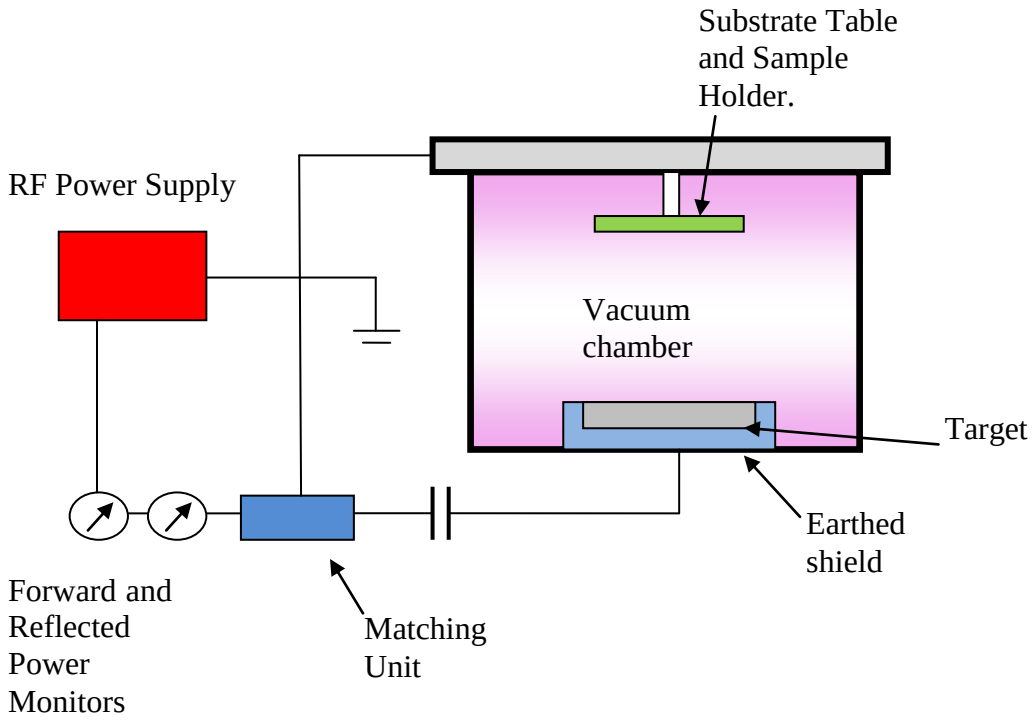

Figure 5-8. Schematic of the Nordiko 1500 Sputterer (after Bashar and Nordiko [114, 212]).

5.6 Wet Processing of active layers

There are a number of methods of depositing thin films of polymers or other materials onto substrates from a solution such as; spin coating, drop casting, painting and printing. The basic premise behind all of these "wet" processes is to find a suitable solvent for the material(s) i.e. one that will adequately dissolve the materials to be deposited without damaging either the substrate or affecting other layers that may already be present e.g. in the case of multi layer devices [213-216]. During this work the most commonly used wet processing technique has been spin coating, however an overview will be given of the other techniques as these have been used occasionally (as in the case of drop casting and painting) or have the potential for large scale preparation of films once the ideal blend has been discovered.

5.6.1 Spin Coating

Spin coating is the main technique by which the polymeric layers were deposited in this work. In the spin coating process a small amount of solution is placed onto the substrate which is then spun at high speeds (up to 10,000 rpm) until the solvent is evaporated and a thin film of uniform thickness is left. The substrate is generally held onto a rotating chuck by means of a vacuum pump, and as the sample is spinning air or a neutral gas such as nitrogen is pumped in to the chamber to aid drying. The spin speed ramps up to the required spin speed, stays at that speed for a specified length of time and then ramps back to a stationary position at which point the substrate can be removed from the spin coater.

Modelling the spin coating process is difficult due to the many different factors involved such as; viscosity of the solution, rate of evaporation, spin speed and air or N_2 flow rate. However, a general term for the relationship between film thickness (d) and the other parameters can be expressed in the form:

$$d = k\omega^{\alpha} \qquad 5.2$$

Where ω is the angular velocity, k and α are empirical constants related to the characteristics of the solution. The value of α is typically around -0.5 and the value of k can vary depending upon such factors as the initial viscosity of the solution [215].

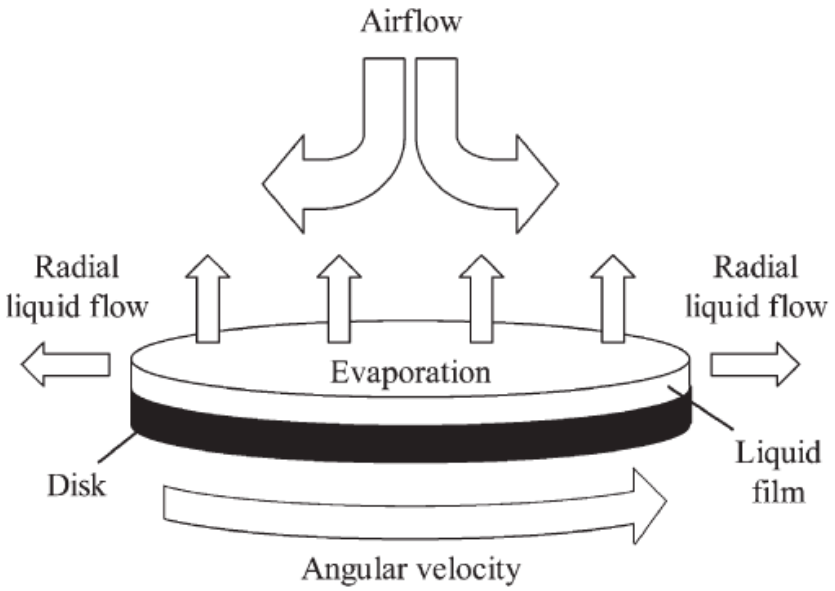

Figure 5-9. Schematic of the major spin coating process (Norrman et al (2005) [217] reproduced with permission).

It is therefore necessary to optimise the process by spin coating a range of samples with the desired viscosity at different spin speeds to determine the optimum speed and viscosity for the required film thickness. In general, as shown in Figure 5-10 below, the film thickness decreases as the angular velocity increases for a given concentration of solution. Spin coating is a good meathod for depositing thin films of organic materials, but is very much dependent on the skill of the operator and requires much practice to produce films of repeatable high quality.

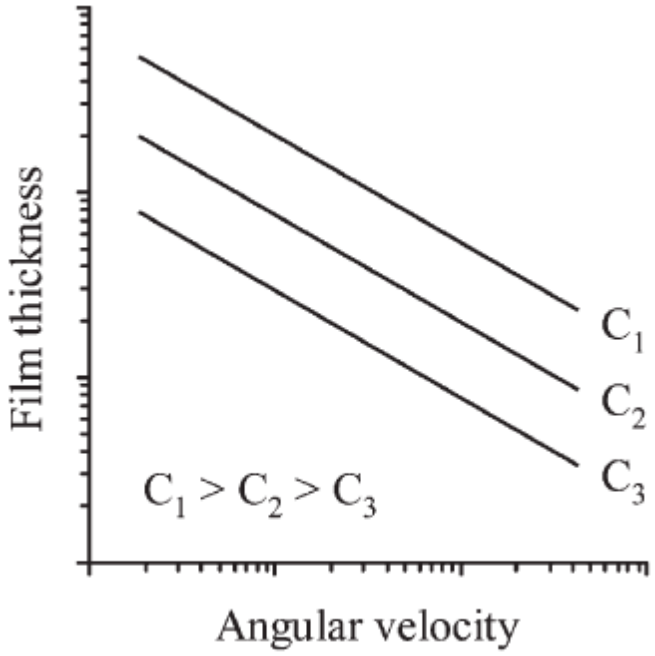

Figure 5-10. Schematic of the relation between film thickness, angular velocity and concentration (Cn) in a spin coating process. The same relation applies for viscosity. (Norrman et al (2005) [217], reproduced with permission).

Typically more concentrated or viscous solutions will produce thicker layers at a given spin speed. This has implications for the fabrication of solar cells and other electrical devices as, in many cases, pure polymer is not the only component in the solution and other materials such as fullerenes and/or other nanomaterials are often added which affects the viscosity and hence the film thickness of the cell. Variations in film quality and thickness can also be achieved by static or dynamic spin coating, in static spin coating the solution is dropped on the substrate prior to it commencing spinning, in dynamic spin coating the solution is dropped onto the already spinning substrate. One of the main drawbacks of this technique is the amount of material wasted in the spinning process is quite high; for example a 100nm film on a 25mm x 25mm substrate occupies a volume of $6.25 \times 10^{-11} m^3$ compared to a starting volume of ~0.5mL (5×10^{-7} m^3). While some fraction of this loss is due to the evaporation of solvent, it can be seen that wastage in terms of polymer and nanoparticles is still a very high proportion of the initial quantity of solution.

5.6.2 Drop Casting

Drop casting is a simple but imprecise method of creating a film on a substrate; it was used primarily to fabricate thick active layers for testing prior to the use of spin coating or other precise and repeatable methods of film preparation. In essence a measured quantity of a solution is dropped onto the upper surface of the substrate and allowed to dry.

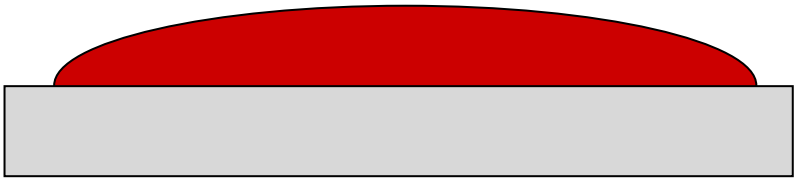

Figure 5-11. Typical section through a drop cast onto a substrate.

As the drop dries a number of factors will come into play that will determine the final thickness and uniformity of the film. The ability of the solvent to "wet" the surface of the substrate will determine the angle between the edge of the film and the surface. This combined with the surface tension of the solution, the volume of the solution and the air flow will influence the way the film dries. Typically drop cast films are much thicker than spin coated layers ~a few hundred nm to a few μm and do not generally have the same uniformity as spin coated layers. Increased film thickness can be an advantage when optimising layers that incorporate conductive or semi-conductive nanoparticles by reducing the probability of short circuits which can occur in very thin films or films where there might be micropores caused by the polymer not be sufficiently soluble in the solvent prior to spin coating. It is, at present, an unsuitable method for fabricating efficient solar cells as the thickness of the material is large compared to the diffusion length of excitons and therefore the majority of excitons produced would recombine before dissociating into charge carriers. The thickness and irregularity also suggests that there would be additional traps that would reduce the current generated by any charge carriers that were generated within one exciton diffusion length of an electrode.

5.6.3 Painting

Painting can be a suitable method for the fabrication of photovoltaic devices from solution, although not investigated as part of this work the method should be mentioned as it is becoming increasingly popular and could potentially allow cheap and easily installed PV systems to be installed at home. For a full description of painting techniques see Appendix A.

5.6.4 Printing and other techniques.

Although not used in this work it is also worth mentioning a variety of other techniques used for depositing films onto substrates for use in photovoltaic devices, these techniques include; ink jet printing, screen printing, pad printing, roll to roll printing, knife over edge coating and a number of other coating methods [215].

5.7 Annealing of Layers

The purpose of annealing the active polymeric layers OPV devices is to increase the crystallinity and order of the active layer(s) and to therefore increase the device efficiency [218]. There are a number of techniques used to anneal these devices including, microwaves, thermal and electric field enhanced thermal annealing [127, 219, 220]. The simplest and most widely used technique is thermal annealing and this is the method that has been adopted for use in this work. Different research groups around the world have used a wide range of temperatures and annealing times ranging between 70^{o}C and 200^{o}C for between 10 minutes and one hour [47, 98, 127, 221, 222]. Furthermore the order in which films are annealed can also have an effect on device efficiency, for example it is possible to anneal each layer individually or to anneal all of the layers at once when the device has been fully fabricated. Gang et al [47] investigated a range of temperatures from 70-150^{o}C for devices of the same thickness (~80nm) and concluded that post production annealing at 110^{o}C for ten minutes provided the best results. There is also debate as to why annealing has the benefits that it appears to, Marsh et al [222] suggest that the increased order in the films causes an increase in the charge transfer time due to exclusion of PCBM as the P3HT becomes more crystalline. This does not seem to have a significant effect on the generation of

excitons or their conversion into electrons and they speculate that the increased order and crystallinity result in a reduction of charge recombination prior to charge transfer to the electrodes.

5.8 Summary

The process of fabricating bulk heterojunction solar cells in this work utilised many of the techniques described above, rather than repeating the descriptions a process based approach is undertaken here to set out which process and materials were used and the parameters that were generally used in these processes. Any variations from these basic parameters will be described in subsequent chapters along with reasons for the variations and a discussion of the results and benefits of these variations. A step by step description of all fabrication processes is presented in Appendix A.

It was initially hoped to be able to fabricate OPV devices entirely from scratch on clean glass substrates, however even though it was possible to fabricate and optimise the ITO layer by sputtering with regard to transparency and conductivity it was difficult and time consuming to obtain suitable reproducible results so a decision was taken to use commercially available ITO coated slides.

Chapter 6

6 Characterisation of Organic Solar Cells

6.1 Overview

Fabrication is only the first step in the process of determining the properties and characteristics of OPV devices. There are a wide range of different techniques that can be used to characterise OPV devices and the ones used in this work are described in detail in this chapter. There are a limited number of measurements that can be taken of finished OPV devices; in many cases the properties of the materials used in these devices can only be determined by fabricating other devices in order to measure a particular parameter. For example; the permittivity of the materials is measured by fabricating a capacitor and using the capacitance to determine the permittivity of the polymer/nanoparticle blend (see 6.4.6 below).

The types of measurements covered in this chapter include electrical measurements, such as capacitance, photoconductivity and photoluminescence, resistivity and solar cell characterisation using the solar cell test circuit and current-voltage (I-V) measurements. Various types of spectroscopy have been used to determine the optical characteristics of the materials such as; ultraviolet and visible (UV-Vis) and Infra red (FTIR). Thicknesses of films were determined using either a profilometer or a monochromatic ellipsometer. Finally a range of microscopy techniques have been used to visualise and characterise the surface properties, morphology and electrical characteristics of the films and nanoparticles these include; scanning electron microscopy (SEM), atomic force microscopy (AFM) and a subset of AFM known as Kelvin probe force microscopy (KPFM).

6.2 Film Thickness Measurements

Before any electrical measurements are taken it is often necessary to determine the thickness of the films whose characteristics are being measured in order to be able to calculate or otherwise determine additional properties from the electrical or optical

measurements. Two techniques were available for determining the thickness of films at EMTERC while this work was carried out these were profilometry and ellipsometry and these are discussed in greater detail below.

6.2.1 Profilometer

One method available to determine the thickness of deposited thin films is profilometry. In this process a fine stylus is moved across the substrate until it encounters the edge of the film, the stylus follows the boundary vertically and the analogue movement is converted into a digital signal and stored as an image. The profilometer used at EMTERC is a Tencor Alpha-Step 200 which, in the mode used here, has a range of up to 800μm laterally and ± 0.16μm vertically. This technique has two main limitations; firstly it requires a reasonably sharp face to the film i.e. the slope of the face of the film from top to bottom is less than the length the stylus travels, secondly the film should be sufficiently dense that the stylus does not become embedded in the film, which can occur with some polymeric materials.

Figure 6-1. The EMTERC Step Profilometer.

A useful secondary function of step profilometry is the ability to carry out surface roughness measurements. By having the stylus travel across the surface of the film, rather than the interface between substrate and the film, irregularities in the film surface can be measured and maximum, minimum and average heights of the peaks and troughs can be recorded.

6.2.2 Ellipsometry

A second method for measuring film thicknesses is Ellipsometry also known as reflection polarimetry [223] , which is a non contact optical method that can also be used to determine the refractive index of the material. The ellipsometer used at EMTERC is a Rudolph Research/AutoEl and has a monochromatic beam of red light (λ=633.2nm). In order to measure a film thickness using this device it is necessary to use a reflective substrate such as silicon wafer. This means that films deposited on glass cannot be measured in this way due to the multiple reflections that occur in glass. Because of the potential difference in film thickness between a sample spin coated onto glass and a sample spin coated onto silicon, caused by the differences in roughness of the surfaces, this approach gives an indication of the film thickness rather than an absolute measurement. For this reason, where possible, profilometer measurements were taken as a comparison.

Figure 6-2. The EMTERC monochromatic ellipsometer.

Newer ellipsometers tend to use Spectroscopic Ellipsometry (SE), which uses a light source with more than one wavelength and allows the measurement of many more parameters including composition, microstructure and temperature of the film surface [56].

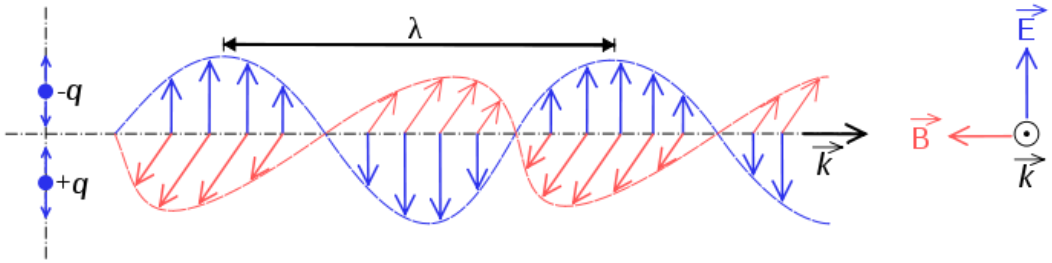

Figure 6-3. Propagating electromagnetic wave showing orthogonal electric and magnetic fields in phase (reproduced from SuperManu (2007) [224])

Ellipsometry depends on the polarisation of a collimated beam of light, Figure 6-3 shows a typical electromagnetic (EM) wave travelling in free space, in this case the electric (E) field and the magnetic (B) field are orthogonal and in phase and have the same amplitude. This case is known as a plane polarised wave, for ellipsometry to work the plane polarised wave has to be converted into an elliptically polarised wave. This is done by a compensator which "slows" one part of the wave relative to another. This results in a wave in which the E and B fields are out of phase with each other, if the phase difference is 90^{o} then the light becomes circularly polarised any other phase angle results in elliptically polarised light.

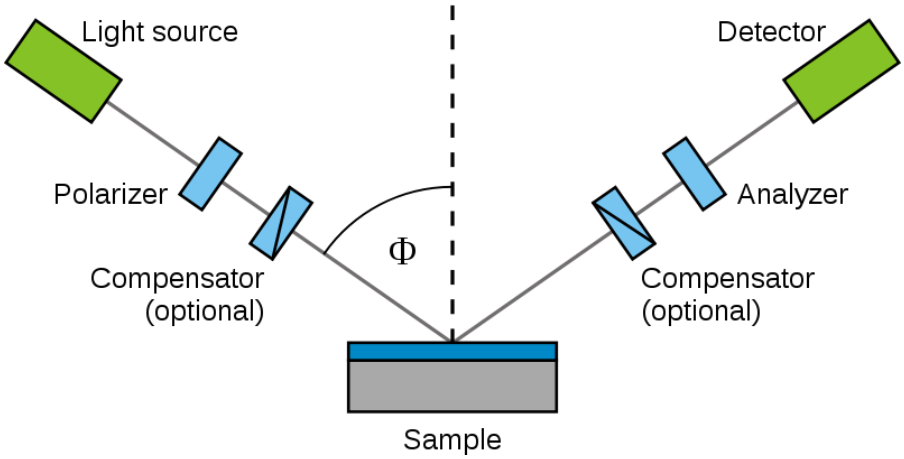

Figure 6-4. General arrangement of an ellipsometer in section (reproduced from Stannered (2008) under license [225])

Figure 6-4 shows the general experimental arrangement of an ellipsometer, in this arrangement three numbers need to be known, the incident angle of the light beam relative to normal (Φ), the differential angular change in the amplitude (ψ) and phase (Δ) of the light beam. A computer then uses Fresnel's Equations to calculate the film thickness and refractive index by means of an iterative process which would take considerable time by hand [56]. The ellipsometer used in this work is a nulling interferometer in which the polarisation of the light is altered until a null reading occurs at the detector.

6.3 Electrical Measurements

As with all photovoltaic devices, whether organic or not it is essential to be able to determine the electrical characteristics of the completed devices and the component materials. This section describes the devices and methodology used to measure such characteristics as I-V and capacitance and details the additional information that can be obtained from these simple measurements.

In general films were deposited using one or more of the methods described in Chapter 5 and top electrodes, usually of aluminium, were deposited using the appropriate shadow mask (see Appendix B). Film thicknesses, where required, were measured

using either profilometry or ellipsometry, whichever was most appropriate to the material and substrate used.

6.3.1 Current Voltage (I-V) Measurements

Current voltage (I-V) measurements are the basis of many of the electrical measurements used in this work, while they are basically a simple process the results can be interpreted in a variety of ways to obtain a number of useful parameters. In this work I-V measurements in conjunction with other techniques have been used to obtain leakage current, resistivity and conductivity characteristics of the component materials of the hybrid OPV devices.

I-V measurements were taken using the Hewlett Packard (now Agilent Technologies) HP 4140B picoammeter and DC voltage source. The ammeter can measure current from ± 1pA to 10mA and can deliver a DC voltage from ± 0 to 100V. The HP 4140B was controlled by a PC connected to the device with a standard IEEE 488-1975 interface cable. The remote commands were given via programs written using the Agilent VEE graphical language environment. With the exception of the program used to measure the I-V characteristics of a solar cell (see section 6.4.4 below), which was written by me, all of the programs were written by Dr Shashi Paul. Some modifications have been made by myself and others to these programs to take into consideration different requirements and upgrades to the software suite since the programs were originally written.

The measurements were taken using a two probe system [56], the probes used were Karl Suss PH100 probeheads connected to the HP 4140B by coaxial cables, one with standard BNC connectors and one with a BNC connector at the probehead and a type E3 coax to triax converter at the current terminal of the HP 4140B. The probes were positioned on the devices manually with the aid of an optical microscope. The experimental arrangement is as shown in the photograph in Figure 6-5 below.

Figure 6-5 – I-V and C-V Measurement Apparatus including isolation box and HP 4140B picoammeter and HP 4192A Impedance Analyser.

The readings were saved as comma separated variable files and then presented graphically using Origin v6.1 or Microsoft Excel.

6.3.2 Resistivity and Conductivity Measurements

Resistivity and conductivity measurements were used to investigate the properties of ITO as a TCO layer. The sheet resistance of the ITO layer was calculated from resistance measurements so that it could then compared with commercially prepared films. This would give an indication of the quality of the layers produced. In order to carry out resistivity measurements of a layer of material the thickness of the layer was determined using ellipsometry or profilometry and a top electrode of aluminium was deposited by thermal evaporation using the gap cell shadow mask (see Appendix B).

Current-Voltage (I-V) measurements were taken using a two probe arrangement (see above) and the data was then used to calculate the sheet resistance and resistivity of the film by the following methodology:

Ohm's Law ($V = IR$) can be re-arranged to determine the resistance $R = V/I$, which is the slope of the I-V graph, from the resistance the resistivity (ρ) can be calculated from [34]:

$$\rho = \frac{RA}{L} = \frac{VA}{IL} \quad 6.1$$

Where ρ is the resistivity in Ωcm, L is the distance between electrodes in the gap cell and A is the area of the film (1mm wide (w) by the thickness of the film (t)). Equation 6.1 can be re-written as:

$$\rho = \frac{Rwt}{L} \quad 6.2$$

The sheet resistance (R_{sh}) is the generally accepted term for discussing the conductivity of uniform thin films that are used as transparent electrodes it has units of ohms, but is usually measured in units of Ω/□ (ohms per square), where the square is a dimensionless term for any square area of film. It is calculated by dividing the resistivity by the thickness of the film, so we have:

$$R_{sh} = \frac{\rho}{t} = \frac{Rw}{L} \quad 6.3$$

Because the thickness of the film was measured and the dimensions w, L and t are fixed by the aluminium layer deposited using the shadow mask calculating the sheet resistance and resistivity was trivial.

6.4 Photovoltaic Electrical Measurements

There are a number of electrical measurements that can be made to characterise PV devices and these are covered in detail below. In order to carry out these measurements a solar simulator was constructed as shown in Figure 6-6 and Figure 6-7 below.

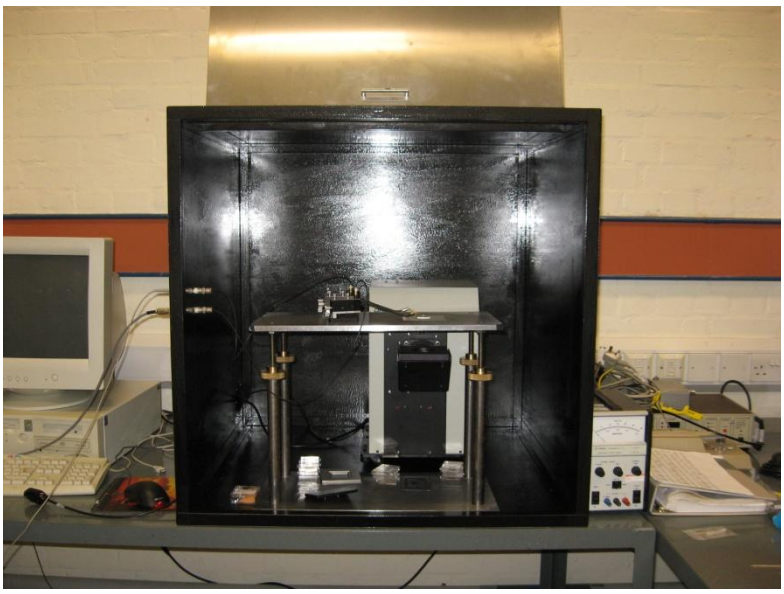

Figure 6-6. Photograph of the EMTERC solar simulator, showing the isolation box containing the probe table and probes and the AM 1.5 lightsource.

By varying the configuration of the wiring to include or exclude the multimeter and variable resistor this experimental arrangement can be used for the full range of electrical tests detailed below, with the exception of photoluminescence.

Photoconductivity and photoluminescence can be used to characterise the properties of the active layer of the device while the other two test methods; OPV test circuit and Forward Bias I-V measurements are used to determine the characteristics of completed solar cells. For the forward bias measurements the previously described Agilent VEE programs control the HP 4140B picoammeter.

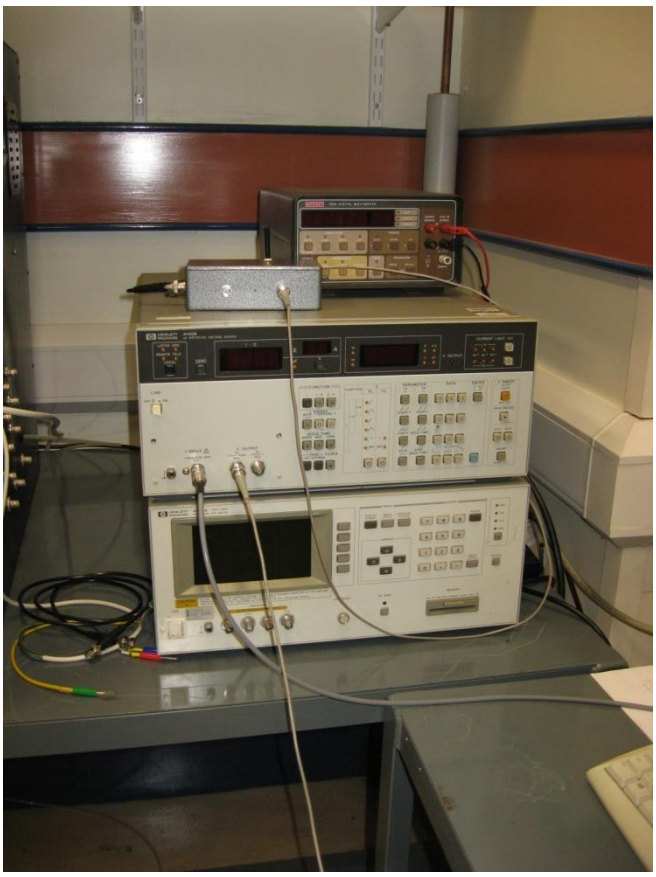

Figure 6-7. HP4140B picoammeter, the Keithley 192A multimeter and a 0-1MΩ variable resistor.

6.4.1 Calibration of Lightsource

The light source used in this work is a Newport Oriel 150W Light unit with an filter, it is designed to output the equivalent of a 1.5W lightsource e.g. 0.1W/cm^2 or 100mW/cm^2. In order to determine that the output of the unit was as described in manual a silicon PV device with a known current and voltage rating was was tested in the solar simulator unit. The test cell was a Sanyo AM-5308 silicon solar cell and has the characteristics presented in Table 3 below.

Table 3. Sanyo AM-5308 characteristics (from Sanyo data sheet [226]).

Parameter	Symbol	Conditions	Ratings			Unit
			min	typ	max	
Open Circuit Voltage	V_{OC}	SS 50kLx		2.5		V
Short Circuit Current	I_{SC}	SS 50kLx		35.3		mA
Operating Voltage and Operating Current	I_{ope}	SS 50kLx, V_{ope} = 1.7V	24.8	31.1		mA
		AM 1.5, 100mW/cm^2, V_{ope} = 1.7V		68.8		mA
Maximum Output (Reference Value)	P_{max}	SS 50kLx, V_{op} = 1.9V, I_{op}=29.2mA.		58		mW
		AM 1.5, 100mW/cm^2, V_{op} = 1.9V. I_{op}=61.5mA.		117		mW
Operating Temperature	T_{opr}		-10 to +60			^{o}C
Storage Temperature	T_{stg}		-20 to +70			^{o}C

As can be seen the operating current under AM 1.5 illumination is typically ~68mA, under the lightsource used in this work the current was ~4mA, which is approximately 17 times lower than it should be. As a second test the solar cell was exposed to natural sunlight on a sunny day and returned a current of ~ 40mA. This indicated that there was a problem with the lightsource.

A light intensity meter was used to measure the power output of the lightsource over a range of wavelengths and the results are presented in Figure 6-8 below.

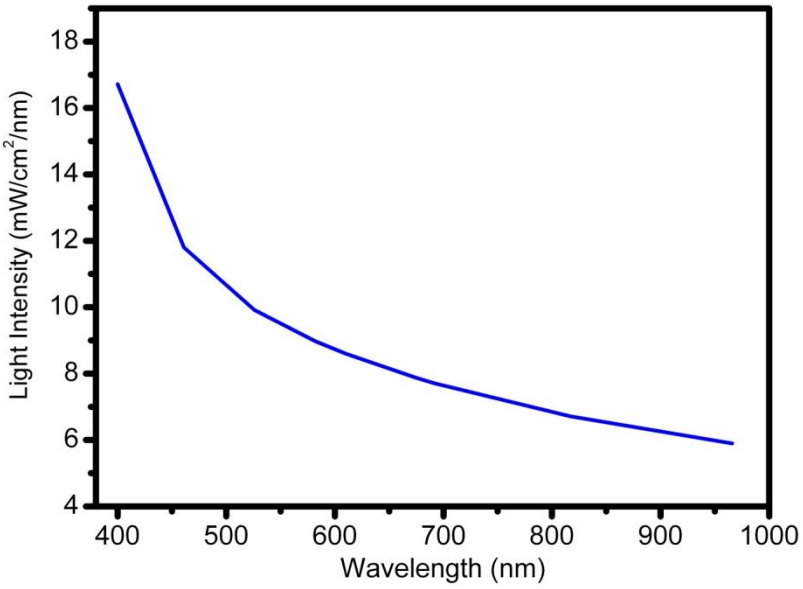

Figure 6-8. Measured Light Curve for Oriel 150W Light Source

The power output was obtained by integrating the area under the curve using the Origin package and dividing by the wavelength range (Area = 4858.6 mW/cm^2/nm, $\Delta\lambda$ = 966 - 400 = 566nm). This obtained a value of ~8.58mW/cm^2, which is considerably lower than the expected value of 100mW/cm^2. Subsequent investigations have been unable to rectify the deficiency in the output of the solar simulator, so all efficiencies calculated here have used a power output of 8.58mW/cm^2 for the lightsource which is close to the value used by other groups who have encountered a similar problem [227].

6.4.2 Photoconductivity Measurements

Photoconductivity is a measure of the response of a conductive material to the presence of light. All of the polymers in the active layers of OPV devices used here are photoconductive and by measuring this effect it could be determined whether the addition of ferroelectric nanoparticles increased the conductive when exposed to a light source. In order to measure the photoconductivity of polymer/nanoparticle blends fabricated by spin coating onto glass substrates it was once again necessary to measure the film thickness by means of the profilometer. Once this step was complete a top set of aluminium electrodes were deposited by thermal evaporation using the gap cell shadow mask (see Shadow Mask 3 in Appendix B).

Two probe I-V measurements were then taken as described above with the samples in the isolation box under illuminated and non illuminated conditions, the results were then compared to determine if the conductivity of the films increased. The applied voltage varied from sample to sample and was generally started low and increased steadily to make sure that the conductivity remained, as much as possible, in the ohmic region. As solar cells are low voltage devices, the applied voltage was generally kept to around ±1V, but for certain films was increased to as much as 20 or even 50V to fully be able to characterise the films. These results are discussed in more depth in section 9.2.2 below.

6.4.3 Photoluminescence Measurements

Unfortunately EMTERC did not possess the equipment necessary to carry out photoluminescence measurements at the time of this work; however, this section will give a brief overview of this technique as it could be used in subsequent work to further validate this work.

Photoluminescence (PL) is a non-destructive technique that is often used to detect impurities in semiconductor material; it relies on optically generated electron-hole pairs recombining radiatively to generate light which can then be measured using a detector and the measured value can be used to obtain an estimate of the amount of excitons created [56].

PL is in principle not a difficult technique to carry out; a light source, usually a laser, with a photon energy greater than the band gap of the material is shone onto the surface of the sample [56, 228]. The energy excites the material leading to the formation of excitons, which recombine and emit new photons which can be detected. There are a number of problems for example; some materials, such as silicon favour different recombination forms such as Shockley-Read-Hall or Auger recombination and therefore do not lend themselves to this technique [56, 228]. However, once a signal has been detected measurements can be taken; the quality of the signal can sometimes be improved by cooling the sample to very low temperatures, this still does not overcome

the inaccuracies that can occur if the ratio of different recombination processes for a given material are not known.

It is hoped that future measurements using PL will be undertaken to investigate exciton production and lifetimes in OPV devices modified by ferroelectric nanoparticles.

6.4.4 The Test Circuit

There are two commonly used methods for determining the electrical characteristics of PV devices; using a variable load resistor in series with the cell and measuring the current and voltage and carrying out forward bias I-V measurements.

Figure 6-9 shows the idealised equivalent circuit of a PV module (see Figure 3-10) with the additional variable load resistor. The load resistor enables the output of the PV device to be tuned so that it operates at its maximum power output. This circuit can also be used to determine the open circuit voltage and short circuit current under illuminated conditions and the dark current when not illuminated.

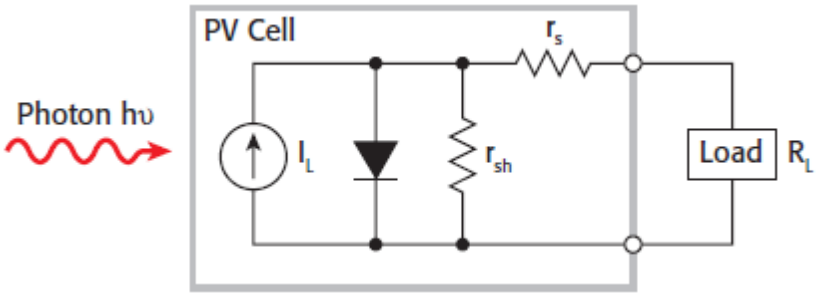

Figure 6-9. Idealised equivalent circuit of a photovoltaic cell, from Keithley (2007) [229].

The current is measured by connecting an ammeter in series with the load resistor and the voltage is measured by placing a Voltmeter in parallel with the cell. By applying the standard AM1.5 light source to the cell in the isolation box and varying the resistance it is possible to obtain the short circuit current, when the resistance is a minimum and the open circuit voltage when the resistance is a maximum. For the purpose of this experiment the resistor used was in the range 0 - 1MΩ. Varying the

resistor creates a curve similar to that shown in Figure 3-12 from which the maximum power point can be obtained and then the fill factor and efficiency can be calculated.

In order to obtain values for the series and shunt resistances it is necessary to carry out measurements at more than one illumination intensity, the value of the series resistance can then be calculated from the variations in maximum power point of each of the I-V curves [56, 230]. Unfortunately as only a single intensity light source was used in this work it was not possible to obtain values for the resistances.

6.4.5 Forward bias IV Measurements

The second method of obtaining values for the V_{oc} and I_{sc} is to carry out standard I-V measurements, as described above, under illuminated and non-illuminated conditions without any additional load resistance. This is the method seemingly most commonly used to determine the characteristics of organic photovoltaic devices [47, 127, 186, 215, 231]. The I-V curve can then be used to determine the FF and PCE of the device as described previously (§3.3). The shunt resistance and diode factor can also be calculated from this data as described in Chapter 2 (§3.3.6).

6.4.6 Capacitance Measurements

The measured capacitance of an OPV device can be used to obtain values for a number of useful characteristics such as permittivity, carrier concentration and the inbuilt potential of the device [57]. The capacitors were fabricated in cross array architecture; see Figure 6-10, which comprises 16 devices.

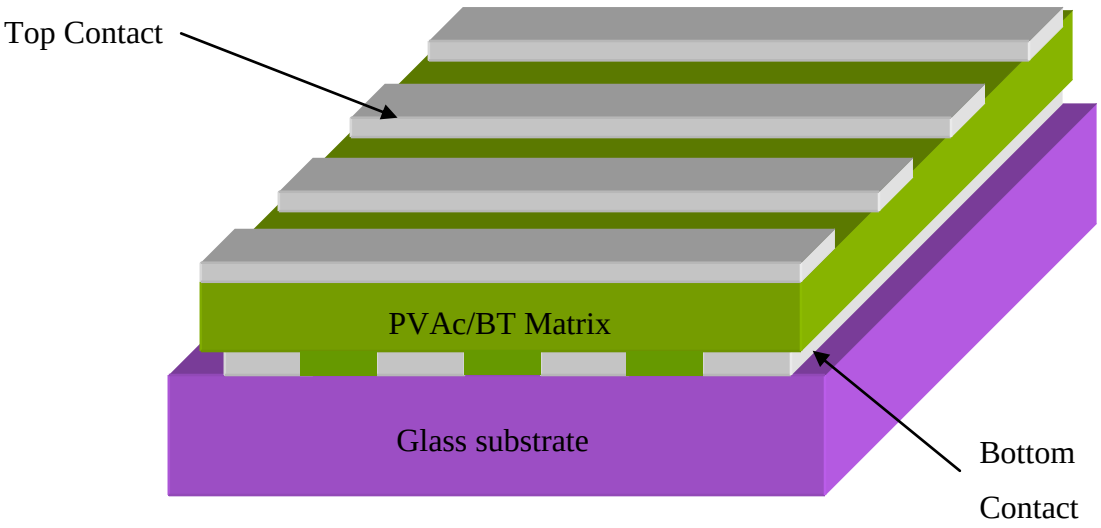

Figure 6-10. Typical sample structure with cross point array architecture.

The cross array of 16 devices was produced by first using shadow mask 1 (see Appendix B) to deposit 4 aluminium tracks by thermal evaporation. The layers of dielectric material were then deposited by spin coating. A top set of aluminium tracks was again deposited by thermal evaporation at 90^{o} to the bottom set. This results in 16 number 1 mm^2 capacitors which can be used to determine the permittivity of the material. The thickness of the film was measured using the profilometer to enable the permittivity to be calculated.

I-V measurements were made to ensure that the leakage current in the devices did not exceed 1nA, a limit agreed by discussion with the supervisory team. Capacitance measurements were then taken using the arrangement described in 6.3.1 above and further detailed in Figure 6-5. The measurements were taken using the HP 4192A impedance analyser which has a range of 5 Hz to 13MHz.

6.4.6.1 Permittivity Measurements

The relative permittivity can be obtained from the measured capacitance by means of the following relationship.

$$\varepsilon = \frac{Cd}{\varepsilon_0 A} \qquad 6.4$$

Where C is the capacitance, ε_0 is the permittivity of free space (8.854 x 10^{-12} F m^{-1}), A is the area of the capacitor and d is the thickness of the capacitor. For a more detailed description of the relationship between permittivity and capacitance see §8.2 below.

6.4.6.2 Carrier Concentration and Built in Potential

Capacitance in OPV devices is voltage dependent and obeys the following relationship [57].

$$\frac{1}{C^2} = \left[\frac{2}{q\varepsilon\varepsilon_0 N_{sc} A^2}\right](V + V_{bi}) \qquad 6.5$$

Where q is the elementary charge, A is the area of the device, N_{sc} is the carrier concentration in the space charge region and V_{bi} is the built in voltage. If the relationship between the reciprocal of the capacitance and the voltage is linear then N_{sc} can be deduced from the slope of the graph and V_{bi} from the intercept with the x axis. However as stated above no PL measurements were able to be taken and therefore no carrier concentrations were obtained meaning that the built in potential could not be calculated.

6.5 Spectroscopy

Although the electrical characteristics of OPV devices are important they cannot be understood fully without access to supplementary information regarding the optical characteristics of the material. The three techniques described below were used to

determine a variety of parameters; UV-Vis measurements can show the absorption and transmission characteristics of solar cells to visible light and can indicate the optimum part of the spectrum and FTIR measurements were used to determine a variety of parameters including the types of bonds in the material. Detailed descriptions of the methodology and processes behind each of these techniques are given below.

6.5.1 UV-Vis Spectroscopy

Ultraviolet and visible light (UV-Vis) spectroscopy was used to investigate the absorption and transmission properties of the various layers making up the solar cells used in this work. The absorption characteristics of the materials were used to quantify those regions where the maximum amount of light was absorbed and to determine the energy of that light. UV-Vis spectroscopy works by measuring the attenuation of light either when the light is transmitted through a transparent material or when light is reflected from a surface [223]. A light beam at each wavelength or range of wavelengths was transmitted through the sample and the absorption measured. This measured loss of light can be accounted for by scattering, absorption, reflection or interference. The absorbed light affects the electrical properties of the material and can result in either the creation of excitons or free charge carriers, hence the interest in this technique regarding the absorption characteristics of solar cells.

The transmittance (T) at each wavelength can be calculated from the ratio between the initial radiant power (P_0) and the final radiant power (P) and is expressed as a percentage. It can also be expressed as the ratio of the initial and final intensity of the light I_0 and I respectively [223].

$$T = \left(\frac{P}{P_0} = \frac{I}{I_0}\right) \times 100\% \qquad 6.6$$

The absorbance (A) of light in the sample can be thought of as being linear within certain limits and obeys the Beer-Lambert law [223]:

$$A = a \times b \times c \qquad 6.7$$

Where *a* is the wavelength dependent absorption coefficient, *b* is the path length and *c* is the analyte concentration, this last term can generally be ignored when not using materials in solution form. In this work I have used only thin films on plain glass or ITO coated glass slides and therefore can ignore this term. The absorbance is related to the transmission by:

$$A = -\log T = -\log \frac{P}{P_0} \qquad 6.8$$

Both T and A have no units and have been expressed in arbitrary units in this work, usually either as a coefficient between 0 and 1 or as a percentage.

The UV-Vis spectrometer used in this work is a Thermo Scientific Evolution 300, it is a dual beam spectrometer that uses a beam splitting device to takes a background scan of clean substrate prior to testing the thin films on the same substrate and uses a clean reference substrate in the scanning process. This allows the substrate to be corrected for automatically during the scanning process and produces a spectrum that is only for the film and not the substrate.

6.5.1.1 Estimation of band gap by Tauc Plotting

An additional useful tool that arises from UV-Vis spectroscopy is the ability to obtain an estimate for the band gap of a material from the transmission spectrum of the material. Tauc first demonstrated this technique in 1966 and 1968 and the remainder of this section is derived from his work [232, 233]. In a Tauc plot the photon energy in electron volts (eV) is plotted on the x axis and the y axis is the square of the photon energy times the absorption coefficient ($(\alpha E)^2$). Typical examples, for the same material, of both the transmission spectrum and the Tauc plot are shown in Figure 6-11 below.

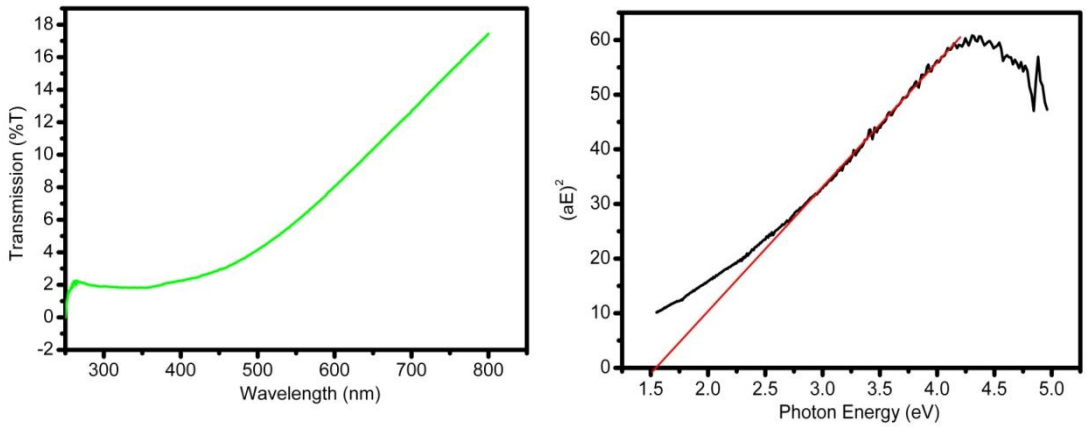

Figure 6-11. a. Typical example of UV-Vis transmission plot, b. Example Tauc Plot showing linear projection onto x axis to derive an estimate for E_g.

The transmission plot is made directly from data obtained using the UV-Vis spectroscope, while the Tauc plot is made from data calculated from these data. The direct transition values can be calculated using the Tauc formula [234]:

$$(\mathrm{E}\alpha)^{1/2} = (h\nu\alpha)^{1/2} = Constant \cdot \left(h\nu - E_g\right) \quad 6.9$$

Where α is the absorption coefficient, ν is the frequency of light and is equal to c/λ and E_g is the band gap. As stated in Chapter 2 E can be calculated from:

$$E(eV) = \frac{1240}{\lambda(nm)} \quad 6.10$$

And α can be calculated from:

$$I = I_0 \cdot e^{-\alpha x} \quad 6.11$$

Taking Logs and rearranging to compare with equation 6.6 we get:

$$\alpha = \frac{1}{x}\ln\frac{I_0}{I} = \frac{1}{x}\ln\frac{100\%}{\%T} \quad 6.12$$

By substituting the values obtained from the UV-Vis spectroscopy it values for $(\alpha E)^{1/2}$ and E can be obtained and plotted to get the Tauc plot. Tauc showed that by manually extending the linear section of the plot back to the x axis an estimate can be obtained for the value of the band gap of the material [233]. The value of the band gap can be converted back into a threshold wavelength by re-arranging equation 6.10, absorption will only take place for photons with greater energy and hence wavelengths below this value.

6.5.2 Fourier Transform Infrared Spectroscopy

Fourier Transform Infrared (FTIR) Spectroscopy is a technique that uses infrared absorption to obtain information on the physical aspects of a material such as the types of bonds and detection of certain impurities such as oxygen and carbon in silicon [56, 235]. It was used in this work to determine if the OPA ligand was present and attached to the BT nanoparticles. FTIR works by using a black body to emit thermal radiation across a range of wavelengths, rather than other spectroscopic techniques which use diffraction gratings to create monochromatic light at each wavelength (such as UV-Vis). The beam is collimated and passes through a Michelson interferometer, see Figure 6-12 below. The beam then passes through a beam splitter, often a prism or half silvered mirror, and is divided into two beams. The beams reflect off of the mirrors and pass through the beam splitter a second time in the opposite direction and are focussed onto the target. A detector measures the intensity of the beam. One of the mirrors is moveable and as the mirror is moved the path length for one leg of the interferometer is varied. When the path length between the two beams is the same they reinforce each other and when the path length is out of phase by 180^{o}, when the change in path length equals $\lambda/2$, they cancel each other due to destructive interference.

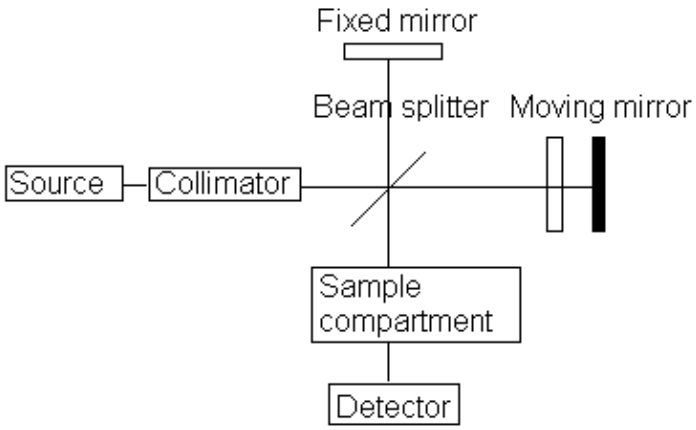

Figure 6-12. Schematic of a Michelson interferometer as used in Fourier Transform Infrared Spectroscopy, (reproduced from Gans (2010) [236], with permission).

By varying the position of the mirror an interference pattern is obtained from the variations in intensity of light at the detector, This consists of a series of maxima and minima that obey the following relationship [56].

$$I(x) = \int_0^f B(f)[1 + \cos(2\pi x f)]\, df \qquad 6.13$$

Where $I(x)$ is the intensity of light varying in accordance with x which is the distance travelled by the mirror, f is the frequency of the light and $B(f)$ is the source intensity modified by the sample. As the source produces a range of frequencies rather than a monochromatic beam, the intensity of the interference pattern is the integral sum over the range of frequencies used. The interference pattern itself not used as it is the spectral response which is of interest. To obtain this a Fourier Transform is carried out by computer using the following relationship [56]:

$$B(f) = \int_{-\omega}^{\omega} I(x)\cos(2\pi x f)dx \qquad 6.14$$

This results in a spectrum where the transmittance or absorption is measured on the y axis and the x axis is measured in cm^{-1} as the Fourier transform inverts the dimension of the length to reciprocal space. This is known as the wavenumber domain.

6.6 Scanning Electron Microscopy (SEM)

An electron microscope is a powerful tool for determining both small scale variations in the surface of a material and for probing into the structure of the material. In essence an electron microscope scans a beam of electrons across the surface of a conductive material, by measuring the electrons produced from ionisation (secondary electrons) and backscattered electrons a raster image is constructed. By using electrons, a resolution down to the wavelength of the electron can be obtained and by making use of the idea of wave particle duality much smaller wavelengths can be achieved and therefore much better resolution can be obtained.

When using an electron microscope to view non conductive materials it is usually necessary to coat them with a conductive material, such as gold, to prevent charge build up on the surface, which would affect the resolution of the image by deflecting incoming electrons away. Some newer electron microscopes do not need to coat the polymer and remove the charge by varying the air pressure in the sample chamber (in normal conditions the pressure is as close to vacuum as it can be achieved with the equipment).

This method produces high quality images of the surface of a material. SEM was primarily used in this work to obtain images of nanomaterials in polymeric matrices.

6.7 Atomic Force Microscopy (AFM)

Scanning Probe Microscopy (SPM) is a technique where a sharp probe is passed back and forth across a sample surface to obtain a two or three dimensional raster image built up in a similar way to the picture on a television screen [56]. It was used in this work to obtain surface images of the polymeric layers. Atomic Force Microscopy (AFM) is a type of SPM that was first used in 1986 to examine the surface of insulators [56].

Figure 6-13 below shows a general schematic of the operation of a typical AFM. In this arrangement the sample is placed onto a table which moves during the scanning operation rather than moving the probe tip. The tip comprises a cantilever with a very sharp tip on the end. The composition of the tip depends upon the type of scan required, but is most commonly made from silicon or silicon oxide, which can be coated in gold or a similar metal if a conductive tip is required for electrical measurements.

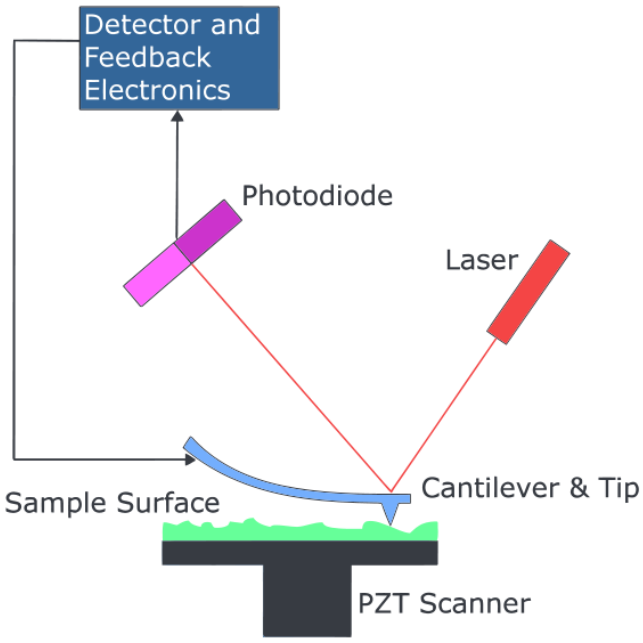

Figure 6-13. Atomic force microscopy block diagram (from Overlord (2008) [237], with permission).

In the above arrangement, the tip is illuminated by a monochromatic laser the reflected light of which is detected by a four segment photodiode. The position of the reflected beam on the photodiode enables the x, y and z position of the cantilever relative to the surface of the sample to be calculated by the detector and feedback electronics. In some modes, for example non contact, the tip can also be driven by a piezoelectric transducer to enable the tip to be vibrated at its resonant frequency, the van der Waals forces at the surface reduce this frequency enabling the tip to be maintained at a known distance above the sample [56].

Depending upon the type of measurements required an AFM has three main modes, which can be adapted to many uses, these are; contact mode, tapping mode and non-contact mode. The names give a clue to the operation in each mode. In contact mode the tip is dragged across the surface to be scanned, this gives an accurate topographical impression of the surface, but can result in damage to both the sample and the tip due to forces between the surface and the tip. In tapping mode the tip makes brief contact with the surface before being lifted up, this is repeated over the surface of the sample. This method is useful for soft or brittle samples. Non contact AFM measures the van der Waal forces between the surface and the tip to obtain an image of the surface. The forces are much weaker than those encountered in either of the contact or tapping modes and need to be supplemented by oscillating the tip and applying an AC voltage. As the bulk of the experimentation in this work has been carried out using polymers non-contact AFM was selected as the most logical way to obtain images without damage to the surface, furthermore given the size of the particles used in this work the resolution of NC-AFM was thought to be sufficient [56].

Figure 6-14. The EMTERC Park System XE- 100 SPM.

6.7.1 Kelvin Probe Force Microscopy (KPFM)

Kelvin probes are small discs 2-4mm in diameter that are used to measure the surface potential of a sample. They are held a small distance above the surface and vibrated vertically, the vibrations cause a change in capacitance between the probe and the surface which can then be interpreted into a potential measurement [56]. It is possible to apply a variation of this methodology to an SPM operating in a non contact electrostatic force microscopy (EFM) mode.

In this mode a conductive tip is placed close to the surface, but not touching, the distance is dependent on a number of factors, such as the surface irregularity of the sample and the tip dimensions, and can vary between a few tens or a few hundreds of nanometres. The tip is driven by both an AC and a DC voltage. The AC voltage is used to drive the tip at close to its resonant frequency while the DC voltage is used to minimise the vibration. This resonance creates an electrostatic force between the tip and the surface which can be measured and used to obtain a value for the surface potential. As with the Kelvin probe this force is related to the voltage (*V*) across the capacitor (capacitance *C*) of the combined probe/surface system [56]. The relationship between the energy of the system (*E*) and the force (*F*) with tip to sample spacing *z* is:

$$F = \frac{dE}{dz} = -\frac{1}{2}\frac{Q^2}{C^2}\frac{dC}{dz} = -\frac{1}{2}V^2\frac{dC}{dz} \qquad 6.15$$

The potential at the tip is given by:

$$V_{tip} = V_{dc} + V_{ac}\sin(\omega t) \qquad 6.16$$

Substituting equation 6.16 into 6.15 gives:

$$F = \frac{1}{2}\frac{dC}{dz}\left[\left(V_{dc} - V_{surf}\right)^2 + \frac{1}{2}V_{ac}^2(1 - \cos(2\omega t)) + 2\left(V_{dc} - V_{surf}\right)V_{ac}\sin(\omega t)\right] \qquad 6.17$$

V_{surf} is the potential at the surface of the sample and the force between the tip and the sample surface consists of three components; the static (F_{dc}), first harmonic (F_{ω}) and second harmonic ($F_{2\omega}$).

$$F_{dc} = \frac{1}{2}\frac{dC}{dz}\left[\left(V_{dc} - V_{surf}\right)^2 + \frac{1}{2}V_{ac}^2\right] \qquad 6.18$$

$$F_{\omega} = \frac{dC}{dz}\left(V_{dc} - V_{surf}\right)V_{ac}\sin(\omega t) \qquad 6.19$$

$$F_{2\omega} = -\frac{1}{4}\frac{dC}{dz}V_{ac}^2 \cos(2\omega t) \quad 6.20$$

Therefore by knowing the potential at the tip of the probe it is possible to use the above equations to obtain values for the surface potential of the sample. In practice this operation is carried out automatically by the software driving the system and the results are presented in graphical form on the screen. To date KPFM has been used to investigate the surface potential properties of thin films [238-240] and work function [241]. It was intended to use KPFM to investigate potential differences in polymer nanoparticle films, but early attempts were not successful. This is likely to improve in future as more experience is gained using this technique.

6.8 Summary

This chapter has described all of the techniques used in this work to investigate and characterise the devices fabricated according to the methodologies described in chapter 4. While many techniques have been used the most important have been the electrical measurements and the spectroscopy measurements. The use of capacitance measurements to determine the permittivity of materials has been described as have I-V measurements under illuminated and dark conditions, using an AM 1.5 lightsource, to determine the electrical characteristics and hence the efficiency of the devices. Uv-Vis spectroscopy has been used to determine the absorption and transmission characteristics and hence enable the calculation of the band gap of the material using the Tauc relationship.

Various methods for characterising the surface characteristics of films such as AFM and SEM are also described along with thickness measurement techniques such as profilometry and ellipsometry.

Chapter 7

7 Optimisation of Transparent Electrode Layer

This first half of this chapter describes an attempt to produce a high quality layer of ITO in order to reduce our dependence upon expensive commercially produced slides. Although this initially produced promising results it was not possible to produce films of sufficient quality and reproducibility to rival those produced commercially. This was due to a number of reasons, including equipment failures and lack of time. Subsequently the second half of this chapter describes the modification of commercially produced ITO coated glass with a layer of PEDOT:PSS.

7.1.1 ITO Film Optimisation

ITO films are most commonly deposited by RF sputtering [114, 117, 242], although it is possible to use other methods such as; thermal evaporation [114, 131], pulsed laser deposition [116, 133], spray pyrolysis [114], or sol gel processing [132]. Initially due to material availability and for economic reasons it was decided that the first step in optimising the ITO layers for this work would be to use thermally evaporated ITO. The material used for this was a granular compound of ITO, this proved unsuitable for the evaporation process due to the high current required to sublimate the material, and subsequently the granules were ground into a powdered form to allow a better chance of evaporation.

Numerous attempts were made to deposit films by thermal evaporation and yellow to brown films visually appearing to be ITO were produced. Aluminium top contacts in a Gap Cell arrangement, Figure 7-1, were deposited by thermal evaporation using a shadow mask to obtain the required orientation and spacing to carry out electrical measurements. Current-Voltage (I-V) measurements were taken using a two probe arrangement [56], and the sheet resistance and resistivity of the film was calculated as previously described (§6.3.2).

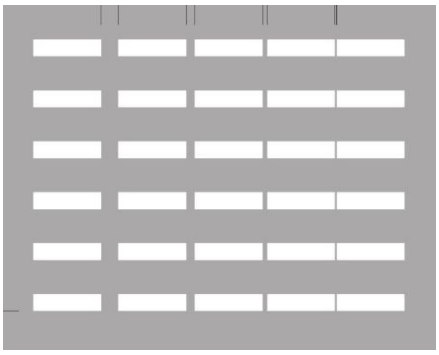

Figure 7-1 – Gap cell shadow mask.

Further optimisation of the films was carried out using the XP-100 Scanning Probe Microscope in Non-Contact Atomic Force Microscopy (NC-AFM) mode to obtain images of the layer and to determine the average roughness of the sample. As can be seen from Figure 7-2 below the grain size was relatively large (~100nm) and the surface was rough and uneven with an average surface roughness of 58.1nm.

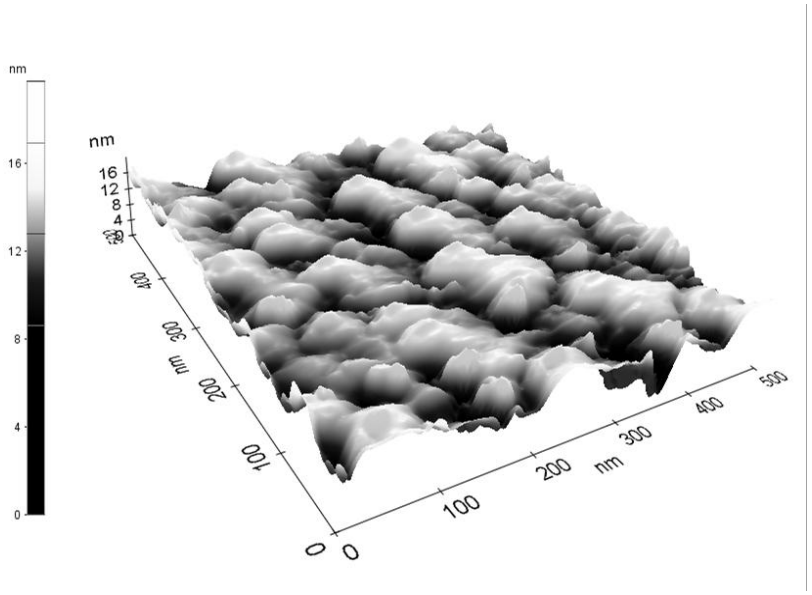

Figure 7-2– Non-contact atomic force microscope image of ITO deposited by thermal evaporation.

The most conductive layer of ITO produced by thermal evaporation resulted in a sheet resistance ~6 x 10^4 Ω/□ which was far too high to use to use as a transparent electrode. It was subsequently decided not to continue with this line of research and to attempt to

optimise the layer using the Nordico RF Sputterer. A circular 225mm diameter target composed of Indium Oxide (99.9% purity) and Tin Oxide (99.9% purity) [114, 242] in a 9:1 ratio, approximately the optimum doping level [119] was obtained and installed in the sputterer. The gases to be used in the sputtering operation were argon (Ar) and oxygen (O_2) and an extensive search of the literature was carried out to determine the appropriate starting parameters to obtain a conductive stoichiometric layer of ITO. The work of Bashar [114] and Meng and Placido [120] were particularly useful in obtaining these starting values, although it must be stated that these values cannot be taken as absolutes given the differences between sputtering machines. It should also be noted that the target used by Bashar was 100mm diameter and as such has different power/cm^2 values to the target used in this work.

Using an Argon flow rate of 30 sccm and no oxygen the optimum power to obtain the desired film thickness was determined by repeat measurements with deposition times of 30 minutes. Film thicknesses were determined by a combination of Ellipsometry and Profilometry.

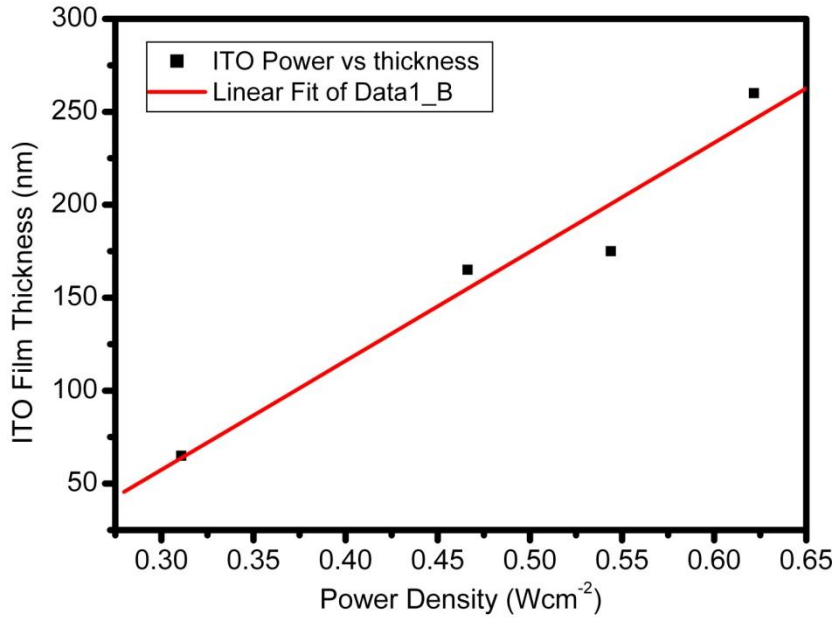

Figure 7-3– Thickness of ITO Films at different sputtering power levels.

The film thicknesses as shown in Figure 7-3 indicated that the optimum power density for the desired film thicknesses (120-150nm) would be in the range 0.4- 0.47 Wcm^{-2} which equates to an overall power to the target of 100-150W, however at 100W the

desired resistivity would not be achievable and that at high powers the ITO layer becomes hard and very resistant to etching and other forms of modification, which may be necessary to obtain functional solar cells [114, 117].

Various works have suggested ranges for annealing temperatures for ITO between 200 and 400^{o}C [114, 117, 120, 122], with the best results in either a vacuum or nitrogen atmosphere or air. For the purpose of this work an intermediate figure of 250^{o}C was used and the samples were annealed in air, under ideal conditions a nitrogen atmosphere would be used to prevent oxygen filling the available vacancies and thus reducing the conductivity, but this is not currently possible at EMTERC. Figure 7-4 below clearly shows a reduced grain size and more ordered state in the sputtered sample compared to that produced by evaporation. Additionally, the average surface roughness measured for ITO samples sputtered in argon was ~4.8nm which is an order of magnitude better than that of ITO deposited by evaporation.

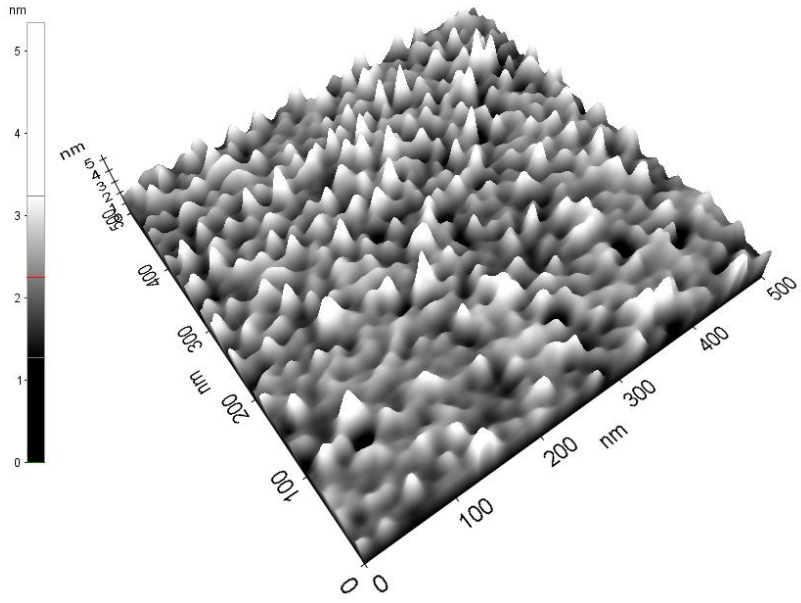

Figure 7-4 – Non-contact atomic force microscope image of radio frequency Sputtered ITO layer.

Two samples were prepared at each power level and following the thickness measurements one set of samples was annealed in air at 250^{o}C for 1hour. Using the

same methodology as described above for the evaporated samples, top contacts were added and the resistivity and sheet resistance of the materials were obtained, the sheet resistance results for the annealed and unaltered samples are presented in Figure 7-5 below:

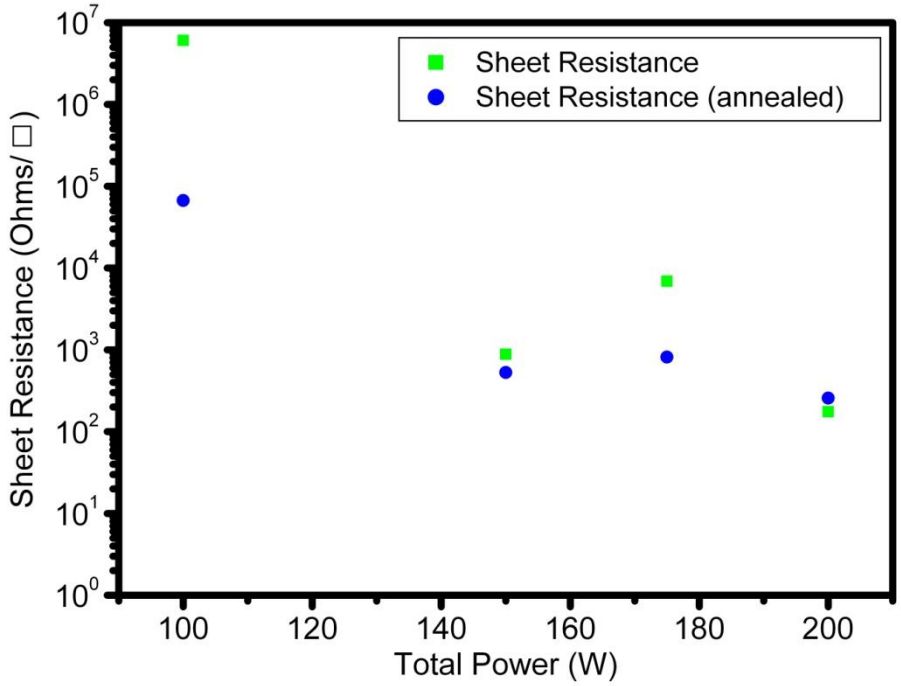

Figure 7-5– Effect of annealing at 250°C in air on sheet resistance at different power levels

As can be seen in Figure 7-5 annealing in air produces a reduction in sheet resistance of films produced at lower power levels but there is little evidence of annealing having any significant effect at higher powers. One possible reason for this effect is that ITO films deposited at higher powers are hard and stable and could be already annealed by the heat generated in this process [133].

AFM images of normally sputtered and annealed samples produced at the same time are presented below in Figure 7-6a and b respectively. A change in the surface structure of the material is suggested in the annealed sample, which appears similar to the improvement in crystalline structure described by Kurdesau et al [122], Meng and Placido [120] and Vink et al [123].

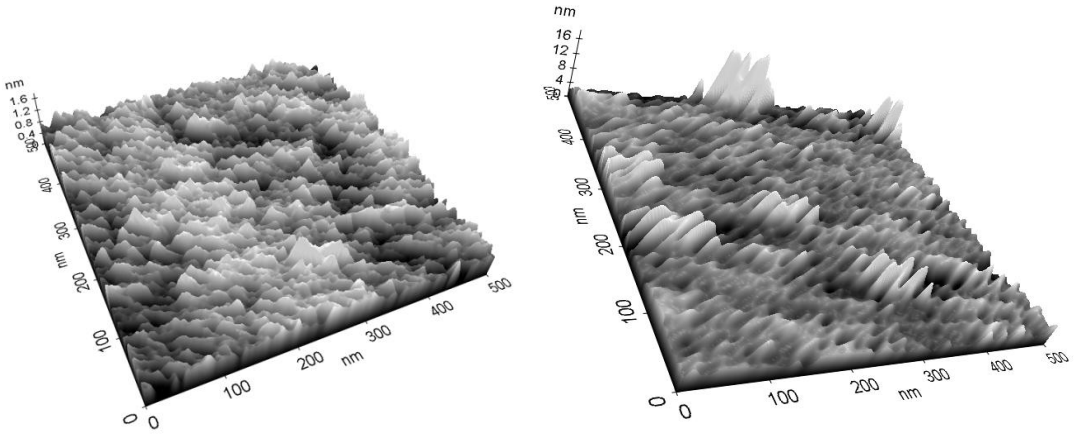

(a) (b)

Figure 7-6 – Non-contact atomic force microscope image of ITO samples produced by sputtering at a power of 150W with 30sccm of argon. Figure 7-6a shows the sample after sputtering, Figure 7-6b shows a sample produced at the same time, but which has been annealed at 250^{o}C for 1 hr in air.

The route mean square (rms) surface roughness of the annealed sample is higher than that of the un-annealed sample; 4.6nm compared to 0.2nm respectively, but overall is much more structured with prominent columnar structures which appear similar to those observed by Kurdesau et al [122]. It should be noted that these values are not actual roughness measurements but are produced by the AFM software and are included as a useful relative comparison between the samples, not an absolute comparison. Alongside these measurements a series of measurements in the ultraviolet and visible parts of the spectrum (UV-VIS) were taken to determine the transparency of the films for light with wavelengths between 250 and 800nm. The data is presented in Figure 7-7 below. The data presented in this figure is raw data that has not been corrected for the variations in thickness that occur due to the different power levels used. Ideally this data could be repeated with different time intervals to ensure that the samples are all of comparable thickness and hence can be compared properly. Although not ideal it can be seen that the relationship between power and transparency is not linear as the 175W sample can clearly be seen to be more transparent than the 150W and 200W sample. It appears that high powers reduce transparency, given that the 200W sample is the least

transparent of all the samples. Given the electrical characteristics and the transparency it was decided that 150W represented the appropriate power level to proceed to the next step which was to determine the oxygen level to improve transparency while maintaining sufficient vacancies to be of use as a conductive layer.

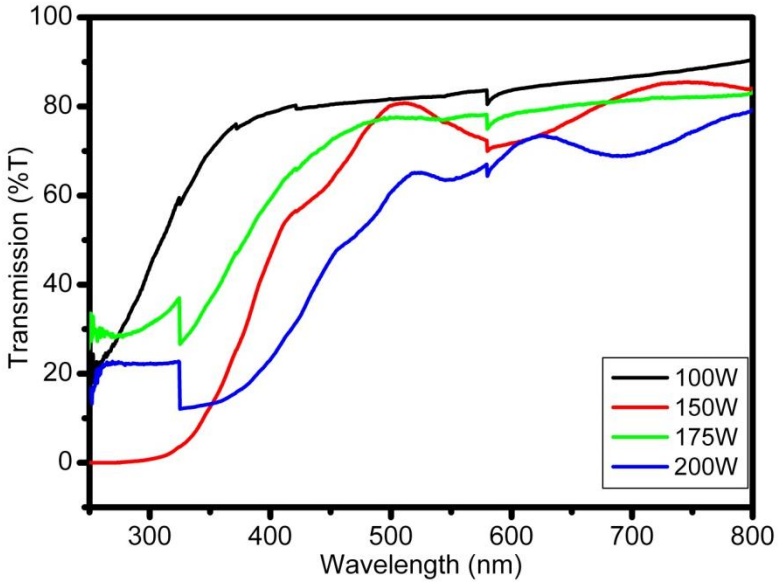

Figure 7-7. UV-Vis Spectra of ITO samples at different power levels, not this data has not been adjusted to correct for variations in thickness.

The samples were sputtered as above and the power was kept constant at 150W and the argon level maintained at 30sccm, of four different concentrations of oxygen were introduced (0.5, 1, 1.5 and 2 sccms) and the transparency measurements for the samples are presented in Figure 7-8.

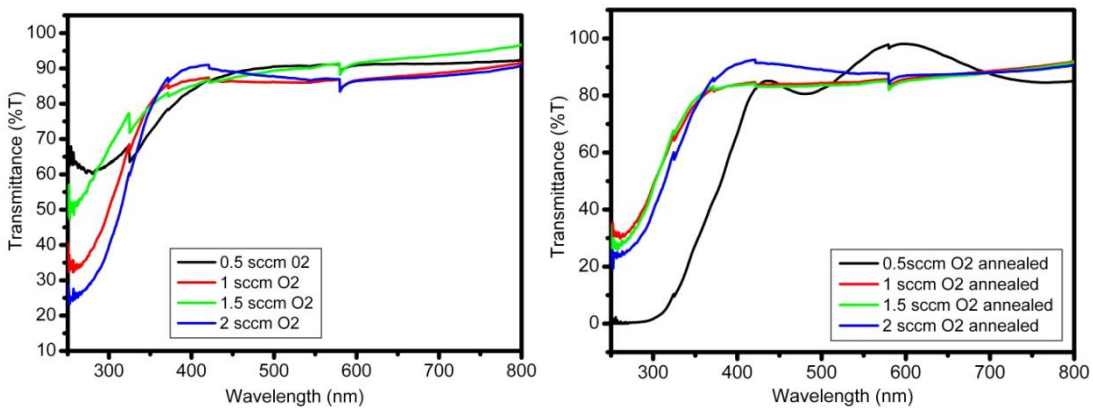

Figure 7-8 – Transmittance of ITO layers with and without using oxygen in the sputtering process.

As can be seen all of the samples containing oxygen exhibit a transmittance in excess of 80% in the visible spectrum (~380-750nm) and in a few cases the transmittance is in excess of 90%. The sample without any oxygen has a lower transmittance (~70-80%). All of the films presented here were produced at the same power level and therefore have a similar film thickness. The I-V results of for the same samples described above produced at a power level of 150W are presented in Figure 7-9 below

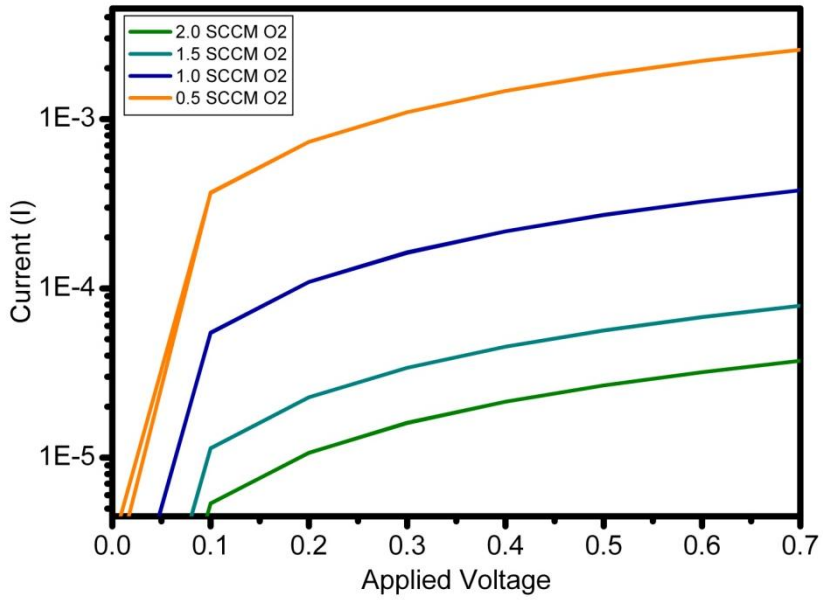

Figure 7-9 – Logarithmic I-V characteristics of ITO layers produced at power level of 150W with varying oxygen levels

Table 4. Charactersitics of ITO samples produced at 150W using varying oxygen levels.

Sample	Oxygen Level (SCCM)	Sheet Resistance (Ω/□)	Average Transparency (250-800nm) (%)	Average Transparency (350-800nm) (%)
1	0.5	30.3	63.9	83.27
2	1.0	1836.5	75.75	85.99
3	1.5	18750.0	74.73	85.47
4	2.0	61349693.0	75.62	88.34

As can be seen from Table 1 only sample 1 has sufficiently high transparency combined with a low sheet resistance. However, multiple runs using the same parameters showed that there was a high variation in quality of the films which affected the ability to consistently reproduce the same characteristics. In the absence of any external variations it seemed that this was due to the sputterer itself. The problem was traced to unstable gas supply due to a faulty mass flow controller (MFC) and high chamber pressure due to an apparent leak in the chamber. The problem with the MFC was resolved but the leak, although small, could not be located and continues to affect attempts to produce consistent ITO films.

7.1.2 Comparison of Commercial ITO layer with and without PEDOT:PSS

In order to facilitate fabrication of samples that are comparable and reproducible and given that the ITO produced in house was not of sufficient quality and reproducibility to fully guarantee that the decision was taken to use commercially bought ITO. The ITO used was obtained from Sigma Aldrich and was Corning glass with a 30-60nm thick layer of ITO which had a surface resistivity of 30-60Ω/□. The quoted transparency is >85% in all visible wavelengths.

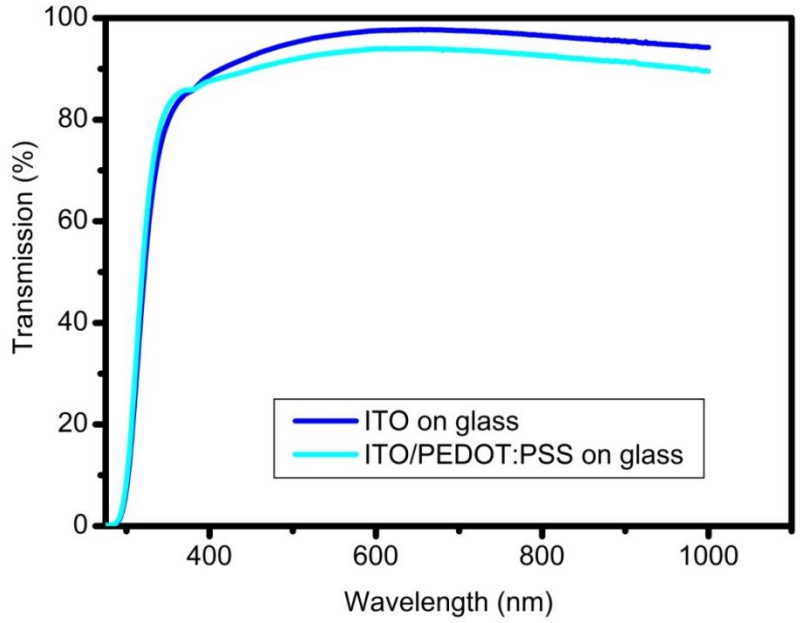

Figure 7-10. Comparison of transparency of Sigma Aldrich ITO coated glass slides with and without PEDOT:PSS layer.

It can be seen from Figure 7-10 that ITO with and without a layer of PEDOT:PSS maintains a transparency greater than the quoted value of the supplier. The sample with the layer of PEDOT:PSS has a reduction in transparency of ~5% compared to that without the layer.

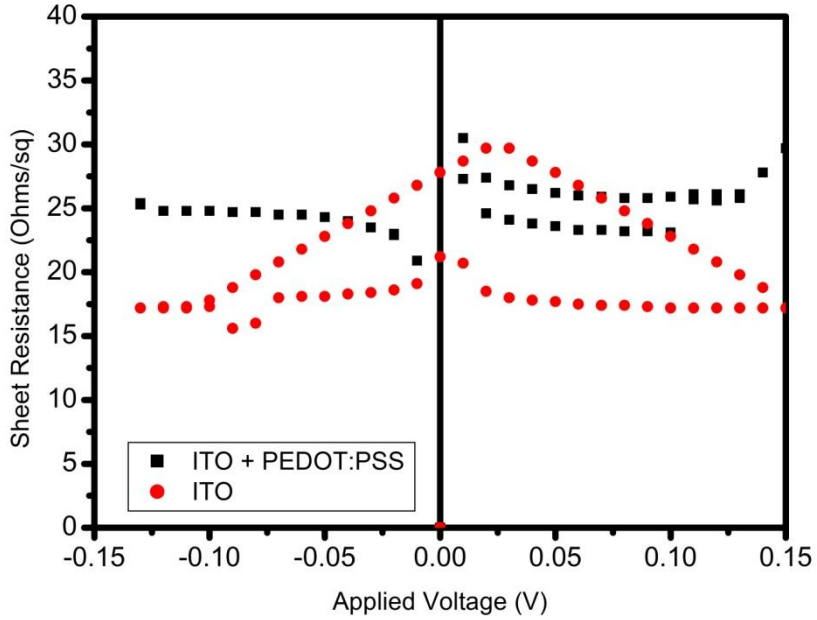

Figure 7-11. Sheet resistance measurements for ITO layer with and without PEDOT:PSS layer.

As can be seen from Figure 7-11 there is little difference in the sheet resistance between the two samples. This indicates that the addition of the PEDOT:PSS layer does not significantly increase the sheet resistance of the ITO layer.

7.2 Summary

Although it has been produced elsewhere and is available commercially ITO has been investigated for the first time at De Montfort University as part of this work. This involved investigation of the various options available for the deposition of thin transparent films such as thermal evaporation and RF magnetron sputtering. After some initial investigation evaporation was abandoned and sputtering was used as the optimum process to produce the films.

Although reasonably successful, for a variety of reasons it was not possible to produce films of sufficient quality of either transparency or conductivity to using in photovoltaic devices without compromising the efficiency of those devices. For this reason the decision was taken to use commercially available ITO films with good transparency and reasonable electrical conductivity to provide a consistent base layer onto which the subsequent layers could be deposited and characterised. The ITO films were modified by the addition of a layer of PEDOT:PSS which did not significantly reduce either the transparency or conductivity by which modified the surface characteristics and work function of the material to enable improved adhesion and electrical contact between the transparent electrode layer and the active layer.

Chapter 8

8 Permittivity in Excitonic Materials

8.1 Introduction

One of the aims of this thesis is to demonstrate that it is possible to use ferroelectric nanostructures to alter the permittivity and hence improve the electrical characteristics of; the hybrid devices fabricated using this approach. This chapter gives an overview of the causes and effects of permittivity in dielectric and semi-conductive media and how this affects the formation of excitons in photoconductive materials.

8.2 Permittivity in a Dielectric Medium

Permittivity can be defined as "a measure of the amount of resistance encountered in a medium to the formation of an electric field". In essence the permittivity of a material is a measure of the ability of the material to polarise in response to an external electric field (**E**). This polarisation then results in a reduction of the field within the material, which results in a net "storage" of electrical energy within the material. It is this feature which gives rise to capacitance. The units of permittivity are Farads per meter (Fm^{-1}) in SI units. The real part of the permittivity (ε') is related to the dimensionless quantity electric susceptibility (χ) by the following relationship:

$$\varepsilon' = (1 + \chi)\varepsilon_0 = \varepsilon_r \varepsilon_0 \qquad 8.1$$

Where ε_r is the relative permittivity of the material and ε_0 is the permittivity of free space. The value for the permittivity of free space can be calculated from the following equation:

$$\varepsilon_0 = \frac{1}{c^2 \mu_0} \qquad 8.2$$

Where c is the speed of light in a vacuum and μ_0 is the vacuum permeability, ε_0 is equal to 8.854×10^{-12} Fm^{-1} [243]. In a medium this becomes:

$$\varepsilon_r \varepsilon_0 = \frac{1}{v^2 \mu_r \mu_0} \quad 8.3$$

Where μ_r is the relative permeability of the medium and v is the speed of the EM wave in the medium. It can be seen that the permittivity is also related to the refractive index of a material from the relationship:

$$n = \frac{c}{v} = \sqrt{\varepsilon_r \mu_r} \quad 8.4$$

At optical frequencies μ_r is approximately 1 and therefore the refractive index is directly proportional to the permittivity of the material.

In a dielectric, the simplest case, the external electric field causes the atoms in the material to polarise as shown in Figure 8-1 below. Initially the atom is at rest and can be considered to be in an electrically neutral state, provided it is not ionised, with a positive nucleus surrounded by a negatively charged cloud of electrons. For simplicity this model assumes that the electron cloud is in a 1s orbital arrangement i.e. is spherical. The ground state is shown in the upper left hand quadrant of Figure 8-1. As the external electric field is applied this causes the atom to polarise, the process is not instantaneous, but that is not relevant to this description. In the polarised state (upper right quadrant) the electron cloud is displaced in response to the external field. This results in a state where the atom, while still overall electrically neutral, has two oppositely charged regions, the centres of which can be thought of as being two point charges a distance d apart (lower left quadrant). This results in a dipole moment being created between the two charges. As the field is removed the atom relaxes back to its ground state (lower right hand quadrant). The dipole moment that results from the polarisation of the atom is a vector (**p**) in the direction of the applied field of magnitude [243]:

$$\mathbf{p} = Zed \quad 8.5$$

Where Z is the number of electrons in the cloud and e is the charge on the electron and d is the distance between the point charges. For a bulk material containing N atoms per

unit volume the total polarisation moment **P** in an electric field perpendicular to the face of the material is equal to:

$$\mathbf{P} = N\mathbf{p} = NZed = \chi\varepsilon_0\mathbf{E} \qquad 8.6$$

In addition an electric displacement field (**D**) is produced and is related to the separation of the charged particles in a dielectric medium.

$$\mathbf{D} = \varepsilon_0\mathbf{E} + \mathbf{P} = (1+\chi)\varepsilon_0\mathbf{E} = \varepsilon\mathbf{E} \qquad 8.7$$

The separation of charges results in a net charge being developed on the face of the material that reduces the applied field within the material by acting in the opposite direction to it. This results in a net storage of charge in the material and leads directly to the concept of capacitance.

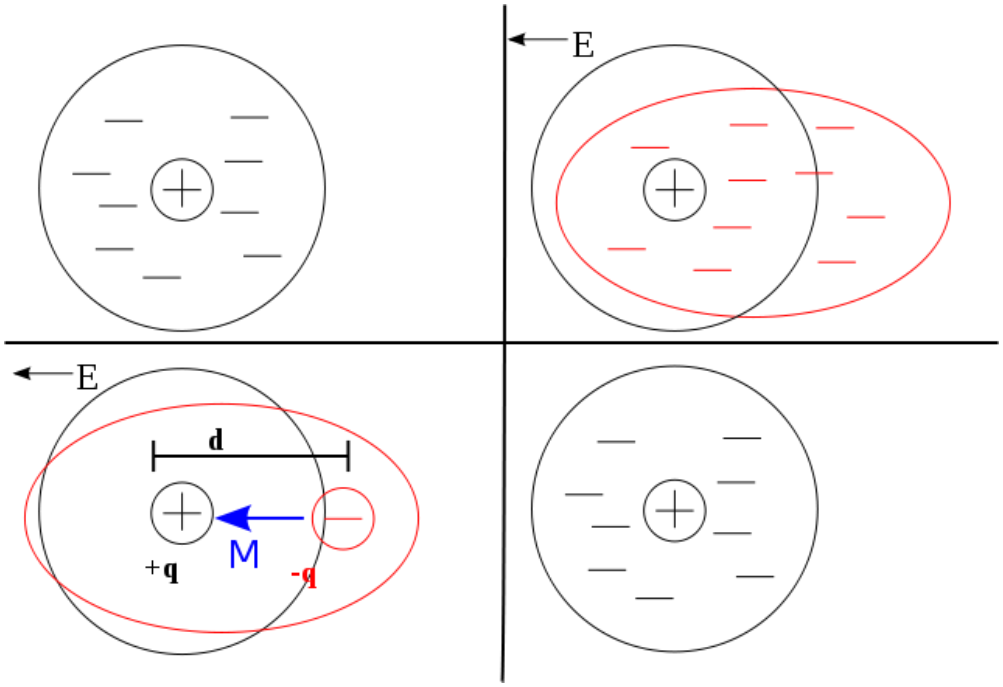

Figure 8-1. Polarisation of dielectric in response to an external electric field (reproduced from Flaschen (2007) [244], with permission).

Figure 8-2 below shows a schematic of a parallel plate capacitor filled with a dielectric medium. It can be seen that the applied electric field causes a build up of positive and

negative charges on opposite faces of the capacitor. This results in the creation of the depolarisation field and the storage of charge in the capacitor. In a vacuum the capacitance (C_0) can be found by applying Gauss's law to the plates, where the flux out of the plates is σA and the Gaussian energy $E_0 = \sigma/\varepsilon_0$ [243].

$$C_0 = \frac{\text{charge}}{\text{potential difference}} = \frac{A\sigma}{E_0 d} = \frac{\varepsilon_0 A}{d} \qquad 8.8$$

When there is a dielectric material between the plates then the capacitance can be increased by the relative permittivity or dielectric constant (ε) of the material. Thus equation 8.8 becomes:

$$C = \frac{\epsilon \epsilon_0 A}{d} \qquad 8.9$$

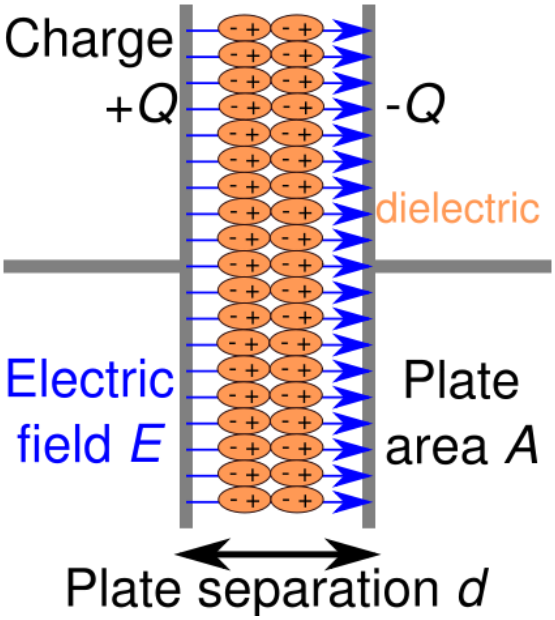

Figure 8-2. Schematic of capacitor filled with a dielectric medium in an electric field (reproduced from November (2008) [245], under license).

8.3 Complex Permittivity and lossy mediums

In free space permittivity is single valued i.e. ε_0 but in materials the dielectric constant varies with the frequency of the applied field. This arises due to the fact that the response of the material to the field does not occur instantly and therefore occurs some time after the field is applied. This results in a difference in phase between the applied field and the displacement field which necessitates representing the permittivity of the material as a complex number under these conditions. The complex relationship between **E** and **D** is given by [197]:

$$\mathbf{D_0} e^{-i\omega t} = \hat{\varepsilon}(\omega)\mathbf{E_o} e^{-i\omega t} \qquad 8.10$$

Where ω is the angular frequency of the applied field, $\hat{\varepsilon}(\omega)$ is the frequency dependent permittivity, t is time and $i = \sqrt{-1}$. For moderate field strengths where **D** and **E** remain proportional we get:

$$\hat{\varepsilon} = \frac{\mathbf{D_0}}{\mathbf{E_0}} = |\varepsilon| e^{i\delta} \qquad 8.11$$

Where δ is the frequency dependent phase difference between **D** and **E**. By splitting equation8.11 into the real and imaginary parts we get:

$$\hat{\varepsilon}(\omega) = \varepsilon^{'}(\omega) + i\varepsilon^{"}(\omega) \qquad 8.12$$

Where ε' is the real part of the permittivity and is responsible for the energy storage in the medium and ε" is the imaginary part and is related to the losses in the material. This can be written in terms of the Kramers-Kronig relation [32, 246]

$$\varepsilon^{'}(\omega) = \varepsilon_0 + \frac{2}{\pi}\int_0^{\infty} \frac{u\varepsilon^{"}(u)}{u^2 - \omega^2} du \qquad 8.13$$

Where u is a complex function and the other terms are as described previously and ε' is as defined in equation 8.1.

In a lossy or conductive medium the imaginary part dominates and losses increase, the total current is a combination of DC conductivity and displacement currents, this current can be written as [247]:

$$I = \sigma_0 \mathbf{E} + {}^{\partial \mathbf{D}}/_{\partial t} \qquad 8.14$$

Where σ_0 is the conductivity of the material and the other symbols are the same as previously mentioned. Taking the Fourier transform of equation 8.14 gives the frequency dependent current response, which can be written as [247]:

$$I(\omega) = \sigma_0 \mathbf{E}(\omega) + i\omega \mathbf{D}(\omega) \qquad 8.15$$

A typical example of the variations of the real and imaginary parts of the permittivity with frequency is shown in Figure 8-3 below. The figure also shows the effects of each frequency domain on processes that take place in the material such as ionic and dipolar relaxation effects which are associated with permanent and induced dipoles and atomic and electronic resonances which arise from vibrations and rotational effects which occur in regions of characteristic absorption frequencies.

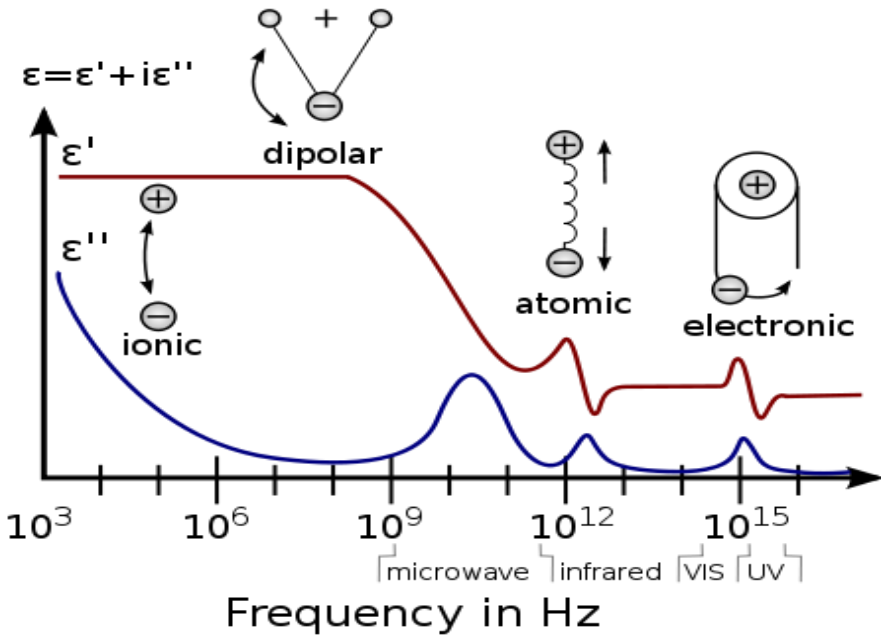

Figure 8-3. Example of Frequency dependent variations in permittivity in a material (reproduced from Mauritz (2008) [248] with permission).

8.4 Permittivity and Coulomb forces in Excitons

Whether a material behaves conventionally or excitonically is strongly dependent upon the permittivity of the material. It is possible to determine whether a material will behave as an XSC or a CSC by comparing the ratios of the Bohr radius with the Coulomb radius. The Bohr radius is defined as [12]:

$$r_B = r_0 \varepsilon \left(\frac{m_e}{m_{eff}}\right) \qquad 8.16$$

Where r_0 = 0.53Å and is the distance between the electron and the nucleus for hydrogen like structures such as silicon and excitons (although in the case of the exciton both particles "orbit" around the centre of mass as they are similar in mass and no large nucleus exists), m_e is the mass of a free electron in a vacuum and m_{eff} is the effective mass of the electron in the semiconductor, it is important to mention here that m_{eff} is not well defined in XSC materials due to the fact that charge transport generally occurs due to a hopping mechanism rather than delocalised band transport.

Coulomb's law determines the force between two particles separated by a distance r, it is usually written as [35]:

$$\mathbf{F} = \frac{kq_1q_2}{r^2} \tag{8.17}$$

Where k =1/4$\pi\varepsilon\varepsilon_0$ n and in the case of an exciton q_1=q_2. So therefore we get:

$$\mathbf{F} = \frac{1}{4\pi\varepsilon\,\varepsilon_0}\frac{q^2}{r^2} \tag{8.18}$$

From this the electrical potential energy between the particles can be integrating equation 8.18.

$$E = \int_0^r \frac{1}{4\pi\varepsilon\varepsilon_0}\frac{q^2}{r^2}dr = \frac{1}{4\pi\varepsilon\varepsilon_0}\frac{q^2}{r} \tag{8.19}$$

A charge carrier is defined as being "free" when the coulomb energy is equal to the thermal energy of the particle, in a typical Frenkel exciton the binding energy is usually in the range 0.4 to 1.4eV [249]. This occurs when [12]:

$$E = \frac{1}{4\pi\varepsilon\,\varepsilon_0}\frac{q^2}{r_c} = k_BT \tag{8.20}$$

Where q is the charge on the electron, ε_0 is the permittivity of free space and r_c is the critical distance between the charges, k_B is Boltzmann's constant and T is the temperature of the system. Re-arranging equation 8.20 gives:

$$r_c = \frac{q^2}{4\pi\varepsilon\,\varepsilon_0 k_BT} \tag{8.21}$$

The material will behave in an excitonic manner if $r_c > r_B$ and where r_B is greater than the radius of the particle. Therefore let the ratio of r_c to r_B be called γ.

$$\gamma = \frac{r_c}{r_B} \approx \left(\frac{q^2}{4\pi\varepsilon_0 k_B r_0 m_e}\right)\left(\frac{m_{eff}}{\varepsilon^2 T}\right) \quad 8.22$$

A value of $\gamma > 1$ indicates that the material will exhibit excitonic behaviour and conversely a value of $\gamma < 1$ indicates a material that will behave as a conventional semiconductor [12].

8.5 Exciton Dissociation and its relation to the Debye Length

The relative permittivity of the material (ε) determines its ability to permit an electric field. It is linked to the Debye Length (L_{Db}) by the following equation [250]:

$$L_{Db} = \left[\left(\varepsilon\varepsilon_0 kT \Big/ q^2 N\right)\right]^{1/2} \quad 8.23$$

Where ε is the relative permittivity, ε_0 is the permittivity of free space, k is Boltzmann's constant, T is the temperature, q is the charge of the particle (typically the elementary charge of the electron) and N is the carrier concentration. The Debye Length is a measure of the distance over which mobile charge carriers' screen out electric fields. As the Debye Length around the nanostructures increases then the exciton dissociation region around each nanostructure also increases proportionately.

In order for the majority of excitons created in a photoconductive material to be able to dissociate the thickness of the material should be approximately the same as the Debye length or, more preferably, less than the Debye length. Therefore, in order for a single layer organic photovoltaic cell to be able to operate the thickness of the layer of organic photoconductive material must be around, or more preferably, less than the Debye length of the material. However, a typical organic photoconductor has a Debye length of around 10nm and when a layer of material of this thickness is exposed to light majority or more of the photons of appropriate wavelength that are incident upon the material will simply pass straight through the material. As a result, very thin single layer organic

photovoltaic cells generally have an efficiency of 1% or less and are not commercially viable.

In order to overcome this problem nanostructures have been incorporated into the photoconductive materials. In a typical bulk heterojunction photoconductive material comprising C_{60} nanoparticles are dispersed within a photoconductive polymer matrix. Due to differences in electron affinity and ionisation potential between the nanostructures and polymer matrix a potential barrier is formed at the interface between them. As a result of this potential barrier, excitons created within the polymer matrix may dissociate into free charge carriers in a region around each interface. The distance from an interface within which excitons may dissociate is proportional to, and approximately equal to, the Debye Length of the polymer matrix, which, as set out above, is generally approximately 10nm. Therefore, in order for efficient charge capture to occur the nanostructures are required to be homogeneously distributed with a separation of the same order as the Debye Length. The typical size of these nanostructures varies up to about 100nm, with the ideal size being the same order as the distance between the nanostructures.

Given the short diffusion length of excitons in polymers, in order for efficient charge capture to occur the nanostructures should be homogeneously distributed with a separation of the same order as the diffusion length. By increasing the permittivity, and hence the Debye Length, the distance between nanostructures can be increased as the dissociation region expands. By correctly choosing suitable materials to ensure the energy barrier is greater than the binding energy of the exciton and by tuning the Debye length it should be possible to maximise the amount of free charge carriers created. This could be done by ensuring that all of the dissociation regions around each nanoparticle overlap and therefore the whole matrix becomes a superposition of these regions. Thus regardless of the short lifetime, and hence diffusion length, of excitons increasing the relative permittivity will increase the likelihood of dissociation into free charge carriers.

8.6 Materials Affecting Permittivity and Debye length

The characteristics and properties of the materials used in this work are all described previously (§3). Barium and strontium tiatanates were used for a number of reasons; firstly they are both high permittivity ceramic materials with a ferroelectric phase that has been demonstrated to increase the permittivity of polymeric materials when combined as filler in a polymer matrix [13, 196, 199, 206]. Secondly they are easily obtainable and can be easily modified into a tetragonal state [18, 176, 251]. Finally they are reasonably safe to use, although strontium titanate is considerably safer than barium titanate [200, 203].

8.7 Modelling Permittivity of Blends of Polymer and Ferroelectric Materials

It has been known for some time that by adding high permittivity (high K) materials, particularly ceramics, to polymers and epoxy resins that the permittivity of the blend of materials will be higher than that of the original polymer or epoxy alone [13, 246, 252-255]. A number of models have been proposed which describe the effective permittivity (ε_{eff}) of the composite material a few of which are presented and compared below. The simplest model is known as the volume fraction average model and is a summation of the relative fractions of each type of material by volume. This method is generally held to be inaccurate, but can be used for a quick first approximation [246].

$$\varepsilon_{eff} = \phi_1 \varepsilon_1 + \phi_2 \varepsilon_2 \qquad 8.24$$

Where Φ is the volume fraction, ε is the permittivity and the subscripts 1 and 2 represent the polymer and ceramic material respectively. This model predicts a sharp increase in permittivity at a relatively small fraction of ceramic filler, which in practice does not occur [246]. More accurate models are based on "mean field theory"which reduces all interactions on a body to a single average interaction thus removing the uncertainty generally associated with a many body problem. The Maxwell-Garnett equation is one such model [246, 255] which can be written as:

$$\varepsilon_{eff} = \varepsilon_1 \frac{\varepsilon_2 + 2\varepsilon_1 - 2(1-\phi_1)(\varepsilon_1 - \varepsilon_2)}{\varepsilon_2 + 2\varepsilon_1 + (1-\phi_1)(\varepsilon_1 - \varepsilon_2)} \quad 8.25$$

This is valid for a single ceramic or ferroelectric particle surrounded by polymer. This equation also has a drawback in that as it is valid only when the filler fraction is infinitesimally small.

The Bruggeman model is another mean field theory model that treats the polymer/ceramic matrix as a series of repeated units of spherical ceramics surrounded by polymer. This can be written as [246, 255]:

$$\phi_1 \left(\frac{\varepsilon_1 - \varepsilon_{eff}}{\varepsilon_1 + 2\varepsilon_{eff}}\right) + \phi_2 \left(\frac{\varepsilon_2 - \varepsilon_{eff}}{\varepsilon_2 + 2\varepsilon_{eff}}\right) = 0 \quad 8.26$$

In this model the value of the dielectric constant increases dramatically for ceramic filler volumes of 20% and greater. The two final equations compared here are the logarithmic Lichtnecker equation:

$$\ln \varepsilon_{eff} = \phi_2 \ln \varepsilon_2 + (1-\phi_2) \ln \varepsilon_1 \quad 8.27$$

And the "effective medium theory (EMT) model" that describes the permittivity of a two part system in terms of the relative fractions of the components:

$$\varepsilon_{eff} = \varepsilon_m \left[1 + \frac{\phi_2(\varepsilon_2 - \varepsilon_1)}{\varepsilon_1 + (n(1-\phi_2)(\varepsilon_2 - \varepsilon_1)}\right] \quad 8.28$$

Where n is a correction factor which compensates for the non spherical nature of the ceramics and is generally less than 0.15 for a polymer/ceramic matrix.

There are numerous other models that due to their complexity and unsuitability have not been investigated here such as the Yamada and Furukawa models [16], the Jayasundere and Smith Model [254], and various field strength related models.

Below shows a comparison between the models described here and real data for barium titanate in a P3HT matrix (§8.9).

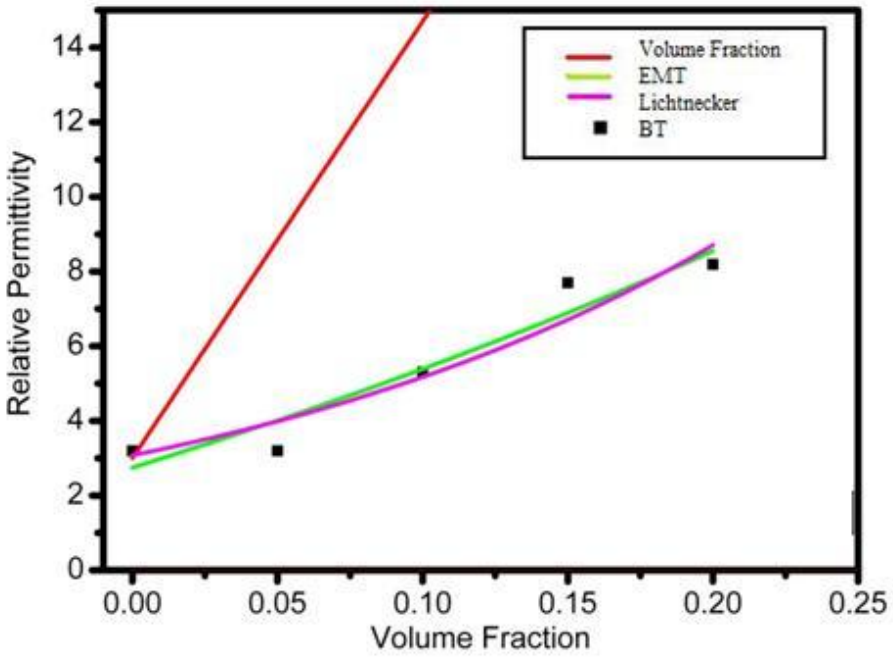

Figure 8-4. Comparison of permittivity models for various filler volume fractions with measured data for barium titanate nanoparticles in a PVAc matrix.

Table 5 below shows the Chi^2 and R^2 distributions for this data, these are statistical measurements of the fit of the curve to the data. The chi-square distribution is a common test for goodness of fit of an observed distribution to a theoretical one and the R^2 value is the proportion of variability in a data set from the statistical model. In this case the results for both were determined automatically by the Origin programme.

Table 5. Correlation of permittivity models with measured data.

Model	Chi^2	R^2	n
Volume Fraction (red)	154.26	-26.189	N/A
EMT (green)	0.86	0.927	0.105
Lichtnecker (magenta)	0.63	0.916	N/A

As expected the volume fraction formula produces a result that is very high the real data. The other three curves all approximate the data to a greater or extent; the Maxwell-Garnett equation has not been included here as it has been to consistently produce a result lower than the measured values and the quantities here are not infinitessimal [246]. The Lichtnecker model and the EMT model both the measured data well, but the EMT model has the best curve fitting as can be seen in

Table 5 below shows the Chi^2 and R^2 distributions for this data, these are statistical measurements of the fit of the curve to the data. The chi-square distribution is a common test for goodness of fit of an observed distribution to a theoretical one and the R^2 value is the proportion of variability in a data set from the statistical model. In this case the results for both were determined automatically by the Origin programme.

Table 5. It was therefore decided to use the EMT curve as the theoretical comparison with which to compare subsequent permittivity measurements with P3HT polymer.

8.8 Permittivity Measurements in PVAc

A base solution of 20 mg/ml PVAc was prepared by dissolving in PVAc pellets in electronic grade methanol obtained from Sigma-Aldrich. The mixture of PVAc pellets and solvent was held in a sealed vial and was placed in an ultrasonic bath until the pellets dissolved completely. The solutions were filtered before use using filter paper with particle retention of 0.7μm. The optimum static spin coating speed was determined by preparing samples on silicon wafer at a range of spin speeds and determining the film thickness using ellipsometry. The results are presented in Figure 8-5 below.

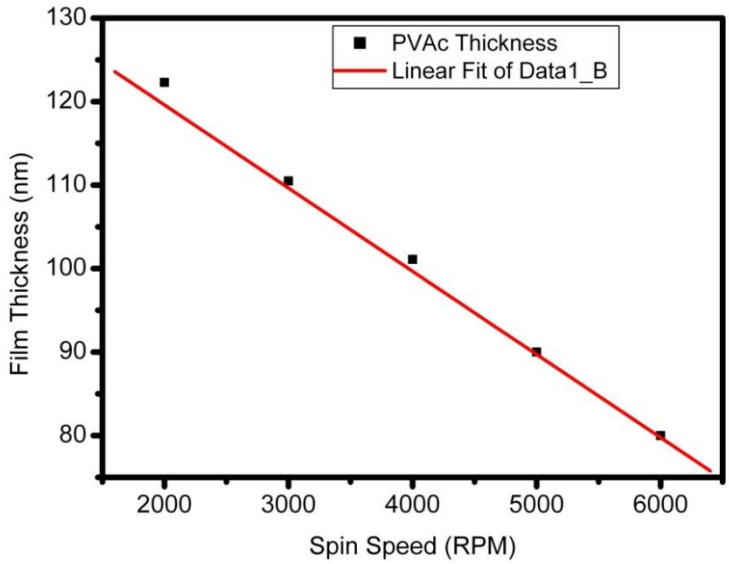

Figure 8-5. Thickness of films prepared from 20mg/ml PVAc solution for varying spin speeds.

The above results led to the decision to use a spin speed of 3000 rpm to obtain film thicknesses ~110nm. The films were of high quality and no significant defects were detected either by visual inspection or by inspection using a Leica GZ6 optical microscope with up to 40X magnification.

In order to confirm the effect that ferroelectric nanoparticles have on the permittivity of polymers a set of sample capacitors using cross point array architecture were constructed as detailed previously (§6.4.6).

Two sets of samples were prepared using two separate solutions of PVAc, the first set contained tetragonal barium titanate with the OPA ligand and the second sample used tetragonal barium titanate without the ligand (§4.3.2.4). The tetragonal phase in both samples was prepared as described previously (§4.3.2.3). A control sample consisting of a layer of PVAc without any barium titanate was also prepared. The $BaTiO_3$ was measured into vials to which were added the PVAc solution. The quantities of BaTiO3 used are shown in Table 6 below. The PVAc/$BaTiO_3$ mixture was then subjected to a further ultrasonic bath until a suspension of $BaTiO_3$ was achieved.

Table 6. Concentrations of barium titanate in the samples used in this work.

Sample No.	PVAc (mg/ml)	$BaTiO_3$ (mg/ml) with Ligand	$BaTiO_3$ (mg/ml) without ligand
0	20	0 (control sample common to both)	
1	20	4.4	4.9
2	20	7.6	9.4
3	20	15.8	14.3
4	20	18.9	20.3
5	20	25.3	-

The test devices were fabricated by thermally evaporating 2mm aluminium strips (bottom contacts) onto 1mm thick corning glass substrate at a pressure of ~$1x10^{-6}$ Torr. The thickness of the contacts was estimated to be ~70-80nm thick using a quartz crystal thickness monitor. Next a sample of solution for each concentration was spin coated at 3000 rpm and allowed to dry. Once all the samples were spin coated they were air dried and moved to the evaporator. For comparison a set of samples were baked at 40^oC to confirm that there was no residual solvent in the samples, but the baking process resulted in poor quality samples many of which failed to work at all. For this reason the air dried samples alone are discussed below. Finally 2mm strip aluminium top contacts were thermally evaporated perpendicular to the bottom contacts to form a MIM (metal insulator metal) structure utilising cross-point array architecture.

In order to confirm the binding of the OPA ligand to the surface of barium titanate nanoparticles the IR spectra of both the pure OPA ligand and $BaTiO_3$ with the OPA ligand was investigated. As can be seen in Figure 8-6 a number of changes occur in the IR spectra of Barium titanate with the OPA compared to OPA alone, firstly and most significantly the IR spectral band around 3000 cm^{-1} corresponds to the C-H stretching mode and which is completely determined by the presence of the ligand [13, 256]. As this peak appears in the both IR spectra of pure OPA ligand and $BaTiO_3$ with the OPA ligand it proves that the ligand has attached to the BT nanoparticles. Also, in the spectra of barium titanate with the OPA is a peak which appears at 2350 cm^{-1} which is caused

by CO_2 [257]. The silicon substrate signature has been accounted for by a background scan of clean silicon wafer prior to measuring the BT and OPA spectra.

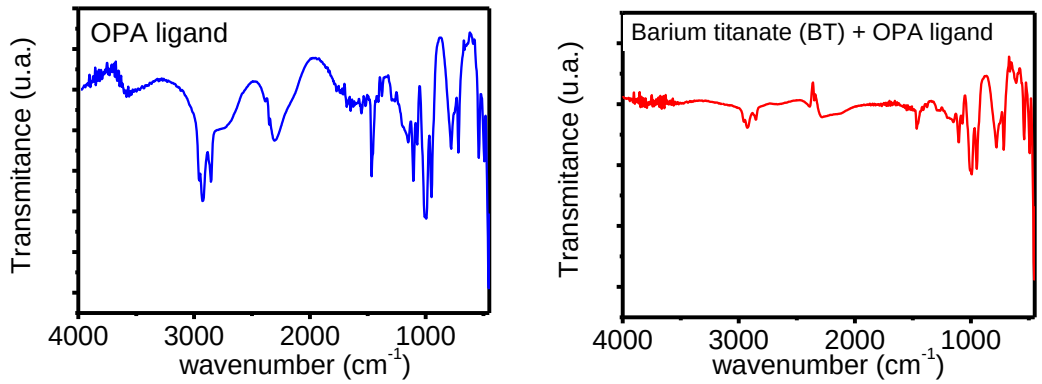

(a) (b)

Figure 8-6. Infra-red spectra of (a) pure OPA ligand (b) and BT+OPA ligand

The samples were then taken for electrical testing, current-voltage (I-V) measurements were taken to determine the leakage current and hence the appropriate voltage to be used in the capacitance-voltage (C-V) measurements, in this case the applied Voltage was ±1V and the frequency of the AC component applied was 1MHz.

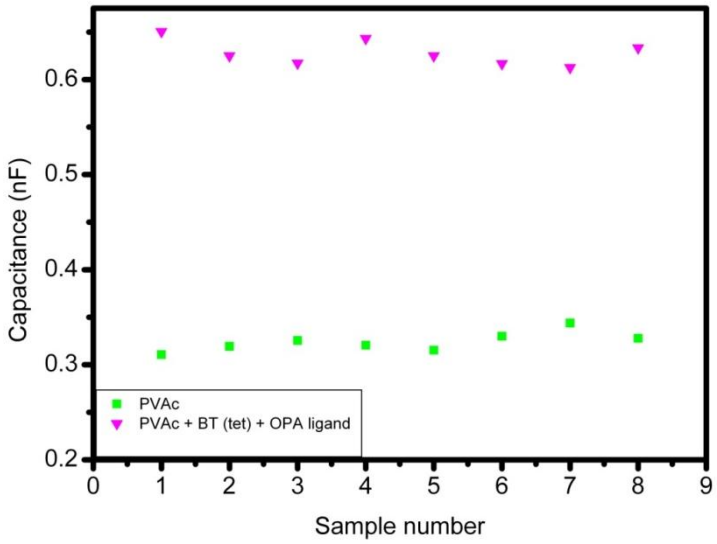

Figure 8-7. Capacitance measurements for sample comprising poly-vinyl acetate with 20mg/ml barium titanate to demonstrate the consistency of the devices.

Overall there were very few failed devices and the largest the variation is generally less than ±0.025 nF.

Using the mean values of the capacitance for the samples containing the various concentrations of barium titanate with and without the OPA ligand the value of the relative permittivity was calculated for each working device and these data are presented in Figure 8-8. The control sample returned a value of relative permittivity of 2.98, which is within the expected range for poly-vinyl acetate at this frequency [175, 258]. The samples of PVAc containing the barium titanate with ligand showed a steady increase in relative permittivity with increased concentration as can be seen in Figure 8-8, once the concentration of the BT/OPA increases past 5mg/ml, there is an obvious increase in the relative permittivity of the material, which was calculated by measuring the capacitance of the devices. BT without the ligand can clearly be seen to produce the greatest increase in permittivity in PVAc.

In order to confirm that the ligand was not affecting the permittivity samples of PVAc were prepared with high concentrations of OPA, these devices were prepared and tested as descibed above and no effect on the relative permittivity of PVAc could be measured. The value of the relative permittivity for these samples was ~3 which is within the accepted range of values for PVAc without additional fillers such as BT. The samples of PVAc that contain tetragonal barium tiatanate nanoparticles without the addition of a ligand are much less consistent, however, they appear to show a relative permittivity which appears to be an order of magnitude greater than the samples with the ligand.

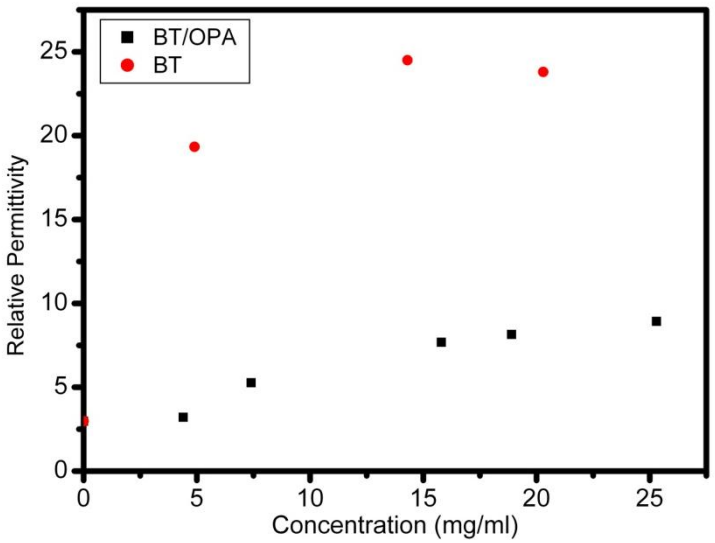

Figure 8-8. Increase in relative permittivity with increasing concentration of barium titanate with phosphonic acid ligand.

The values of the leakage current were measured for each sample over a range of ±1V and these are presented in Figure 8-9 below. It can clearly be seen that for the samples containing the OPA ligand the leakage current remains low, typically in the range of 10-25pA, whereas for the samples without the ligand the leakage current generally increases as the concentration of the barium titanate increases. The increased leakage current is indicative of some kind of conduction mechanism occuring in the polymer. There are five possible types of conduction mechanisms that occur in thin dielectric films; ionic conduction, space charge limited current, tunnelling and internal field emission, Schottky emisison, Poole-Frenkel effect and Impurity conduction [259]. Mehendru et al determined that the Poole Frenkel effect, where the electric field strength reduces the amount of thermal energy required for an electron to be freed from its valence atom, is the dominant conduction mechanism in PVAc [45, 260].

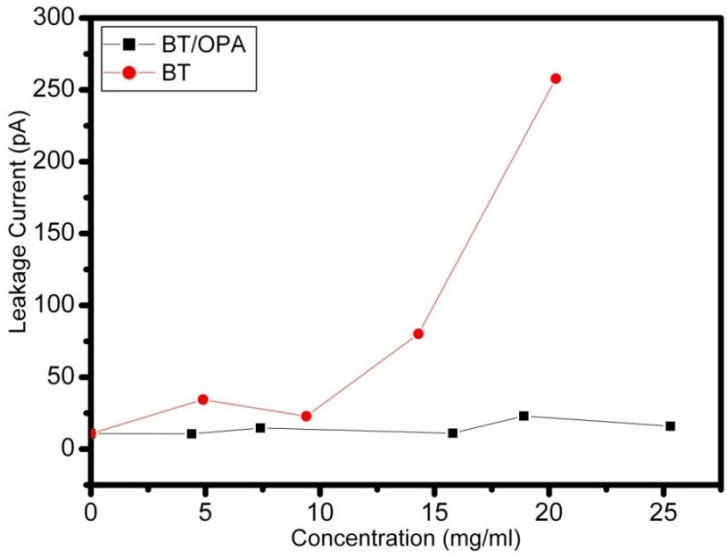

Figure 8-9. Comparison of leakage current for samples of poly-vinyl acetate and varying concentrations of barium titanate with and without the phosphonic acid ligand.

It has also been suggested that by adding barium titanate nanoparticles with a phosphonic acid ligand to a PVAc matrix it is possible to reduce the tendency of the nanoparticles to form clumps and to increase the consistency and reproducibility of the devices produced. One possible explanation of the reduction in clumping that was expressed by Kim et al [13] is that multiple ligands attach to each nanoparticle by their hydroxyl ions, this forms a partial coating to the nanoparticle which may then go some way to reducing the tendency of nanoparticles to form clumps. The reduced tendency to form clumps combined with the improved miscibility with solvents could, at least partly, explains why the presence of the ligand allows the formation of high quality films with well distributed nanoparticles that are contained in the polymer matrix. Preliminary investigation with Non-Contact Atomic Force Microscopy (NC-AFM) as shown in Figure 8-10 below appears to further this idea as there does appear to be a subtle difference between the sample containing the ligand (a) and the sample without (b). These images show a 10µm area from each sample that is representative of the general appearance of each sample. The average surface roughness is similar for both samples (~11nm for the sample with ligand and ~13nm for the sample without). The general morphology of both samples is still very similar, but there is evidence of regions of increased density, indicative of clumping, in Figure 8-10 (b). Further investigation of

this phenomenon is beyond the scope of this document at present, but it is anticipated that a more detailed investigation of the morphology of these films will be included in any subsequent study.

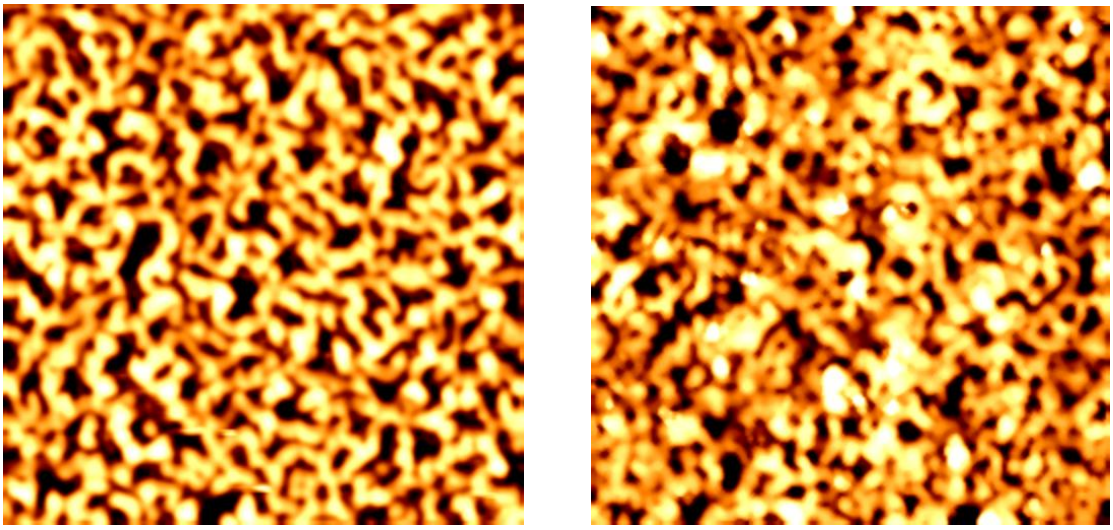

(a) (b)

Figure 8-10. Comparison of NC-AFM Measurements of (a) 10µm region of samples with OPA ligand and (b) 10µm region of sample without OPA ligand.

These films are reproducible and have excellent electrical qualities, such as almost linear increase of permittivity with nanoparticle concentration and low leakage currents. The films without the ligand do not share these qualities; this is likely to be due to a combination of clumping, resulting in the formation of large particles that have a diameter that is greater than the thickness of the film thus allowing a direct path for conduction, and poor distribution of the particles in the polymer matrix. It is possible that the clumping increases the likelihood of the filler reaching the percolation limit and therefore leading to conductive behaviour as discussed by Varlow et al [261]. The highest permittivity measured was in the films without the ligand and although the leakage current was suppressed in the insulating material it was later seen that this property reduced photoconductivity in conducting polymers. For this reason the majority of the subsequent work with titanates was carried out without the use of ligands. Clumping was generally overcome by longer ultrasonic treatment of the polymer/nanomaterial blends before spin coating.

In order to build modern organic electronic devices it is essential that it is possible to consistently modify their electrical properties. Tuning the dielectric constant of polymeric materials by adding nanoparticle filler materials is one method of controlling the band gap of polymers without doping the polymer chain directly. By tuning the dielectric constant sufficiently it may be possible to retain the advantages of organic semiconductors e.g. flexibility and ease of manufacture but to incorporate the better features of conventional semiconductors such as direct production of charge carriers.

8.9 Permittivity Measurements in P3HT

After numerous attempts two methodologies were adopted to obtain comparative permittivity measurements for samples of P3HT containing varying quantities of barium and strontium titanate. The first set of samples used the capacitance measurements described previously and after some optimisation produced reliable results. It is thought that the problems in making reliable measurements with this technique were twofold, firstly any minor imperfection in the layer such as pinholes could cause the device to fail and secondly any clumping of nanoparticles could provide a semiconductive path. Also high leakage currents can lead to unusual results such as negative capacitances and unusually high or low results [197, 247, 262]. Once high quality films were produced with regularity the majority of these issues disappeared and reliable measurements could be taken. In order to overcome the difficulties in making these measurements the polymer/nanoparticle solution was left in the ultrasonic bath over night to maximise the dispersion of the nanoparticles in the polymer. Furthermore the quality of spin coated films is partially dependent on the skill of the operator and increased practice also aided in producing higher quality films.

Given that barium titanate and strontium titanate caused an increase in photoconductivity both were investigated to determine what, if any, effect they would have on the permittivity of P3HT.

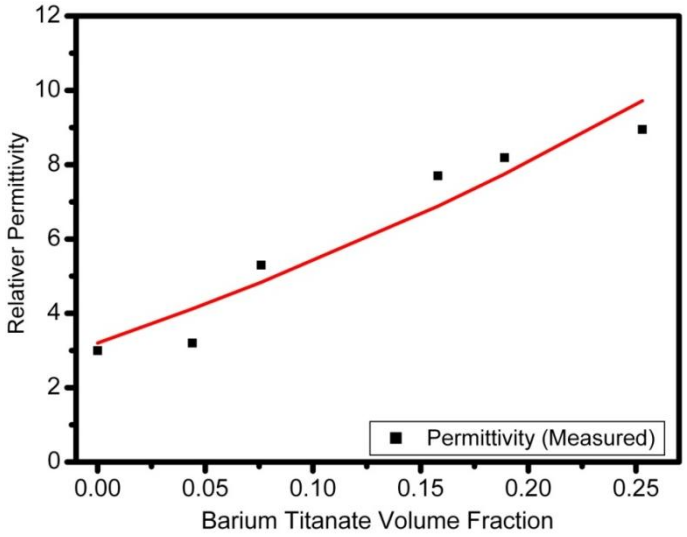

Figure 8-11. Relative permittivity of P3HT with increasing volume fractions of barium titanate.

Figure 8-11 above clearly demonstrates an almost linear increase in the permittivity of P3HT with increasing volume fraction of barium titanate. The upper limit of this effect has not been investigated as the concentration levels required to determine this would be far in excess of the levels required to fabricate functional photovoltaic devices. The EMT model fits the data well with an R^2 value of 0.925. The measured value of permittivity for the closest result to 20mg/ml concentration is 8.24 compared to 7.74 as predicted by the model.

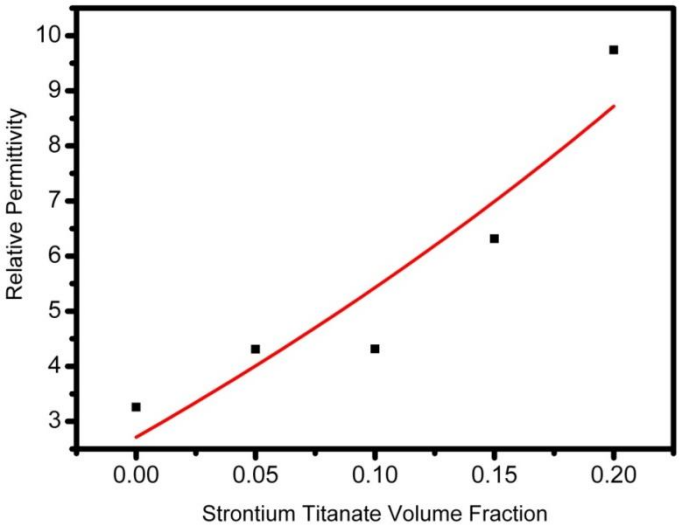

Figure 8-12. Relative permittivity of P3HT with increasing volume fractions of Strontium Titanate.

Figure 8-12 shows the results of the permittivity measurements for samples of P3HT with varying concentrations of strontium titanate. The increase in permittivity in this case is significantly higher than that produced by barium titanate with similar levels of concentration, which could be expected from the fact that strontium titanate is naturally a higher k material. The EMT model does not track the data as well as with the BT data and returns an R^2 value of only 0.882 it is included here only as a guide for the eye. The measured value of permittivity for 20mg/ml concentration is 9.76 compared to 8.71 as predicted by the model.

These data confirm that both barium and strontium titanates are suitable candidate materials to be added to P3HT/PCBM blends to potentially increase the efficiency of this type of solar cell.

8.10 Summary

This chapter has presented a description of the concept of permittivity and how this effect applies to both insulating and conducting materials. In essence permittivity is an expression of polarisation of the atoms within a material in response to an external applied electrical field; this polarisation creates an opposing field within the material which limits the strength of the external field within the material. In conducting media the response is described in a complex manner due to the fact that in this case the response is frequency dependent.

The permittivity of a material is linked to a number of electrical characteristics such as capacitance and the coulomb force to name but two. In semiconductive devices, the balance of the coulomb force with the thermal energy of the charge carriers determines whether free charge carriers or excitons are produced. In materials with low permittivities, such as many polymers, excitons are produced which need to dissociate in order to produce charge carriers.

This chapter has shown that by adding ferroelectric nanoparticles to insulating and conductive polymers it is possible to increase the relative permittivity of the material.

Chapter 9

9 Characterisation of active layer and complete hybrid photovoltaic devices

This chapter contains the major results of this work along with a discussion of the implications of the results. The results are presented in an order that is as close as possible to the chronological order of the work.

The overall aim of this project project was to investigate and understand the effect of using ferroelectric nanoparticles to affect the permittivity of the active layer with the intention of increasing the PCE of these devices. It has been demonstrated by other groups such as that of Roman and other that the efficiency of photovoltaic devices is increased by incorporating nano-particulates into the organic photoconductive materials [186].

9.1 Initial Photoconductivity Measurements with DH6T

Two main photoconductive polymers were used in this work; P3HT and DH6T, both of which are dscribed previously (§4.2). The optimisation phase of the work took place using DH6T, which is significantly cheaper than P3HT while still possessing useful photoconductive properties; this enabled a larger number of samples to be investigated initially. Samples were prepared in two ways; by spin coating and by thermal evaporation. The bulk of this work concentrates on the spin coated samples, which is the most successful method of preparing heterojunction devices, but some success was had in preparing photoconductive samples by sublimation. A base solution of DH6T in dichlorobenzene (DCB) was prepared at a concentration of 20mg/ml, 1 ml was added to each of 4 vials into which different quantities of BT, 10, 20, 30 and 40 mg respectively, had been measured. The vials were the ultrasonicated until the BT was held in suspension. It should be noted that even with the OPA ligand that BT did not dissolve

in the DH6T/DCB solution. The samples were spin coated at 3000rpm and allowed to dry; an aluminium gap cell was then deposited by thermal evaporation. The samples were investigated using UV-Vis spectroscopy and photoconductivity measurements as described previously.

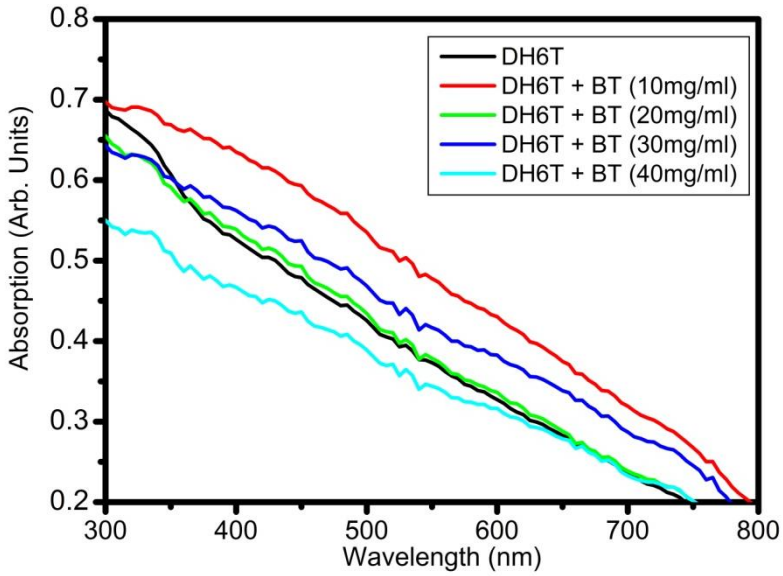

Figure 9-1. Absorption spectra of DH6T samples with varying concentrations of BT.

It can be seen from Figure 9-1 above that the addition of barium titanate made little difference to the absorption spectrum of DH6T. While there are differences in the total absorption of each sample the shape of the spectrum and the absorption peaks are virtually the same regardless of concentration of BT. Any slight differences in the spectrum are most likely due to small variations in thickness of the samples caused by the increasing viscosity with increased concentration of BT.

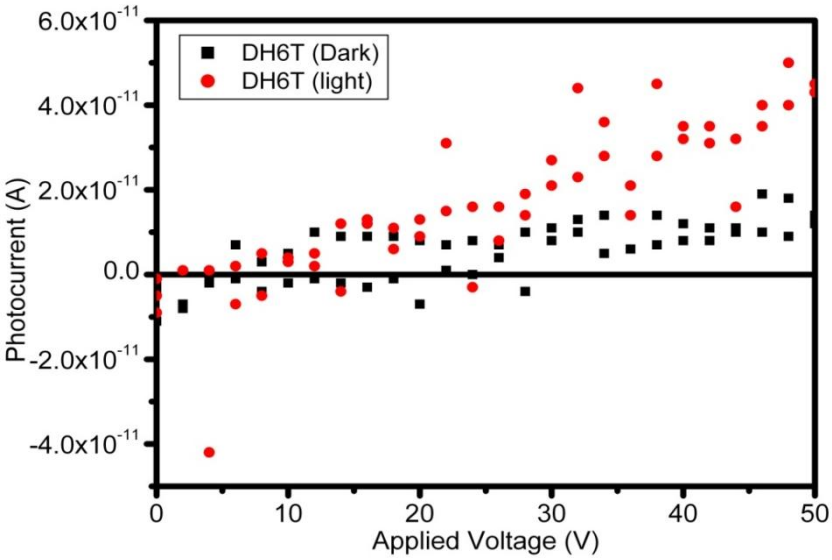

Figure 9-2. DH6T control sample under illuminated and dark conditions.

Figure 9-2 above shows the control sample of DH6T at 20 mg/ml concentration under dark and illuminated conditions with an applied voltage that increased from 0V to 50V and then returned to 0V. The illumination was provided by the Oriel light source described previously. Although a clear difference between illuminated and non illuminated states is apparent, the actual difference in terms of photocurrent is small.

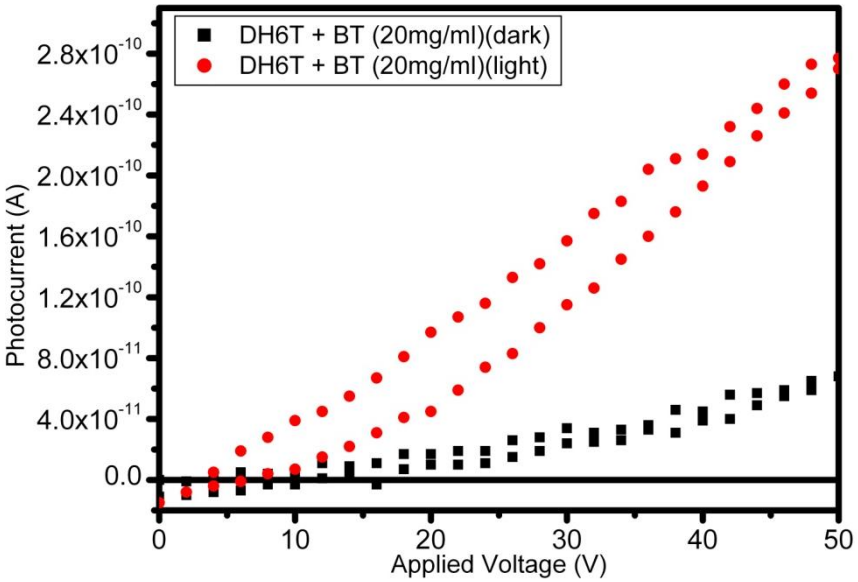

Figure 9-3. DH6T with 20mg/ml BT under illuminated and dark conditions.

Figure 9-3 above shows the sample of DH6T with 20mg/ml of BT, to prevent needless repetition only the 20mg/ml and 40 mg/ml samples are presented here, the others were sufficiently similar to be covered by the descriptions of these samples. As can be seen the sample shows a significant increase in conductivity under test conditions, which were the same as for the control sample.

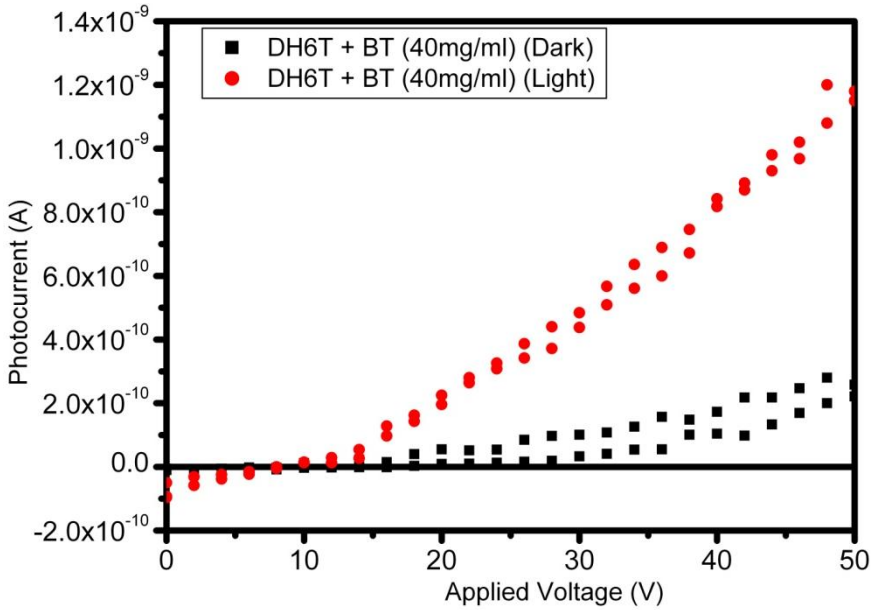

Figure 9-4. DH6T with 40mg/ml BT under illuminated and dark conditions.

The DH6T sample containing 40mg/ml BT is presented in Figure 9-4 above, as can be seen the maximum photoconductivity at 50V is an order of magnitude higher than the maximum photoconductivity for the 20mg sample. Only the 40mg/ml sample returned a photoconductivity of this magnitude, the 10, 20 and 30 mg/ml samples were all in the same range (~2-3 x 10^{-10} A). Although the maximum photocurrent achieved with this material was not high in terms of total current produced it did demonstrate that by adding BT to DH6T that an improvement in photoconductivity could be achieved. Furthermore, as the concentration of BT was increased the hysteresis in the illuminated part of the curve was reduced; one possible explanation for this is that charge trapping was reduced and that the material was approaching ohmic behaviour in one region of the graph (14 – 50V). Overall the entire photoconductive curve is slightly diode like, indicating that this material is suitable for inclusion in a PV device. Although the highest photoconductivity was achieved by the 40mg/ml sample the quality of these

films was generally poor as the higher viscosity produced films that repeatedly contained visible defects. The decision was taken to use the 20mg/ml concentration which still had a significant effect on photoconductivity and was repeatable and produced films of high quality.

Throughout this period of the work it was apparent that the main drawback of using DH6T was that it had generally poor solubility in many common solvents [139], which led to poor quality films when spin coated. Having read in the literature that DH6T was capable of being deposited by sublimation [148], a decision was taken to investigate the quality of thin films of DH6T and BT deposited by this method [27].

For simple comparative purposes two samples were prepared one with DH6T and 20mg/ml BT was prepared in the same way as the spin coated samples described above. The second sample was a 1:1 blend of DH6T and BT by mass, with 20mg of each material being used. This was placed in a tungsten boat and evaporated onto glass substrate as described in section 5.4. For each blend two samples were produced, one on plain glass for the spectroscopy measurements and one with a thermally evaporated gap cell for photoconductivity measurements (§Appendix B). UV-Vis absorption and photoconductivity measurements were taken for the respective samples. Additional samples were prepared on silicon substrates so that the ellipsometer could be used to obtain thickness measurements for each sample. The thickness of the spin coated sample was 78nm and the sublimated sample was 66nm thick [27].

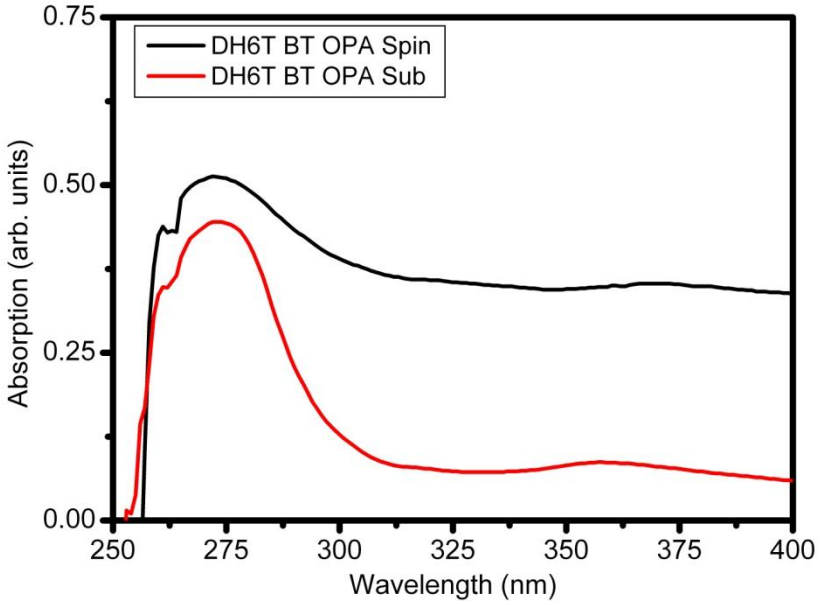

Figure 9-5. UV-Vis absorption spectra for spin coated and sublimated blends of DH6T and BT with OPA ligand.

The UV-Vis spectroscopy reveals that both the spin coated and sublimated samples contain an absorption peak at ~275nm, a second peak at ~360nm was expected but was not apparent in these samples. Duhm et al [148], postulate that these energy levels (4.5 and 3.44eV respectively) represent a group of 6 narrowly spaced localized π-states, which would be excited by the absorption of photons in this wavelength, potentially leading to the release of Frenkel singlet excitons as suggested by Horowitz et al [141]. It can clearly be seen that the absorption of the spin coated sample is comparable in the 275nm region and any apparent differences are most likely to be due to the differences in thickness of the samples.

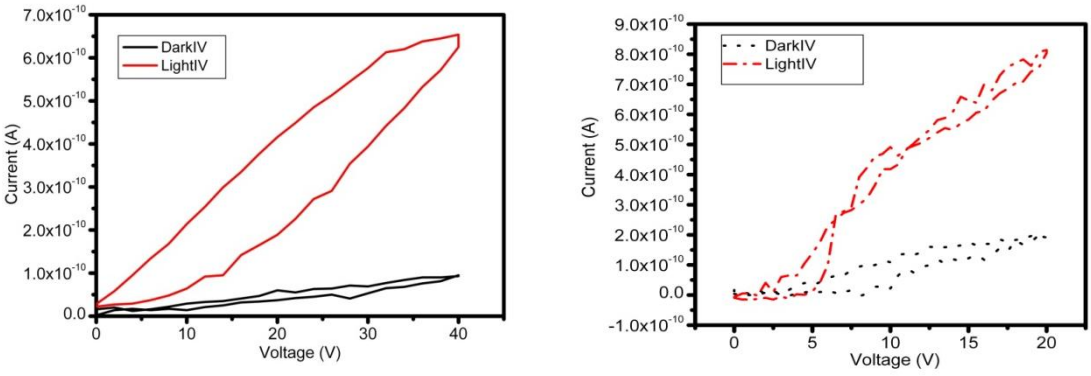

(a) (b)

Figure 9-6. IV characteristics of DH6T and BT/OPA samples prepared by (a) sublimation and (b) spin coating.

As can be seen from Figure 9-6 the spin coated sample has the highest photoconductivity (8.5x 10^{-10}A) and reaches this at only 20V whereas both sublimated samples achieve comparable photoconductivity at approximately twice that voltage. It can be seen that the photoconductivity of all of the samples in dark conditions are generally similar, although again the spin coated film is higher than that of the sublimated films at similar voltages.

There are two potential reasons for the higher photoconductivity in the spin coated films as opposed to the sublimated films, firstly the spin coated films are thicker than the sublimated films which may account for the slightly higher absorption in the visible spectrum, secondly and most importantly there is no method currently available to ensure that the density of nanoparticles per unit area is the same in both sets of samples. Inspection with optical microscopy reveal that there is an apparently higher density of nanoparticle clumps in the spin coated sample as these materials were created from a homogeneous solution containing equal amounts of polymer and nanoparticles by mass. The sublimated samples were prepared using dry powders of equal mass, but due to the potential differences in evaporation rates of the components it was not possible, at this time, to determine a methodology to ensure that the ratio was maintained in the sublimated film. The generally lower performance of sublimated films combined with the lack of control over the final ratios of materials means that spin coating was determined to be the preferred methodology for ongoing work in this area. However, it

should be noted that sublimation may offer the ability to orient the polymer chains, relative to particular substrates, in such a way as to optimize their electrical properties as described by Duhm et al [148].

Having demonstrated that it was possible to use BT to increase photoconductivity on a material such as DH6T the decision was then taken to apply this material to P3HT and see if the effect could be replicated in that material.

9.2 Optimisation of the P3HT Layers

9.2.1 Film thickness

Early work with P3HT was carried out using dichlorobenzene as a solvent in order to continue from the work with DH6T, however the films produced were of poor quality and irregularities could be easily detected visually and under the optical microscope. The decision was taken to investigate alternative solvents, after a brief review of the literature and given the resources available chloroform was selected as the optimum solvent for this work.

A base solution of 20 mg/ml P3HT was prepared by dissolving in P3HT powder in electronic grade chloroform obtained from Sigma-Aldrich. The mixture was held in a sealed vial and was placed in an ultrasonic bath until the powder had dissolved completely. The solutions were filtered before use using a 0.7µm filter.

The optimum spin coating speed was determined by preparing samples on silicon wafer at a range of spin speeds and determining the film thickness using ellipsometry. The results are presented in Figure 9-7 below. The thickness appears to reduce in a linear manner with increased spin speed. Ideally the optimum thickness of the P3HT layer is 100nm or less because of the need to balance photon absorption with the distance excitons need to travel to reach a dissiciative interface. All of the layers in this test achieved the desired thickness so therefore additional criteria were required in order to fully differentiate between films [47]. The primary criteria were that the layer should be thick enough to fully coat the embedded nanoparticles while maintaining good light

absorption characteristics. Furthermore it was noted that at spin speeds beyond 5000rpm visible defects began appearing in the films due to insufficient coverage. Once again the result of this process was that an optimum spin speed of 3000rpm was selected.

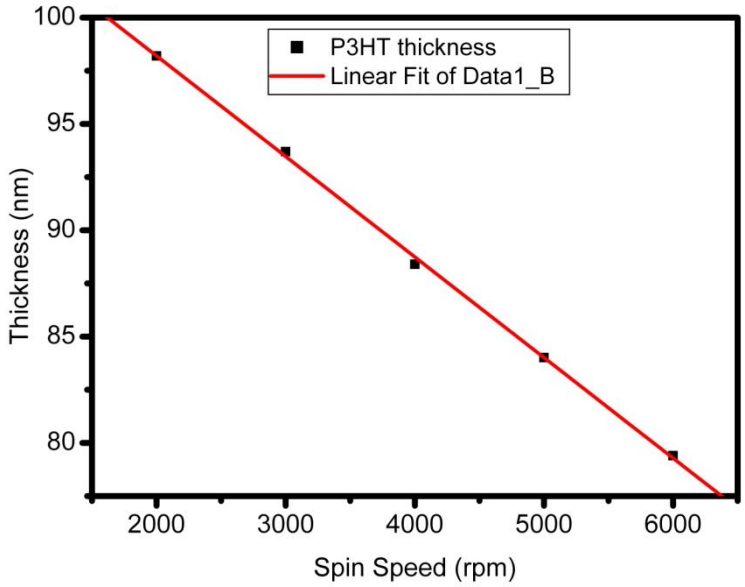

Figure 9-7. Thickness of films prepared from 20mg/ml P3HT solution for varying spin speeds.

The thickness of the polymer films was not easy to measure in a reproducible way for a number of additional reasons. Firstly the films were quite soft and therefore did not lend themselves to verification by the profilometer, as the probe would more often than not cut into the film rather than following the material profile therefore ellipsometry was used. Although it should be stated that this method has been used successfully by other groups [47]. Tests on PVAc with both profilometry and ellipsometry showed that there is approximately a 10% difference between the two techniques on the same sample with ellipsometry seeming to err on the lower side. The results presented here are the average results of repeated measurements.

9.2.2 P3HT Photoconductivity Measurements

The first test of photoconductivity using P3HT films used only barium titanate, although subsequent tests also included strontium titanate. The test process was identical to that described previously for spin coated DH6T. Figure 9-8 below shows the results of the first test, with a base 20mg/ml solution of P3HT was divided into two vials, one was kept as a control and the other was added to pre-measured barium titanate, which produced a solution with a concentration of BT of 20mg/ml. The solution was ultrasonicated until the BT was in full suspension and then spin coated onto glass. Top electrodes were deposited as previously described.

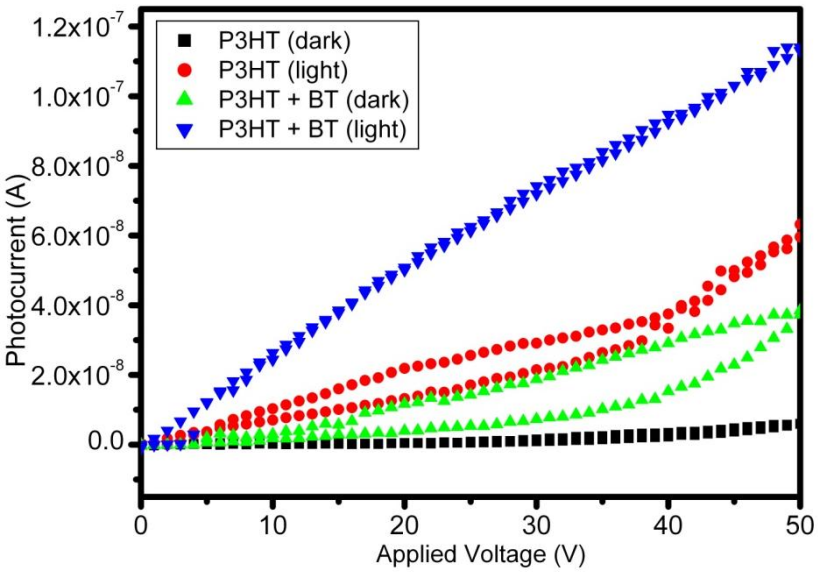

Figure 9-8. Initial photoconductivity measurements for P3HT samples containing 20mg/ml barium titanate.

It can be seen that P3HT alone has better photoconductive properties than DH6T having a maximum photocurrent of ~6 x 10^{-8} A under illumination at 50V. The sample containing BT (blue line), clearly improves this to ~1.1 x10^{-7} A and also reduces the hysteresis in the curve, producing an almost linear state.

9.3 Solar Cell Measurements

This section details successful and not so successful measurements of photovoltaic characteristics in the devices fabricated in this work.

9.3.1 Early attempts

Numerous attempts were made before any successful photovoltaic devices could be fabricated, the reasons for the failure of the initial devices are varied but in the main a common theme occurred in this phase of the work. The most common indicator of failure, in the early devices, was that they behaved in an ohmic rather than diode like manner.

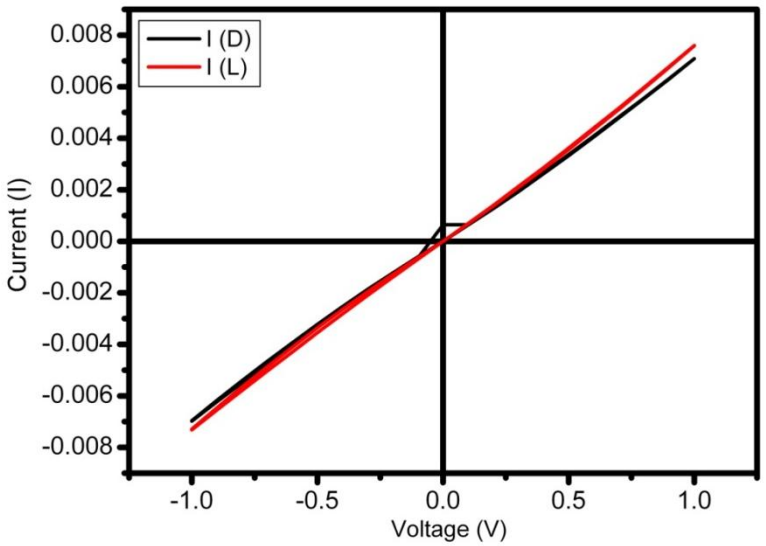

Figure 9-9. Typical failure mode of early hybrid photovoltaic devices fabricated in this work.

Figure 9-9 above shows an example of the ohmic behaviour for a typical early P3HT/PCBM solar cell prepared by spin coating the active layer. This mechanism occurred in samples that contained ferroelectric particles and in those that did not, so could not be a result of the material properties of the samples. Early test cells had used dichlorobenzene as a solvent and it soon became apparent that this resulted in poor quality layers being spin coated. These layers had pin-hole defects that when the top aluminium electrode was deposited led to conductive paths through the cell which

resulted in the exhibited ohmic behaviour. However, subsequent devices fabricated from solutions using chloroform instead of dichlorobenzene also exhibited this behaviour. Inspection of the films using optical microscopy before and ofter testing showed that there was no surface damage prior to the deposition of the top electrode, but that there was damage to the top electrode and the film after testing. This was determined to have occurred as a result of the fine tips of the probes piercing the sample and creating a conductive path, which once again resulted in an ohmic IV curve. This problem was overcome by replacing the probe needle with a new needle that had a rounded head and was less likely to puncture the samples. Since this time no repetition of this failure mode has occurred.

A concentration of 20mg/ml of P3HT is used by many research groups [47, 98], it was decided to test this by fabricating test cells comprising P3HT/PCBM at concentrations of 20, 30 and 40 mg/ml in a 1:1 ratio. The comparison of these samples is presented in Figure 9-10 below.

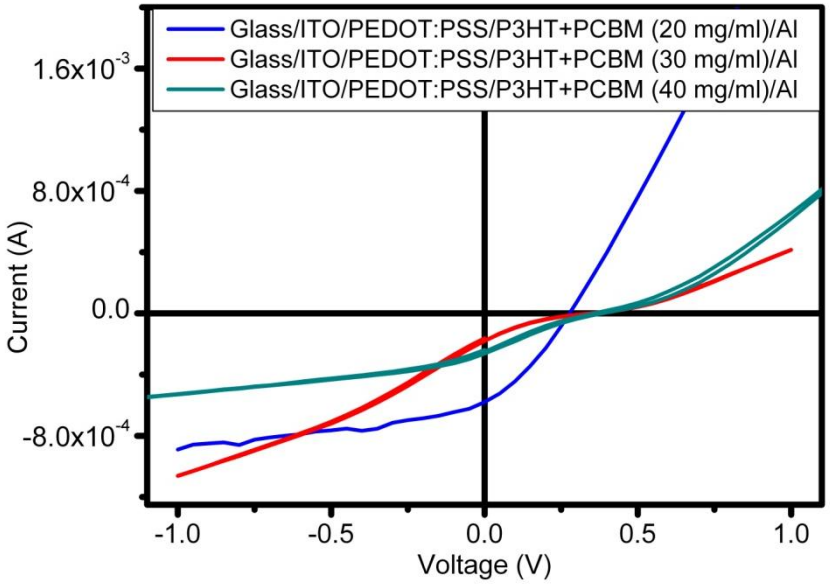

Figure 9-10. Comparison of control P3HT/PCBM samples with 20, 30 and 40mg/ml concentrations in a 1:1 ratio.

It is clear from both the shape of the curves and the fill factor and efficiency that sample 1 (20mg/ml) has the highest overall efficiency. The open circuit voltage is higher for both samples 2 and 3, but the fill factor is reduced for these samples. The flattening of

the curves is indicative of an increased effect from resistances which reduce the squareness of the ideal diode (§3.3.6). The FF, PCE, diode factor and shunt resistance have been calculated as described previously (§3.3.6 and 3.3.7) and are presented in Table 7 below.

Table 7. Fill factor (FF), power conversion efficiency (PCE), diode Factor (m) and shunt resistance (r_{sh}) calculated for solar cells presented in Figure 9-10 above.

Sample	FF	PCE (%)	m	r_{sh}
20 mg/ml	0.30	0.64	1.16	5.62×10^6
30 mg/ml	0.13	0.14	1.52	6.40×10^6
40mg/ml	0.24	0.23	1.63	7.20×10^6

As can be seen from the above results, the sample containing 20mg/ml of BT had the lowest value of m indicating that it performed more like an ideal diode than the other samples, for an ideal diode m~2 as the dark current is reduced, maximising the I_{sc} (§ 3.3.6 in particular equation 3.39). The shunt resistances were all in the same order of magnitude and could not be used to differentiate between the samples in any meaningful way. The 20mg/ml sample also returned higher values for both the fill factor and power conversion efficiency. Based upon these initial results the decision was taken to use a base solution of 20mg/ml and to add the ferroelectric nanoparticles to this solution for all subsequent work.

9.3.2 Barium Titanate Cells with and without OPA ligand

The first attempts at fabricating hybrid heterojunction devices incorporating ferroelectric nanoparticles were carried out using BT with an OPA ligand, the results were generally disappointing with very low short circuit currents being produced. In order to test the cause of the low currents two sets of samples were produced from a single batch of P3HT/PCBM solution; both had a concentration of 20 mg/ml of barium titanate one with the OPA ligand attached and one without.

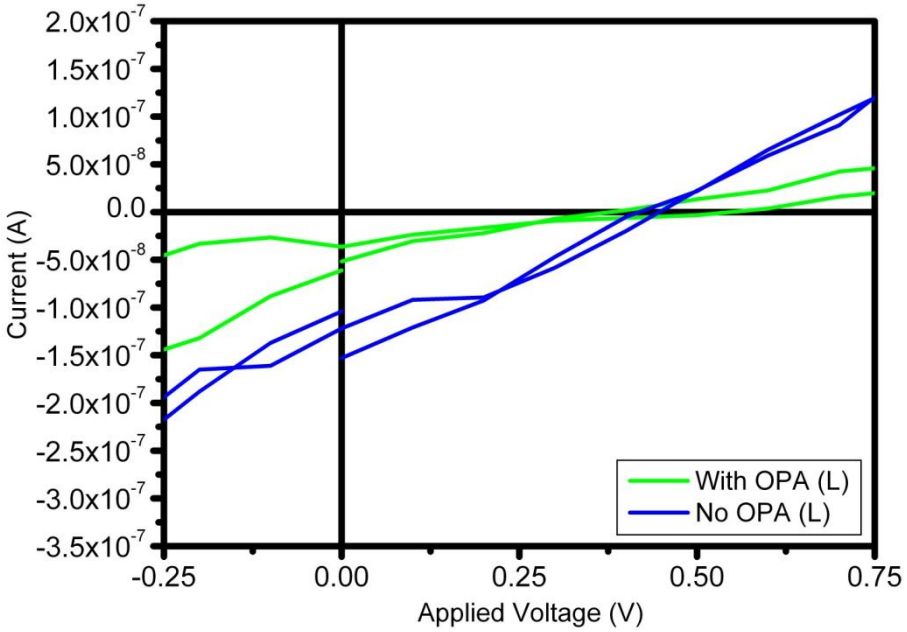

Figure 9-11. Comparison of P3HT/PCBM solar cells containing BT/OPA 20mg/ml (green line) and BT 20/mg/ml (blue line) under illuminated conditions.

The samples were tested using the standard I-V measurements in the solar simulator, the applied voltage was ±1V. Figure 9-11 above shows the data for the devices under illumination, it can clearly be seen that the sample containing OPA, while in every other way identical, produces a much lower current than the sample without OPA. Repetition of these measurements confirmed that this is true in the majority of cases, therefore in order to maximise the current output of the devices OPA was omitted from subsequent sets of samples. The exact reason for this is not fully understood, but one possible explanation is that the OPA ligand when attached to BT suppresses leakage current (see Figure 8-9) in an insulating medium. It is possible that this effect when applied to a conductive medium will reduce the current carrying capacity of the material. This is, of course, the exact opposite of the effect that it was intended to create.

9.3.3 Comparison of Barium and Strontium Titanate

Three sets of sample solar cells were fabricated with a base matrix of P3HT/PCBM with different concentrations of strontium titanate and barium titanate nanoparticles. The base solution for each concentration was a blend of P3HT and PCBM, to which was

added either no nanoparticles to form a control sample, ST or BT. The concentration for the P3HT/PCBM samples was 20mg/ml in a 1:1 ratio. The P3HT/PCBM/nanoparticle blend was a 1:1:0.5 ratio. The concentrations of the samples are detailed in Table 8 below.

Table 8. Polymer-nanoparticle blends used in active layers

Sample	P3HT (mg/ml)	PCBM (mg/ml)	BT (mg/ml)	ST (mg/ml)
1	20	20	0	0
2	20	20	0	10
3	20	20	10	0

The structure of the samples was as shown in Figure 9-12 below.

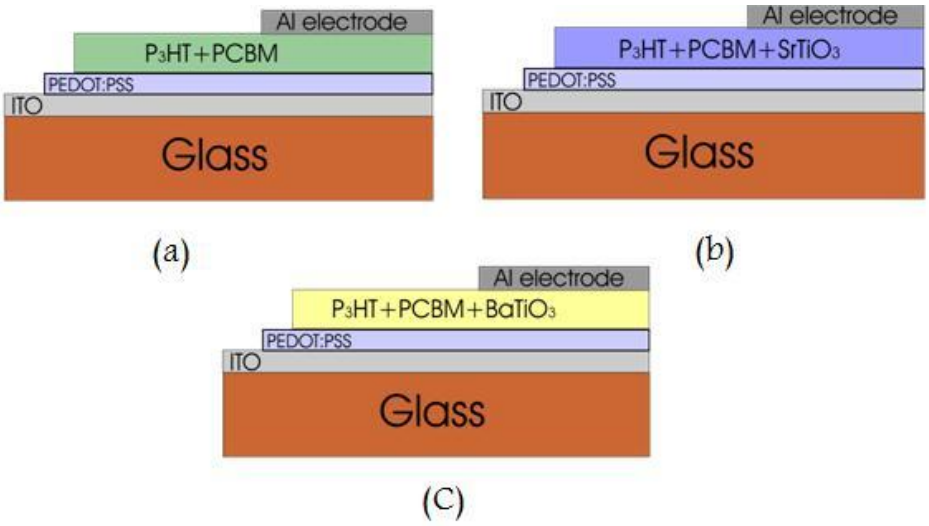

Figure 9-12. Typical structure of organic heterojunction solar cells as used in this work, (a) control sample 1 of P3HT/PCBM, (b) sample 2, P3HT/PCBM plus strontium titanate and (c) P3HT/PCBM plus barium titanate.

The devices were prepared by first spin coating a layer of PEDOT:PSS onto cleaned ITO coated glass substrate at 5000rpm. Next the active layer was deposited by spin coating at 3000rpm to produce a layer ~100nm thick. Aluminium top electrodes, 1 cm^2, were deposited by thermal evaporation at a chamber pressure of ~1x 10^{-6} mbar and the completed devices were annealed at 110^oC for 10 minutes.

UV-Vis measurements were carried out on samples deposited on ITO coated glass substrates. The UV-Vis spectroscopy measurements shown below reveal that all three samples tested (1, 2 and 3) share peaks at two wavelengths which are typical of the absorption by P3HT in the optical region of the spectrum. The first peak is around 334nm and the second at 490nm which corresponds to the peak optical absorption by P3HT [263] . The first peak is slightly shifted to 331nm in sample 2 containing strontium titanate but remains at 334nm in the other two samples. The 490nm peaks correspond in all three samples and are characteristic of the absorption peaks in the green part of the spectrum for P3HT. The absorption shoulders that are expected between 500 and 600 nm are not very pronounced in these samples. This may be a characteristic of the solvent which in this case was chloroform. Samples with chlorobenzene based solvents have been shown by Vanlaeke et al to show flatter regions in this area [263]. It can clearly be seen that the relative absorbance of both polymer blends containing ferroelectric nanoparticles is greater than those of P3HT/PCBM alone, given that all three samples are ~100nm thick.

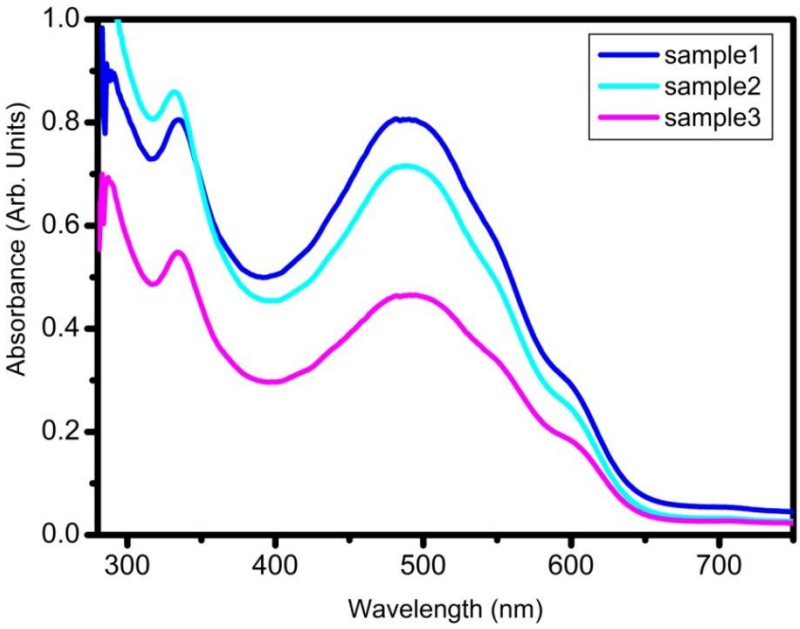

Figure 9-13. UV-Vis spectrum of sample 1 (magenta), sample 2 (cyan) and sample 3 (blue) for comparison.

Electrical tests were carried out on the samples using standard current-voltage (I-V) tests in both illuminated and non-illuminated conditions. The illumination used was an Oriel AM1.5 150W Xenon lamp light source, which for a solar cell of test area 1 cm^2 has an incident power equivalent to 8.8 mW (§6.4.1). Figure 9-14 below shows the I-V characteristics of the samples.

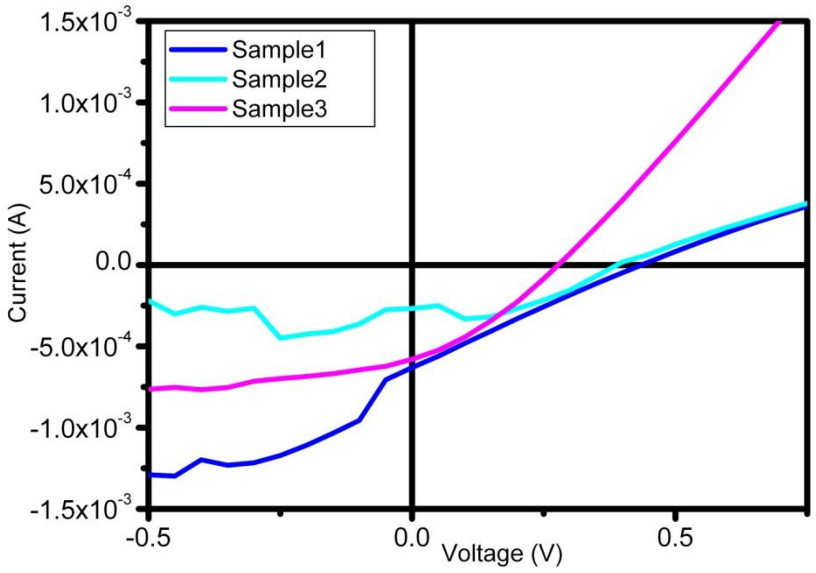

Figure 9-14. I-V curve for sample 1- P3HT/PCBM+BT(10mg/ml) (blue), sample 2 – P3HT/PCBM + ST (10mg/ml) (cyan) and sample 3 – P3HT/PCBM (magenta) control sample.

The curve of the control sample, (sample 3 the magenta line) has a shape close to the expected shape for an OPV device but with characteristics indicating that the shunt resistance of the device is small [57] leading to the slope of the graph in the upper quadrant to move away from the vertical. This device although not as efficient as the best devices currently being researched has reasonable values for the V_{oc} and I_{sc}. The other two samples containing the ferroelectric particles both exhibit similar behavior to the control sample, but the curves in the bottom right quadrant are flattened suggesting increased series resistance in the devices [57]. In an ideal PV device the shunt resistance should be infinite while the series resistance should be as close to zero as possible to give ideal diode like behavior. All of the devices have the same geometry and only a single concentration (10mg/ml) of both BT (sample 1) and ST (sample 2)

was used in this work. The generally low currents measured in this work are most likely the result of a combination of factors including; the low power output of the solar simulator and possible absorption of water and oxygen as a result of being fabricated in a non neutral atmosphere.

Although these devices are not ideal, it can clearly be seen that both devices containing the ferroelectric nanoparticles exhibit higher V_{oc} than the control and the sample containing barium titanate also exhibits a higher I_{sc} than the control sample.

Given the success of these devices, three further samples were prepared and tested in the same way. The I-V characteristics of these samples are presented and compared in Figure 9-15 and Figure 9-16 below. Figure 9-15 shows a comparison the control sample and the sample containing ST. Both samples exhibit curves of similar shape, presenting the expected diode like behaviour. The sample containing ST clearly produces higher open circuit voltage and short circuit current than the control P3HT/PCBM sample. From the theory stated above one explanation for the increase in current is the increased numbers of excitons that can dissociate into charge carriers, due to both a decrease in coulomb forces and an increase in the volume of the dissociation region. The reason for the increase in open circuit voltage is less clear but is likely to be linked to the ferroelectric particles increasing the built in potential of the devices [53, 54].

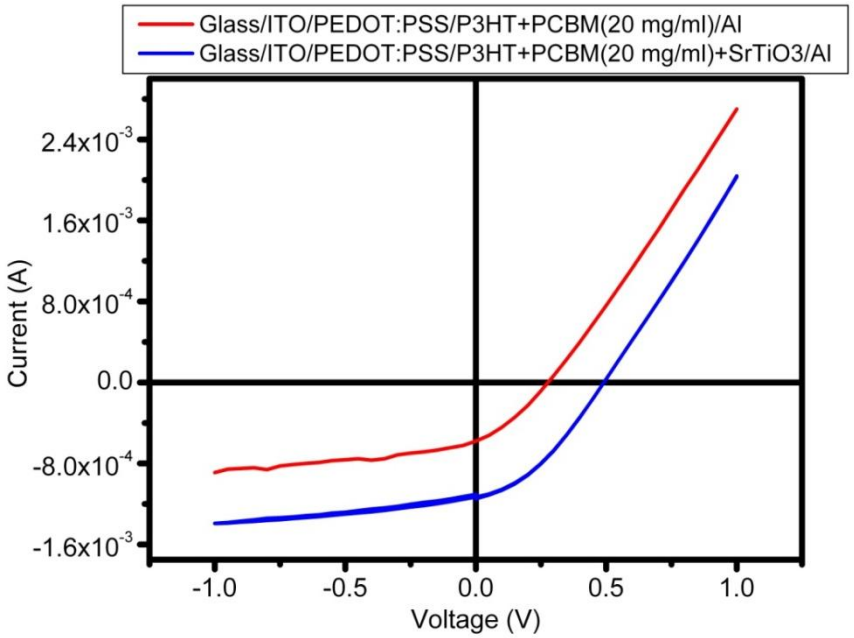

Figure 9-15. I-V characteristics of control P3HT/PCBM sample (red) with P3HT/PCBM/ST device (blue).

Figure 9-16 shows a comparison between the control sample and the sample containing BT, as with the ST sample the open circuit voltage and short circuit current are increased, but the curve of this sample does not retain the expected ideal diode like shape compared to sample 1. In any solar cell, XSC or CSC, there are two resistances; a series resistance (r_s) related to the contact and bulk resistances and a shunt resistance (r_{sh}) arising from the contact alone, in an ideal device $r_s = 0$ and $r_{sh} = \infty$. As r_s increases and r_{sh} decreases the diode moves away from perfect diode like behaviour and the shape of the curve is flattened. For reasons not currently clear the resistances in the BT sample are obviously affecting the behaviour of the material, why this is not evident in the ST sample is also not known at present.

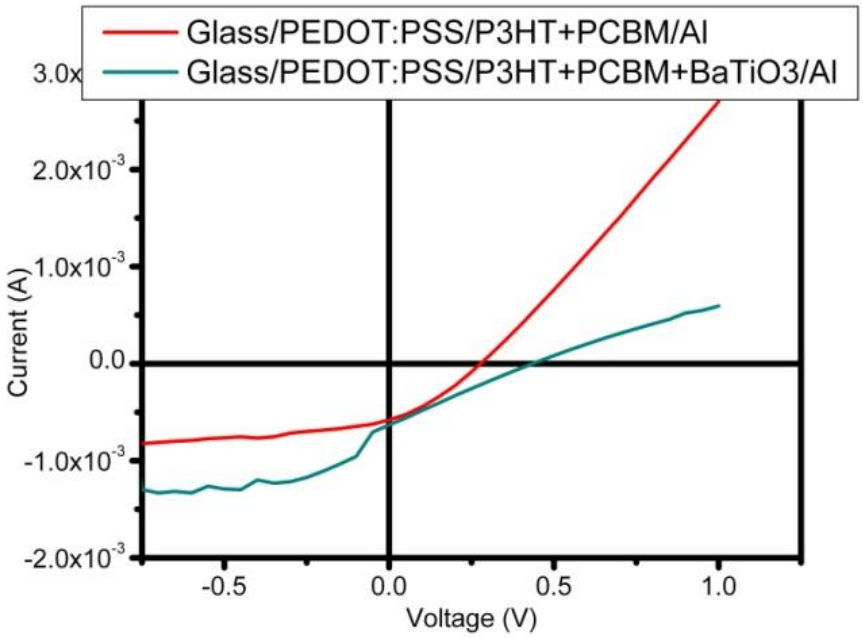

Figure 9-16. I-V characteristics of control P3HT/PCBM sample (red) with P3HT/PCBM/BT device (green).

The fill factor, power conversion efficiency, diode factor and shunt resistance of all 3 samples was calculated in the same way as described above. The results are presented in Table 9 below.

Table 9. Open circuit voltage (Voc), short circuit current (Isc), Fill factor (FF), power conversion efficiency (PCE), diode Factor (m) series resistance (r_s) and shunt resistance (r_{sh}) calculated for 1 cm^2 devices from data presented in Figure 9-15 and Figure 9-16 above.

Sample	V_{OC} (V)	I_{SC} (mA)	FF	PCE (%)	m	r_s (Ω)	r_{sh} (Ω)
P3HT/PCBM	0.27	0.50	0.296	0.53	1.13	142	5.40×10^6
P3HT/PCBM+ST	0.48	1.10	0.351	2.52	1.32	125	5.33×10^8
P3HT/PCBM+BT	0.43	0.70	0.240	0.70	1.48	614	4.78×10^7

By comparing the relative efficiencies of these devices it can clearly be seen that the devices which incorporate ferroelectric nanoparticles are more efficient than those

without, although are not yet close to the theoretical limit of these devices. Sample 2 presents an overall PCE of 2.52% which is a factor of four greater than the control sample.

The V_{oc} of the samples containing the ferroelectric nanoparticles is higher than that of the control sample, this phenomenon also arises in solid state ferroelectric semiconductor layers where the the differing polarisation of adjacent domains in the material can be added in series and can result in a voltage greater than the band gap which is the usual limit of these devices [264, 265].

All three samples have diode factors in the expected range (1-2) and it can clearly be seen that the samples containing titanates have the highest diode factor. The shunt resistances are not in the tens or hundreds of GΩ range as would be expected [266], although the samples containing titanates are higher than the sample without. The series resistances are all high compared to good results previously described (<1Ω) [59], but are noticeably lower in the control sample and the sample containing strontium titanate than in the sample containing barium titanate. This indicates that the flattening of the curves is in the first two samples is likely to be due to the relatively low shunt resistance arising from being a non perfect diode, while the shape of the curve of the device with BT filler indicates that there may be a resistance built up at the interface of the electrode with the polymer [57, 267, 268]. However, the results here indicate that both barium and strontium titanates show great promise as additives to improve the performance of OPV devices. It is anticipated that by continuing to use ferroelectric nanoparticles in these devices that their efficiency can continue to increase compared to traditional P3HT/PCBM devices alone.

9.4 Summary

In this chapter the effect of ferroelectric nanoparticles on the material properties of has been demonstrated. It has been clearly shown that the addition of strontium titanate and/or barium titanate to photoconductive polymers can increase the permittivity of the material which it is thought would then increase the volume of the charge separation region resulting in the increase in charge production. This has also been demonstrated

in the increase in photoconductivity that accompanies the increase in permittivity of the material.

Control solar cells comprising P3HT/PCBM heterojunctions were prepared and the results were compared to identical cells that also incorporated ferroelectric nanoparticles. A relative improvement in the efficiency of the samples containing ferroelectric nanoparticles could clearly be seen when compared to the P3HT/PCBM control: 2.52 and 0.53 respectively. This relative increase demonstrates that the principle of modifying the permittivity of photoconductive materials has the potential to allow hybrid organic/inorganic heterojunction devices to become commercially viable.

The addition of nanomaterials to the active layer has the additional benefit of increasing the photon absorption, which could be a further reason for the enhanced efficiency demonstrated by these devices compared to the control samples.

Chapter 10

10 Conclusions

This chapter is divided into three main sections; the first section details the conclusions that can be drawn from the results in the previous three chapters. Section 9.2 details potential improvements that could be made to this work. The final section outlines possible future work that could follow on from this work.

10.1 Main Conclusion

The permittivity of a photovoltaic material is critical in determining whether it behaves as a conventional semiconductor (CSC) or as an excitonic semiconductor (XSC). Typically where the coulomb forces are greater than the thermal energy of the charge carriers the device will behave in an excitonic manner and where this case is reversed unbound electron hole pairs will be produced.

ITO was optimised, to produce a transparent conductive layer, however, the quality of the layer was not equivalent to commercially available films and it was decided to use the purchased films in order to guarantee that the transparent electrode was consistent across all of the fabricated devices so that the effect of modifying the active layer could be measured without prejudice.

It has been known for some time that the permittivity of certain materials such as polymers and epoxy resins can be increased by adding ferroelectric materials to a blend of these materials. In this work barium titanate and strontium titanate, both high k materials, were bought in their cubic paraelectric phase and were modified by annealing at 1000^{o}C in air to alter their structure to the tetragonal phase, which is ferroelectric. Initial the improvement in permittivity was demonstrated in PVAc and subsequently the same effect was seen in P3HT. The addition of an OPA ligand to the barium titanate was shown to decrease the leakage current in PVAc and to increase the quality of the

layer, however this property when applied to organic photovoltaic devices reduced the current produced by the devices and was then removed from subsequent devices.

DH6T and P3HT films were optimised for thickness and quality when spin coated and to these optimised blends was added quantities of BT and ST. A significant increase in the photoconductivity was noted in both materials although this was more pronounced in P3HT which was determined to be the optimum material for the active layer of a hybrid photovoltaic device.

Bulk heterojunction photovoltaic devices comprising P3HT and PCBM were fabricated and optimised and then samples identical to the optimised cells were fabricated with additional ferroelectric nanoparticles. The devices showed a significant relative increase in both open circuit voltage and short circuit current in the ferroelectric samples compared to the control P3HT/PCBM devices. For the control devices the best efficiency achieved to date is 0.52% compared to 2.52% for samples containing ferroelectric strontium titanate.

10.2 Improvements

There are a number of ways in which the work carried out here could be improved should future funding and research opportunities be available. Firstly by using materials of higher quality; for example, in this work regular P3HT of 99% purity was used, but P3HT of 99.9% purity is available. This could potentially offer an increase in efficiency due to the reduced impurities and related reduction in potential charge trapping locations combined with the increase in conjugation length. The same applies to the transparent electrode layer, in this work ITO with a resistivity of ~30-60 Ω/□ was used, but there are commercially available films with resistivity of ~5-10 Ω/□. These combined with the most conductive PEDOT: PSS, which was not available during this work for reasons beyond the control of the supplier would certainly not be detrimental to the functioning of a high efficiency device. The addition of an optimised exciton blocking layer could also potentially increase the efficiency of these devices by preventing excitons quenching at the cathode. However, the single most significant thing that could be done to improve the quality of the films would be to carry out the

entire fabrication process, from measuring of materials in powder form through to annealing, in a neutral atmosphere such as nitrogen. This would prevent the absorption of water and oxidation of the films which it has been shown has a detrimental effect of the functioning of organic photovoltaic devices.

10.3 Next Steps

One logical next step is to investigate if the addition of any ferroelectric material has the same effect on permittivity, photoconductivity and efficiency in photovoltaic devices. In fact some progress has been made in this area as Dr Iulia Salaoru has begun to investigate the effect of ferroelectric polymers on sexithiophene devices. Other materials that warrant further investigation include silver nanoparticles and silver nanowires.

In order to take advantage of the potential benefits of this improvement a multidisciplinary approach needs to be adopted; firstly a full theoretical treatment of the link between permittivity and exciton transport and dissociation needs to be built up. This can then be supplemented by photoluminescence measurements to determine the levels of excitons generated in the active layers, carrier lifetime measurements to determine if the exciton diffusion is increased and surface potential measurements, possibly with KPFM to determine what, if any, charging effects are taking place around the nanomaterials in the layer. Other possibilities are to carry out QE measurements, PE measurements to determine the exciton diffusion length and other techniques should be investigated to see if it is possible to differentiate between the types of excitons produced. This would show one of two things; if the majority of the excitons measured are of the Frenkel type then it is likely that the dissociation region increases as hypothesised in Chapter 8. If Mott-Wannier or no excitons are measured then this indicates that the addition of ferroelectric nanoparticles causes the solar cell to behave as a CSC device rather than an XSC device.

Fully optimising ITO to commercial quality would be a useful complementary activity, this is easily achievable with sufficient time. However, it should be noted that other

materials such as SnO_2:F are used commercially and these should be considered as an alternative to ITO in the TCO layer.

Appendix A – Detailed Methodologies

Pumping Down Process

A typical pumping down process is as follows:

1. The mechanical pump is switched on
2. The cryo pump (if used is cooled down) or the diffusion pump is warmed up.
3. The roughing and high vacuum valves are closed and the foreline valve is opened, the pipework between the mechanical pump and the two valves is evacuated to a pre-set level which is monitored using the Pirani gauge.
4. Once the foreline is evacuated the roughing valve can be opened and the mechanical pump engaged to pump the chamber down to the operating pressure of the high vacuum pump.
5. The roughing valve is closed.
6. The high vacuum valve is opened and the high vacuum pump is engaged.
7. The high vacuum pump is used to evacuate the chamber to a pressure low enough that the intended deposition process can take place under optimum conditions (typically ~10^{-6} mbar). This pressure is measured using the Penning gauge.
8. After deposition, the high vacuum valve is closed and the chamber is vented.

Thermal Evaporation Procedure

The procedure for thermally evaporating materials is as follows:

1. Vent the chamber.
2. Place the material to be evaporated into either a tungsten or molybdenum boat or filament.
3. Use appropriate shadow masks (see Appendix B) to determine the device structure.
4. Place substrates onto substrate holder or shadow masks as required.
5. Pump down the chamber as described in Vacuum Systems in General above.

6. When the chamber pressure reaches ~10^{-6} mbar the current can be switched on.
7. When the required thickness of material is reached switch off the current. Additionally many evaporators have a screen that can be swung into position once the desired thickness is reached to prevent further deposition.
8. Vent the chamber and remove samples.
9. Pump down the chamber again to prevent contamination of the chamber.

Sputtering Process used in this work

The procedure for sputtering used in this work is as follows:

1. Vent the chamber and insert sample(s)
2. Close chamber door.
3. Pump down the chamber in the way described in 5.3 above.
4. When the chamber pressure is ~10^{-6}mbar the sputtering process can commence.
5. Select the appropriate target (ITO, ZnO or Al are the targets usually in the sputterer).
6. Select RF sputtering.
7. Switch on the RF power supply and apply 10W of power
8. Balance the power so that the reflected power is zero or as close as possible.
9. Open the valves and allow the sputtering gas into the chamber, usually Argon (Ar) or a mixture of Ar and O_2 at the required rate (measured in standard cubic centimetres per second (sccm)).
10. Adjust gas flow rates so that the appropriate chamber pressure is reached (typically 5-10mTorr)
11. The plasma should strike at this point. If not increase the power slowly. If this fails close the gas inlet valves, allow the pressure to build up and open the valves, the inrush of gas should strike the plasma. Repeat these steps until a plasma is struck.
12. Rebalance the system and increase the power in 25W steps until the desired power is reached, continually rebalance the system after each increase of power.

13. Once the desired power is reached open the shutter so that the substrate is exposed to the plasma.
14. Leave for the required length of time to achieve the film thickness.
15. Close the shutter.
16. Reduce the power in the reverse of step 11 rebalancing the system constantly.
17. Once zero power is reached switch off the RF power supply and close the gas inlets.
18. Allow the chamber to cool.
19. Vent chamber and remove samples.
20. Pump down chamber and leave under vacuum.

There are a number of parameters that are important to the sputtering process; chamber pressure, power per unit area and the combination of gasses. The chamber pressure controls the amount of gas molecules available to bombard the surface of the target and the power per unit area controls the velocity that the individual ions will strike the surface with. The ratio of gasses will determine the type of plasma and whether any vacancies in oxides are filled with oxygen atoms.

Attaching Ligands to Titanates

Neither barium titanate nor strontium titanate are particularly soluble in the organic solvents typically used in the fabrication of organic photovoltaic devices. In order to produce the types of high quality film necessary for photovoltaic devices it is necessary to modify the particles without losing their inherent properties. One method of doing this is by attaching a ligand, a particle or molecule that bonds to metallic ions while having a free end molecule that renders the combined molecule more soluble in a group of solvents compatible with the end molecule.

The procedure for attaching ligands to titanates is as follows (based on the methodology of Kim et al [13]):

1. A stoichiometric amount of phosphonic acid – C_8H_{17}-$PO(OH)_2$ also called n-octylphosphonic acid (OPA) or 1-octylphosphonic acid (in the UK) is dissolved

in a 95:5 solution of ethanol and water. Typically 0.2mmol ligand in 1mL solvent mixed with 0.4g/10mL titanate.

2. The solution of OPA and titanate is ultrasonicated for 10 min and then stirred at 80^{o}C for 1 hr. The solution will turn a cloudy white and will become turbid.

3. The nanoparticles are separated by settling and rinsed repeatedly with 50:50 ethanol/water solution using ultrasonication at 30-40^{o}C for 1 hr followed by further settling. After being washed the supernatant liquid is dried overnight at 80^{o}C in air.

Unfortunately the addition of the ligand to BT and ST was ultimately unsuccessful as the ability of the ligand to reduce the leakage current also appears to reduce the short circuit current of the OPV devices containing titanates with ligands compared to those that did not have ligands attached to the titanates.

Spin Coating Procedure

The general procedure for preparing solutions and spin coating polymer/nanoparticle blends is a follows:

1. **Preparation of the Solution of Polymer and the Polymer Blend (all operations to take place in the laminar flow bench)**

    a. Weigh (in mg) the required amounts of polymer and transfer into clean glass vials.
    b. Weigh (in mg) the required amounts of filler and add to the polymer vials.
    c. Measure (in ml) the required amounts of solvent or mixture of solvents (e.g. 95:5 ratio Cl-napth:DCB) and pour into the vials.
    d. Sonicate the vials for at least 15 minutes prior to spin coating.

2. Deposition of Thin Films from the Chemicals Prepared in Section 1

a. Turn on the mains power to the spin coater in the laminar flow bench
b. Turn the vacuum power switch on
c. Select the appropriate spin programme
d. Remove the lid
e. Place the substrate on the chuck and ensure that the substrate is firmly held in place
f. Replace the lid of the spin coater
g. Take the required amount of solution in a pipette
h. Drop the required amount of solution through the hole in the lid onto the spin substrate
i. Activate the spin programme
j. Wait until spin cycle is complete
k. Switch off the power to the spin coater
l. Remove the substrate in a similar manner to stages d and e
m. Place substrate in sample box
n. Clean the spin coater using acetone and dispose of the tissue paper into a closed lid disposal box
o. Replace lid
p. Switch mains power supply off
q. Leave working area neat and tidy
r. Note: Repeat steps d to m to build up layers as required, this process is for static spin coating, for dynamic spin coating action i should take place prior to action h.

Painting

Painting can be sub-divided into two main techniques; hand painting and spray painting.

Hand painting using a brush or similar device can be used for experimental work fabricating test devices or for large areas such as a roof at home. Hand painting a blend of P3HT and PCBM using a simple brush on a heated surface coated with ITO has been investigated by Kim et al [269] and shows promise as a fabrication technique. In fact they suggest that the shear stresses between the ITO layer and the solvent and the brush impart increased order to the molecular structure as the layer dries. As discussed previously molecular order and the orientation of the molecules with regard to the ITO

layer influences the absorbance and efficiency of the material. They suggest that painting offers a quick and easy way to impart order to the blends and have shown using XRD that the crystallinity of the material is increased compared to a similar sample that has been spin coated with no post processing such as annealing. Whether it is possible to consistently achieve the same film thickness has not yet been demonstrated with this technique.

Spray painting using a hand held airbrush to fabricate a nanocrystalline CdTe/CdSe solar cell has been investigated by Javier and Foos [270]. They started with an ITO coated substrate and spray applied layers of CdSe nanorods, CdTe nanorods and silver, the latter using a commercially available silver paint, the nanorods were both suspended in a pyridine matrix. The control of the spray system meant that waste material was reduced significantly compared to spin coating which produces a high quantity of wasted materials, furthermore the known spray rate allowed layers of 20 to 500nm thickness to be fabricated with repeatable accuracy. As with other thin film devices, the cells with a thickness of less than 200nm were shown to have the best performance. It is easy to visualise this technique being scaled up for use in fabricating large area photovoltaics at home or commercially either by individuals or trained application operatives. It can be seen that spray application holds a number of advantages over brush application from a repeatability perspective, however, it is not yet known if it can impart the same level of crystallinity as the painting technique described

Typical OPV Device Fabrication

The process for fabrication of OPV devices as used at EMTERC is as follows:

1. Clean ITO Coated slides as detailed in 5.2.1.
2. Plasma treat in barrel etcher (if necessary) as detailed in 5.2.2 for 10 minutes in argon.
3. Prepare blends of polymers and solvents in ultrasonic bath and allow materials to dissolve fully in the solvent.
4. Spin coat PEDOT: PSS layer at 5000rpm.
5. Allow film to dry.

6. Anneal in air at 130^{o}C for 10 minutes and leave to cool.
7. Spin coat active layer (P3HT + PCBM + nanoparticles as required) at 3000 rpm.
8. Allow film to dry.
9. Anneal film at 130^{o}C for 10 minutes and leave to cool.
10. Move to evaporator and deposit 100nm thick top electrode of appropriate size using shadow masks (see appendix B) made from either aluminium or silver.
11. Remove from evaporator and carry out electrical testing in solar simulator as soon as possible after fabrication to prevent moisture and oxidation damage to the polymer. See section 6.3 for details of appropriate electrical measurements.

SPM Modes and Operation

The Park XE-100 SPM used in this work has a of additional functions that allow the measurement of a wide range of physical and electrical characteristics including [271, 272];

In the basic Basic mode:

- Atomic force microscopy (AFM) (Contact, Non-contact, Intermittent) : Topography
- Force Distance (F/D) curve , Nanoindention : Adhesion force, Hardness
- Lateral Force Microscopy (LFM) : Surface Friction
- Phase imaging : Adhesion, Friction and Viscoelastic properties.

In the External mode:

- Magnetic Force Microscopy (MFM) : Magnetic force
- Electrostatic Force Microscopy (EFM) (EFM,EFM(ext),DC-EFM): Potential, Charge, Electrical Domain,
- Work function, Piezoelectric response mode : d33 measurement
- Force Modulation Microscopy (FMM): Hardness
- Scanning Tunnelling Microscopy (STM), I-AFM, SSRM : Current, Resistance
- Open liquid cell: Image measurement in liquid condition
- Lithography (XEL) : Lithography software
- Scanning Thermal Microscopy (SThM) : Temperature, Thermal Conductivity.
- Scanning Capacitance Microscopy (SCM): Capacitance, Dopant Concentration

The mode used most often after NC-AFM is Kelvin Probe Force Microscopy, which is a subset of EFM and is described below.

The XE-100 is situated in a cabinet to prevent contamination and has an anti-vibration platform to isolate he microscope from external effects. The AFM is set up as described in the literature provided by Park Systems Ltd [271, 272]. In simple terms the operation is as follows:

1. The appropriate tip is selected and installed in the scanning head
2. The sample is positioned on the PZT table.
3. The isolation table is enabled
4. The camera is switched on
5. The laser is switched on.
6. The laser is focussed on the tip
7. The Mode is selected and the driving frequency is set.
8. The beam is centred as closely as possible on the centre of the photodiode
9. The scanning measurements are selected.
10. Using the camera and z measurement on screen the tip is approached to the sample
11. The sample is scanned

Appendix B – Shadow Masks for Device Fabrication

1. Scope of Document

This document is designed to give basic background information relating to the set of shadow masks designed to be used in the evaporator and sputtering equipment. It should be used in conjunction with the related mask design files:

i) Shadow Mask 1 - 1mm Lines.jpg
ii) Shadow Mask 2 - 100,250um Lines.jpg
iii) Shadow Mask 3 - Gap Cell.jpg
iv) Shadow Mask 4 - Dots.jpg
v) Shadow Mask 5 - Source, Drain Contact.jpg
vi) Shadow Mask 6 - Contact Pads.jpg

Please note that as far as possible these masks have been designed to be as generic as possible. As such, they can be used to construct various different structures depending upon the characteristic that needs to be investigated. This document aims to outline some example structures that each mask can be used to fabricate, but in no means should it be viewed as an exhaustive list of what is capable of being created with the masks.

2. Shadow Mask General Information

The shadow masks are specifically designed to be small feature size, high precision masks for use with processes where a material is patterned through vapour deposition:

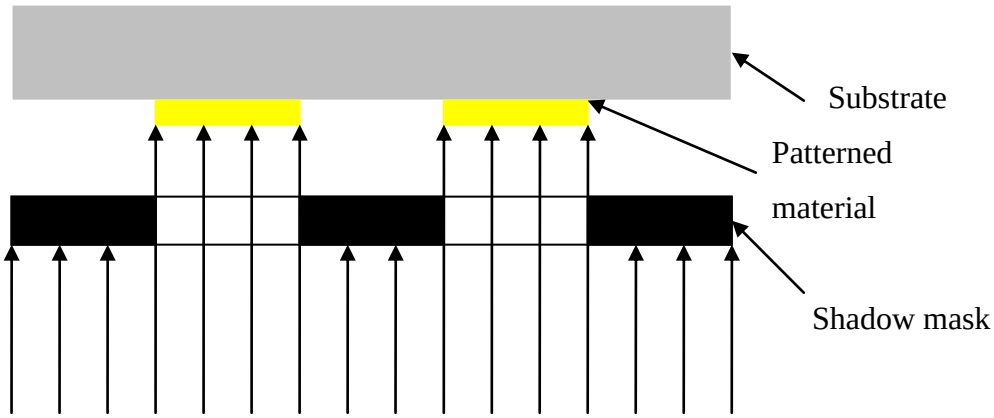

Evaporation Source

The physical mask dimensions will be 50mm^2, with 250µm thick aluminium sheet to be used for fabrication of the masks.

3. Shadow Mask 1 - 1mm Lines

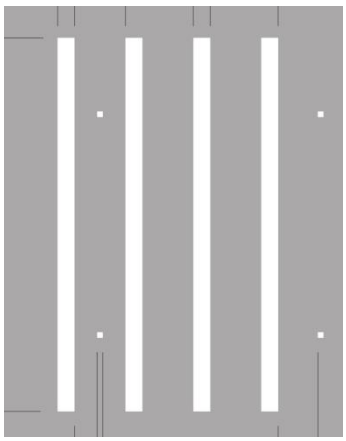

Pattern Description: Four, 1mm wide tracks with a length of 22mm. Tracks are on a 4mm pitch.

1mm squares are also included for alignment purposes.

Example uses: Top/bottom contacts to devices.

Each mask consists of two such structures.

4. Shadow Mask 2 – 100, 250µm Lines

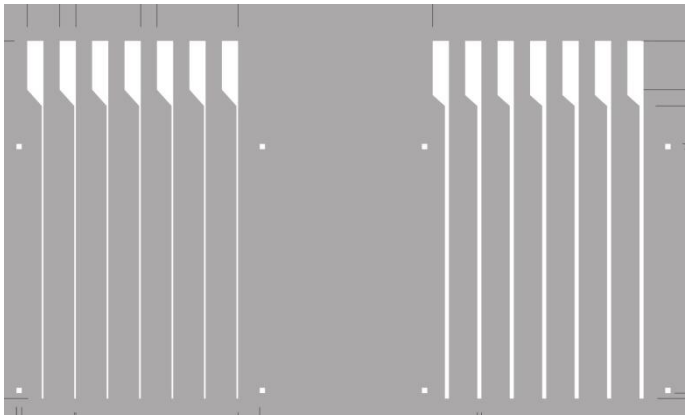

Pattern Description: First pattern on the mask consists of eight, 100µm wide tracks with a length of 22mm. 1mm wide contact pads at the end of each track. Tracks are on a 2mm pitch.
Second Pattern on the mask consists of eight, 250µm wide tracks with a length of 22mm. 1mm wide contact pads at the end of each track. Tracks are on a 2mm pitch.
1mm squares are also included for alignment purposes.

Example Uses: Top/bottom contacts to devices. Similar uses to 1mm lines, but larger amount of contacts can be made.

5. Shadow Mask 3 – Gap Cell

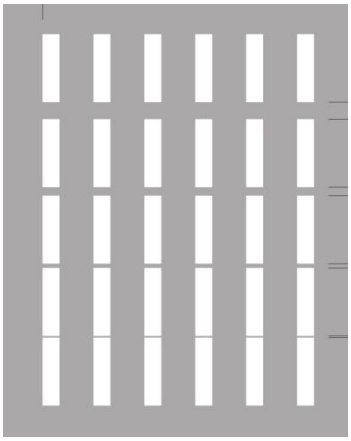

Pattern Description: Six, 1mm wide tracks, with each track having four gaps of 100µm, 250µm, 500µm and 1000µm size. Tracks are on a 3mm pitch.

Example Uses: Can be used for determining electrical characteristics of various materials, where small separation between contacts is required. eg dark and photoconductivity of a-Si

Each mask consists of two such structures.

6. Shadow Mask 4 – Dots

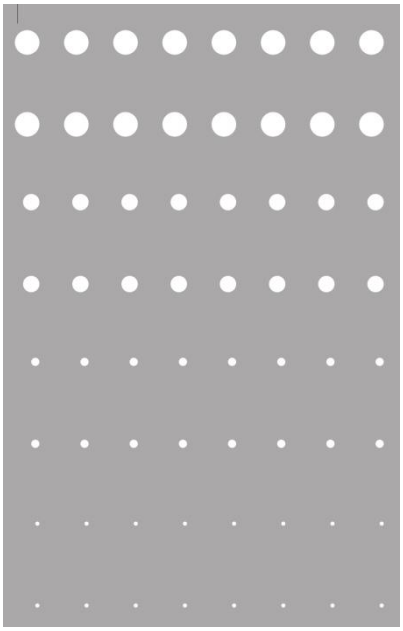

Pattern Description: Mask contains an array of four different sizes of dots, with two lines of each size of dots. Dots are available in sizes of 1.5mm, 1.0mm, 500μm and 250μm diameters. Dots are on a 3mm pitch horizontally, and 5mm pitch vertically.

Example Uses: Top contacts to vertical devices.
Top contacts for MIS capacitors

Whole useable area of mask is taken up with the array, to allow the contact dots to positions wherever need on the substrate.

7. Shadow Mask 5 - Source, Drain Contact

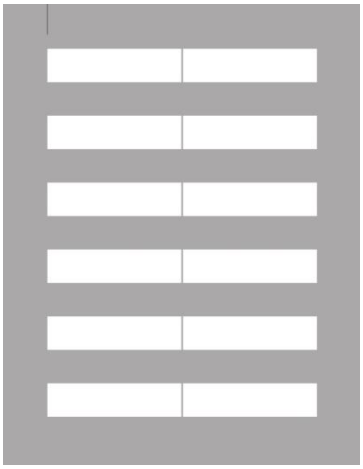

Pattern Description: Array of 2mm wide contact pads with 100μm spacing between left and right pads.

Example Uses: Source and drain contacts for transistor structures.

Each mask consists of two such structures.

8. Shadow Mask 6 - Contact Pads

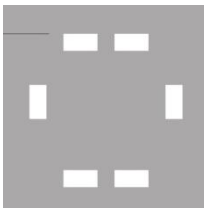

Pattern Description: An array of six, 1mm x 2mm contact pads, positioned to allow a $5mm^2$ sample to be places in the centre of the pads.

Example Uses: Bond pads to any material that needs to be electrically characterised. Bond pads can be connected to any point on the DUT depending upon the experiment that needs to be conducted.

Each mask consists of four such structures, allowing the user to choose a variety of bond pad configurations.

Appendix C - Silver Nanostructures

Silver is a useful and versatile material which has a number of forms on nanoscales including; nanoparticles, nanowires and nanorods. As a bulk material silver is the most conductive metallic element and this property is retained on the nanoscale, but as with many other materials silver develops different properties on the nanoscale to the bulk material. Although silver was not used in the hybrid solar cells fabricated as part of this work it was originally considered as a material with potential to improve photovoltaic performance and some time was spent investigating methods to fabricate silver nanowires. Investigations into the use of silver nanomaterials were discontinued when the success of ferroelectric nanoparticles was demonstrated. This section details the properties and characteristics of silver nanoparticles and nanowires, which could be included in subsequent investigations into hybrid photovoltaic devices, either as a constituent of the transparent electrode layer or as part of the active layer.

Silver Nanoparticles

Silver nanoparticles have a number of interesting properties including; high conductivity (silver is the most conductive metal), anti bacterial properties [273] and a number of interesting optical properties arising from surface plasmon resonances (SPR) [274-276]. In SPR the conduction electrons at the surface of the metal can oscillate when excited by electromagnetic (EM) radiation, which occur as a result of the following phenomena; the conduction electrons are accelerated by the electric field of the incident EM radiation, polarization of the particles result in a restoring force and electrons are confined to regions dimensions smaller than the wavelength of the incident light [277].

The process of SPR is as follows; the incoming EM radiation excites electrons from their equilibrium state, this produces a restoring force that results in the electrons oscillating with the SPR frequency. The polarization results in a counter force to this which in turn reduces the frequency of the SPR. By altering the dielectric constant of

the medium in which the silver is dispersed the wavelength of the SPR can be tuned [277]. In order for SPR to occur the particles need to be very small <10nm so that phase matching can take place between the particle and the incident EM field. This phase matching is linked closely to the permittivity of the surrounding material by the following formula [277]:

$$\epsilon_1(\omega) = -2\epsilon_m \qquad 10.1$$

Where $\varepsilon_1(\omega)$ is the real part of the frequency dependent permittivity of the metal and ε_m is the permittivity of the material. For SPR to occur the imaginary part of the permittivity of silver must be small otherwise losses take place which prevent the oscillations that led to SPR.

Silver nanoparticles have been shown, by Ihara et al, to improve the absorption characteristics of dye sensitised solar cells when blended with a polyacrylate polymer instead of the usual ruthenium dye [278]. The absorption is a result of SPR for small particles, as particle size increases scattering and extinction increase relative to absorption [277]. This phenomena has also been used to modify the effectiveness of photon absorption of solar cells by adding a spin coated layer of very small ~4nm silver nanoparticles in a colloidal suspension onto the ITO layer prior to the deposition of the PEDOT:PSS layer. Yoon et al, have shown that this method increases the photon absorption efficiency and results in an increased short circuit current due to increased exciton production at the SPR interface [15]. Symonds et al have demonstrated a strong coupling effect between excitons and SPR in metallic nanoparticles, both in colloidal suspensions [279] and in patterned films with nanoscale holes [280]. Other groups have also made this connection including Bellessa et al [281], the process also occurs in different types of structures including evaporated silver films [274], other lattice like structured films [277] and metallic structures with nanoscale cavities [282].

Essentially silver nanoparticles seem to offer a way to enhance the performance of organic solar cells by increasing the photon absorption efficiency of the transparent electrode [15, 274, 283]. Another characteristic of silver nanoparticles of interest to this

work is the ability to increase the permittivity of materials when used as a filler, in particular the permittivity of epoxy films can be increased by the addition of silver nanoparticles [14, 284]. This ability to modify permittivity along with a similar property in barium and strontium titanate is discussed in more detail in Chapter 8.

Silver Nanowires

Silver nanowires share many of the same properties of silver nanoparticles; they are highly conductive and even though much larger exhibit SPR like behaviour. They are typically ~1μm long and can vary from a few tens to hundreds of nanometres in diameter. They generally have a hexagonal cross section except when insufficient atoms (< 7) are present to fully form the structure [285, 286].

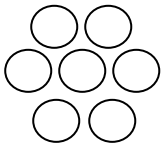

Figure 10-1. Smallest complete hexagonal cross sectional structure in silver nanowires comprising 7 silver atoms.

Early attempts to produce a novel solar cell suggested that silver nanowires (AgNW) would be suitable electron acceptors and would increase photon absorption due to surface plasmon resonance [276]. Although it was possible to purchase AgNW on the open market it is not possible to obtain wires of sufficiently small diameter and adequate length. It was therefore decided to attempt to fabricate AgNW for inclusion in the active matrix of hybrid solar cells. While this was ultimately unsuccessful (see Appendix A), it is worthwhile to include the methodologies attempted as they have been used with success elsewhere.

Electrochemical Growth and manipulation of Silver Nanowires

The first method used to attempt to fabricate silver nanowires was to reproduce the work of Shi et al [287] using an electrochemical process based on rubidium silver iodide. Rubidium silver iodide is unusual in that it is a room temperature superionic

conductor; in a superionic conductor the charge carriers are ions and electrons which are both free to move within the crystal lattice of the material. Previously carbon nanotubes and silicon nanowires have been shown to develop a preferential orientation in along field lines in the presence of an external applied DC electric field [288]. It was anticipated that silver would respond in a similar manner by Cao et al [106] and others.

The process of producing nanowires is as follows [287]:

1. Deposit a layer of rubidium silver iodide on a glass substrate by thermal evaporation ~ 80nm thick [106]
2. Deposit silver electrodes 1mm apart onto the rubidium silver iodide layer
3. Apply a DC electric field of 60V/m across the electrodes.
4. Leave for ~5hr
5. Remove nanowires by rinsing with de-ionised water.
6. Dry product and use as required.

The mechanism by which the growth process occurs is not fully certain, but it is thought that silver ions were created at the anode and then migrate along the electric field lines and can somehow nucleate to form a cluster of ions which then grow as additional ions are added by the system.

Chemical growth of Silver Nanoparticles and Nanowires

One of the most widely used methods for producing silver nanoparticles and nanowires is the reduction of silver nitrate ($AgNO_3$) in the presence of polyvinyl pyrrolidone (PVP) and ethylene glycol (EG). The process is essentially done in two main parts with a third purification stage after the main reaction has taken place. The first part is the creation of "seeds" from which the nanowires or particles can grow, these can be produced from a number of metallic precursor materials including; potassium chloride [289], copper chloride [290], silver nitrate [291] and gold chloride [292]. By adding further silver nitrate and EG to the seed solution growth of nanoparticles, nanowires or nanorods is facilitated. The nanostructures are thought to grow by a mechanism known as Ostwald Ripening, in which larger crystals grow preferentially to smaller crystals

[292], this is the same process that gives ice cream its crunchy texture if frozen too rapidly with constant stirring to break up the large crystals.

Phase 1 – Nanoparticle (NP) seed formation

1. 2ml ethylene glycol (EG) heated in three necked flask (50ml) in oil bath at 160^{o}C for ~20 min.
2. 1ml AgNO3 solution (2x10-4M in EG) added within 5s of achieving temperature
3. Heat for further 20 min until silver NP seeds form

Phase 2 – Nanowire (NW) formation

1. 5ml AgNO3 solution (0.1M in EG) added within 20s of seed formation
2. 10ml poly(vinylpyrrolidone) (PVP) injected dropwise by syringes within 10 min.
3. Reaction kept at 160^{o}C for 20 minutes to produce nanowires

Phase 3 – Purification

1. Dilute with acetone (6x by volume)
2. Centrifuge at 4000 rpm for 30 min (this stage was omitted at EMTERC due to a lack of a centrifuge, instead the solution was allowed to settle naturally.
3. Remove supernatant EG by syringe.
4. Add ethanol to tubes
5. Ultrasonic bath to disperse products and dissolve residual PVP
6. Repeat step 2-5 until sample is clean and allow to dry.

The figure below shows examples of nanowires and nanoparticles produced by the above process. As can be seen the ratio of nanowires to nanoparticles is low and even multiple repetitions with differing concentrations and times failed to produce a significant increase in the number of nanowires produced. Silver is the most conductive

metal and hence any silver nanowires that could be incorporated into a solar cell could potentially create a short between electrodes, which would eliminate any beneficial increase in photon absorption due to SPR. The lack of success in producing large quantities of nanowires combined with the potential for shorting led to this avenue of work being abandoned.

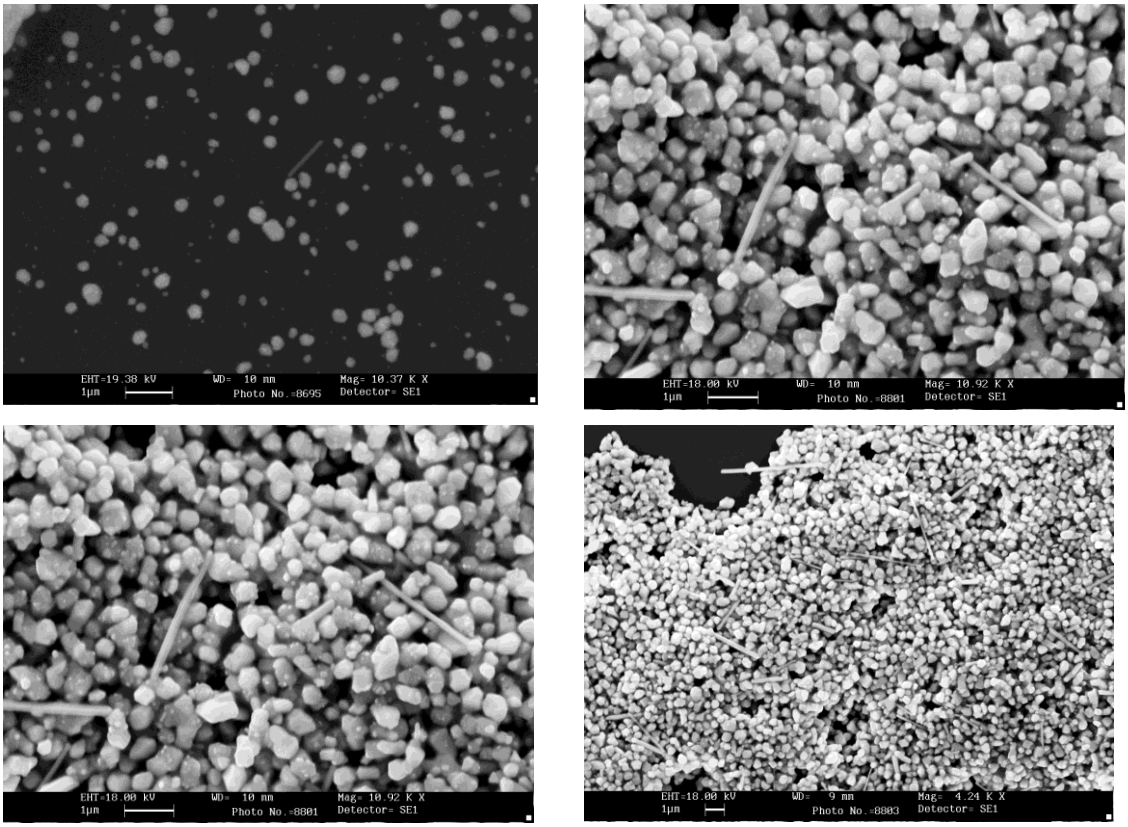

Silver nanoparticles and nanowires produced by polyol reduction process.

Appendix D– Acronyms Used in this Work

a-Si.....Amorphous Silicon
AFM.....Atomic Force Microscopy
AM.....Air Mass
BT.....Barium Titanate ($BaTiO_3$)
CIGS.....Copper Indium Gallium Selenide ($CuIn(Ga)Se_2$)
CdTe.....Cadmium Telluride
CdS.....Cadmium Sulphide
CSC.....Conventional Semiconductor
CNT.....Carbon Nanotube
eV.....Electron Volt
FF.....Fill Factor
GaAs.....Gallium Arsenide
HOMO.....Highest Occupied Molecular Orbital
HWCVD.....Hot Wire Chemical Vapour Deposition
ITO.....Indium Tin Oxide
I-V.....Current Voltage
LUMO..... Lowest Unoccupied Molecular Orbital
mc-Si.....Multi-crystalline Silicon
MOCVD.....Metal Organic Chemical Vapour Deposition
MIM.....Metal Insulator Metal
MOM.....Metal Organic Metal
NC-AFM.....Non Contact Atomic Force Microscopy
OPA..... n-octyl phosphonic acid
OPV.....Organic Photovoltaic
P3HT.....Poly (3-hexylthiophene)
PECVD..... RF Plasma Enhanced Chemical Vapour Deposition
PCBM.....Phenyl-C_{61}-butyric acid methyl ester
PEDOT:PSS.....Poly(3,4-ethylenedioxythiophene) poly(styrenesulfonate)
PV.....Photovoltaic
PVAc.....Poly Vinyl Acetate

QE.....Quantum Efficiency

RF.....Radio Frequency

Si.....Silicon

SNW.....Silver Nanowire

SPM.....Scanning Probe Microscopy

ST.....Strontium Titanate

STC.....Standard Test Conditions

TW.....Terra Watts

UV-VIS.....Ultraviolet-Visible

V_{OC}. .....Open Circuit Voltage

XRD.....X-Ray Diffraction

XSC.....Excitonic Semiconductors

References

1. Kazmerski, L. *Best Research Cell Efficiencies*. 2010 [cited 2010 April 2010]; Available from: http://en.wikipedia.org/wiki/File:PVeff%28rev100414%29.png.
2. Hauch, J.A., et al., *Flexible organic P3HT:PCBM bulk-heterojunction modules with more than 1 year outdoor lifetime.* Solar Energy Materials and Solar Cells, 2008. **92**(7): p. 727-731.
3. Krebs, F.C., *Degradation and stability of polymer and organic solar cells.* Solar Energy Materials and Solar Cells, 2008. **92**(7): p. 685.
4. O'Regan, B. and M. Gratzel, *A low-cost, high-efficiency solar cell based on dye-sensitized colloidal TiO2 films.* Nature, 1991. **353**(6346): p. 737-740.
5. Hoppe, H. and N.S. Sariciftci, *Organic Solar Cells: An overview.* J. Mater. Res., 2004. **19**(7): p. 1924-1944.
6. Brabec, C.J., et al., eds. *Organic Photovoltaics*. 1st Edition ed. Springer Series in Materials Science, ed. R.M. Osgood Jr., R. Hull, and J. Parisi. 2003, Springer: New York. 297.
7. Konarka. *Konarka's Power Plastic Achieves World Record 8.3% Efficiency Certification from National Energy Renewable Laboratory (NREL).* 2010; Available from: http://www.konarka.com/index.php/site/pressreleasedetail/konarkas_power_plastic_achieves_world_record_83_efficiency_certification_fr.
8. Gratzel, M., *Conversion of sunlight to electric power by nanocrystalline dye-sensitized solar cells.* Journal of Photochemistry and Photobiology A: Chemistry, 2004. **164**(1-3): p. 3-14.
9. Tian, H. and F. Meng, *Solar Cells Based on Cyanine and Polymethine Dyes*, in *Organic Photovoltaics: Mechanisms, Materials and Devices*, S.S. Sun and N.S. Sariciftci, Editors. 2005, Taylor and Francis: Boca Raton. p. 217-237.
10. Grätzel, M., *Photovoltaic performance and long-term stability of dye-sensitized meosocopic solar cells.* Comptes Rendus Chimie, 2006. **9**(5-6): p. 578-583.
11. Agranovich, V.M., et al., *Charged Frenkel Excitons in Organic Crystals.* Chemical Physics, 2001(272): p. 159-169.

12. Gregg, B.A., *Coulomb Forces in Excitonic Solar Cells*, in *Organic Photovoltaics: Mechanisms, Materials and Devices*, S.S. Sun and N.S. Sariciftci, Editors. 2005, Taylor and Francis: Boca Raton. p. 139-159.
13. Kim, P., et al., *Phosphonic acid-modified barium titanate polymer nanocomposites with high permittivity and dielectric strength.* Advanced Materials, 2007. **19**(7): p. 1001-1005.
14. Yang, R. and C.P. Wong. *Ultra high dielectric constant epoxy silver composite for embedded capacitor application*. in *Electronic Components and Technology Conference, 2002. Proceedings. 52nd*. 2002.
15. Yoon, W.-J., et al., *Plasmon-enhanced optical absorption and photocurrent in organic bulk heterojunction photovoltaic devices using self-assembled layer of silver nanoparticles.* Solar Energy Materials and Solar Cells, 2010. **94**(2): p. 128-132.
16. Dias, C.J. and D.K. Das-Gupta, *Inorganic ceramic/polymer ferroelectric composite electrets.* Dielectrics and Electrical Insulation, IEEE Transactions on, 1996. **3**(5): p. 706-734.
17. Black, D., S. Paul, and I. Salaoru, *Ferroelectric Nanoparticles in Polyvinyl Acetate (PVAc) Matrix - A Method to Enhance the Dielectric Constant of Polymers.* Nanoscience and Nanotechnology Letters, 2010. **2**: p. 41-45.
18. Kwon, S.-W. and D.-H. Yoon, *Tetragonality of nano-sized barium titanate powder prepared with growth inhibitors upon heat treatment.* Journal of the European Ceramic Society, 2007. **27**(1): p. 247-252.
19. EIA, U. *International Energy Outlook 2010 - Highlights*. 2008 October 2008 [cited 2011 01 February]; Available from: http://www.eia.doe.gov/oiaf/ieo/highlights.html.
20. Nelson, J., *The Physics of Solar Cells*. 1st ed. 2003: Imperial College Press.
21. Goetzberger, A. and C. Hebling, *Photovoltaic materials, past, present, future.* Solar Energy Materials and Solar Cells, 2000. **62**: p. 1-19.
22. Zulehner, W., *Czochralski growth of silicon.* Journal of Crystal Growth, 1983. **65**(1-3): p. 189-213.

23. Perlin, J., *The Story of Solar Cells*, in *Organic Photovoltaics: Mechanisms, Materials and Devices*, S.S. Sun and N.S. Sariciftci, Editors. 2005, Taylor and Francis: Boca Raton. p. 217-237.
24. JRC, *Solar modules production world-wide almost doubled in 2008*, in *Press Release*, E. Commision, Editor. 2009, JRC: Brussels.
25. Solarbuzz. *Solar Energy Market Growth*. 2010; Available from: http://www.solarbuzz.com/facts-and-figures/markets-growth/market-growth.
26. Black, D., S. Paul, and I. Salaoru, *Ferro-electric Nanoparticles in Polyvinyl Acetate (PVAc) Matrix - A Method to Enhance the Dielectric Constant of Polymers.* Journal of Nanoscience and Nanotechnology Letters, 2010. **2**: p. 1-5.
27. Black, D. and S. Paul, *Photoconductivity Measurements of Sublimated Organic Polymer/Nanostructure Blends compared with similar blends prepared by spin coating*, in *MRS Spring 2010*. 2010, MRS: San Francisco.
28. Lewis, G.N., *THE ATOM AND THE MOLECULE.* Journal of the American Chemical Society, 1916. **38**(4): p. 762-785.
29. Langmuir, I., *THE ARRANGEMENT OF ELECTRONS IN ATOMS AND MOLECULES.* Journal of the American Chemical Society, 1919. **41**(6): p. 868-934.
30. De Broglie, L., *The wave nature of the electron*, in *Nobel Lecture*. 1929, Nobel Committee.
31. Schrodinger, E., *An undulatory theory of the mechanics of atoms and molecules.* Physical Review, 1926. **28**(6): p. 1049-1070.
32. Tanner, B.K., *Introduction to the Physics of Electrons in Solids*. 1st ed. 1995: Cambridge University Press.
33. Rae, A.I.M., *Quantum Mechanics*. 4th ed. 2002: Institute of Physics.
34. Woan, G., *The Cambridge Handbook of Physics Formulas*. 2000, Cambridge: Cambridge University Press.
35. Tipler, P.A., *Physics for Scientists and Engineers*. 4th ed. 1999, New York: W. H. Freeman.
36. Eisberg, R. and R. Resnick, *Quantum Physics of Atoms, Molecules, Solids, Nuclei and Particles*. 2nd ed. 1985, New York: Wiley.

37. Gibson, K. *The Nature of the Dirac Equation*. 2010 [cited 2010 01 July 2010]; Available from: http://www.mc.maricopa.edu/~kevinlg/i256/Nature_Dirac.pdf.
38. Wikipedia. *Quantum Number*. 2010 [cited 2010 02 July 2010]; Available from: http://en.wikipedia.org/wiki/Quantum_number.
39. Softley, T.P., *Atomic Spectra*. 2nd ed. Oxford Chemistry Primers, ed. R.G. Compton, et al. Vol. 19. 1996, Oxford: Oxford University Press. 91.
40. Fidi, P. and L. Paul. *Electron Orbitals*. 2006 [cited 2010 2nd July]; Available from: http://en.wikipedia.org/wiki/File:Electron_orbitals.svg.
41. Janssen, R., *Introduction to polymer solar cells.* 2002.
42. Nalwa, H.S., ed. *Handbook of Organic Conductive Molecules and Polymers*. 1 ed. Conductive Polymers: Synthesis and Electrical Properties. Vol. 2. 1997, Wiley. 865.
43. Kittel, C., *Introduction to Solid State Physics*. 5th ed. 1976: John Wiley and Sons Inc.
44. Dang, C. *Miller Indices Cubes*. 2009 [cited 2010 5th July]; Available from: http://commons.wikimedia.org/wiki/File:Miller_Indices_Cubes.svg.
45. Sze, S., *Physics of Semi-Conductor Devices*. 2nd ed. 1991: Wiley-India.
46. Ge, Y. and J.E. Whitten, *Energy level alignment between sexithiophene and buckminsterfullerene films.* Chemical Physics Letters, 2007(448): p. 65-69.
47. Gang, L., et al., *Investigation of annealing effects and film thickness dependence of polymer solar cells based on poly(3-hexylthiophene).* Journal of Applied Physics, 2005. **98**: p. 043704.
48. squirmymcphee. *Solar Cell Equivalent Circuit*. 2008 19 October 2008 [cited 2010 15th July]; Available from: http://en.wikipedia.org/wiki/File:Solar_cell_equivalent_circuit.svg.
49. Brendel, R., J.H. Werner, and H.J. Queisser, *Thermodynamic efficiency limits for semiconductor solar cells with carrier multiplication.* Solar Energy Materials and Solar Cells, 1996. **41-42**: p. 419-425.
50. Forrest, S.R., *The Limits to Organic Photovoltaic Cell Efficiency*, in *MRS Bulletin*. 2005, MRS. p. 28-32.
51. Florescu, M., et al., *Improving solar cell efficiency using photonic band gap materials.* Solar Energy Materials and Solar Cells, 2007. **91**: p. 1599-1610.

52. Park, S.H., et al., *Bulk heterojunction solar cells with internal quantum efficiency approaching 100%*. Nat Photon, 2009. **3**(5): p. 297-302.
53. Brabec, C.J., et al., *Origin of the Open Circuit Voltage of Plastic Solar Cells.* Advanced Functional Materials, 2001. **11**(5): p. 374-380.
54. Lo, M.F., et al., *Limits of open circuit voltage in organic photovoltaic devices.* Applied Physics Letters, 2010. **96**(11): p. 113303-3.
55. Emery, K. and D. Myers. *Reference Solar Spectral Irradiance: Air Mass 1.5*. 2003 March 10 2009 [cited 2011 Janaury 19]; Available from: http://rredc.nrel.gov/solar/spectra/am1.5/.
56. Schroder, D.K., *Semiconductor Material and Device Characterization*. 3rd Edition ed. 2006: Wiley-Interscience.
57. Bernede, J.C., *Organic photovoltaic cells: History, principle and techniques.* Journal of the Chilean Chemical Society, 2008. **53**(3): p. 1549-1564.
58. Kippelen, B., et al., *Liquid-Crystal Approaches to Organic Photovoltaics*, in *Organic Photovoltaics: Mechanisms, Materials and Devices*, S.S. Sun and N.S. Sariciftci, Editors. 2005, Taylor and Francis: Boca Raton. p. 217-237.
59. Xue, J., et al., *4.2% efficient organic photovoltaic cells with low series resistances.* Applied Physics Letters, 2004. **84**(16): p. 3013-3015.
60. Shockley, W. and H.J. Queisser, *Detailed Balance Limit of Efficiency of p-n Junction Solar Cells.* Journal of Applied Physics, 1961. **32**(3): p. 510-519.
61. Henry, C.H., *Limiting efficiencies of ideal single and multiple energy gap terrestrial solar cells.* Journal of Applied Physics, 1980. **51**(8): p. 4494-4500.
62. Osbourne, M. *NREL validates Konarka's 8.3% 'Power Plastic' efficiency record*. 2010 [cited 2011 21 March]; Available from: http://www.pv-tech.org/news/nrel_validates_konarkas_8.3_power_plastic_efficiency_record.
63. Laikhtman, B., *Are excitons really bosons?* Journal of Physics: Condensed Matter, 2007. **19**(29): p. 295214.
64. Xu, Z., B. Hu, and J. Howe, *Improvement of photovoltaic response based on enhancement of spin-orbital coupling and triplet states in organic solar cells.* Journal of Applied Physics, 2008. **103**(4).

65. Gutmann, F. and L.E. Lyons, *Organic Semiconductors*. Wiley Series on the Science and Technology of Materials, ed. J.H. Hollomon, et al. 1967, London: Wiley. 858.
66. Petelenz, P. and M. Andrzejak, *Davydov splitting in the sexithiophene crystal.* Chemical Physics Letters, 2001. **343**(1-2): p. 139-142.
67. Shaw, P.E., A. Ruseckas, and I.D.W. Samuel, *Exciton Diffusion Measurements in Poly(3-hexylthiophene).* Advanced Materials, 2008. **20**(18): p. 3516-3520.
68. Burin, A.L. and M.A. Ratner, *Exciton Migration and Cathode Quenching in Organic Light Emitting Diodesâ€* The Journal of Physical Chemistry A, 2000. **104**(20): p. 4704-4710.
69. Sun, S.S. and C.E. Bonner, *Optimization of Organic Solar Cells in Both Space and Energy-Time Domains*, in *Organic Photovoltaics: Mechanisms, Materials and Devices*, S.S. Sun and N.S. Sariciftci, Editors. 2005, Taylor and Francis: Boca Raton. p. 183-214.
70. Haugeneder, A., et al., *Exciton diffusion and dissociation in conjugated polymer/fullerene blends and heterostructures.* Phys. Rev. B, 1999. **59**(23): p. 15346-15351.
71. Stubinger, T. and B. W., *Exciton diffusionand optical interference in organic donor-acceptor photovoltaic cells.* J. Appl. Phys., 2001. **90**(7): p. 3632-3641.
72. Kurrle, D. and J. Pflaum, *Exciton diffusion length in the organic semiconductor diidenoperylene.* Applied Physics Letters, 2008. **92**: p. 133306-1.
73. Ghosh, A.K. and T. Feng, *Merocynanine organic solar cells.* Journal of Applied Physics, 1978. **49**(12): p. 5982-5989.
74. Yang, C.L., et al., *Exciton diffusion in light-emitting organic thin films studied by photocurrent spectra.* Applied Physics Letters, 2003. **83**(9): p. 1737-1739.
75. StuÂ¨binger, T. and W. BruÂ¨tting, *Exciton diffusion and optical interference in organic donorâ€“acceptor photovoltaic cells*, in *Journal of Applied Physics*. 2001, American Institute of Physics. p. 3632.
76. Terao, Y., H. Sasabe, and C. Adachi, *Correlation of hole mobility, exciton diffusion length, and solar cell characteristics in phthalocyanine/fullerene organic solar cells.* Applied Physics Letters, 2007. **90**(10): p. 103515.

77. Lunt, R.R., J.B. Benziger, and S.R. Forrest, *Relationship between Crystalline Order and Exciton Diffusion Length in Molecular Organic Semiconductors.* Advanced Materials, 2009. **22**(11): p. 1233-1236.
78. Persson, N.-K. and O. Inganas, *Simulations of Optical Processes in Organic Photovoltaic Devices*, in *Organic Photovoltaics: Mechanisms, Materials and Devices*, S.S. Sun and N.S. Sariciftci, Editors. 2005, Taylor and Francis: Boca Raton. p. 107-138.
79. Kalinowski, J. and K. Szybowska, *Photoconduction in the archetype organic hole transporting material TPD.* Organic Electronics, 2008. **9**(6): p. 1032-1039.
80. Moliton, A. and J.-M. Nunzi, *How to model the behaviour of organic photovoltaic cells.* Polymer International, 2006. **55**(6): p. 583-600.
81. Taylor, S. *Electronic State Diagram*. 2009 29th April [cited 2010 2nd November]; Available from: http://depts.washington.edu/cmditr/mediawiki/index.php?title=File:Opv18_energylevel.JPG.
82. Yuan, Y., et al., *Efficiency enhancement in organic solar cells with ferroelectric polymers.* Nat Mater. **10**(4): p. 296-302.
83. Bagnall, D.M. and M. Boreland, *Photovoltaic technologies.* Energy Policy, 2008. **36**(12): p. 4390-4396.
84. Müller, G., et al., *Study of oxygen transport in Czochralski growth of silicon.* Microelectronic Engineering, 1999. **45**(2-3): p. 135-147.
85. Tomaszewski, P.E., *Jan Czochralski--father of the Czochralski method.* Journal of Crystal Growth, 2002. **236**(1-3): p. 1-4.
86. Stahlkocher, *Monokristalines Silizium für die Waferherstellung*. 2005.
87. Myong, S.Y., et al., *Silicon-based thin film solar cells fabricated near the phase boundary by VHF PECVD technique.* Solar Energy Materials and Solar Cells, 2008. **92**: p. 639-645.
88. Hepp, A.F., S.G. Bailey, and R.P. Raffaelle, *Inorganic Photovoltaic Materials and Devices: Past Present and Future*, in *Organic Photovoltaics: Mechanisms, Materials and Devices*, S.S. Sun and N.S. Sariciftci, Editors. 2005, Taylor and Francis: Boca Raton. p. 217-237.

89. Anderson, W.A., A.E. Delahoy, and R.A. Milano, *Thin metal films as applied to Schottky solar cells: optical studies.* Appl. Opt., 1976. **15**(6): p. 1621-1625.
90. Zhu, M., et al., *Microstructure of poly-Si thin films prepared at low temperatures.* Solar Energy Materials and Solar Cells, 2000. **62**(1-2): p. 109-115.
91. Beaucarne, et al., *Thin Film polycrystalline Si solar cells on foreign substrates: film formation at intermediate temperatures (700 – 1300o C).* Appl. Phys. A, 2004. **79**: p. 469-480.
92. Blankenship, R.E., *Natural Organic Photosythetic Solar Energy Transduction*, in *Organic Photovoltaics: Mechanisms, Materials and Devices*, S.S. Sun and N.S. Sariciftci, Editors. 2005, Taylor and Francis: Boca Raton. p. 217-237.
93. Lane, P.A. and Z.H. Kafafi, *Solid-State Organic Photovoltaics: A Review of Molecular and Polymeric Devices*, in *Organic Photovoltaics: Mechanisms, Materials and Devices*, S.S. Sun and N.S. Sariciftci, Editors. 2005, Taylor and Francis: Boca Raton. p. 217-237.
94. Loutfy, R.O., et al., *Phthalocyanine organic solar cells: Indium/x-metal free phthalocyanine Schottky barriers.* Journal of Applied Physics, 1981. **52**(8): p. 5218-5230.
95. Tang, C.W., *Two-layer organic photovoltaic cell.* Applied Physics Letters, 1986. **48**: p. 183.
96. Sariciftci, N.S., et al., *Photoinduced electron transfer from a conducting polymer to buckminsterfullerene.* Science, 1992. **258**(5087): p. 1474-1476.
97. Janssen, R.A.J., D. Moses, and N.S. Sariciftci, *Electron and energy transfer processes of photoexcited oligothiophenes onto tetracyanoethylene and C_{60}.* The Journal of Chemical Physics, 1994. **101**(11): p. 9519-9527.
98. Kim, Y., et al., *Device annealing effect in organic solar cells with blends of regioregular poly(3-hexylthiophene) and soluble fullerene.* Applied Physics Letters, 2005. **86**(6): p. 063502.
99. Kambili, A., et al. *Electron transport in the dye sensitized nanocrystalline cell*. 2001; Available from: http://arxiv.org/abs/cond-mat/0107551v1.
100. Minami, T., *Transparent conducting oxide semiconductors for transparent electrodes.* Semiconductor Science and Technology, 2005. **20**(4): p. S35.

101. Morana, M., et al., *Bipolar Charge Transport in PCPDTBT-PCBM Bulk-Heterojunctions for Photovoltaic Applications.* Advanced Functional Materials, 2008. **18**(12): p. 1757-1766.
102. Ulbricht, R., et al., *Transparent carbon nanotube sheets as 3-D charge collectors in organic solar cells.* Solar Energy Materials and Solar Cells, 2007. **91**(5): p. 416-419.
103. Williams, C.D., et al., *Multiwalled carbon nanotube sheets as transparent electrodes in high brightness organic light-emitting diodes.* Applied Physics Letters, 2008. **93**(18): p. 183506-183506-3.
104. Lee, J.-Y., et al., *Solution-Processed Metal Nanowire Mesh Transparent Electrodes.* Nano Letters, 2007. **8**(2): p. 689-692.
105. Tao, A., et al., *Langmuir-Blodgett Silver Nanowire Monolayers for Molecular Sensing Using Surface-Enhanced Raman Spectroscopy.* Nano Letters, 2003. **3**(9): p. 1229-1233.
106. Cao, Y., et al., *A technique for controlling the alignment of silver nanowires with an electric field.* Nanotechnology, 2006. **17**: p. 2378-2380.
107. Hass, J., et al., *Highly ordered graphene for two dimensional electronics.* Applied Physics Letters, 2006. **89**(14): p. 143106-3.
108. Wang, X., L. Zhi, and K. Mullen, *Transparent, Conductive Graphene Electrodes for Dye-Sensitized Solar Cells.* Nano Letters, 2007. **8**(1): p. 323-327.
109. Hatton, R.A., et al., *A robust ultrathin, transparent gold electrode tailored for hole injection into organic light-emitting diodes.* J. Mater. Chem., 2003. **13**: p. 722-726.
110. Armstrong, N., et al., *Interface modification of ITO thin films: organic photovoltaic cells.* Thin Solid Films, 2003(445): p. 342-352.
111. Tripathi, V., et al., *Role of exciton blocking layers in improving efficiency of copper phthalocyanine based organic solar cells.* Journal of Non-Crystalline Solids, 2008. **354**(19-25): p. 2901-2904.
112. Malyshev, A.V., V.A. Malyshev, and F. Domínguez-Adame, *Low-temperature quenching of one-dimensional localized Frenkel excitons.* Chemical Physics Letters, 2003. **371**(3-4): p. 417-425.

113. Yoo, S., et al., *Analysis of improved photovoltaic properties of pentacene/C60 organic solar cells: Effects of exciton blocking layer thickness and thermal annealing.* Solid-State Electronics, 2007. **51**: p. 1367-1375.
114. Bashar, S.A., *Study of Indium Tin Oxide (ITO) for Novel Optoelectronic Devices*, in *Electrical Engineering*. 1997, King's College: London.
115. Eite, J. and A.G. Spencer, *Indium Tin Oxide for transparent ECM shielding and Anti-static applications,*, in *EMCUK 2004*. 2004: Newbury.
116. Kim, H. and C.M. Gilmore, *Electrical, optical and structural properties of indium-tin-oxide thin films for organic light emitting devices.* Journal of Applied Physics, 1999. **86**(11): p. 6451-6461.
117. Kim, H., et al., *Indium tin oxide thin films deposited by RF-magnetron sputtering for organic electro-luminesence devices.* Ceramic Processing Research, 2003. **4**(2): p. 96-100.
118. Mason, M.G., et al., *Characterization of treated indium-tin-oxide surfaces used in electroluminescent devices.* Journal of Applied Physics, 1999. **86**(3): p. 1688-1692.
119. Eite, J. and A.G. Spencer, *Indium Tin Oxide for transparent ECM shielding and Anti-static applications*, in *EMCUK 2004*. 2004: Newbury.
120. Meng, L.-J. and F. Placido, *Annealing effect on ITO thin films prepared by microwave-enhanced dc reactive magnetron sputtering for telecommunication applications.* Surface and Coatings Technology, 2003. **166**(1): p. 44-50.
121. May, C. and J. Strümpfel, *ITO coating by reactive magnetron sputtering-comparison of properties from DC and MF processing.* Thin Solid Films, 1999. **351**(1-2): p. 48-52.
122. Kurdesau, F., et al., *Comparative study of ITO layers deposited by DC and RF magnetron sputtering at room temperature.* Journal of Non-Crystalline Solids, 2006. **352**(9-20): p. 1466-1470.
123. Vink, T.J., et al., *On the homogeneity of sputter-deposited ITO films Part I. Stress and microstructure.* Thin Solid Films, 1995. **266**(2): p. 145-151.
124. Wu, C.C., et al., *Surface modification of indium tin oxide by plasma treatment: An effective method to improve the efficiency, brightness, and reliability of*

organic light emitting devices. Applied Physics Letters, 1997. **70**(11): p. 1348-1350.

125. Steim, R., et al., *Interface modification for highly efficient organic photovoltaics.* Applied Physics Letters, 2008. **92**(9).
126. Valentini, L., M. Cardinali, and J.M. Kenny, *Selective deposition of semiconducting single-walled carbon nanotubes onto amino-silane modified indium tin-oxide surface for the development of poly(3-hexylthiophene)/carbon-nanotube photovoltaic heterojunctions.* Carbon, 2010. **48**(3): p. 861-867.
127. Kim, Y., et al., *Effects of thickness and thermal annealing of the PEDOT:PSS layer on the performance of polymer solar cells.* Organic Electronics, 2009. **10**(1): p. 205-209.
128. Girtan, M. and M. Rusu, *Role of ITO and PEDOT:PSS in stability/degradation of polymer:fullerene bulk heterojunctions solar cells.* Solar Energy Materials and Solar Cells, 2010. **94**(3): p. 446-450.
129. Gibson, D.R., et al. *Closed field magnetron sputtering: New generation sputtering process for optical coatings*. in *Proceedings of SPIE - The International Society for Optical Engineering*. 2008.
130. Walls, J.M., et al. *Super smooth metal oxide thin films using closed field reactive magnetron sputtering*. in *Proceedings, Annual Technical Conference - Society of Vacuum Coaters*. 2005.
131. Belo, G.S., et al., *A simplified reactive thermal evaporation method for indium tin oxide electrodes.* Applied Surface Science, 2008. **255**(3): p. 755-757.
132. Toki, M. and M. Aizawa, *Sol-Gel Formation of ITO Thin Film from a Sol Including ITO Powder.* Journal of Sol-Gel Science and Technology, 1997. **8**: p. 717-720.
133. Kim, H., et al., *Indium tin oxide thin films grown on flexible plastic substrates by pulsed-laser deposition for organic light-emitting diodes.* Applied Physics Letters, 2001. **79**(3): p. 284-286.
134. Ephemeronium. *Thiophene 2D Full*. 2010 1st September 2010 [cited 2010 28th September]; Available from: http://en.wikipedia.org/wiki/File:Thiophene-2D-full.svg.

135. Wang, Z., et al., *Facile synthesis of dispersible spherical polythiophene nanoparticles by copper(II) catalyzed oxidative polymerization in aqueous medium.* Synthetic Metals. **160**(9-10): p. 921-926.
136. Seshadri, V. and G.A. Sotzing, *Progress in Optically Transparent Conducting Polymers*, in *Organic Photovoltaics: Mechanisms, Materials and Devices*, S.-S. Sun and N.S. Sariciftci, Editors. 2005, Taylor and Francis: Boca Raton.
137. Kanazawa, S., et al., *Photoluminescence and Optical Gain Properties of a Crystalline Thiophene/Phenylene Co-oligomer.* Jpn. J. Appl. Phys., 2008. **47**(12): p. 8961-8964.
138. Bassani, D.M., et al., *Harnessing supramolecular interactions in organic solid-state devices: Current status and future potential.* Coordination Chemistry Reviews. **254**(19-20): p. 2429-2445.
139. Lu, M., et al., *Structure, physical properties and thin-film transistor characteristics of sexithiophene isomers.* Molecular Crystals and Liquid Crystals, 2007. **472**(1): p. 137-143.
140. Yoshikawa, G., et al., *Fabrication of a stable lying sexithiophene ultrathin film on a SiO2 substrate*, in *Photon Factory Activity Report #24 Part B*. 2007, High Energy Accelerator Research Organization (KEK): Tsukuba.
141. Horowitz, G., et al., *Optoelectronic properties of sexithiophene single crystals.* Synthetic Metals, 1997. **90**(3): p. 187-192.
142. Whitman, J.C., et al., *Sexithiophene thin films epitaxially oriented on polytetrafluoroethylene substrates: Structure and morphology.* Thin Solid Films, 1997(303): p. 207-212.
143. Ivanco, J., et al., *Sexithiophene films on ordered and disordered TiO2(1 1 0) surfaces: Electronic, structural and morphological properties.* Surface Science, 2007. **601**(1): p. 178-187.
144. Casado, J., et al., *Infrared spectra of two sexithiophenes in neutral and doped states: a theoretical and spectroscopic study.* Vibrational Spectroscopy, 2002. **30**(2): p. 175-189.
145. Tian, H., et al., *Novel thiophene-aryl co-oligomers for organic thin film transistors.* Journal of Materials Chemistry, 2005. **15**(29): p. 3026-3033.

146. Kwon, J.-H., et al., *p-type semiconducting Î±,Ï‰-dihexylsexithiophene for an organic thin film transistor.* Journal of Applied Physics, 2007. **101**: p. 1-5.

147. Lang, P., et al., *Orientation and structure of thin films of α-ω- dihexyl sexithiophene deposited onto PTFE oriented by friction.* J. Chim. Phys., 1998. **95**(6): p. 1286-1290.

148. Duhm, S., et al., *Vacuum sublimed dihexylsexithiophene thin films: Correlating electronic structure and molecular orientation.* Journal of Applied Physics, 2008. **104**: p. 033717.

149. Barbarella, G., A. Bongini, and M. Zambianchi, *Regiochemistry and Conformation of Poly(3-hexylthiophene) via the Synthesis and the Spectroscopic Characterization of the Model Configurational Triads.* Macromolecules, 1994. **27**(11): p. 3039-3045.

150. Chen, T.-A., X. Wu, and R.D. Rieke, *Regiocontrolled Synthesis of Poly(3-alkylthiophenes) Mediated by Rieke Zinc: Their Characterization and Solid-State Properties.* Journal of the American Chemical Society, 1995. **117**(1): p. 233-244.

151. Bredol, M., et al., *P3HT/ZnS: A new hybrid bulk heterojunction photovoltaic system with very high open circuit voltage.* Solar Energy Materials and Solar Cells, 2009. **93**(5): p. 662-666.

152. Xie, X., *Band gap enhancement by covalent interactions in P3HT/PCBM photovoltaic heterojunction.* THE JOURNAL OF THE KOREAN PHYSICAL SOCIETY. **57**(1): p. 144-148.

153. Bundgaard, E. and F.C. Krebs, *Low band gap polymers for organic photovoltaics.* Solar Energy Materials and Solar Cells, 2007. **91**(11): p. 954-985.

154. Sensfuss, S. and M. Al-Ibrahim, *Optoelectronic Properties of Conjugated Polymer/Fullerene Binary Pairs with Variety of LUMO Level Differences*, in *Organic Photovoltaics: Mechanisms, Materials and Devices*, S.-S. Sun and N.S. Sariciftci, Editors. 2005, Taylor and Francis: Boca Raton.

155. Geiser, A., et al., *Poly(3-hexylthiophene)/C60 heterojunction solar cells: Implication of morphology on performance and ambipolar charge collection.* Solar Energy Materials and Solar Cells, 2008. **92**(4): p. 464-473.

156. Guo, T.F., et al., *Effects of film treatment on the performance of poly(3-hexythiophene)/soluble fullerene-based organic solar cells.* Thin Solid Films, 2008(516): p. 3138-3142.
157. Truong, N.T.N., W.K. Kim, and C. Park, *Effect of CdSe/P3HT composition on electrical and structural properties of bulk hetero-junction solar cell active layer.* Solar Energy Materials and Solar Cells, 2010. **In Press, Corrected Proof**.
158. Flanagan, D. *Polythiophenes Bipolaron.png*. 2007 18th March 2007 [cited 2010 5th October]; Available from: http://en.wikipedia.org/wiki/File:Polythiophenes_Bipolaron.png.
159. Izumi, T., et al., *Synthesis and Spectroscopic Properties of a Series of Î²-Blocked Long Oligothiophenes up to the 96-mer:â€‰ Revaluation of Effective Conjugation Length.* Journal of the American Chemical Society, 2003. **125**(18): p. 5286-5287.
160. Nakanishi, H., et al., *Synthesis and Properties of the Longest Oligothiophenes: The Icosamer and Heptacosamer.* The Journal of Organic Chemistry, 1998. **63**(24): p. 8632-8633.
161. Ten Hoeve, W., et al., *Substituted 2,2':5',2'':5'',2''':5''',2'''':5'''',2''''':5''''',2'''''':5''''''-undecithiophenes, the longest characterized oligothiophenes.* Journal of the American Chemical Society, 1991. **113**(15): p. 5887-5889.
162. Flanagan, D. *Polythiophenes Conjugation*. 2007 19th March 2007 [cited 2010 5th October]; Available from: http://en.wikipedia.org/wiki/File:Polythiophenes_Conjugation.png.
163. Kim, T.-H., et al., *Electroluminescent Characteristics of Conjugated Polymer/Ionomer Blend Devices According to Ionic Contents.* Molecular Crystals and Liquid Crystals, 2006. **444**: p. 107 - 112.
164. Park, J., Y. Kwon, and T.W. Lee, *Layer-by-Layer Spin Self-Assembled Hole Injection Layers Containing a Perfluorinated Ionomer for Efficient Polymer Light-Emitting Diodes.* Macromolecular Rapid Communications, 2007. **28**(12): p. 1366-1372.
165. Shaddack. *PEDOT*. 2007 24th January 2007 [cited 2010 6th October]; Available from: http://en.wikipedia.org/wiki/File:PEDOT.png.

166. Yan, H., et al., *Poly(3,4-ethylenedioxythiophene)/poly(4-styrenesulfonate): Correlation between colloidal particles and thin films.* Thin Solid Films, 2009. **517**(11): p. 3299-3303.
167. Zhang, X., A.G. MacDiarmid, and S.K. Manohar, *Chemical synthesis of PEDOT nanofibers.* Chemical Communications, 2005(42): p. 5328-5330.
168. Aldrich, S. *Poly(3,4-ethylenedioxythiophene)-poly(styrenesulfonate).* 2010 [cited 2010 7th October]; Available from: http://www.sigmaaldrich.com/catalog/ProductDetail.do?lang=en&N4=655201|ALDRICH&N5=SEARCH_CONCAT_PNO|BRAND_KEY&F=SPEC.
169. Yan, J., et al., *Electropolymerized poly(3,4-ethylenedioxythiophene):poly(styrene sulfonate) (PEDOT:PSS) film on ITO glass and its application in photovoltaic device.* Solar Energy Materials and Solar Cells, 2010. **94**(2): p. 390-394.
170. Soo Kim, Y., et al., *Highly conductive PEDOT/silicate hybrid anode for ITO-free polymer solar cells.* Solar Energy Materials and Solar Cells, 2010. **In Press, Corrected Proof**.
171. Chiang, W.-T., et al., *Increasing the Fill Factor and Power Conversion Efficiency of Polymer Photovoltaic Cell Using V_2O_5/CuPc as a Buffer Layer*. Japanese Journal of Applied Physics, 2010. **49**: p. 4.
172. Zhang, F. and O. Inganas, *Conducting and Transparent Polymer Electrodes*, in *Organic Photovoltaics: Mechanisms, Materials and Devices*, S.-S. Sun and N.S. Sariciftci, Editors. 2005, Taylor and Francis: Boca Raton.
173. Han, Y.F., et al., *Kinetics of ethylene combustion in the synthesis of vinyl acetate over a Pd/SiO2 catalyst.* Journal of Catalysis, 2004. **224**(1): p. 60-68.
174. Aldrich, S. *Poly (Vinyl Acetate).* 2011 [cited 2011 28 January]; Available from: http://www.sigmaaldrich.com/catalog/ProductDetail.do?lang=en&N4=189480|ALDRICH&N5=SEARCH_CONCAT_PNO|BRAND_KEY&F=SPEC.
175. Baskaran, R., et al., *Dielectric and conductivity relaxations in PVAc based polymer electrolytes.* Ionics, 2004. **10**(1-2): p. 129-134.
176. Salaoru, I. and S. Paul, *Electrical bistability in a composite of polymer and barium titanate nanoparticles.* Philosophical Transactions of the Royal Society

A: Mathematical, Physical and Engineering Sciences, 2009. **367**(1905): p. 4227-4234.

177. Salaoru, I. and S. Paul, *Electrically Re-writable Non Volatile Memory Device - Using a Blend of Sea Salt and Polymer.* Advances in Science and Technology, 2008(54): p. 486-490.
178. Soldano, C., A. Mahmood, and E. Dujardin, *Production, properties and potential of graphene.* Carbon, 2010. **48**(8): p. 2127-2150.
179. Avouris, P. and J. Chen, *Nanotube electronics and optoelectronics.* Materials Today, 2006. **9**(10): p. 46-54.
180. Azami, S.M., R. Pooladi, and M.H. Sheikhi, *Local [sigma]-[pi] mixing in C60 buckminsterfullerene.* Journal of Molecular Structure: THEOCHEM, 2009. **901**(1-3): p. 153-156.
181. Belin, T. and F. Epron, *Characterization methods of carbon nanotubes: A review.* Materials Science and Engineering B: Solid-State Materials for Advanced Technology, 2005. **119**(2): p. 105-118.
182. Kebes. *CNT names*. 2005 [cited 2010 20th September]; Available from: http://en.wikipedia.org/wiki/File:CNTnames.png.
183. Bellucci, S. *Carbon nanotubes: Physics and applications*. in *Physica Status Solidi C: Conferences*. 2005.
184. Billups, W.E., *Buckminsterfullerenes*. 1993.
185. Mills, B. *Buckminsterfullerene*. 25th April 2007 [cited 2010 14th September]; Available from: http://en.wikipedia.org/wiki/File:Buckminsterfullerene-2D-skeletal.png.
186. Roman, L.S., *Photovoltaic devices Based on Polythiophene/C60,* in *Organic Photovoltaics: Mechanisms, Materials and Devices,* S.S. Sun and N.S. Sariciftci, Editors. 2005, Taylor and Francis: Boca Raton. p. 367-386.
187. Bruetting, W., et al., *Ambipolar blends of CuPc and C60: charge carrier mobility, electronic structure and its implications for solar cell applications*. 2007.
188. Bhalla, A.S., R. Guo, and R. Roy, *The perovskite structure – a review of its role in ceramic science and technology.* Materials Research Innovations, 2000. **4**(1): p. 3-26.

189. Cadmium. *Perovskite*. 2007 6th August 2007 [cited 2010 7th October]; Available from: http://en.wikipedia.org/wiki/File:Perovskite.jpg.
190. Yang, T.-I. and P. Kofinas, *Dielectric properties of polymer nanoparticle composites.* Polymer, 2007. **48**(3): p. 791-798.
191. Suresh, M.B., et al., *Dielectric and Ferroelectric Properties of Polyvinylidene Fluoride (PVDF)-Pb0.52Zr0.48TiO3 (PZT) Nano Composite Films*, in *Ferroelectrics*. 2009, Taylor & Francis Ltd. p. 80-86.
192. Wang, J., et al., *Enhanced dielectric response in P(VDF-TrFE) based all-organic Nanocomposites.* Journal of Polymer Science, Part B: Polymer Physics. **48**(4): p. 490-495.
193. Ioannou, G., A. Patsidis, and G.C. Psarras, *Dielectric and functional properties of polymer matrix/ZnO/BaTiO3 hybrid composites.* Composites Part A: Applied Science and Manufacturing. **42**(1): p. 104-110.
194. Wang, J.-W., et al., *A large enhancement in dielectric properties of poly(vinylidene fluoride) based all-organic nanocomposite.* Polymer, 2009. **50**(2): p. 679-684.
195. Liu, W.C., et al., *Optical properties of ferroelectric nanocrystal-containing polymer BaTiO₃/polycarbonate films.* Journal of Applied Physics, 2005. **98**: p. 024112.
196. Arlt, G., D. Hennings, and G. de With, *Dielectric properties of fine‐grained barium titanate ceramics.* Journal of Applied Physics, 1985. **58**(4): p. 1619-1625.
197. Scaife, B.K.P., ed. *Complex Permittivity*. 1971, The English Universities Press Ltd: London. 170.
198. Alldredge, L.M.B., et al., *Phase transitions and the temperature dependence of the dielectric properties in tetragonally strained barium strontium titanate films.* Applied Physics Letters, 2009. **94**(5): p. 052904.
199. Hoshina, T., et al., *Composite structure and size effect of barium titanate nanoparticles.* Appl. Phys. Lett., 2008. **93**: p. 192914.
200. Sigma-Aldrich. *Barium Titanate*. Materials Safety Data Sheet [cited 2011 7 February]; Available from: http://www.sigmaaldrich.com/catalog/DisplayMSDSContent.do.

201. Guennou, M., et al., *Pressure-temperature phase diagram of SrTiO3 up to 53 GPa.* Physical Review B. **81**(5): p. 10.
202. Mohan, C.R.K. and P.K. Bajpai, *Effect of sintering optimization on the electrical properties of bulk BaxSr1-xTiO3 ceramics.* Physica B: Condensed Matter, 2008. **403**(13-16): p. 2173-2188.
203. Sigma-Aldrich. *Strontium Titanate*. Materials Safety Data Sheet [cited 2011 07 February]; Available from: http://www.sigmaaldrich.com/catalog/DisplayMSDSContent.do.
204. Xu, J., et al., *Dielectric properties of Y-doped Ba1-xSrxTiO3 ceramics.* Optica Applicata. **40**(1): p. 255-264.
205. Dec, J., et al., *Unique Features of Strontium Titanate*, in *Ferroelectrics*. 2005, Taylor & Francis Ltd. p. 7-18.
206. Hayward, S.A., F.D. Morrison, and J.F. Scott, *Interaction between quantum paraelectricity and ferroelasticity in SrTiO3.* Journal of Physics-Condensed Matter, 2005. **17**(43): p. 7009-7022.
207. Stuart, R.V., *Vacuum Technology, Thin Films and Sputtering, An Introduction*. 1983, London: Academic Press Inc. 151.
208. Murray, K.K. *Schematic of a diffusion pump.* 2008 [cited 2010 25 August]; Available from: http://en.wikipedia.org/wiki/File:Diffusion_pump_schematic.gif.
209. Harris, N., *Modern Vacuum Practice*. 3rd ed. 2007, Glasgow: Bell and Bain Ltd.
210. Walls, M. and D. Gibson, *High-throughput optical coating.* Photonics Spectra, 2008. **42**(8): p. 56-59.
211. Nordiko, *Operation of RF Power Supply Systems*, in *Handbook on RF Sputtering*. 1984, Nordiko: Havant.
212. Nordiko, *Explanation of RF Sputtering Systems*, in *Handbook on RF Sputtering*. 1984, Nordiko: Havant.
213. Chen, F.C., H.C. Tseng, and C.J. Ko, *Solvent mixtures for improving device efficiency of polymer photovoltaic devices.* Applied Physics Letters, 2008. **92**: p. 103316.
214. Cheng, H.-L., W.-Q. Lin, and F.-C. Wu, *Effects of solvents and vacancies on the electrical hysteresis characteristics in regioregular poly(3-hexylthiophene)*

organic thin-film transistors. Applied Physics Letters, 2009. **94**(22): p. 223302-3.

215. Krebs, F.C., *Fabrication and processing of polymer solar cells: A review of printing and coating techniques.* Solar Energy Materials and Solar Cells, 2009. **93**(4): p. 394-412.

216. Yan, H. and H. Okuzaki, *Effect of solvent on PEDOT/PSS nanometer-scaled thin films: XPS and STEM/AFM studies.* Synthetic Metals, 2009. **159**(21-22): p. 2225-2228.

217. Norrman, K., A. Ghanbari-Siahkali, and N.B. Larsen, *Studies of Spin-coated polymer films.* Annu. Rep. Prog. Chem., Sect. C., 2005(101): p. 174-201.

218. Dittmer, J.J., et al., *Crystal network formation in organic solar cells.* Solar Energy Materials and Solar Cells, 2000. **61**(1): p. 53-61.

219. Ko, C.J., Y.-K. Lin, and F.C. Chen, *Microwave Annealing of Polymer Photovoltaic Devices.* Adv. Mater., 2007. **19**(21): p. 3520-3523.

220. Park, J.H. and E. Kim, *Effect of electric-field-assisted thermal annealing of poly(4-vinylphenol) film on its dielectric constant.* Applied Physics Letters, 2008. **92**: p. 103311.

221. Song, et al., *The effect of annealing treatment on the performance of bulk heterojunction solar cells with donor and acceptor different weight ratios*. Vol. 52. 2009, Heidelberg, ALLEMAGNE: Springer. 5.

222. Marsh, R.A., et al., *Effect of Annealing on P3HT:PCBM Charge Transfer and Nanoscale Morphology Probed by Ultrafast Spectroscopy.* Nano Letters, 2010. **10**(3): p. 923-930.

223. Kaufmann, E.N., ed. *Characterization of Materials Volume 2*. Characterization of Materials. Vol. 2. 2003, John Wiley and Sons: Hoboken. 1392.

224. SuperManu. *Onde Electromagnetique*. 2007 15th May 2007 [cited 2010 28th October]; Available from: http://en.wikipedia.org/wiki/File:Onde_electromagnetique.svg.

225. Stannered. *Ellipsometry Setup*. 2008 3rd January 2008 [cited 2010 28th October]; Available from: http://en.wikipedia.org/wiki/File:Ellipsometry_setup.svg.

226. Sanyo, *Data Sheet: Sanyo Amorphous Solar Cell, AM-5308*. 2008, Sanyo Semiconductor Co., Ltd. p. 2.
227. Morgan, M.J., G. Jakovidis, and I. McLeod, *An experiment to measure the I-V characteristics of a silicon solar cell.* Physics Education, 1994. **29**(4): p. 252-254.
228. Gfroerer, T.H., *Photoluminescence in Analysis of Surfaces and Interfaces*, in *Encyclopedia of Analytical Chemistry*, R.A. Meyers, Editor. 2000, John Wiley and Sons Ltd.: Chichester. p. 9209-9231.
229. Keithley, *Making I-V and C-V Measurements on Solar/Photovoltaic Cells Using the Model 4200-SCS Semiconductor Characterization System*, K. Instruments, Editor. 2007, Keithley Instruments.
230. Lee, M.-K., et al., *Extraction of solar cell series resistance without presumed current-voltage functional form.* Solar Energy Materials and Solar Cells. **94**(3): p. 578-582.
231. Djurisic, A.B. and C.Y. Kwong, *The Influence of the Electrode Choice on the Performance of Organic Solar Cells*, in *Organic Photovoltaics: Mechanisms, Materials and Devices*, S.-S. Sun and N.S. Sariciftci, Editors. 2005, Taylor and Francis: Boca Raton.
232. Tauc, J., R. Grigorovici, and A. Vancu, *Optical Properties and Electronic Structure of Amorphous Germanium.* physica status solidi (b), 1966. **15**(2): p. 627-637.
233. Tauc, J., *Optical properties and electronic structure of amorphous Ge and Si.* Materials Research Bulletin, 1968. **3**(1): p. 37-46.
234. Huxter, V., *Optical and Material Properties of Colloidal Semiconductor Nanocrystals*, in *Chemistry*. 2009, Toronto: Toronto. p. 222.
235. Brabec, C.J., et al., *Photo-induced FT-IR spectroscopy and CW-photocurrent measurements of conjugated polymers and fullerenes blended into a conventional polymer matrix.* Solar Energy Materials and Solar Cells, 2000. **61**: p. 19-33.
236. Gans, P. *FTIR Interferometer*. 2010 30th July [cited 2010 16th November]; Available from: http://en.wikipedia.org/wiki/File:FTIR_Interferometer.png.

237. Overlord, Q. *Atomic Force Microscope Block Diagram*. 2008 6 October 2009 [cited 2011 28 January]; Available from: http://en.wikipedia.org/wiki/File:Atomic_force_microscope_block_diagram.svg.
238. Palermo, V., et al., *The Relationship between Nanoscale Architecture and Function in Photovoltaic Multichromophoric Arrays as Visualised by Kelvin Probe Force Microscopy*. J. AM. Chem. Soc., 2008(130): p. 14605-14614.
239. Palermo, V., M. Palma, and P. Samori, *Electronic Characterization of Organic Thin Films by Kelvin Probe Force Microscopy*. Adv. Mater., 2006. **18**: p. 145-164.
240. Palermo, V., et al., *A Kelvin Probe Force Microscopy Study of the Photogeneration of Surface Charges in All-Thiophene Photovoltaic Blends.* Adv. Funct. Mater., 2007(17): p. 472-478.
241. Palermo, V., et al., *Influence of Molecular Order on the Local Work Function of Nanographene Architectures: A Kelvin-Probe Force Microscopy Study*. ChemPhysChem, 2005. **6**: p. 2371-2375.
242. Medvedovski, E., et al., *Advanced indium-tin oxide ceramics for sputtering targets.* Ceramics International, 2008. **34**(5): p. 1173-1182.
243. Grant, I.S. and W.R. Philips, *Electromagnetism*. 2nd ed. Manchester Physics Series. 1999, Chichester: Wiley. 525.
244. Flaschen, M. *Dielectric Model*. 2007 5th December [cited 2010 2nd December]; Available from: http://en.wikipedia.org/wiki/File:Dielectric_model.svg.
245. November, P. *Capacitor schematic with dielectric*. 2008 11th May [cited 2010 2nd December]; Available from: http://en.wikipedia.org/wiki/File:Capacitor_schematic_with_dielectric.svg.
246. Barber, P., et al., *Polymer Composite and Nanocomposite Dielectric Materials for Pulse Power Energy Storage.* Materials, 2009. **2**(4): p. 1697-1733.
247. Jonscher, A.K., *Dielectric Relaxation in Solids*. 1996, London: Chelsea Dielectrics Press. 380.
248. Mauritz, K.A. *Dielectric Response*. 2008 28th April [cited 2011 11th January]; Available from: http://en.wikipedia.org/wiki/File:Dielectric_responses.svg.

249. Capsal, J.-F., et al., *Nanotexture influence of BaTiO3 particles on piezoelectric behaviour of PA 11/BaTiO3 nanocomposites.* Journal of Non-Crystalline Solids. **356**(11-17): p. 629-634.
250. Kymakis, E. and G.A.J. Amaratunga, *Solar Cells Based on Composites of Donor Conjugated Polymers and Carbon Nanotubes*, in *Organic Photovoltaics: Mechanisms, Materials and Devices*, S.-S. Sun and N.S. Sariciftci, Editors. 2005, Taylor and Francis: Boca Raton.
251. Kim, Y.S., et al., *Observation of room-temperature ferroelectricity in tetragonal strontium titanate thin films on SrTiO[sub 3] (001) substrates.* Applied Physics Letters, 2007. **91**(4): p. 042908.
252. Dang, Z.-M., et al., *Enhancement of dielectric permittivity in the ZnO/PZT ceramic matrix nanocomposites.* Materials Chemistry and Physics, 2008. **109**(1): p. 1-4.
253. George, S. and M.T. Sebastian, *Three-phase polymer-ceramic-metal composite for embedded capacitor applications.* Composites Science and Technology, 2009. **69**(7-8): p. 1298-1302.
254. Ogitani, S., S.A. Bidstrup-Allen, and P.A. Kohl, *Factors influencing the permittivity of polymer/ceramic composites for embedded capacitors.* Advanced Packaging, IEEE Transactions on, 2000. **23**(2): p. 313-322.
255. Subodh, G., et al., *Dielectric response of high permittivity polymer ceramic composite with low loss tangent.* Applied Physics Letters, 2009. **95**(6): p. 062903.
256. Kamalasanan, M.N., N.D. Kumar, and S. Chandra, *Structural and microstructural evolution of barium titanate thin films deposited by the sol-gel process.* Journal of Applied Physics, 1994. **76**(8): p. 4603.
257. Yun, F., et al., *Study of structural and optical properties of nanocrystalline silicon embedded in SiO2.* Thin Solid Films, 2000. **375**(1-2): p. 137-141.
258. Metals, A.S.o., *Characterization and Failure Analysis of Plastics*. 2003: ASM International. 482.
259. Lamb, D.R., *Electrical Conduction Mechanisms in Thin Insulating Films*. Methuen's Monographs on Physical Subjects, ed. B.L. Worksnop. 1967, London: Spottiswoode, Ballantyne & Co. Ltd. 114.

260. Mehendru, P.C., et al., *Electrical conduction in pure and iodine-doped polyvinyl acetate thick films.* physica status solidi (a), 1977. **42**(1): p. 403-407.
261. Varlow, B.R., J. Robertson, and K.P. Donnelly, *Nonlinear fillers in electrical insulating materials.* IET Science, Measurement and Technology, 2007. **1**(2): p. 96-102.
262. Pradhan, B. and A.J. Pal, *Role of dielectric properties in organic photovoltaic devices.* Chemical Physics Letters, 2005. **416**(4-6): p. 327-330.
263. Vanlaeke, P., et al., *Polythiophene based bulk heterojunction solar cells: Morphology and its implications.* Thin Solid Films, 2006. **511-512**: p. 358-361.
264. Huang, H., *Solar energy: Ferroelectric photovoltaics.* Nat Photon. **4**(3): p. 134-135.
265. Yang, S.Y., et al., *Above-bandgap voltages from ferroelectric photovoltaic devices.* Nat Nano. **5**(2): p. 143-147.
266. Shinar, R. and J. Shinar, *Organic Electronics in Sensors and Biotechnology*. 2009: McGraw-Hill Professional.
267. Denhoff, M.W. and N. Drolet, *The effect of the front contact sheet resistance on solar cell performance.* Solar Energy Materials and Solar Cells, 2009. **93**(9): p. 1499-1506.
268. Muhsin, B., et al., *Influence of polymer solar cell geometry on series resistance and device efficiency.* physica status solidi (a), 2009. **206**(12): p. 2771-2774.
269. Kim, S.S., et al., *Efficient Polymer Solar Cells Fabricated by Simple Brush Painting*. 2007. p. 4410-4415.
270. Javier, A. and E.E. Foos, *Nanocrystal Photovoltaic Paint Sprayed With a Handheld Airbrush.* Nanotechnology, IEEE Transactions on, 2009. **8**(5): p. 569-573.
271. Park, S., *2008 3rd Training Workshop*, C. Team, Editor. 2008, Park Systems Ltd.
272. Park, S., *Option Training*, C.S. Team, Editor. 2008, Park Systems Ltd.
273. Choi, O., et al., *Role of sulfide and ligand strength in controlling nanosilver toxicity.* Water Research, 2009. **43**(7): p. 1879-1886.

274. Bharathi Mohan, D., K. Sreejith, and C.S. Sunandana, *Surface plasmon exciton transition in ultra-thin silver and silver iodide films.* Applied Physics B: Lasers & Optics, 2007. **89**: p. 59-63.
275. Nath, S., et al., *Silver organosol: Synthesis, characterisation and localised surface plasmon resonance study.* New Journal of Chemistry, 2005. **29**(12): p. 1527-1534.
276. Kim, S.-S., et al., *Plasmon enhanced performance of organic solar cells using electrodeposited Ag nanoparticles.* Applied Physics Letters, 2008. **93**(7): p. 073307.
277. Evanoff, D.D. and G. Chumanov, *Synthesis and Optical Properties of Silver Nanoparticles and Arrays.* ChemPhysChem, 2005. **6**(7): p. 1221-1231.
278. Ihara, M., M. Kanno, and S. Inoue, *Photoabsorption-enhanced dye-sensitized solar cell by using localized surface plasmon of silver nanoparticles modified with polymer.* Physica E: Low-dimensional Systems and Nanostructures, 2010. **In Press, Corrected Proof**.
279. Symonds, C., et al., *Particularities of surface plasmon–exciton strong coupling with large Rabi splitting.* New Journal of Physics, 2008(6): p. 065017.
280. Symonds, C., et al., *Exciton/plasmon mixing in metal-semiconductor heterostructures.* Superlattices and Microstructures, 2010. **47**(1): p. 50-54.
281. Bellessa, J., et al., *Strong coupling between surface plasmons and excitons in an organic semiconductor.* Physical Review Letters, 2004. **93**(3): p. 036404-1.
282. Lindquist, N.C., et al., *Plasmonic nanocavity arrays for enhanced efficiency in organic photovoltaic cells.* Applied Physics Letters, 2008. **93**: p. 123308.
283. Reilly, T.H., et al., *Surface-plasmon enhanced transparent electrodes in organic photovoltaics.* Applied Physics Letters, 2008. **92**(24): p. 243304-3.
284. Jiongxin, L., M. Kyoung-Sik, and C.P. Wong. *Development of novel silver nanoparticles/polymer composites as high K polymer matrix by in-situ photochemical method*. in *Electronic Components and Technology Conference, 2006. Proceedings. 56th*. 2006.
285. Liu, X., J. Luo, and J. Zhu, *Size Effect on the Crystal Structure of Silver Nanowires.* Nano Letters, 2006. **6**(3): p. 408-412.

286. Rodrigues, V., et al., *Quantum conductance in silver nanowires: Correlation between atomic structure and transport properties.* Physical Review B, 2002. **65**(15): p. 153402.
287. Shi, S., et al., *The growth of thin silver nanowires bundle using $RbAg_4I_5$ crystal grain thin film and the ionic conductivity of the thin film.* Physica B, 2005(362): p. 266-270.
288. Englander, O., et al., *Electric Field Assisted Growth and Self-Assembly of Intrinsic Silicon Nanowires.* Nano Letters, 2005. **5**(4): p. 705-708.
289. Sun, Y., et al., *Crystalline Silver Nanowires by Soft Solution Processing.* Nano Letters, 2001. **2**(2): p. 165-168.
290. Korte, K., *Rapid Synthesis of Silver Nanowires*. 2007.
291. Chen, C., et al., *Study on the growth mechanism of silver nanorods in the nanowire-seeding polyol process.* Materials Chemistry and Physics, 2008. **107**(1): p. 13-17.
292. Sun, Y., et al., *Polyol Synthesis of Uniform Silver Nanowires:â€‰ A Plausible Growth Mechanism and the Supporting Evidence.* Nano Letters, 2003. **3**(7): p. 955-960.